ISBN : 978-9924-9047-48

Techno-Science Research Journal
Volume 13, Special Issue on
Earth Resources and
Geo-Environment Technology

ORGANIZED & HOSTED BY
FACULTY OF GEO-RESOURCES AND GEOTECHNICAL ENGINEERING,
INSTITUTE OF TECHNOLOGY OF CAMBODIA

PARTNERED WITH:

- **JAPAN INTERNATIONAL COOPERATION AGENCY, JICA**
- **KYUSHU UNIVERSITY, JAPAN**
- **UNIVERSITI SAINS MALAYSIA, MALAYSIA**
- **CARAGA STATE UNIVERSITY, PHILIPPINES**
- **IGCP 700, MAHASARAKHAM UNIVERSITY, THAILAND**

INSTITUTE OF TECHNOLOGY OF CAMBODIA
PHNOM PENH, CAMBODIA
2024

Table of Contents

Techno-Science Research Journal V13 (Special Issue) (2025) P 1-7

Content list available at ITC

Techno-Science Research Journal

Journal Homepage: http://techno-srj.itc.edu.kh/

Techno-Science Research Journal

Causes of structural collapse and sandstone deterioration in the Angkor monument

Etsuo Uchida*

Department of Resources and Environmental Engineering, Faculty of Science and Engineering, Waseda University, Ohkubo 3-4-1, Shinjuku, Tokyo 169-8555, Japan

Received: 1 November 2024; Revised: 1 January 2025; Accepted: 20 June 2025; Available online: October 2025

Abstract: *The Angkor monument in Cambodia was constructed mainly between the 9th and 13th centuries and was added to the World Heritage List of UNESCO in 1992. The Angkor monument is built with sandstone, laterite, and bricks. The most commonly used sandstone, specifically gray to yellowish-brown sandstone, did not show any differences in the chemical or constituent mineral composition among the investigated temples. However, significant differences were found in the average magnetic susceptibility of sandstone. The sandstone blocks were obtained from the southeastern foothills of Kulen Mountain, situated 30 km northeast of the Angkor monument, and transported via a canal. Physical, chemical, and biological weathering contribute to structural collapse and sandstone deterioration, with water playing an indispensable role in this complex chain of events. This paper describes seven causes related to structural collapse and sandstone deterioration in the Angkor monument: (1) uniaxial compressive strength of sandstone; (2) salt weathering; (3) thermal expansion–contraction cycle caused by sunlight; (4) uneven ground subsidence; (5) traditional construction techniques; (6) biological activity; and (7) human activity.*

Keywords: Angkor monument; uniaxial compressive strength; salt weathering; thermal expansion–contraction cycle; uneven ground subsidence; traditional construction techniques; biological activity; human activity

1. INTRODUCTION

The Angkor monument is the most famous historical site in Southeast Asia, and is located approximately 250 km northwest of Phnom Penh, around Siem Reap city. The Angkor monument was constructed as a Hindu or Buddhist temple complex mainly during the 9th to 13th centuries, but was abandoned in the 15th century because of the Ayutthaya invasion. The Angkor monument was added to the World Heritage List of UNESCO in 1992.

Sandstone and laterite are the main construction materials in the Angkor monument [1]. Bricks have also been used in relatively old temples constructed between the 9th and 10th centuries. Three types of sandstone are used in the Angkor monument, with gray to yellowish-brown sandstone being the most common. For laterite, two types can be distinguished: porous laterite and pisolitic laterite [2].

Fig. 1(a–c) shows Prasat Kravan, Baksei Chamkron, and East Mebon constructed in the 10th century, respectively. Prasat Kravan is built with bricks. The Baksei Chamkron and East Mebon sanctuaries are also built with bricks, but their platforms are built with laterite. The Angkor Wat and Bayon temples are the most beautiful and famous temples in the Angkor monument. Bayon temple is characterized by many faced towers. Both temples were constructed in the 12th century. The surface of the Angkor Wat and Bayon temples consists of gray to yellowish-brown sandstone. However, laterite is used inside the platform (Fig. 1(d–f)).

The gray to yellowish-brown sandstone is the most important stone material in the Angkor monument. This sandstone exhibits color variation ranging from gray to brown, and mainly consists of quartz, plagioclase, K-feldspar, biotite, muscovite, and rock fragments. Micas are arranged along the bedding plane [1].

The whole rock chemical composition of sandstones obtained from representative temples were analyzed [1]. Systematic differences in the whole rock chemical composition, including minor elements, were not found [1]. However, systematic differences in magnetic susceptibility were found. Based on magnetic susceptibility, 11 construction stages involving sandstone during the Angkor period were identified [3]. This means that the quarry changed over time.

The gray to yellowish-brown sandstone was supplied from the Phu Kradung Formation of the Jurassic to Cretaceous age [4]. In Cambodia, this geological formation is known as the Red

* Corresponding author: Etsuo Uchida
E-mail: weuchida@waseda.jp

Terrain Formation, and is widely distributed in the northeastern area. Around the Angkor monument, this formation is found only in the southeastern foothills of Kulen Mountain, where 145 ancient quarries have been discovered in the foothills [5–6].

The sandstone blocks are considered to have been transported using a canal connecting Kulen Mountain and the Angkor area [5].

Fig. 1. (a) Prasat Kravan temple built with bricks; (b) Baksei Chamkron temple built with bricks (sanctuary) and laterite (platform); (c) East Mebon temple built with bricks (sanctuary) and laterite (platform); (d) Angkor Wat temple built with sandstone; (e) Bayon temple built with sandstone; (f) laterite blocks inside a platform of Angkor Wat temple.

2. STRUCTURE COLLAPSE AND SANDSTONE DETERIORATION

The structure collapse and sandstone deterioration in the Angkor monument can be attributed to the following seven causes: (1) uniaxial compressive strength of sandstone, (2) salt weathering, (3) thermal expansion–contraction cycle by sunlight, (4) uneven ground subsidence, (5) traditional construction methods, (6) biological activity, and (7) human activity.

2.1 Strength of sandstone

The uniaxial compressive strength of gray to yellowish-brown sandstone blocks with a size of 10 cm × 10 cm × 20 cm obtained from the Angkor Wat temple was measured. The uniaxial compressive strength of the sandstone depends on the orientation of the bedding plane. The uniaxial compressive strength along the bedding plane is 300–350 kgf/cm^{2,} and 380–540 kgf/cm^2 in the direction perpendicular to the bedding plane. These values are similar to the strength of concrete. Therefore, sandstone has sufficient uniaxial compressive strength as a construction material.

However, because micas are arranged along the bedding planes and exhibit a preferred orientation in sandstone [1], the sandstone tends to be broken along the bedding planes (Fig. 2).

Fig. 2. Deterioration related to bedding planes of sandstone. (a) Fissures along bedding planes in pillar of Angkor Wat temple; (b) exfoliation along bedding planes in window frame of Prasat Suor Prat (N3 tower); (c) fissures along bedding plane in platform of Ta Keo temple.

2.2 Salt weathering

2.2.1 Salt weathering related to bat guano

This type of weathering is typical in the Angkor Wat temple (Fig. 3(a)). The Phnom Krom temple situated on the top of a small mountain exhibits the most severe deterioration in the Angkor monument (Fig. 3(b)) [7–8]. The sandstone blocks have been changed into brownish color and exhibit exfoliation. Some sandstone blocks exhibit large holes. A large number of bats still inhabit the Angkor monument, and deposit excrement (guano) daily. Bat guano contains sulfur and phosphorus, which dissolve into rainwater. Then, the rainwater containing sulfur and phosphorus rises up the walls and pillars. When the water evaporates, the dissolved sulfur and phosphorus crystallize as sulfates and phosphates near the sandstone surface. Owing to crystallization pressure, the sandstone exfoliates near the surface.

Fig. 3. Deterioration of sandstone caused by salt weathering related to bat guano: (a) pillars in cruciform gallery of Angkor Wat temple; (b) severely deteriorated sandstone in Phnom Krom temple

Gypsum and phosphate minerals, such as brushite, newberyite, whitlokite, taranakite, wavellite, and berlinite, have formed by salt weathering related to bat guano.

Table 1 lists the components that dissolve from bat guano into rainwater [9]. Substantial amounts of sulfate, phosphate, and nitrate have dissolved into rainwater as anions.

Table 1. Components leached from bat guano; 30 g of bat guano was dissolved into 150 ml of rainwater over a period of 2 hours [9].

	Sample A	Sample B	Sample C
pH	4.55	5.35	5.95
Chlorine	85	127	143
Nitrite	3.9	3.2	23.5
Nitrate	130.5	156	165
Sulfate(S)	66.7	103.3	68.3
Phosphate	240.8	260.9	374.6
Ammonium	82.5	87.5	142.5
Sodium	92.9	111	108.5
Potassium	195	214.5	251.9
Calcium	21.6	44.8	3.2
Magnesium	31.1	68	21.2
Iron			810
Total Sulfur(S)	530	610	460

mg/100gH_2O

Fig. 4 shows the results of Sr isotope ratio measurements [8]. The Sr isotope ratios are low for bat guano, but high for fresh sandstone. The Sr isotope ratios of salts fall in between them, but are closer to the Sr isotope ratios of bat guano. This means that bat guano has contributed significantly to the deterioration of sandstone in the Angkor monument.

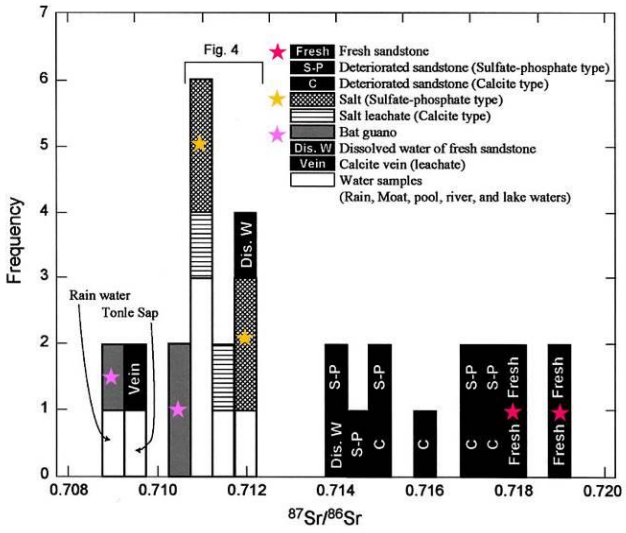

Fig. 4. Sr isotope ratios for samples obtained from Angkor area [8].

Fig. 5 shows the result of sulfur isotope measurements [8]. The $\delta^{34}S$ of bat guano is in the range of 5–10‰, but the typical range is approximately 5–7‰. Moreover, the $\delta^{34}S$ of salts is in the range of 6–7.5‰. Because these ranges almost coincide, it is deduced that the sulfur in the salts originated from bat guano.

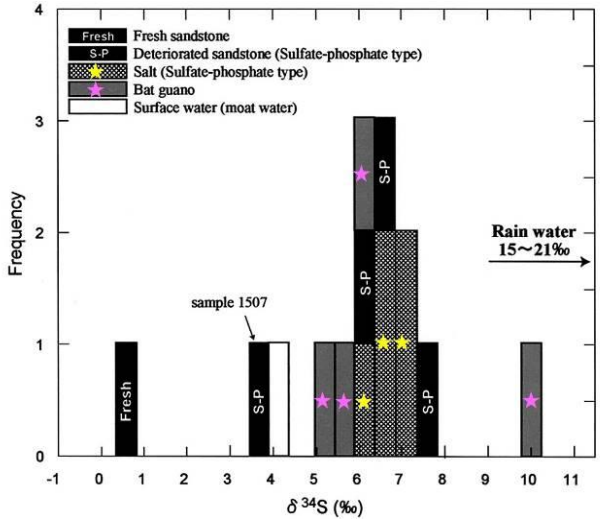

Fig. 5. S isotopic compositions for samples obtained from Angkor area [8].

2.2.2 Salt weathering related to calcite precipitation

The second type of salt weathering is related to calcite precipitation [8, 10]. This type of deterioration is observed in the upper frame of the door and window openings, and also on the inner surface of the roof (Fig. 6). Additionally, this type of deterioration is observed in the reentrant part of the platform.

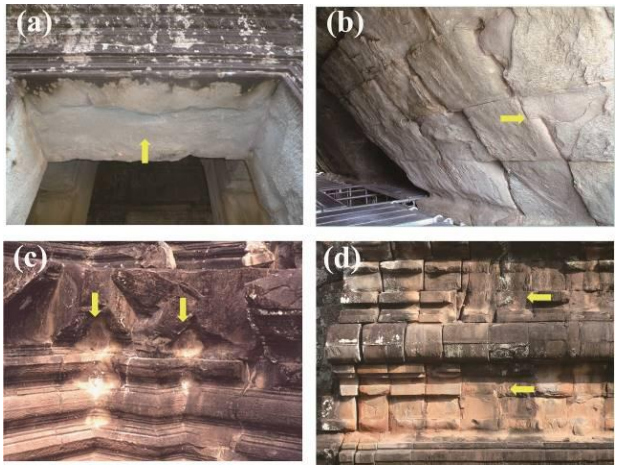

Fig. 6. Deterioration of sandstone caused by calcite precipitation: (a) underbed of window frame in Angkor Wat temple; (b) inner surface of roof in Angkor Wat temple; (c) reentrant part of platform in Angkor Wat temple; (d) detachment of molding on surface of platform in Ta Keo temple.

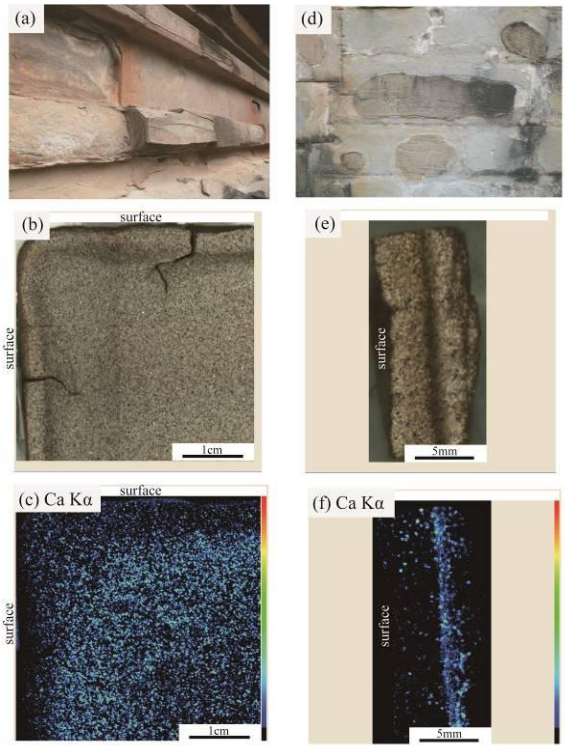

Fig. 7. Deteriorated sandstones and their samples caused by calcite precipitation on surface of platform of Ta Keo temple (a and b) and Phnom Bakheng temple (d and e), and calcium mappings for deteriorated sandstones obtained by X-ray fluorescence analyzer from (c) Ta Keo temple and (d) Phnom Bakheng temple [10].

Fig. 7 shows the distribution of Ca inside the sandstone fragments detached from the surface of the platform [10]. These photos show the Ca concentration inside the detached sandstone fragments.

Fig. 8 shows the mechanism of calcite precipitation. The rainwater falls on the outer surface of the roof, and then penetrates into the sandstone. Finally part of the rainwater evaporates from the inner surface. The Ca that dissolves into the water crystallizes as calcite by reacting with carbon dioxide from the air. This calcite precipitation causes exfoliation. This type of deterioration occurs in locations where water evaporates one-sidedly but rainwater does not fall directly. Salts accumulate in these sites because they are not washed away by rainwater. A strontium isotope study revealed that the calcium in the crystallized calcite was mainly derived from sandstone (Fig. 6).

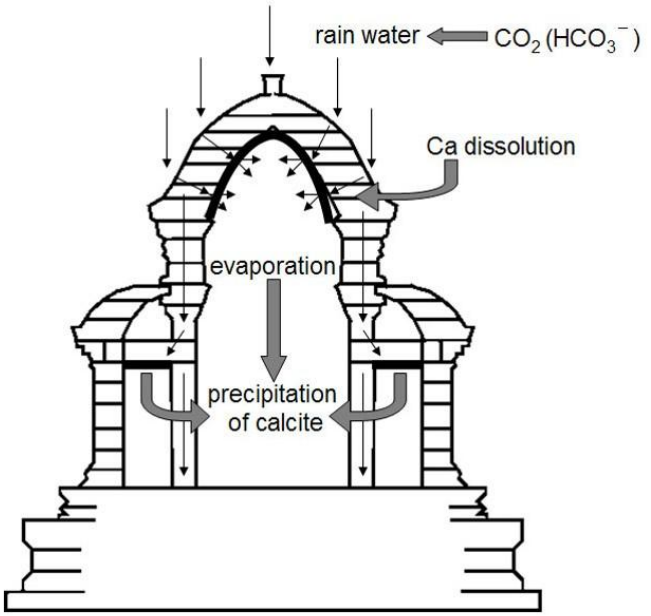

Fig. 8. Mechanism of calcite precipitation on inner surface of roof and on underbed of beams.

2.2.3 Tafoni

Tafoni is considered to be a type of salt weathering, but the detailed mechanism has not been elucidated. Tafoni is a rare phenomenon in the Angkor monument, and it is typically observed in the outer gallery of Bayon temple, particularly on the surface of the inner pillars. Fig. 9(a) shows an original relief of dancing Apsaras, which have deteriorated over time and now resemble skeletons (Fig. 9(b)). Large holes resembling a honeycomb have formed on the surface of the pillar (Fig. 9(c)). Because of tafoni, the lamina structure of the sandstone blocks used for the pillar has become more pronounced (Fig. 9(d)).

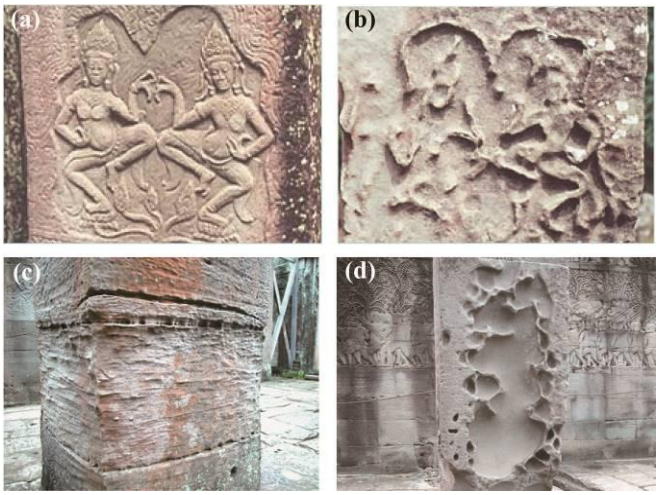

Fig. 9. Tafoni observed in Bayon temple. (a) Non-deteriorated bas-relief of dancing Apsaras; (b) deteriorated bas-relief of dancing Apsaras; (c) pronounced lamina structure caused by tafoni; (d) typical tafoni phenomenon on surface of pillars of outer gallery.

Fig. 10 shows the tafoni distribution in Bayon temple. Tafoni is observed in the outer gallery of Bayon temple, particularly in the inner pillars. Tafoni is localized in the south part of the outer gallery and is severe in the outer surface. Therefore, tafoni seems to be related to sunlight. However, the detailed mechanism of tafoni remains unclear.

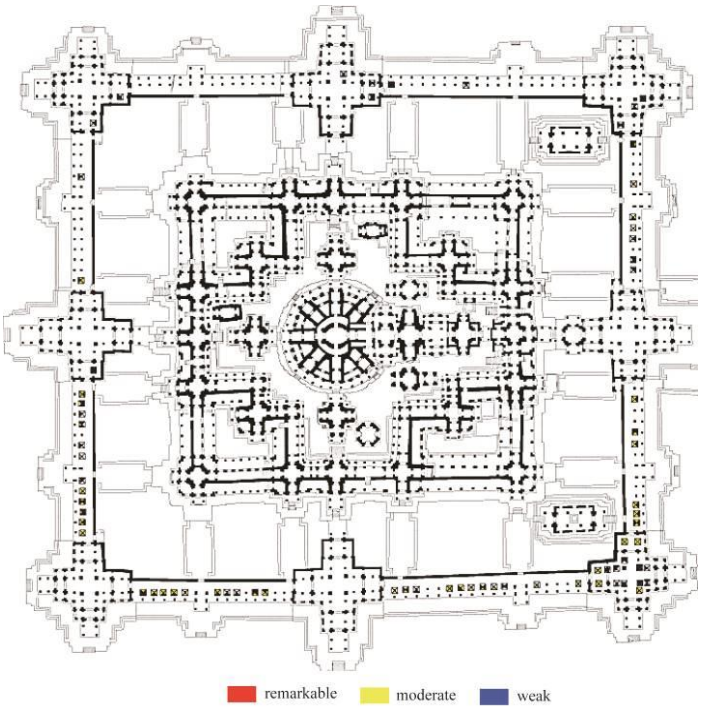

Fig. 10. Distribution of tafoni phenomena in Bayon temple. Tafoni is observed only in outer gallery.

2.3 Thermal expansion–contraction cycle

The exfoliation of the sandstone surface related to the thermal expansion–contraction cycle caused by sunlight is typically observed on the roof surface (Fig. 11). The daily change of surface temperature of the sandstone blocks was measured on the roof surface in the Northern Library of Angkor Wat temple. The minimum temperature was recorded at 6 a.m., and the maximum temperature was recorded at 2 p.m. on December 28th, 2002. The minimum temperature on the roof is approximately 22 °C, while the maximum temperature is approximately 57 °C. Therefore, the daily temperature change on the roof surface reaches 35 °C. This temperature change may cause the deterioration of the sandstone surface, owing to thermal expansion–contraction cycle by sunlight. Sudden daytime rainfall, such as squalls, seems to promote this type of deterioration.

Fig. 11. Exfoliation of sandstone surface on roof related to thermal expansion–contraction cycle by sunlight.

2.4 Structural collapse related to uneven ground subsidence

Fig. 12(a) shows Prasat Suor Prat, which declined toward the adjacent pond owing to uneven ground subsidence. Fig. 12(b) shows the surrounding enclosure of Ta Prohm temple. As can be seen, the wall is wavy. Uneven ground subsidence seems to be caused by the load of structures and soil movement triggered by the seasonal change of the groundwater level.

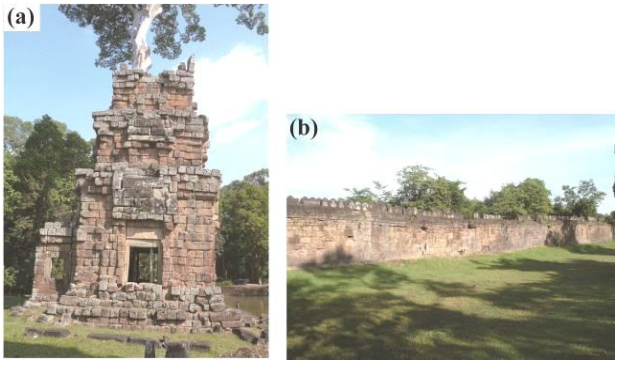

Fig. 12. Uneven ground subsidence: (a) S1 tower of Prasat Suor Prat; (b) surrounding enclosure of Ta Prohm temple.

2.5 Structural collapse related to traditional construction techniques

In the Angkor monument, the corbel arch technique was used for the construction of roofs (Fig. 13). This arch structure differs from a "true" arch structure. The Khmer people constructed an arch by offsetting stone blocks until they met at the apex of the arch structure. A roof with a corbel arch structure tends to be easily affected by uneven ground subsidence. Additionally, cement-like materials have not been used in the Angkor monument (dry masonry), which is also a factor contributing to structural collapse.

Fig. 13. Corbel arch structure in outer gallery of Ta Prohm temple. Cement-like materials have not been used (dry masonry).

2.6 Biological activity

In the Angkor monument, trees often grow on the monument and their roots destroy the structures [7]. A typical example is observed in Ta Prohm temple (Fig. 14(a)). Even if trees are not growing directly on the structures, those growing nearby may still damage the structures if they fall because of strong winds. Therefore, the felling of trees around the temples is an important conservation task.

The surface of the stone blocks typically exhibits black color (Fig. 14(b)) owing to the growth of blue-green algae (cyanobacteria) [7]. Moreover, abundant white spots, specifically lichens (Fig. 14(c)), are observed on the stone surface. As algae and lichens grow, their roots and the acid secreted from lichens damage the stone surface gradually. Therefore, algae and lichens should be removed from the surface of stone blocks.

Another blacking phenomenon is observed in the Angkor monument (Fig. 14(d)). This results from the activity of manganese–oxidizing bacteria [11]. This phenomenon is extensively observed in the Koh Ker monument.

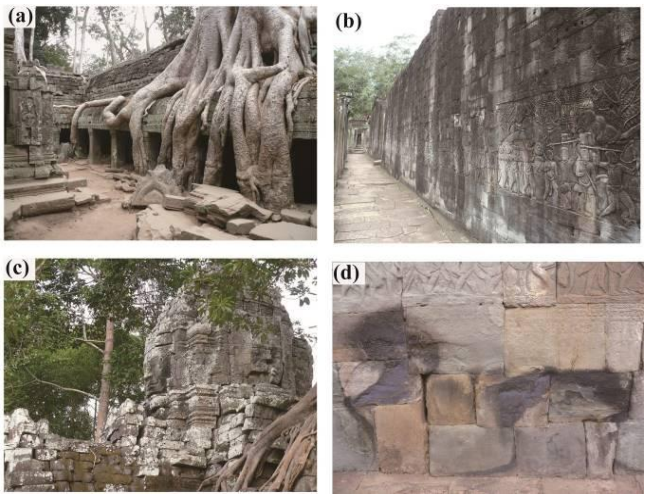

Fig. 14. (a) Trees growing on structures; (b) algae and (c) lichens on surface of sandstone blocks; (d) blackening phenomenon on surface of sandstone blocks. (a) Ta Prohm temple, (b,d) Bayon temple, (c) Ta Som temple.

2.7 Human activity

In terms of human activity, looting is one of the main causes of damage to the monuments. The heads of Devata reliefs are frequently looted (Fig. 15(a)). Additionally, there are many bullet holes on the surface of the monument (Fig. 15(b)). Considerable damage were caused to the Angkor monument during the civil war period starting in 1970. Inappropriate restoration has also damaged the monuments. Because the sandstone surface was cleaned using a strong chemical as a restoration activity, the surface of the sandstones was dissolved, and the bas-relief became unclear.

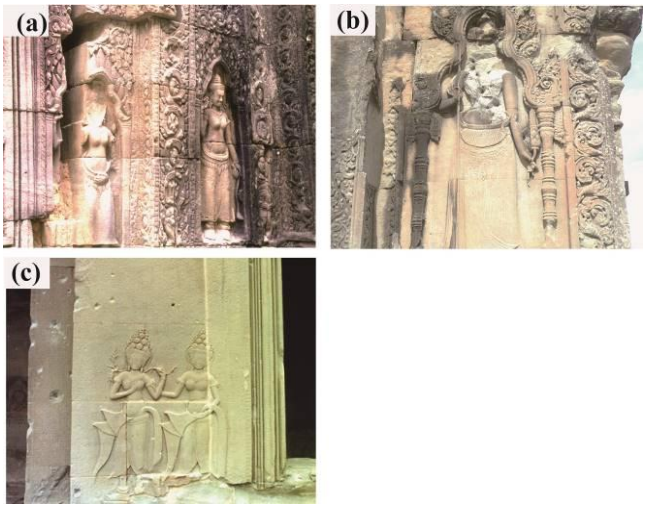

Fig. 15. (a) Looting is a cause of human-induced damage to the monument. The heads of Devata reliefs are frequently looted (Ta Som temple). (b) Bullet holes on the surface of the Devata relief in the

sanctuary of Phnom Bakheng temple. (c) Apsaras bas-relief in Angkor Wat became unclear due to cleaning using a chemical.

ACKNOWLEDGMENTS

The author gratefully acknowledges the support provided to the field survey from members of the Japanese Government Team for Safeguarding Angkor. This study was financially supported in part by Grants-in-Aids for Scientific Research of Japan Society for the Promotion of Science (Uchida: nos. 14404016, 17403001, 23401001, and 19KK0016) and Waseda University Grants for Special Research Projects (Uchida: no. 2016B-137).

REFERENCES

[1] Uchida, E., Ogawa, Y., Nakagawa, T., 1998. The stone materials of the Angkor monuments, Cambodia – The magnetic susceptibility and the orientation of the bedding plane of the sandstone. J. Min. Pet. Econ. Geol. 93, 411–426.

[2] Uchida, E., Maeda, N., Nakagawa, T. 1999. The laterites of the Angkor monuments, Cambodia, The grouping of the monuments on the basis of the laterites, J. Min. Pet. Econ. Geol. 94, 162-175.

[3] Uchida, E., Cunin, O., Suda, C., Ueno, A., Nakagawa, T., 2007. Consideration on the construction process and the sandstone quarries during Angkor period based on the magnetic susceptibility. J. Archaeol. Sci. 34,924–935.

[4] Meesook, A. 2011. 8. Cretaceous. In The Geology of Thailand; Ridd, M.F., Barber, A.J., Crow, M.J., Eds.; The Geological Society: London, UK, pp.169–184.

[5] Uchida, E., Shimoda, I., 2013. Quarries and transportation routes of Angkor monument sandstone blocks. J. Archaeol. Sci. 40, 1158–1164.

[6] Uchida, E., Watanabe, R., Murasugi, M., Sakurai, Y., Shimoda, I., 2020. The sandstone quarries of the Angkor monuments in the southeastern foothills of Kulen Mountain. Archaeol. Discovery 8, 207–227.

[7] Uchida, E., Ogawa, Y., Maeda, N., Nakagawa, T. 1999b. Deterioration of stone materials in the Angkor monuments, Cambodia. Eng. Geol., 55, 101-112.

[8] Hosono, T., Uchida, E., Suda, C., Ueno, A., Nakagawa, T. 2006. Salt weathering of sandstone at the Angkor monuments, Cambodia: identification of the origins of salts using sulfur and strontium isotopes, Jour. Archaeol. Sci., 33, 1541–1551.

[9] Fusey, P., 1991. Altération biologiques des grès Cambodgiens et recherche de moyens de protection. École Française d'Extrême-Orient, Paris, 91pp.

[10] Uchida, E., Shimoda, I., Takubo, Y., Toyouchi, K. 2012. Moisture content measurement and surface water absorption test in the inner gallery of Bayon for the conservation of the bas-relief. Jour. Archaeol. Sci., 39, 1420-1435.

[11] Uchida, E., Watanabe, R., Osawa, S., 2016. Precipitation of manganese oxides on the surface of construction materials in the Khmer temples, Cambodia. Heritage Sci., 4, 1-17.

Techno-Science Research Journal V13 (Special Issue) (2025) P 8-13

I.T.C

Content list available at ITC

Techno-Science Research Journal

Journal Homepage: www.ric.itc.edu.kh

Techno-Science Research Journal

Application of Shallow Seismic Surveys for Non-Destructive Internal Exploration of Kofun Mounds in Japan

Yutaro Hara [1*], Reiko Kuwano[1,2]

[1]*The University of Tokyo, Graduate School of Engineering, Department of Civil Engineering, 1-3-1 Hongo, Bunkyo-ku, Faculty of Engineering Building 1, The University of Tokyo, Tokyo, Japan.*
[2] *Institute of Industrial Science, The University of Tokyo, 4-6-1 Komaba, Meguro-ku, Tokyo, Japan*

Received: 1 November 2024; Revised: 1 January 2025; Accepted: 20 June 2025; Available online: October 2025

Abstract: *This study applied non-destructive shallow seismic exploration techniques using high-frequency, high-power vibrations and high-density receivers to investigate the shallow internal structures (e.g., cracks, sinkhole) of Tumulus No. 1 and No. 2 at the Sakuradani Kofun Tumuli. Surface wave exploration and reverse time migration of horizontal shear wave fields were conducted on three-component seismic data to analyze subsurface features from two perspectives. Surface wave analysis detected zones of decreased S-wave velocity at multiple depths, notably identifying low-velocity layers at depths of approximately 1–3 meters in the center and 5–6 meters at the edges of the investigation line. These results suggest the presence of loose soil layers, which may be remnants of ancient burial facilities or damage from the recent Noto Peninsula earthquake. RTM results supported this finding by revealing a strong reflector at about 2 meters depth in the center of the mound, indicating a layer boundary with different physical properties and suggesting the existence of an unexcavated burial facility. These findings provide insights into the internal structures of ancient burial mounds and demonstrate the potential for non-destructive seismic exploration techniques in archaeological studies.*

Keywords: Archaeological Geotechnics, Seismic survey, Non-destructive exploration

1. INTRODUCTION

Non-destructive internal exploration is an important theme in the restoration and preservation of historical heritage. As the opportunities to excavate archaeological sites are extremely limited, use of non-invasive techniques can enhance the assessment of ancient structures as a means of preliminary investigation to effectively plan work processes.

Investigating the internal structures of burial mounds and buried artifacts provides insights into the political culture and civil engineering practices of ancient Japan. Therefore, there is an urgent need to develop technology that can investigate the internal structures of burial mounds without causing damage. Numerous studies have focused on non-destructive investigation of internal structure of historical heritage using ground penetrating radar (GPR) [1,2], seismic reflection survey [3,4] or seismic topography [5]. However, from a geophysical perspective, tumuli are difficult targets to measure, because the scale of typical tumuli, which are 5 to 10 meters high, is too large for ground penetrating radar (GPR) to penetrate, while the resolution of seismic surveys such as surface wave exploration is insufficient, which leads to the fact that the internal structures such as absence of berial chambers of many Kofun mounds remain undiscovered.

In this study, shallow seismic exploration whose target was less than 10m deep was carried out into the preliminary survey of archaeological investigation of Sakuradani kofun tumuli, using high-frequency, high-power excitation sources and high-density reception, to investigate the internal structure of an archaeological site and to assess the damage caused to the site by the 2024 Noto Peninsula Earthquake. Surface wave exploration and reverse time migration (RTM) of horizontal shear (SH) wave fields for the three-component seismic traces were conducted, attempted to analyze the data from two different perspectives.

* Corresponding author: Yutaro Hara
E-mail*: yutarohara13579@g.ecc.u-tokyo.ac.jp;*
Tel*: +81 03 5452 6843*

2. DATA ACQUISITION

2.1 Acquisition Site

The Sakuradani tumuli consist of more than a dozen ancient burial mounds called 'Kofun', located in Takaoka City, Toyama Prefecture, Japan. The investigation target of this study was tumulus No.1 and tumulus No.2. The overall view of tumuli are shown in Fig..1. The two burial mounds were constructed in the early 4th century and mid-4th century, respectively. Mound No.1 has a maximum horizontal length of 62 m and a height of 8 meters, while Mound No.2 measures 50 m in length with a height of 5 m [6]. Although Sakuradani Kofun tumuli are said to be one of the largest burial mounds of a leader of Toyama region, and they contain extremely important information for understanding the history of ancient Japan.

While the burial internal facilities are not clear, it is inferred to have been a pit-type grave with a wooden coffin covered in clay. from a estimated construction point of view [6]. As shown in the Fig.2, the wooden coffin in this type of burial chamber decomposes and disappears over time, leaving behind a loose layer of soil that sinks into the ground above it [7].

In January 2024, the Noto Peninsula earthquake caused serious damage to both the tumulus No.1 and No.2. At tumulus No.1, subsidence and slope failures occered, and at tumulus No.2, slope failures, deformation and sinkhole occurred due to the earthquake. In particular, the sinkhole which was represented in southern slope of the mound was as deep as 6m, needed to be precise incestigation for restriction of the tumuli. These failures are shown in Fig.3.

Fig. 1 Sakuradani Kofun Tumuli [8]

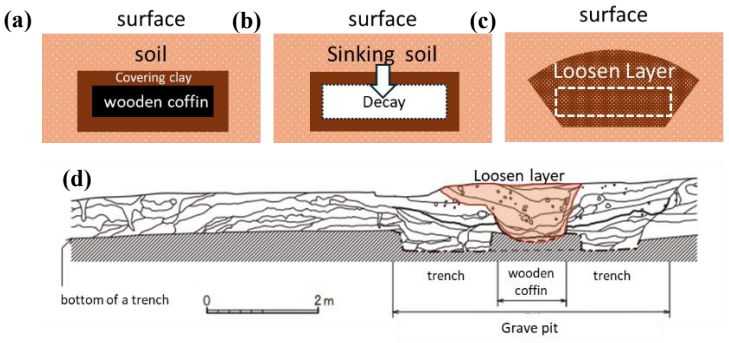

Fig. 2 The structure of the presumed pit grave mound and its transitional diagram of age and deterioration (a, b, c in chronological order), and examples of excavations in burial mounds with similar burial types [7] (d).

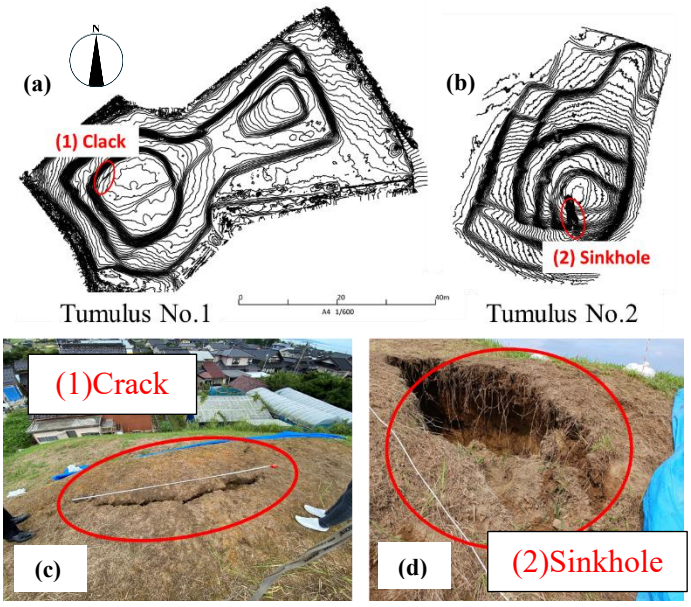

Fig. 3 Contour Map of Tumulus No.1(a), No.2(b) and Damage to the mounds at Tumuli No.1(c), No.2(d)

2.2 Arquisition condition

This study aimed to estimate the internal structure of the ruins and to understand the extent of damage caused by the Noto peninsula earthquake disaster. Since there were economic and time constraints on the selection of the survey lines for this survey, the targets were on the main part of both burial mounds, where the burial facilities were most likely to be located, for both Tumulus No.1 and Tumulus No.2. The approximate locations of the acquisition sites of Tumulus No.1 and No.2 are shown in Fig.4.

In order to improve the resolution of the shallow layer, the sensor spacing needed to be close and the vibration frequency to be high. In this survey, with this objective, 24 three-component geophones with a frequency of 4.5Hz were placed at intervals of 0.5 m (therefore the total length of the survey lines were both 11.5 m). In addition, considering the impact of source energy on the

ruins, vibration speakers capable of generating vibrations of up to around 1,000 Hz to generate a wide range of vibrations of 20-400 Hz on the ground surface were used as the source. The logger was of Geo-Seis 5 with 72 channels for x,y,z axis of 24 geophones. The acquisition axes of this study are shown in Fig.5.

The resolution of seismic exploration is proportional to the wavelength. The higher the excitation frequency, the shallower the layer that can be visualized [9]. In this study, two 80W vibration speakers capable of excitation up to around 1000Hz were used, instead of using the conventional hammer excitation. The average surface elastic wave velocity measured at the survey site was approximately 110 m/s, and based on this result, the relationship between the wavelength and amplitude of the vibration excited by the vibration speaker was compared with hammer excitation (Fig.6). Excitation using a vibration speaker excited shorter wavelength waves, and the resolution was improved. In addition, parallel installation and stucking multiple vibration data considering the time lags and removed noise was conducted to address the issue of attenuation in high-frequency excitation.

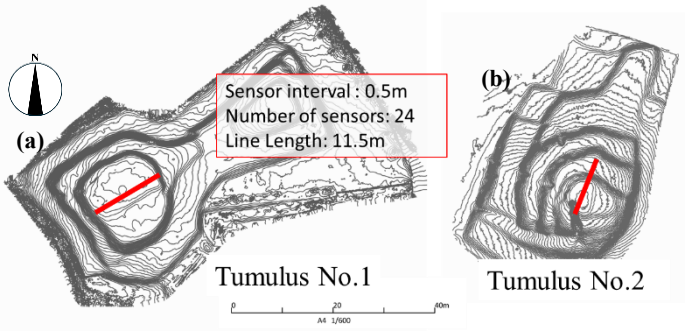

Fig.4 Acquisition site in which survey lines were represented in red, tumulus No.1(a) and No.2(b).

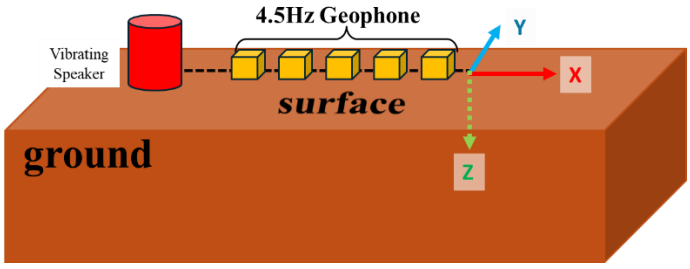

Fig. 5 Image of the acquisition of seismic wave exploration. The relationship between the x,y,z axes of triaxial measurement data. The y direction is horizontal shear wave (SH) axis.

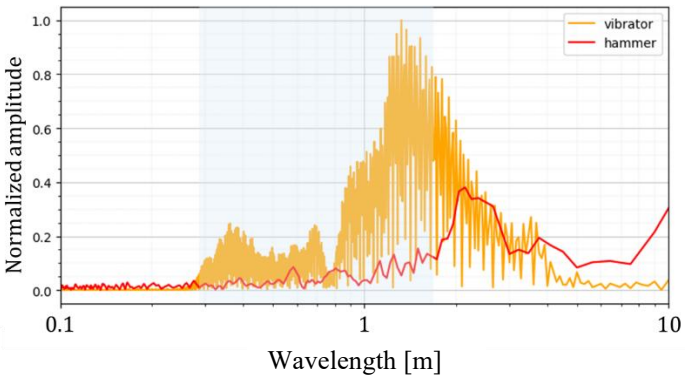

Fig. 6 Relationship between Amplitude and wavelength when the wave velocity was 110 m/s.

3. Data Analysis

3.1 Multichannel Analysis of Surface wave survey.

In this survey, surface wave exploration and reverse time migration were used as multi exploration methods of each axes data. In the surface wave exploration, the x and z axis data were used. Cross-correlation was performed on raw trace data processing for drawing the dispersion curve. For each data of different source, the inverse analysis of the S-wave velocity was performed using SeisImager by Geo-Seis. The dispersion curves $V(\omega,\ c)$ were described the following equation [10]

$$V(\omega,\ c\ ) = \sum_{x=x_0}^{Nx} e^{icx} \left[{U(x,\omega)} \Big/ {|U(x,\omega)|} \right]$$

$$U(x,\omega) = \sum_{t=0}^{Nt} e^{i\omega t} u(x,t)\Delta t$$

Where x is the location of the record position, t is time, ω is angular frequency and c is wave propagation velocity. $U(x,\ \omega\ )$ is time-domain discrete fourier transformation of the time trace $u(x,t)$ of receiver at position x.

3.1 2D Reverse Time migration of SH wavefield

Reverse time migration was carried out for a two-dimensional SH wave field from y axis data [12]. The direction is horizontal to the ground surface and perpendicular to the side line as shown in Fig.4. After amplitude correction process, the observed trace and source data was processed to Reverse time migration of SH wave field in elastic media. The wave propagation equation used in RTM was as follows.

$$\frac{\partial}{\partial t}\boldsymbol{v} = \frac{\partial}{\partial x}\boldsymbol{\sigma_{xy}} + \frac{\partial}{\partial z}\boldsymbol{\sigma_{yz}}$$

$$\frac{\partial}{\partial t}\boldsymbol{\sigma_{xy}} = \boldsymbol{\mu}\frac{\partial}{\partial x}\boldsymbol{v}$$

$$\frac{\partial}{\partial t}\boldsymbol{\sigma_{yz}} = \boldsymbol{\mu}\frac{\partial}{\partial z}\boldsymbol{v}$$

Where $\boldsymbol{v}$ is velocity, $\boldsymbol{\sigma_{yx}}, \boldsymbol{\sigma_{yz}}$ is shear stress, $\boldsymbol{\rho}, \boldsymbol{\mu}$ is density and shear modulus, respectively. The wavefield was analyzed using a two-dimensional finite difference method with staggered grid with free surface boundary condition. Absorbing layers were applied to the right, left, and bottom boundaries. The reflection surface was derived by cross-correlating the wave field generated from the source waveform with the wave field generated by time-reversing the waveform observed in the field. The imaging process is expressed as follows

$$I(\boldsymbol{x}) = \sum_{t=1}^{Nt} S_s(\boldsymbol{x}, t) S_r(\boldsymbol{x}, t)$$

Where $S_s(\boldsymbol{x}, t)$ are source field trace and $S_r(\boldsymbol{x}, t)$ are backward wavefield by observed trace data at the location $\boldsymbol{x}$. The pc used for RTM was an EPSY 9654P + RTX A5500, and was run in an environment with python 3.12.2 and cuda 11.5.rll.5.

4. RESULTS AND DISCUSSION

4.1 The result of the Tumulus No.1

Fig.7 shows the surface wave dispersion image obtained at the Tumulus No.1. Shear wave velocity near the surface was about 110m/s. One interesting point was that in the data at around 30 Hz, multiple peaks were observed diverging to infinite velocity, thought that these peaks were due to the observation of multiple surface wave dispersion modes, such as guided waves. Normally, these higher-order modes are ignored in the inversion analysis of Vs velocity distribution in surface wave exploration, but it was thought that exploration that includes these higher-order modes will be necessary when finding abnormal layers.

Fig.8 shows the results of Vs velocity surface wave inversion and SH wavefield RTM. Inversion of surface wave data showed that there was a location where the S-wave velocity decreased at a depth of around 1~3m near the center of the mound (P2 in Fig.4). In addition, there was also a low S-wave velocity at a depth of 5~6m at the eastern end of the side line (P1 in Fig.4), and at a depth of 2~6m at the western end of the side line (P3 in Fig.4).

Considering that the height of the burial mound is about 8m, the low-velocity soil layer found at a depth of 5m suggests that there is a loose layer in the deeper part of the burial mound fill. In contrast, a low-velocity layer was detected in a wide area extending more than 2m below ground level in the center of the burial mound. This was hypothesized to be a loose layer that has become vulnerable due to the Noto earthquake disaster that occurred this year. On the other hand, it also was thought of as the remains of a burial chamber that had been created at the time of construction of the mound, because the burial chambers of direct burials in wooden coffins, etc. decay over time and often sink in, appearing as loose layers. Considering the burial facilities in the ancient burial mounds around Sakuradani Kofun from the early Kofun period, it was suggested that the loose layer may be the remains of an unexcavated burial chamber in Tumulus No.1.

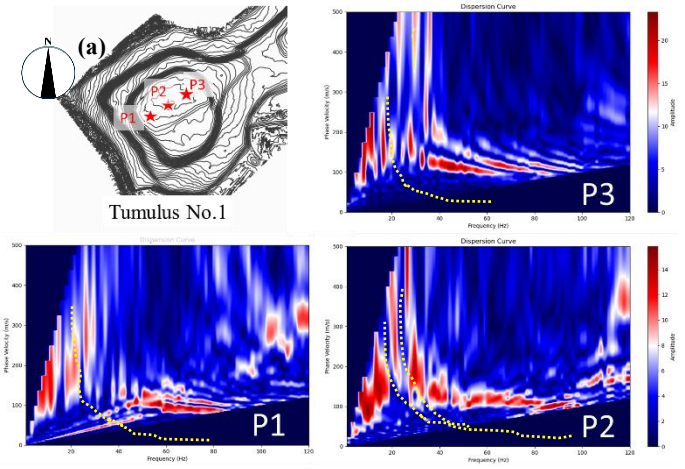

Fig. 7 Surface wave dispersion images obtained at the point P1, P2, and P3 on Tumulus No.1, shown in (a). Yellow dot lines represent the peak dispersion curve.

As a result of reverse time migration in the SH wave field, a reflecting surface, in terms of amplitude, was detected at a depth of about 2m from the surface of the central part of the mound. In particular, given the characteristic of RTM that it was sensitive to directions parallel to the receiving surface, it was suggested that there was a layer boundary with different physical properties from the surrounding area. In general, it is the product of density and elastic wave velocity that affects the reflection and transmission of elastic waves, and the lower the density and the slower the speed, the more pronounced the reflection surface becomes. When combined with the results of inversion in surface wave exploration, there might be a possibility of some kind of foreign layer existing at a depth of around 2m in the center of the burial mound.

4.2 The results of the Tumulus No.2

Fig.9 shows the surface wave dispersion images obtained at the Tumulus No.2. As one notable condition in the analysis, there was a sinkhole on the southern slope, which leads to a high possibility that it reached the center of the tumulus.

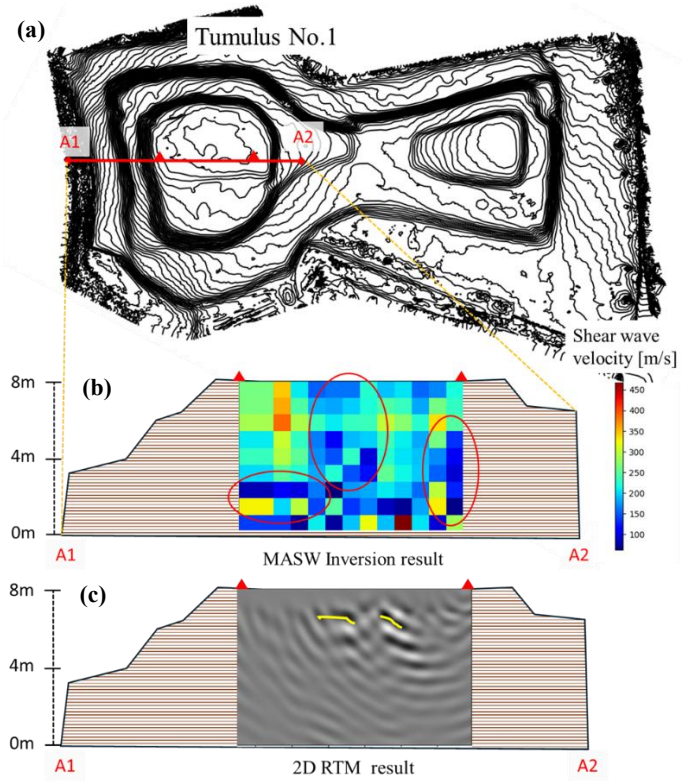

Fig. 8. The results of Surface wave inversion (b) and 2D Reverse time migration (c) at the Tumulus No.1 (a). Red circle in (b) and Yellow line in (c) represent low-velocity zone and reflection boundary, respectively.

The depth of the sinkhole reaches 6m, and from visual observation on the day of the survey, it was observed that the ceiling of the cavity was at a depth of about 3m from the center of the tumulus. At the point where the surface wave was acquired, the influence of the cavity and the loose layer that follows it is thought to be particularly apparent in the Q1 data.

On the other hand, looking at the dispersion image of the surface wave, the dispersion curve for Q1 bends to the high-speed side at around 30Hz, resulting in a high S-wave velocity. This trend was investigated in the inversion results shown in Fig.10. This was an interesting result because it contradicted the assumption that cavities were extensions of the loose layer. Investigating the dispersion images for Q2 and Q3, Q3 showed the same trend as Q1, suggesting the possibility of abnormalities such as cavities in the lower part. Since there was a lot that was unknown about the research field of elastic wave propagation around cavities in the ground, further research, for example, the higher-order modes analysis of surface wave dispersion, would be needed.

The results of the reverse-time migration of SH wave fields at the Tumulus No.2 in Fig.10 showed that a uniform reflecting surface was confirmed at a point about 2m deep from the top of the burial mound, that was, at the horizontal part of the second step. This cross-section corresponds to the middle of the southern slope, where there was a high possibility of a cavity. Although only the reflective surface estimation was conducted in this study, improvement of the accuracy and continuation of detailed exploration are conducting by analyzing the distribution of reflection coefficients and impedance ratios taking into account the wave attenuation of the ground, based on these data obtained in this survey.

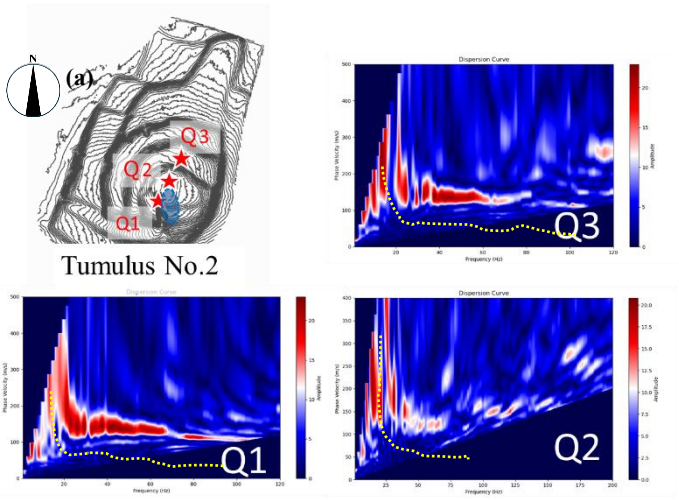

Fig. 9 Surface wave dispersion images obtained at the point Q1, Q2, and Q3 on Tumulus No.2. Yellow dot lines represent the peak dispersion curve.

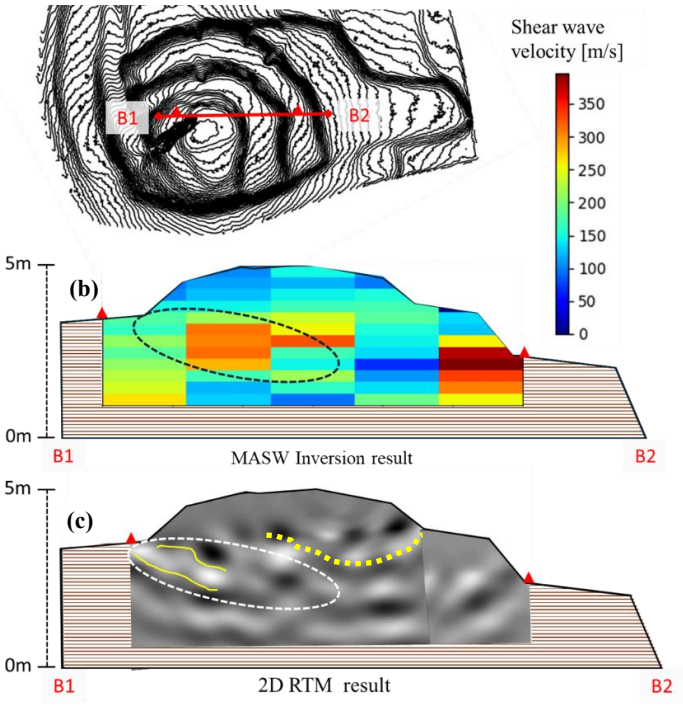

Fig. 10 The results of Surface wave inversion (b) and 2D Reverse time migration (c) at the Tumulus No.2 (a). Black circle in (b), yellow line in (c) was the area with a high probability of cavities .

5. CONCLUSIONS

In this study, shallow seismic exploration techniques using high-frequency, high-power vibrations and high-density receivers were applied to the internal structure survey of the No. 1 and No. 2 tumuli in the Sakuradani Kofun Tumuli, targeting the shallow underground region to a depth of about 10 m. Surface wave exploration and reverse time migration of SH wave fields for the three-component seismic trace were conducted, attempted to analyze the data from two different perspectives.

In the Tumulus No.1, the surface wave analysis detected areas where S-wave velocity decreased at multiple depths. In particular, low-velocity layers were identified at depths of approximately 1 to 3 meters in the center of the burial mound and at depths of approximately 5 to 6 meters at the edge of the investigation line. These results suggested the possibility of loose soil layers inside the burial mound, and that they might be the remains of ancient burial facilities or damage caused by the recent Noto Peninsula earthquake. The results of reverse time migration also support this, with a reflector detected at a depth of about 2 meters in the center of the burial mound. This reflection layer indicated a layer boundary with different physical properties, suggesting the existence of an unexcavated burial facility.

In the Tumulus No. 2, despite the large depression on the southern slope, surface wave analysis showed a high S-wave velocity, contrary to expectations. This anomaly suggested the underground conditions when there was a cavity or other such feature inside the burial mound. Reverse time migration results showed a uniform reflection surface at a depth of about 2 meters, corresponding to the area that might be affected by the sinkhole.

These observation results emphasize the need for further detailed research on elastic wave propagation in the presence of underground cavities.

ACKNOWLEDGMENTS

We would like to thank the Cultural Properties Protection and Utilization Division of the Takaoka City Board of Education for their cooperation in conducting this survey.

REFERENCES

[1] A. Martindale, W. T. D. Wadsworth, E. Simons, B. Whiting , C. Grier, “The challenges of signal interpretation of burials inground-penetrating radar”, Archaeological Prospection. 2023;1–15, https://doi.org/10.1002/arp.1920

[2] E. Forte, M. Pipan "Integrated seismic tomography and ground-penetrating radar (GPR) for the high-resolution study of burial mounds (tumuli)”, Journal of Archaeological Science 35 (2008) 2614–2623, doi:10.1016/j.jas.2008.04.024

[3] M. Zolchow1, D. Köhn1, D. Wilken1, E. Erkul1, S. Dreibrodt, N. Pickartz, E. Corradini1, J. Müller and W. Rabbel “Multi-Method Structural Investigation of the Schneiderberg–Baalberge Burial Mound (Saxony-Anhalt, Germany) Including Seismic Full-Waveform Inversion (FWI)”, Archaeological Prospection, 2024; 0:1–26 https://doi.org/10.1002/arp.1961

[4] R. Mecking, M. Meinecke, E Erkul, F. Pirson and W. Rabbel " The Yıgma Tepe of Pergamon: Internal construction of a monumental burial mound from shear wave reflection sounding and wavefield modelling" Wiley. 2021

[5] L. Polymenakos, D. Tweeton “Non-invasive characterization of a burial tumulus with use of seismic P-wave velocity and attenuation tomography”, Journal of Archaeological Science:Reports 13 (2017) 36-48, http://dx.doi.org/10.1016/j.jasrep.2017.03.025

[6] 櫻谷古墳群調査概報, 高岡市埋蔵文化財調査概報第 33 冊, 1996

[7] 沼津市教育委員会, “高尾山古墳発掘調査報告書”, 沼津市文化財調査報告書,第 104 集 p38, 2012

[8] https://www.city.takaoka.toyama.jp/soshiki/kyoikuiinkaibunkazaihogokatsuyoka/1/4/1/2393.html

[9] A.Takahashi,”Vertical resolusion and seismic data interpretation”, Butsuri-tansa, vol.75 pp 79-88, 2022, https://doi.org/10.3124/segj.75.79

[10] C. B. Park, R. D. Miller, and J. Xia, “Imaging dispersion curves of surface waves on multi-channel record“ SEG technical program expanded abstracts. 1998

[11]https://xilinx.github.io/Vitis_Libraries/hpc/2021.1/user guide/L1/rtm_intr.html

Techno-Science Research Journal V13 (Special Issue) (2025) P 14-21

Content list available at ITC

Techno-Science Research Journal

Journal Homepage: www.ric.itc.edu.kh

Techno-Science Research Journal

Electrical Resistivity Tomography at the Sakuradani Tumuli, Japan

Shotaro Hijikata[1*], Reiko Kuwano[2], Makoto Kuno[2]

[1] *Department of Civil Engineering, The University of Tokyo, Tokyo, Japan*
[2] *Institute of Industrial Science, The University of Tokyo, Tokyo, Japan*

Received: 1 November 2024; Revised: 1 January 2025; Accepted: 20 June 2025; Available online: October 2025

Abstract: *The Noto Earthquake, which struck Japan in January 2024, caused damage to the Sakuradani Tumulus in Takaoka City, Toyama Prefecture, including sinkholes and cracks. To better understand the extent of the damage and inform future remedial treatment plans, we conducted an electrical resistivity tomography (ERT) survey along two orthogonal lines on Tumulus No. 1 and one on Tumulus No. 2. Additionally, a portable dynamic cone penetration test (DCPT) was performed to measure ground strength and to investigate a method currently under development that utilizes the DCPT device, with modifications, as an electrode for ERT. The ERT survey confirmed the presence of a small sinkhole and a loose slope on Tumulus No. 1, as well as a sinkhole on Tumulus No. 2. Furthermore, by using the DCPT device as an electrode, we identified areas of relatively high water content, likely resulting from loosening and surface cracks, which could not be visualized using traditional ERT with only surface electrodes. On the other hand, further research is recommended to explore the high resistivity anomalies detected in the center of Tumulus No. 1 and near the top of Tumulus No. 2, and their potential relationship to the earthquake.*

Keywords: electrical resistivity tomography (ERT), penetration test, sinkholes, tulmulus, tomb

1. INTRODUCTION

On January 1st, 2024, at 16:10 (JST), a powerful earthquake struck the Noto Peninsula in Ishikawa Prefecture. The 2024 Noto Earthquake was an inland earthquake that occurred at a depth of 16 km, with a magnitude of 7.6 [1]. This earthquake caused widespread damage across the region, including strong shaking, significant ground movements around the Noto Peninsula, and a subsequent tsunami [2], [3]. Among the areas affected, cultural properties sustained considerable damage. In response to this, several comprehensive reports on the damage to cultural properties were compiled by the Cultural Property Rescue Project Committee, which was established by both Ishikawa and Toyama Prefectures to address the issue [4], [5].

Among the affected cultural properties, the Sakuradani tumuli in Toyama Prefecture suffered extensive damage, including significant cracks and sinkholes in burial mounds. Generally, a mound's fill not only provides structural stability through its weight but also plays a crucial role in stabilizing the thermal environment inside the stone chamber, thus protecting the artifacts and human remains within [6], [7]. At the time of submission of this paper, Takaoka City was considering a preliminary trench investigation plan and remedial treatments for the tumuli. However, trench excavation with insufficient understanding of mounds can cause significant and often irreversible damage to the internal structures, potentially compromising the very heritage they seek to protect. Therefore, non-invasive survey techniques are recommended as a first step to minimize the risk of further damage. Electrical Resistivity Tomography (ERT) was employed as a non-destructive technique to conduct a preliminary investigation into the extent of the damage and to assess the internal structure of the tumuli.

In this paper, we present the results of a 2D ERT survey of the Sakuradani tumuli and provide interpretations of the findings. The results of this survey offer a detailed view of the subsurface conditions and highlight areas of potential concern. Additionally, the authors are currently conducting a feasibility study on a simplified ERT method using a portable dynamic cone penetration test (DCPT) device. This device was adopted as a tool to complement traditional ERT methods, aiming to enhance

* Corresponding author: Shotaro Hijikata
E-mail:*shotaro-hijikata@g.ecc.u-tokyo.ac.jp*

resolution and improve the efficiency of data collection compared to surveys using only surface electrodes. The study aims to assess the effectiveness of this new approach in providing rapid and reliable assessments of subsurface conditions. We also summarize the results.

2. METHODOLOGY

2.1 Site Location and Description

The Sakuradani tumuli are located in Takaoka City, Toyama Prefecture, along the northwest coast of Japan (Fig. 1). Located on a plateau at an altitude of around 20 m above sea level, it consists of more than 13 tumuli within an area of approximately 300 m east to west and 150 m north to south. Among these, the largest, Tumulus No. 1, 62 m long and 5.45 m high, and Tumulus No. 2, 50 m long and 6 m high, were designated as National Historic Sites in 1934. These tumuli were believed to have been constructed around the 4th century and serve as the tombs of a king from a group of maritime traders active along the Sea of Japan. The city manages the Sakuradani tumuli because of its archaeological significance, which is evident in its structure and the excavated artifacts [8].

The Noto Earthquake of January 1st, 2024, caused extensive damage to the northwest coast region of Japan [2], [3]. This was no exception for the Sakuradani tumuli, 83km from the epicenter; severe damage was caused to Tumulus No. 1 and 2.

Fig. 1. The overiview of the Sakuradani Tumuli **[8]**.

Table 1. Details of observed damages.

Tumulus No.	Damage	Deteils
1	Sinkhole	Diameter: 0.5 m, Depth: 0.3 m
	Crack	Length: 4m, Width: 0.1m, Depth: 0.3 m
2	Sinkhole	Diameter of opening: 1.2 m, Length: 6.4 m (34.7 deg downwards)

The details of the damage revealed with preliminary surveys are shown in Table 1 and Fig. 2-Fig. 4. The depth of the sinkhole in Tumulus No. 2 was measured with an electro-optical distance meter.

2.2 Technique of ERT

ERT, also known as Electrical Resistivity Imaging (ERI), is one of the oldest and most commonly used geophysical exploration methods [9]

Fig. 2. A small sinkhole at the side slope of Tumulus No. 1. Temporarily filled with sandbags to prevent further enlargement of the hole.

Fig. 3. A crack at the edge of the mound of Tumulus No. 1. Temporarily covered with a blue tarp for protection except during photography.

Fig. 4. A opening of a sinkhole at Tumulus No. 2. Temporarily covered with a blue tarp for protection except during photography.

and is referred to as electrical prospecting in combination with IP and natural potential methods. It has been widely used in environmental, geotechnical, hydrological, mineral, and archaeological exploration [10]-[16]. The resistivity method is a technique of exploration that uses the fact that resistivity changes depending on the mineral content in the ground, the porosity, the amount and quality of pore water, the ground temperature and other related factors, as shown in

Table 2. Resistivity is a physical property that indicates the degree to which electricity passes through a material; the unit is Ω·m [17]. That is, non-aquiferous sinkholes, cavities and loosened area are considered to exhibit high resistivity, while water-bearing regions are expected to show low resistivity. The measurements for the resistivity survey are made by injecting a current into the ground through two current electrodes (usually metal stakes or capacitive metal plates [18]) and measuring the difference in the resulting voltage at two potential electrodes. In its most basic form, the resistivity meter has a current source and voltage-measuring circuitry connected by cables to a minimum of four electrodes. The essential data from a resistivity survey are the positions of the current and potential electrodes, the current (I) injected into the ground, and the resulting voltage difference (ΔV) between the potential electrodes (**Fig. 5**). The current and voltage measurements are then converted into an apparent resistivity (ρ_a) value by using the following formula

$$\rho_a = 2\pi\left(\frac{1}{r_{11}} - \frac{1}{r_{21}} - \frac{1}{r_{12}} + \frac{1}{r_{22}}\right)^{-1}\frac{\Delta V}{I}, \qquad \text{(Eq. 1)}$$

where ρ_a = apparent resistivity [$\Omega \cdot$ m]. For 2D surveys, a large number of electrodes are connected to a resistivity meter by cable, and 2D profile of the subsurface is obtained by making measurements with different spacings at different locations along the survey line.

2D ERT with surface electrodes is superior in terms of cost and time, but the resolution decreases as the depth of exploration increases. As a solution to this, by installing buried electrodes, it is possible to measure close to the target of exploration, and an improvement in accuracy is expected. Although measurement using boreholes is standard, the time and cost required to prepare them limits the situations in which they can be used [17]. In contrast, methods of installing buried electrodes with direct push technology have been researched as low-cost and easy methods [19]-[24]. The authors are considering installing buried

Table 2. Relationships between resistivity and its main parameters [17].

Low	←	Resistivity [Ω·m]	→	High
Low	←	Void ratio	→	High
High	←	Degree of saturation	→	Low
Low	←	Pore water resistivity	→	High
High	←	Clay content	→	Low
High	←	Conductive mineral content	→	Low
Low	←	Temperature	→	High

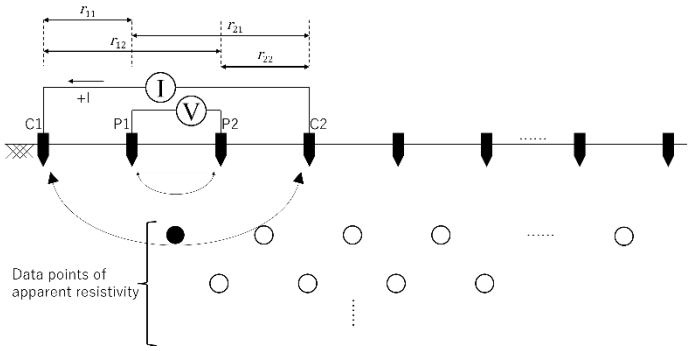

Fig. 5. Schematic diagram of a typical 2D ERT survey.

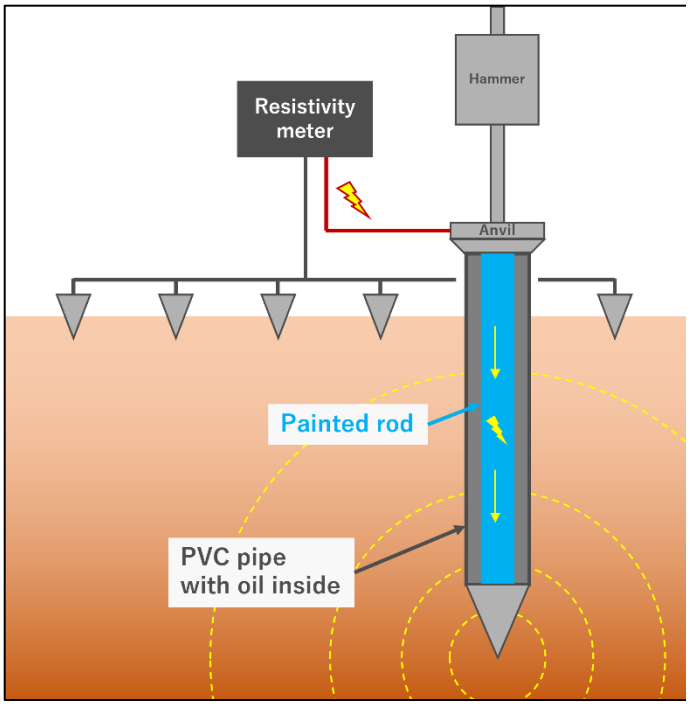

Fig. 6. Schematic diagram of ERT with the DCPT-based buried electrode system.

electrodes using the portable dynamic cone penetration test (DCPT) instruments as a more accessible and economical method than these. Fig. 6 shows the schematic. By carrying out DCPT at one or more points and using the tip cone as a buried electrode for measurement, the resolution deep underground is expected to be improved.

2.3 Equipment and Data Acquisition

Fig. 7 shows the locations of the profiles and the DCPT, and Table 3 shows the information on survey lines. The rationale behind our choices for electrode configuration (including electrode spacing and array type) and profile length and location in the ERT method was based on several critical factors:

subsurface resolution, depth of investigation, and cost and time constraints.

The electrode spacing was set at 1 m. Narrowing the electrode spacing is expected to improve resolution. However, there are also disadvantages, such as reduced time efficiency and the adverse effect on inversion analysis since the influence of the electrode's penetration depth cannot be ignored [17], [25]. 1 m electrode spacing achieved both sufficiently reduced ground resistance through electrode embedment and the resolution requirement.

The length of the ERT profile was determined by the dimensions of the area under investigation, aiming to cover the entire region of interest for a comprehensive view of subsurface conditions. Arranging the location of all the profiles to run across the center of the burial mounds enabled us to delineate the entire area inside the tumuli while reducing negative impacts on analysis due to topographical changes in the direction perpendicular to the profiles as much as possible. Also, for Tumulus No. 1, Installing two orthogonal profiles, a-a' and b-b', empowered us to obtain a more detailed and comprehensive view.

A frequently occurring problem with ERT is determining which of the many existing electrode configurations is the best for the subsurface anomalies. In this study, we used a dipole-dipole array, which was the most effective configuration in mapping shallow subsurface areas because it provides good resolution of fractures and caves [26]. In addition, the DCPT was driven to a depth of 1 m at each point. Penetration resistance was recorded, and the cone installed at the rod tip was used as an electrode. Since the penetration of the cone had the risk of causing severe damage to the internal structure of the tumuli, the penetration position and penetration depth were determined to be up to 1 m from the perspective of cultural property protection.

The measurement procedure was as follows: measurements were first taken using only the surface electrodes for each profile, with dipole spacing of 2 m, 3 m, 4 m, and 5 m. Then, at the points indicated in Fig. 7 (a) and (b), the surface electrodes were replaced with DCPT electrodes along with recording penetration resistance, and additional measurements were taken with surface electrodes and buried electrodes. In this case, the buried electrodes were used as one of the current electrodes. The dipole spacing was also 2 m, 3 m, 4 m, and 5 m. Note that measurements using buried electrodes were not carried out for a-a' due to bad weather and time constraints.

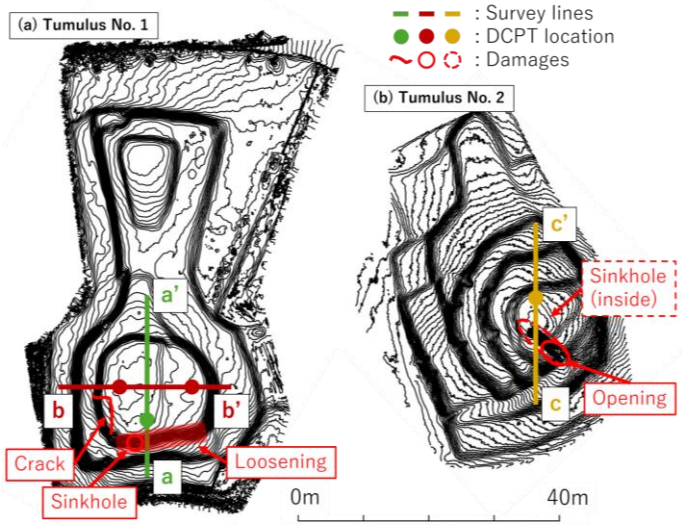

Fig. 7. Plan view for the ERT profiles damage locations indicated on the contour map of (a) Tumulus No. 1 and (b) Tumulus No. 2.

Table 3. Profile information.

Line	Length [m]	No. of Data Points with	
		Surface Electrodes Only	Buried Electrodes
a-a'	30	324	-
b-b'	26	170	37
c-c'	27	110	60

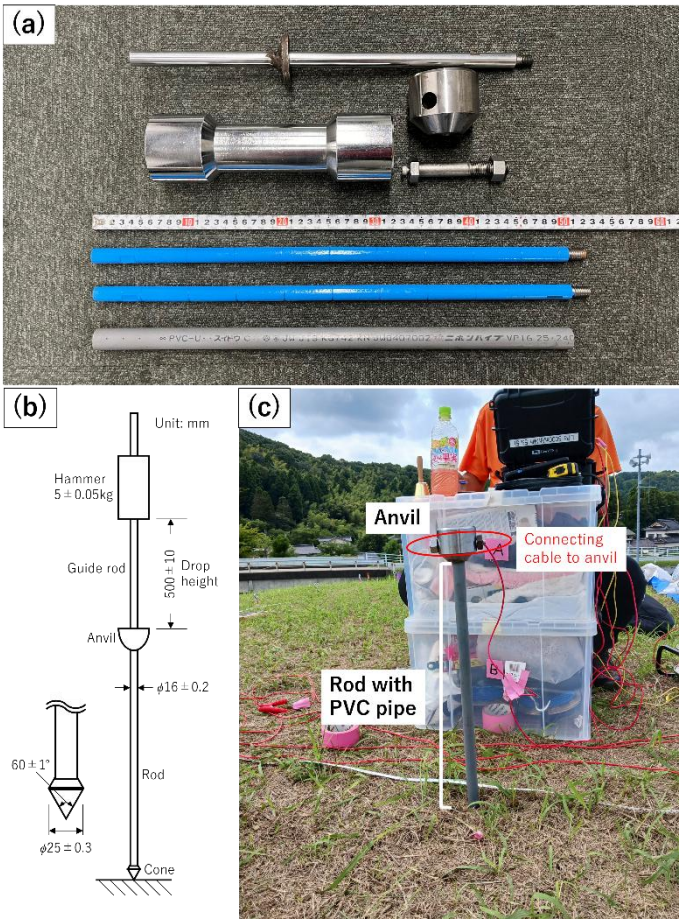

Fig. 8. (a) The overall structure of the DCPT devices. The blue rods were driven into the ground with the PVC pipe below. (b) Schematic of the DCPT device. (c) The DCPT device driven into the ground being used as a buried electrode.

For the DCPT test, we used a modified version of the test device specified in JGS 1443 [17], as shown in Fig. 8(a). Fig. 8(b) shows a schematic diagram of the test device, which consists of a cone, a rod, an anvil, a guide rod, and a hammer. All of the devices were made of metal. The hammer was dropped from a height of 50 cm to penetrate the cone dynamically, and the number of blows was recorded at 10 cm intervals of penetration. For this study, rods were painted beforehand to insulate the equipment except for the cone electrically, and the penetration test was carried out using a polyvinyl chloride (PVC) pipe (I.D. = 16 mm, O.D. = 22 mm) covering the painted rod. When using the cone as a ground electrode, a cable was connected to the anvil so the current could pass through the rod to the cone (Fig. 8(c)).

All ERT surveys were conducted with a GeoVES-1 resistivity meter (Geo5 Co., Ltd., Japan). For this survey, voltage and current were measured with electrode positions, thus obtaining the apparent resistivity.

2.4 Data processing

Data processing is a critical step in ERT surveys, as it involves transforming raw field measurements into meaningful subsurface resistivity structures. We used EarthImager 2D (Version 2.4.0) software for the resistivity data processing and inversion. Outliers with incorrect resistivity values, caused by poor contact between the electrode surface and the ground owing to dry surface soil or ambient noise, were excluded from the analysis.

The inversion performed in EarthImager 2D is based on the smoothness-constrained least squares method. The 2D model used in the inversion process divided the subsurface into a fine mesh of rectangular blocks from shallow to deep that are limited at depth by the approximate depth of investigation. The program iteratively determines the model blocks' resistivity, producing an apparent resistivity pseudo-section that matches the field data. Through inversions, the electrical resistivity method produces a geoelectric cross-section. The cross-section is developed by gridding the resistivity as a function of depth, showing areas of higher or lower resistivity than the background resistivity of the entire cross-section [27], [28].

3. RESULTS AND DISCUSSION

3.1 DCPT results

Fig. 9(a) shows the blow counts for the penetration depth for the DCPT tests conducted at four locations shown in Fig. 9(b) and (c). In JGS 1443 [17], the following equation is given in relation to the standard penetration test (SPT):

$$N_d = 1.5N \qquad \text{(Eq. 2)}$$

where N_d = blow counts of DCPT, $N = N$ values of SPT.
Again, we note that the hammer of 5 kg was dropped from a height of 50 cm for each blow, as stated in JGS 1443. However, in this study, since the rod was wrapped around the PVE pipe (Fig. 8(c)), the friction between the rod and the ground was probably more significant, so the use of Eq. 2 should be limited.

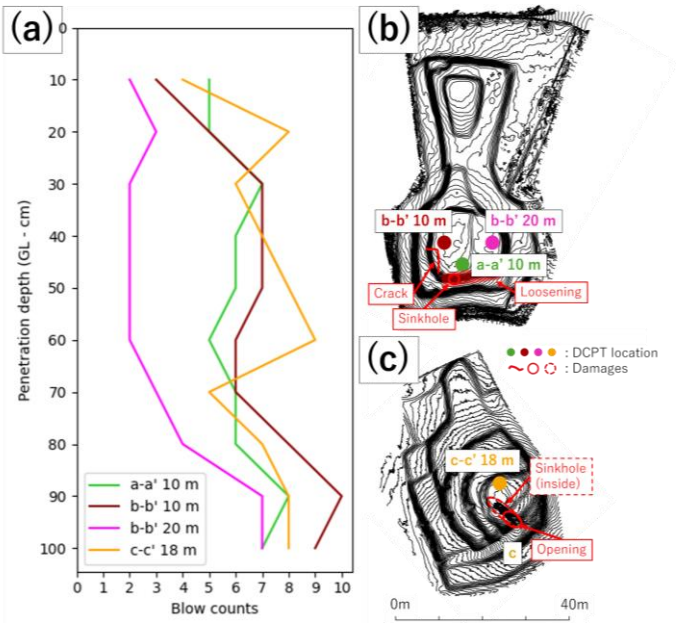

Fig. 9. (a) DCPT results. (b), (c) Locations of DCPT.

The ground was generally loose at all points, and in particular, the ground at the 20 m point on b-b' was remarkably soft. This ground is thus considered vulnerable to earthquake damage, such as cracks or sinkholes. As the DCPT was only carried out at one point in Tumulus No. 2, it is unclear whether there is any inhomogeneity in the distribution of ground loosening within the tumulus.

3.2 ERT results on Tumulus No. 1

Fig. 10-Fig. 12 are the results of ERT analysis for a-a' and b-b' on Tumulus No. 1. The background resistivity values for Tumulus No. 1 lay around 700 Ω·m, which means the mound is constructed with uniform material. In all profiles, a high resistivity zone between 1,500 and 2,500 Ω·m situated to the depth of 2 m existed in the center of the mound (12-17 m on Line a-a' and 12-16 m on Line b-b'). It could be interpreted as the central burial facility from an archaeological perspective. All profiles also showed a low resistivity area under 300 Ω·m under a depth of about 2.5 m or more from the top of the burial mound. This area can be attributed to the moist soils due to earlier rainfalls.

In terms of visualizing observed damages, Fig. 10 exhibited a high resistivity area ranging from 1,000 to 2,500 Ω·m on the slope near the 3-6 m point on a-a. This area is associated with the small sinkhole and the loosened slope (Fig. 2 and 7), where the void was mainly filled with resistive materials (sandbags or air), as observed during the preliminary survey. On the other

hand, neither Fig. 11 nor Fig. 12 displayed high resistivity anomalies, which are recognized as the crack (Fig. 3) because the electrode spacing was larger than the crack dimension.

There were some differences in the detailed resistivity distribution when comparing Fig. 11 and Fig. 12, which can be interpreted as the evidence of the method's superiority using buried electrodes. Fig. 12 showed a localized low resistivity area of about 300 Ω·m or lower below the 9 m point on b-b', which was not seen in Fig. 11. It can be inferred that more rainwater had penetrated from the known crack nearby (Fig. 3, Fig. 7) into the mound to the interpreted depth of 2-4 m, which is beyond the observed depth of the crack (Table 1). This result provides valuable insights into protecting cultural property, revealing that some influence may extend further inside than the observable damage. Moreover, the low resistivity area below the 20 m point on b-b' was shown clearer in Fig. 12 than in Fig. 11. Taken together with the DCPT results at this point (Fig. 9), it may correspond to the higher degree of water saturation than at other points, leading to a drop in resistivity and a decrease in ground strength. It can be said that the possibility of detecting localized underground anomalies increases with the installation of DCPT and the array configuration with buried electrodes.

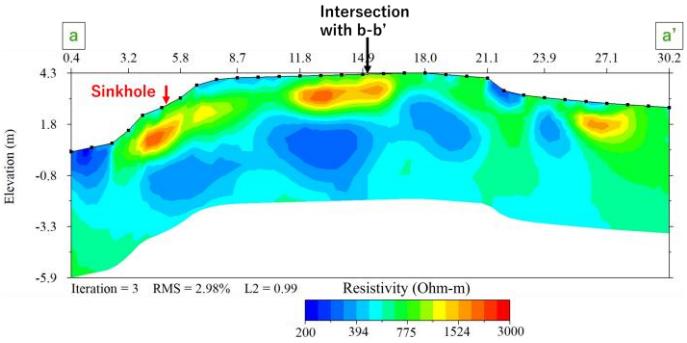

Fig. 10. 2D inversion model of Line a-a', with surface electrodes only.

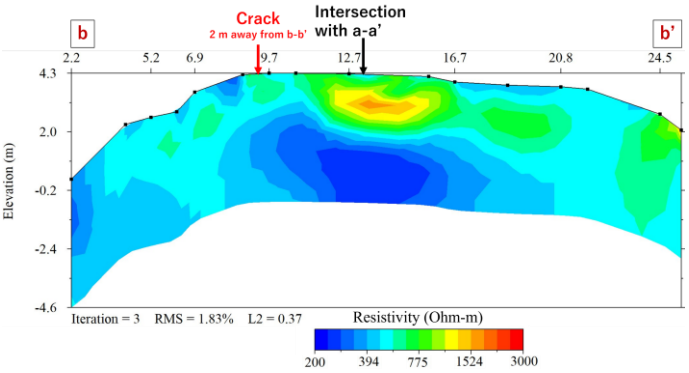

Fig. 11. 2D inversion model of Line b-b', with surface electrodes only.

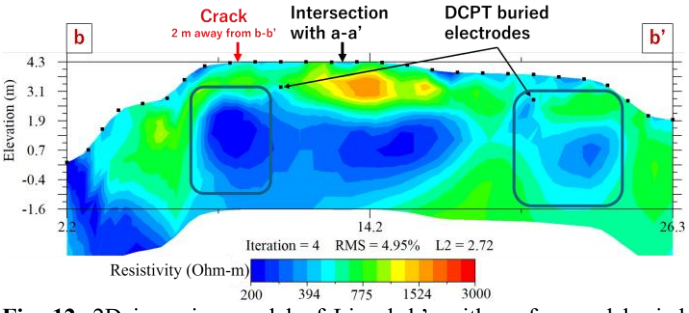

Fig. 12. 2D inversion model of Line b-b', with surface and buried electrodes. Localized low resistivity anomalies (surrounded by blue lines) were newly exhibited by installing buried electrodes.

3.3 ERT results on Tumulus No. 2

Fig. 13 and Fig. 14 show the results of ERT analysis for c-c' on Tumulus No. 2. In both figures, a region where the resistivity increased to about 2,000 Ω·m was positioned at the 8 m and below the 10-15 m point, which corresponds to the opening and the air-filled sinkhole, respectively (shown in Fig. 4). The interpreted length of the sinkhole is about 7 m and is consistent with the results of the preliminary survey shown in Table 3. In addition, the area about 1.5 m underground at the 8 m point exhibited low resistivity under 300 Ω·m, probably because rainfalls had been easily entered from the sinkhole opening next to it.

No significant differences were found when comparing Fig. 13 and Fig. 14. This tells us that, to obtain the effect of improving resolution using buried electrodes, it is necessary to make more measurements with buried electrodes placed in deeper ground.

The significantly high resistivity area over 3,000 Ω·m extended to about 2 m underground at the 17-22 m point. While

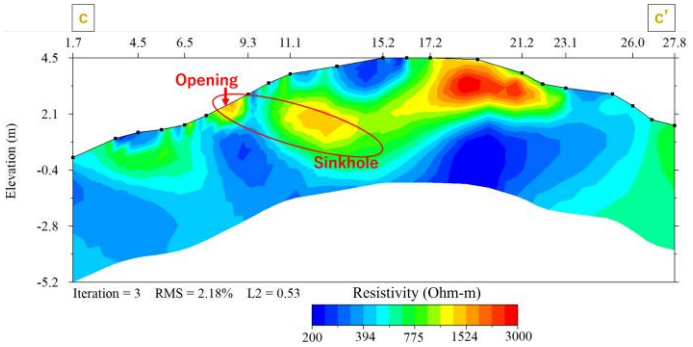

Fig. 13. 2D inversion model of Line c-c', with surface electrodes only.

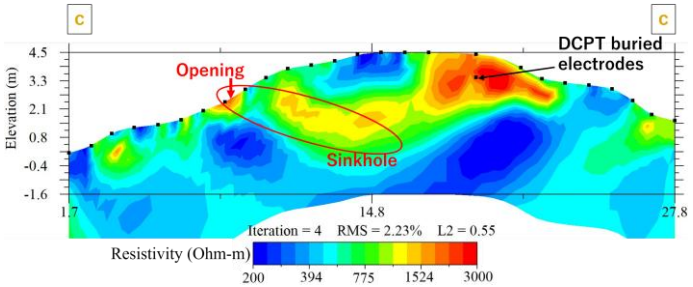

Fig. 14. 2D inversion model of Line c-c', with surface and buried electrodes.

this area represented a tremendous geo-electrical characteristic, as shown in Fig. 9(a), there was no significant difference mechanically from the results of the DCPT conducted at the 18 m point on c-c' compared to the results of Tumulus No. 1. Therefore, this high resistivity area may indicate the distribution of fill material with similar strength to the surrounding area but with different electrical characteristics. Although the high resistivity area corresponding to the known sinkhole (Fig. 4) and the high resistivity area on the right are displayed as if they are one continuous area in both Fig. 13 and Fig. 14, it is unlikely that the high resistivity area on the right is a cavity, since it should be observed that penetration resistance decreases if the cone reached a cavity or peripheral loosened area [29]. It is also possible that a high resistivity body is buried close to the 18 m point or that the inversion results are affected by a sudden change in the nearby terrain. Further investigation is desired.

CONCLUSIONS

In response to the damage caused by the 2024 Noto Earthquake, an ERT survey was conducted at the Sakuradani tumuli as a preliminary investigation for future remedial works. This study aimed to assess the extent of the damage and the internal structure of the burial mounds. In addition to the conventional ERT method, a novel ERT approach using a DCPT device under development was applied. The survey included four DCPT locations and three survey lines, employing two different measurement patterns: one using surface electrodes only and the other incorporating buried electrodes installed by the DCPT.

The inversion results effectively delineated subsurface structures and features associated with the observed damages. For Tumulus No. 1, the imaging revealed a small sinkhole and slope looseness, while for Tumulus No. 2, a sinkhole was identified, consistent with findings from previous observational studies. However, due to the 1 m spacing of electrodes, the crack observed at Tumulus No. 1 was too narrow to be resolved.

In addition to resistivity anomalies linked to observed damage, high resistivity zones were detected at the center of Tumulus No. 1 and near the 18 m point of Tumulus No. 2. The origins and implications of these anomalies remain uncertain, warranting further investigation to determine their connection to the earthquake.

Notably, the configuration employing buried electrodes successfully captured the relationship between rainwater infiltration through cracks and the relatively high water content in the ground-loosened area. This highlights the DCPT-based buried electrode system's capability to detect localized resistivity anomalies, emphasizing its importance for cultural heritage preservation. Despite these promising results, measurements at Tumulus No. 2 showed no significant difference between the use of surface-only electrodes and the DCPT-based buried electrodes, indicating the current system's limitations in resolving deeper subsurface features. Enhancements are recommended to improve resolution at greater depths, such as increasing the penetration depth of the DCPT device.

Future trench excavation surveys may provide opportunities to validate the resistivity interpretations presented in this study, potentially advancing the understanding of subsurface structures and contributing to effective remedial measures for preserving cultural heritage sites.

ACKNOWLEDGMENTS

We would like to express our gratitude to Takaoka City and Dr. Mai Sawada for providing us with the opportunity to conduct this field survey. We also thank Geo5 Co., Ltd. for their valuable comments on the inversion technique, which helped improve this manuscript.

REFERENCES

[1] US Geological Survey (USGS), "M 7.5 - 2024 Noto Peninsula, Japan Earthquake." Accessed: Nov. 07, 2024. Available:https://earthquake.usgs.gov/earthquakes/eventpage/us6000m0xl/executive

[2] C. Mizuno, X. Wang, and J. Dang, "A fast survey report about bridge damages by the 2024 Noto Peninsula Earthquake," *Earthquake Research Advances*, vol. 4, no. 4, p. 100312, Oct. 2024, doi: 10.1016/j.eqrea.2024.100312.

[3] A. Suppasri, M. Kitamura, D. Alexander, S. Seto, and F. Imamura, "The 2024 Noto Peninsula earthquake: Preliminary observations and lessons to be learned," *International Journal of Disaster Risk Reduction*, vol. 110, p. 104611, Aug. 2024, doi: 10.1016/j.ijdrr.2024.104611.

[4] Adachi T., "Rescue and Condition Assessment of Damaged Cultural Properties [Translated from Japanese]," Kanazawa University. Accessed: Nov. 06, 2024. [Online]. Available: https://www.kanazawa-u.ac.jp/research/centers/kud/adachi-1/

[5] Adachi T., "Rescue and Condition Assessment of Damaged Cultural Properties #2 [Translated from Japanese]," Kanazawa University. Accessed: Nov. 06, 2024. [Online]. Available: https://www.kanazawa-u.ac.jp/research/centers/kud/adachi-2/

[6] H. Aoki, "An Analytical Study on Construction Techniques of Tombs through Geoarchaeology: Focusing on Tombs Subjected to Geotechnical Investigation [Translated from Japanese]," *Bulletin of the Graduate Division of Letters, Arts and Sciences of Waseda University. 4*, vol. 56, pp. 79–95, 2010.

[7] S. Wakiya, "Efforts for the Conservation of Damaged Decorated Tombs [Translated from Japanese]," Mar. 2021, Accessed: Nov. 07, 2024. [Online]. Available: https://repository.nabunken.go.jp/dspace/handle/11177/9455?mode=full

[8] "Sakuradani Tomb," Takaoka City Official HP. Accessed: Oct. 31, 2024. [Online]. Available:

https://www.city.takaoka.toyama.jp/soshiki/kyoikuiinkai_bunkazaihogokatsuyoka/1/4/1/2393.html

[9] M. H. Loke, J. E. Chambers, D. F. Rucker, O. Kuras, and P. B. Wilkinson, "Recent developments in the direct-current geoelectrical imaging method," *Journal of Applied Geophysics*, vol. 95, pp. 135–156, Aug. 2013, doi: 10.1016/j.jappgeo.2013.02.017.

[10] T. Dahlin, "The development of DC resistivity imaging techniques," *Computers & Geosciences*, vol. 27, no. 9, pp. 1019–1029, Nov. 2001, doi: 10.1016/S0098-3004(00)00160-6.

[11] M. A. H. Ali *et al.*, "Mapping Leachate Pathways in Aging Mining Tailings Pond Using Electrical Resistivity Tomography," *Minerals*, vol. 13, no. 11, p. 1437, 2023.

[12] Y. Hussain *et al.*, "The potential use of geophysical methods to identify cavities, sinkholes and pathways for water infiltration," *Water*, vol. 12, no. 8, p. 2289, 2020.

[13] M. Van Schoor, "Detection of sinkholes using 2D electrical resistivity imaging," *Journal of Applied Geophysics*, vol. 50, no. 4, pp. 393–399, Jul. 2002, doi: 10.1016/S0926-9851(02)00166-0.

[14] A. M. Youssef, H. El-Kaliouby, and Y. A. Zabramawi, "Sinkhole detection using electrical resistivity tomography in Saudi Arabia," *Journal of Geophysics and Engineering*, vol. 9, no. 6, pp. 655–663, 2012.

[15] H. Kamei, Y. Marukawa, H. Kudo, Y. Nishimura, and M. Nakai, "Geophysical survey of Hirui-Otsuka Mounded Tomb in Ogaki, Japan," *Archaeological Prospection*, vol. 7, no. 4, pp. 225–230, Dec. 2000, doi: 10.1002/1099-0763(200012)7:4<225::AID-ARP136>3.0.CO;2-C.

[16] W. Edwards, M. Okita, and D. Goodman, "Investigation of a subterranean tomb in Miyazaki, Japan," *Archaeological Prospection*, vol. 7, no. 4, pp. 215–224, Dec. 2000, doi: 10.1002/1099-0763(200012)7:4<215::AID-ARP135>3.0.CO;2-G.

[17] The Japanese Geotechnical Society, "Electrical Prospecting," in *Japanese Geotechnical Society Standards*, 3rd ed., vol. 1, 2 vols., 2016, pp. 120–126.

[18] Y. Yamashita, D. Groom, T. Inazaki, and K. Hayashi, "Rapid near surface resistivity survey using the capacitively-coupled resistivity system: OhmMapper," in *Proceeding of the 7th SEGJ International Symposium*, 2004, pp. 292–295. Accessed: Nov. 04, 2024. [Online]. Available: https://www.geometrics.com/wp-content/uploads/2018/10/segj-oyo-om-levee.pdf

[19] D. Harro and H. Kiflu, "Imaging of Deep Sinkholes Using the Multi-electrode Resistivity Implant Technique (MERIT) Case Studies in Florida," in *The 2018 Sinkhole Conference*, 2018, pp. 341–346. doi: 10.5038/9780991000982.1026.

[20] H. G. Kiflu, "Improved 2D and 3D resistivity surveys using buried electrodes and optimized arrays: The multi-electrode resistivity implant technique (MERIT)," Ph.D. dissertation, University of South Florida, 2016. Accessed: Oct. 31, 2024. [Online]. Available: https://digitalcommons.usf.edu/etd/6524/

[21] M. H. Loke, H. Kiflu, P. B. Wilkinson, D. Harro, and S. Kruse, "Optimized arrays for 2D resistivity surveys with combined surface and buried arrays," *Near Surface Geophysics*, vol. 13, no. 5, pp. 505–518, Jun. 2015, doi: 10.3997/1873-0604.2015038.

[22] D. Harro and S. Kruse, "Improved imaging of covered karst with the multi-electrode resistivity implant technique," in *Proceedings of the Thirteenth Multidisciplinary Conference on Sinkholes and the Engineering and Environmental Impacts of Karst*, 2013. Accessed: Oct. 31, 2024. [Online]. Available: https://digitalcommons.usf.edu/cgi/viewcontent.cgi?article=1129&context=sinkhole_2013

[23] F. Jiang *et al.*, "Resistivity tomography based on multichannel electrodes," *Appl. Geophys.*, Mar. 2024, doi: 10.1007/s11770-024-1059-x.

[24] H. IKEGAMI and T. FUJIWARA, "Development of Readily Installable Electrodes Mounted on the Driving-Pipes for Resistivity Measurements," *TAISEI ADVANCED CENTER OF TECHNOLOGY TECHNICAL REPORT*, no. 56, p. 50, 2023.

[25] Sean, "How To Do Small-Scale Electrical Resistivity Imaging Lab Tests," AGIUSA. Accessed: Nov. 04, 2024. [Online]. Available: https://www.agiusa.com/blog/how-do-small-scale-electrical-resistivity-imaging-lab-tests

[26] F. M. Abdullah, M. H. Loke, M. Nawawi, and K. Abdullah, "Assessing the reliability and performance of optimized and conventional resistivity arrays for shallow subsurface investigations," *Journal of Applied Geophysics*, vol. 155, pp. 237–245, Aug. 2018, doi: 10.1016/j.jappgeo.2018.06.018.

[27] M. H. Loke and R. D. Barker, "Least-squares deconvolution of apparent resistivity pseudosections," *Geophysics*, vol. 60, no. 6, pp. 1682–1690, Dec. 1995, doi: 10.1190/1.1443900.

[28] M. H. Loke and T. Dahlin, "A comparison of the Gauss–Newton and quasi-Newton methods in resistivity imaging inversion," *Journal of Applied Geophysics*, vol. 49, no. 3, pp. 149–162, Mar. 2002, doi: 10.1016/S0926-9851(01)00106-9.

[29] M. Sato and R. Kuwano, "Influence of location of subsurface structures on development of underground cavities induced by internal erosion," *Soils and Foundations*, vol. 55, no. 4, pp. 829–840, Aug. 2015, doi: 10.1016/j.sandf.2015.06.014.

Techno-Science Research Journal V13 (Special Issue) (2025) P 22-28

I.T.C

Content list available at ITC

Techno-Science Research Journal

Journal Homepage: www.ric.itc.edu.kh

Techno-Science Research Journal

Wave Propagation Analysis for Exploration of Ground Loosening at Great Depths

Kazuki Kuwashiro [1*], Masahide Otsubo [2], Reiko Kuwano[1]

[1] *Institute of Industrial Science (IIS), The University of Tokyo, 4-6-1 Komaba, Meguro-ku, Tokyo, 153-8505, Japan*
[2] *Port and Airport Research Institute, 3-1-1 Nagase, Yokosuka-shi, Kanagawa, 239-0826, Japan*

Received: 1 November 2024; Revised: 1 January 2025; Accepted: 20 June 2025; Available online: October 2025

Abstract: *It has recently become clear that ground loosening and subsurface cavities, created by shield tunnel excavation around 50 meters deep, can cause ground cave-ins. Although the ground-penetrating radar method has been utilized to detect subsurface cavities, its applicability is limited to the relatively shallow ground about 1.5 meters below the ground surface and does not target the loosened soil directly above a deep tunnel. As an alternative method of finding deeper cavities, the surface wave surveys are being studied and explored. This research is a fundamental study involving elastic wave surveys conducted inside the tunnel to assess the potential for detecting ground loosening at great depths. The discrete element method (DEM) with spherical particles was adopted to understand wave propagation and particle-scale response around the loosened region. Some model ground samples with loosening were created and the positions of excitation and receiver sensors were varied to investigate the method of excitation and the best sensor position for each. The time-spatial domain dynamic response obtained from each sensor revealed how the elastic waves generated by excitation are affected by the loosened region. The analysis suggests the potential to identify loosened regions by comparing excitation positions and their corresponding frequency characteristics at each sensor.*

Keywords: Wave propagation, Loosening, Discrete element method, Geophysical survey, Model test

1. INTRODUCTION

In recent years, ground cave-ins, the sudden collapse of the ground surface, have been occurring in various locations both in Japan and abroad. It is known empirically that cohesionless sandy soils are more prone to cave-ins than plastic fine silt or clayey soil. As a countermeasure, the ground-penetrating radar method has been utilized for detecting subsurface cavities caused by buried pipes, etc., in practice. However, its applicability is limited to the relatively shallow ground about 1.5 m below the ground surface. Although studies using dynamic wave surveys have been considered to detect deeper cavities, they are all targeted at detecting cavities several meters deep by surveying from the ground surface. Furthermore, it is important to detect regions of soil loosening before the formation of underground cavities. However, detecting soil loosening regions seems more difficult than detecting underground cavities.

The ground cave-in accident caused by shield tunnel excavation in Chofu, Japan in 2020 revealed that cave-ins could be triggered by ground loosening or cavities even deep underground.

The Therefore, this study aims to understand the propagation characteristics of elastic waves in order to detect loosening of the deep underground from the inside of a tunnel. A series of discrete element method (DEM) simulations is performed to assess the particle-scale response around the loosened region by varying the positions of excitation and receiver sensors as well as excitation methods. To understand how elastic waves propagate or reflect around the loosened region, the present simulation approach broadly follows Nakata et al. [1] who investigated the wave propagation characteristics around a subsurface cavity. This study builds on an earlier work for laboratory element-scale simulations by Otsubo et al. [2] where wave reflection characteristics at dense and loose interfaces were investigated. This contribution extends their findings by exploring model-scale responses to understand how elastic waves propagate or reflect around loosened regions in comparison with dense ground without loosening.

* Corresponding author: Kazuki Kuwashiro
E-mail: *kkuwa39@iis.u-tokyo.ac.jp;* Tel: *+81 3 5452 6843*

2. DEM SIMULATION

This study performed DEM simulations using granular LAMMPS software [3]. To ensure the validity of the DEM simulations, Otsubo et al. [4] have compared shear failure behavior in FCC-packed granular materials using LAMMPS with theoretical solutions. Their results demonstrated that the shear strength and energy balance behavior are generally consistent with theoretical expectations. To simplify complicated model test conditions, spherical particles with typical glass bead properties were adopted (Young's modulus: 71.6 GPa, Poisson's ratio: 0.23, and specific gravity: 2.65). While spherical particles cannot fully replicate the shape effects of real soil particles [5], they are sufficient for achieving qualitative insights into the effects of ground loosening on wave propagation. Furthermore, using non-spherical particles in a DEM simulation of this scale would result in computational costs that are currently impractical. The particle stiffness was set to reflect realistic values, as it directly influences shear wave velocity (V_s) and small-strain shear modulus (G_0) [6]. Although mineralogical properties influence the particle stiffness, this effect was not considered in this study. The diameters of spherical particles range from 1.4 mm to 2.2 mm, representing a uniformly graded sandy soil. Broadening the particle size distribution while maintaining D_{50} (median particle size) significantly increases the required particle count and computational cost, making large-scale simulations impractical. A simplified Hertz-Mindlin contact model without cohesion was adopted to calculate contact responses following the Itasca Consulting Group [7].

In this study, ground samples in dry conditions, where no capillary forces exist, were considered. To represent the ground preparation method in the model test such as Nakata [8], air-pluviation process in a dry condition was simulated. Firstly, the original model ground samples for the following "patchwork" process were prepared. The base of the ground was modeled as frictionless rigid wall boundary, while periodic boundaries were used in the horizontal (X and Y) directions. Interparticle frictions (μ) of 0.01 and 0.5 were used respectively to create dense and loose ground samples (hereafter referred to as "dense only" and "loose only"). In this study, μ was carefully set to highlight the differences between dense and loose soils. However, during wave propagation analysis, μ was increased to focus on elastic behavior and reduce excessive energy dissipation caused by particle slippage. While damping was prioritized for efficient model preparation, it was intentionally set to zero during wave propagation analysis. This decision allows isolating geometric wave attenuation and reflection behaviors at dense-loose boundaries, rather than introducing artificial damping effects. After the pluviation process, the resultant void ratio (e) values were found to be 0.581 for dense only and 0.726 for loose only, and dry bulk density was 1.68 [g/cm^3] for the former and 1.54 [g/cm^3] for the latter.

To simulate loosening directly above a tunnel, the patchwork method was intentionally chosen in this study to precisely control the location and extent of the loosened region. This approach ensures a reproducible configuration, enabling a more systematic investigation of wave propagation characteristics around loosened zones. Combining parts of dense only and loose only samples, a mixed model ground sample (1.2 m in length (X), 0.2 m in height (Z), and 0.02 m in depth (Y)) with a locally loosened region was created as shown in Fig.1. A small gap was provided at the loose-dense boundary when the mixed model ground sample was generated, and an additional simulation was performed until the gap was closed and the entire ground reached a static equilibrium, where μ was increased to 0.5 for all the particles. This dense-loose mixed model is refeered to here as "Case Loosened S". For comparison, uniformly dense ("Case Dense Only") and uniformly loose ("Case Loose Only") model ground samples were also prepared.

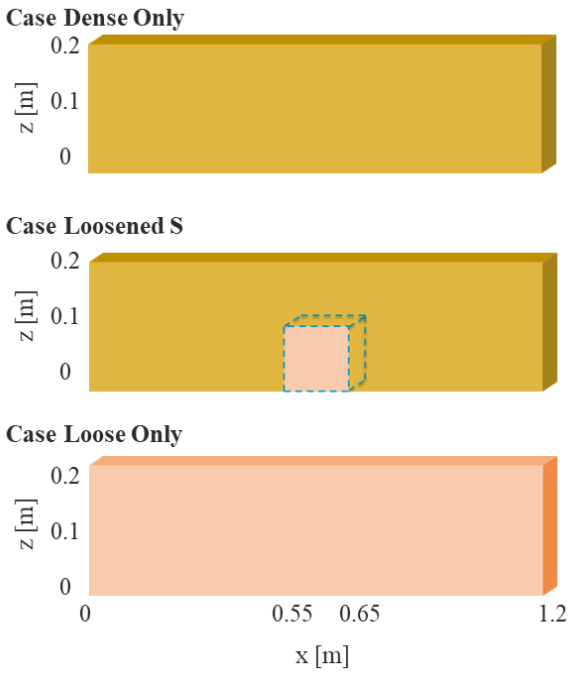

Fig. 1. Prepared three ground models. The color of the particles corresponds to the value of friction coefficient (μ), with orange indicating a dense region and pink indicating a loose region.

3. PHYSICAL CHARACTERISTICS OF MODELS

The distribution of inter-particle forces in the three ground models was examined prior to performing wave analysis (Fig. 2). The normalized forces proportional to the vertical position of the contact points were calculated, with data below a threshold of 30% omitted to visualize only significant contacts. Due to the absence of gravity effects, the force distribution in Cases Dense Only and Loose Only remained uniform, whereas in Case

Loosened S, significant soil arching occurred over the loosened region. This phenomenon can be considered similar to the study that soil surrounding a subsurface cavity becomes loosened, where an arch is created over the cavity to support the upper ground in laboratory model tests [9]. Furthermore, Ali et al. [10] justified that the development of soil arching was able to be discussed even when the periodic boundaries in the horizontal direction were used.

Subsequently, the distribution of the coordination number (*CN*), which represents the number of contacts per particle, was examined (Fig. 3). This value indicates the contact relationships between particles and plays a crucial role in the mechanical properties of the ground and particle packing structures. For example, it is known that an increase in fine particles or a decrease in *CN* reduces G_0 [11] [12]. In densely packed

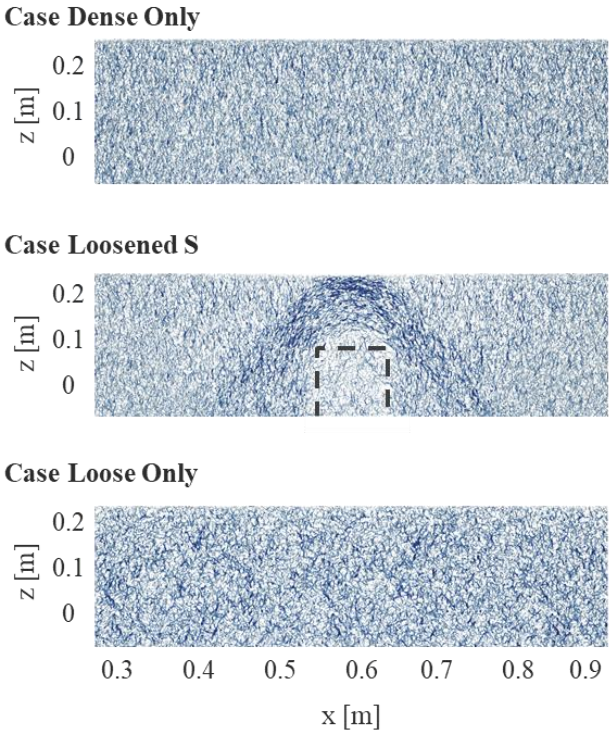

Fig. 2. Distribution of inter-particle forces in the ground models. These images were enlarged in the range of x = 0.3~0.9 [m].

conditions, the number of adjacent particles in contact with an individual particle increases, resulting in a higher *CN*. In Case Loosened S, a decrease in *CN* was observed not only within the designated loosened region (x = 0.55–0.65 [m], z = 0.00–0.10 [m]) but also across a broader area, extending from the outer side of the soil arch toward the upper surface. This phenomenon closely resembles the behavior observed in natural soils when voids or cavities are artificially created in laboratory experiments [1]. The final stabilized state after equilibrium analysis can be considered to approximate a naturally stable condition.

4. WAVE PROPAGATION SIMULATIONS

In this study, the excitation and receiver sensors with a region of length (X) 0.004 m, height (Z) 0.004 m, and depth (Y) 0.02 m were placed at each position of the ground models. Particles within the excitation region were vibrated to generate a one-period cosine wave (double amplitude displacement: 10 nm). Following Otsubo et al. [2], μ was further increased to 0.6 in the wave propagation simulation so that the elastic response of the propagating wave could be analyzed. Neither local nor viscous damping was used during wave propagation.

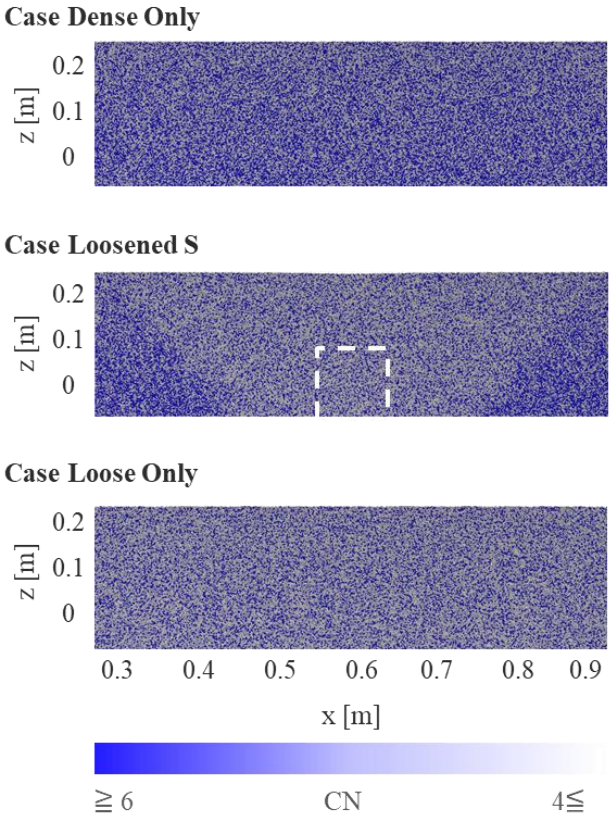

Fig. 3. Distribution of *CN* in the ground models. These images were enlarged in the range of x = 0.3~0.9 [m].

Note that, as shown by Kuwashiro et al. [13], observing the particle kinetic energy in the Y direction of the Y excitation reduces the interference of the P-wave signal and allows only S-wave propagation characteristics in the XZ plane to be analyzed. To observe wave propagation more clearly, in this study, only Y- directional excitation was used for excitation, and the positions of the excitation and the receiver sensors were changed for comparison.

4.1 Frequency filtering

It is known that the ground acts as a cutoff filter for high-frequency components of vibrations propagating in the ground [14]. The maximum value of the frequency component of the elastic wave does not continue to decrease during the propagation process, but rather remains at a constant value after settling at a ground-specific value [15]. This maximum value is referred to as the lowpass frequency (f_{lp}); the granular aggregate simulated by the DEM acts as a lowpass filter for the stress/sound waves propagating through the aggregate, and the f_{lp} is dependent on packing density, stress, and grain size [16] [17] [18].

Focusing on f_{lp} could facilitate the detection of ground loosening. The Fast Fourier Transform (FFT) was applied to the measured data to evaluate f_{lp}. The frequency components of the input wave were designated as FFT_{in} and those of the output wave as FFT_{out}. The proportion of frequency components that passed through the ground was calculated using (Eq. 1). A threshold can be applied to FFT_{gain}, and the frequency at which the amplitude falls below this threshold is defined as f_{lp}.

$$FFT_{gain} = |FFT_{out}| / |FFT_{in}| \quad \text{(Eq. 1)}$$

4.2 Excitation from the bottom of the model

To investigate the loosening directly above a tunnel using elastic waves, excitation and receiver sensors were installed at the bottom surface of the model (z = 0.0 [m]). For the excitation positions in Case Loosened S, three cases were considered for comparison: (a) outside the arch where the *CN* is high (dense area), (b) inside the arch where the *CN* is low (dense area), and (c) within the loosened area. The excitation position were placed at (a) x = 0.3 [m], (b) x = 0.5 [m], and (c) x = 0.6 [m], respectively. Receiver sensors were positioned at distances of x = 0.1, 0.2, and 0.3 [m] from the excitation to record wave propagation data. Initially, elastic waves with various frequency components ranging from 1 to 10 kHz were generated. It was visually confirmed that frequency filtering occurred in the loosened area for waves above approximately 3 kHz. Based on this trial, a sufficiently high-frequency wave of 10 kHz was applied to each model to discuss the cutting of high-frequency components.

Fig. 4 shows time-history snapshots of the Y-directional particle kinetic energy in each model ground during Y-direction excitation. Since waves propagate faster in the dense ground, the snapshot times differ only for Case Dense Only. For comparison, the snapshots were not taken at the same time but rather at the same wave positions: each snapshot was selected to align the position of the red wave across all cases. In the loosened soil region, the wave energy dissipates due to weak inter-particle connections and small contact and frictional forces. High-frequency components tend to attenuate due to energy loss during the rapid oscillation cycle. Reflected waves could not be clearly captured.

Next, FFT_{gain} was calculated for each excitation position, normalized by the maximum value (Normalized gain factor), and compared for each receiver sensor (Fig. 5). Here, when calculating FFT_{gain}, the designed single wave was extracted as the input wave data, and the first wave transmitted to the receiver sensor was extracted as the output wave data. To define the first wave at the receiver sensor, the following process was conducted. First, using the time-history displacement data obtained at the receiver sensor, the time difference of wave energy, $\Delta E(t)$, was calculated according to (Eq. 2). $u(t)$ represents the displacement data at the time.

$$E(t) = u(t)^2 \quad \text{(Eq. 2)}$$

Using the energy difference $\Delta E(t)$, the timing of the first wave was defined based on the following steps:

1. Detect the first time, t_{start}, when $\Delta E(t)$ exceeds 5% of the maximum value (threshold) in the entire dataset. (This marks the rise of the first wave.)
2. After exceeding the threshold, detect t_{peak} when $\Delta E(t)$ first becomes zero or less. (This marks the peak of the first wave.)
3. Calculate t_{end} for the fall of the first wave according to (Eq. 3).

$$t_{end} = t_{peak} + (t_{peak} - t_{start}) \quad \text{(Eq. 3)}$$

Regardless of the excitation position, in Case Dense Only, the high-frequency components of the waves were observed to attenuate as the receiver sensor distance increased. In Case Loose Only, high-frequency waves above approximately 2–3 kHz did not propagate at any excitation or receiver sensor positions. The loosened model ground prepared for this study exhibited a stable f_{lp} of approximately 2–3 kHz, below which low-frequency components propagated with minimal attenuation. In Case Loosened S, when excitation was performed at (a), high-frequency components propagated at x = 0.4 [m] in the high-*CN* region but were abruptly filtered at x = 0.5 [m] and x = 0.6 [m], where *CN* is low. In contrast, when excitation was performed at (b) or (c), no high-frequency components propagated to any receiver sensors.

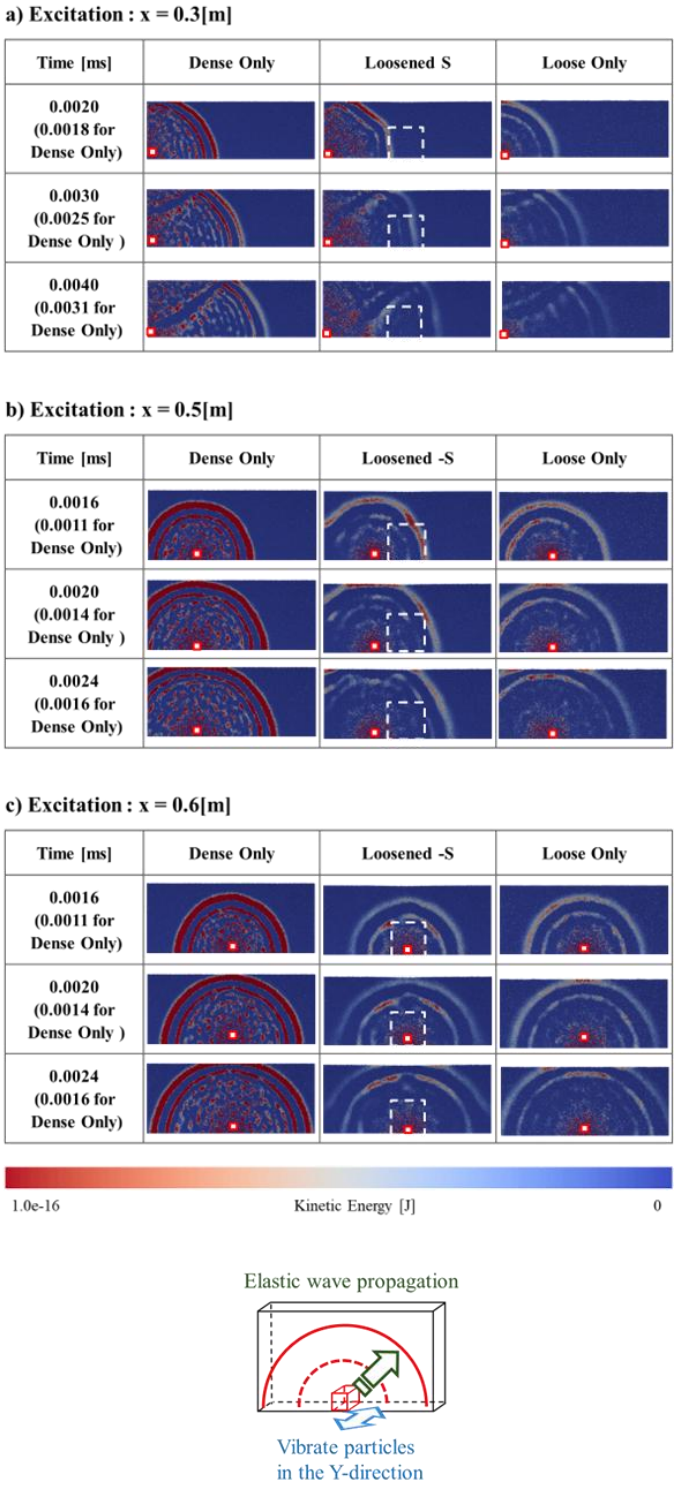

Fig. 4. The time-history snapshots of the Y-directional particle kinetic energy of the Y excitation (Excitation at x = 0.3, 0.5, 0.6 m). These images were enlarged in the range of x = 0.3~0.9 [m]

The shear wave components confirmed by Y-direction excitation are known to exhibit slower wave velocities as *CN* decreases [12] [19]. Based on the same principle, f_{lp} for shear waves is also considered to strongly depend on *CN*, decreasing as *CN* decreases. By varying the excitation positions and comparing the frequency characteristics obtained at each receiver sensor, it was suggested that anomalies indicating the presence of loosened soil could be detected, and their locations identified.

4.3 Excitation from the model side

Subsequently, an attempt was made to characterize the physical features of the model by focusing on wave propagation velocity. An excitation position was placed at x = 0.3 [m], and receiver sensors were arranged along the measurement line from x = 0.3 [m] to x = 0.9 [m] at intervals of d = 0.004 [m]. These sensor sets were designed at depths of z = 0, 0.05, 0.1, 0.15, and 0.2 [m], and the X-direction propagation data of waves generated by Y-direction excitation were observed.

For each sensor, the time corresponding to the peak (t_{peak}) of the first wave was obtained. The time difference between adjacent sensors, Δt_{peak}, was calculated, and the wave velocity V_s was determined based on (Eq. 4).

$$V_s = d / \Delta t_{peak} \quad \text{(Eq. 4)}$$

The results were visualized as a color map in Fig. 6. Missing values in some sensors were interpolated using linear interpolation, and extrapolation at the endpoints was performed using the nearest neighbor values. Although geometric dispersion effects become apparent over longer wave propagation distances, the ground model prepared for this study is nearly symmetrical, so the data on the left side was mirrored to the right side using x=0.6 [m] as the axis of symmetry. Immediately after excitation at x = 0.3 [m], higher V_s values were observed in a specific deeper region, which is considered to be due to high *CN*, as corroborated by overlaying this result with Fig. 3. Subsequently, a narrow band of high V_s values was observed around the loosened region. When cross-referenced with Fig. 2, this region corresponds to the region where arching occurs. The increase in V_s along the arch is likely due to the increased Y-direction contact forces on the arch. When waves entered the loosened area, *Vs* showed a tendency to decrease.

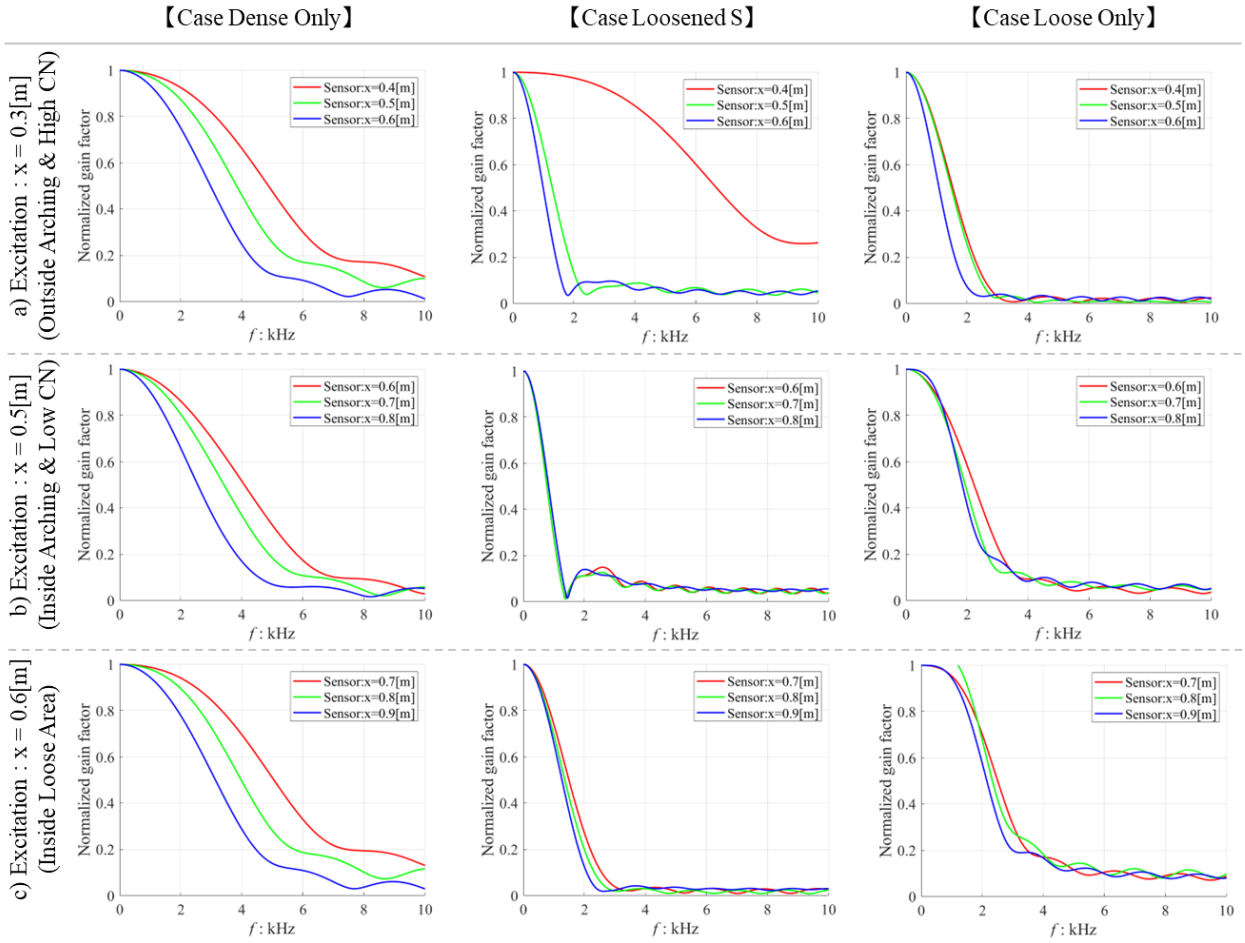

Fig. 5. The calculation of normalized gain factor (Excitation at x = 0.3, 0.5, 0.6 m). These images were enlarged in the range of x = 0.3~0.9 [m]

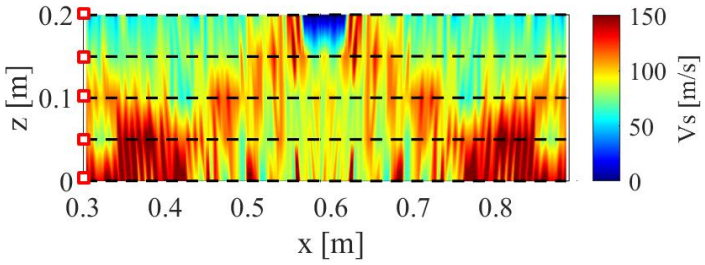

Fig. 6. Color map of shear wave velocity that propagets in the X-direction and occilate in the Y-direction. The excitation position is indicated by red squares, and the receive sensors' lines are represented by dashed lines. These images were enlarged in the range of x = 0.3~0.9 [m]

5. CONCLUSIONS

In this study, DEM simulations were used to investigate the wave propagation characteristics around loosened regions in a ground model. Wave analysis was conducted by focusing on the lowpass frequency and adjusting the positions of excitation and receiver sensors as well as the wave frequency. The following conclusions were drawn by comparing the results with those of ground models without loosening:

- From the DEM simulation, it was observed that the coordination number (*CN*) decreases from the outer side of the arch formed by soil loosening toward the upper surface.
- The propagation characteristics of shear waves are significantly influenced by *CN*, suggesting the potential to identify the location of loosened regions by relatively comparing sensor positions and frequency characteristics.
- The calculated S-wave velocity contour in the loosened ground effectively represented the physical properties

of the modeled ground, such as changes in CN caused by loosening and the formation of arches.

Further research, including laboratory model experiments, is necessary to detect ground loosening from inside tunnels.

ACKNOWLEDGMENTS

This work was supported by Penta-Ocean Construction Co., Ltd., and JSPS KAKENHI Grant Number 22K14322. The simulations presented in this contribution were conducted using the FUJITSU Supercomputer PRIMEHPC FX1000 (Wisteria/BDEC-01) in the Information Technology Center, The University of Tokyo.

REFERENCES

[1] Y. Nakata, M. Otsubo, U. Ali, and R. Kuwano, "Influence of soil arching and loosening around a subsurface cavity on wave propagation," 20th International Conference on Soil Mechanics and Geotechnical Engineering, Sydney, 2022.

[2] M. Otsubo, Y. Nakata, and R. Kuwano, "Effect of Locally Loosened Soil on Wave Propagation," 6th International Conference on Geotechnical and Geophysical Site Characterization, Budapest, 2020.

[3] S. Plimpton, "Fast parallel algorithms for short-range molecular dynamics," Journal of Computational Physics 117 (1), pp.1-19, 1995.

[4] M. Otsubo, C. O'Sullivan, and T. Shire, "Empirical assessment of the critical time increment in explicit particulate discrete element method simulations," Computers and Geotechnics, 86, 67–79, 2017.

[5] Y. Li, M. Otsubo, and R. Kuwano, "Elastic wave velocities during triaxial shearing influenced by particle morphology," Soils and Foundations, 64, 101443, 2024.

[6] M. Otsubo, C. O'Sullivan, K. J. Hanley, and W. W. Sim, "Influence of packing density and stress on the dynamic response of granular materials," Granular Matter, 19(50), 2017.

[7] Itasca Consulting Group, "PFC3D, version 4.0, User's manual. Minneapolis, " Itasca (MN, USA), 2007.

[8] Y. Nakata, "Stress transmission around an underground cavity evaluated using elastic waves," Master thesis, The University of Tokyo, 2020.

[9] R. Kuwano, R. Sera, and Y. Ohara, "Model tests to simulate formation and expansion of subsurface cavities, " Proc. 9th Int'l Conf. on Physical Modelling in Geotechnics, London, 1087-1092, 2018.

[10] U. Ali, M. Otsubo, H. Ebizuka, and R. Kuwano, "Particle-scale insight into soil arching under trapdoor condition, " Soils and Foundations 60 (5), 1171-1188, 2020.

[11] T. Wichtmann , M. A. Navarrete Hernández, and T. Triantafyllidis, "On the influence of a non-cohesive fines content on small strain stiffness, modulus degradation and damping of quartz sand," Soil Dyn. Earthq. Eng., 69, 103–114, 2015.

[12] Y. Li, M. Otsubo, and R. Kuwano, "DEM analysis on the stress wave response of spherical particle assemblies under triaxial compression," Computers and Geotechnics, 133, 104043, 2021.

[13] K. Kuwashiro, R. Kuwano, and M. Otsubo, "Exploration for Wave Propagation Around Ground Loosening Using Discrete Element Method, " Proceedings of the 7th International Conference on Geotechnical and Geophysical Site Characterization, 2024.

[14] A. da Fonseca , C. Ferreira, and M. Fahey, "A framework interpreting bender element tests, combining time-domain and frequency domain methods, " Geotech. Test. J. 32(2), 1–17, 2009.

[15] J. O'Donovan, E. Ibraim, C. O'Sullivan, S. Hamlin, D. Muir Wood, and G. Marketos, "Micromechanics of seismic wave propagation in granular materials," Granul. Matter. 18, 2016.

[16] B. P. Lawney and S. Luding, "Frequency filtering in disordered granular chains," Acta Mechanica 225(8), pp. 2385–2407, 2014.

[17] O. Mouraille and S. Luding, "Soundwave propagation in weakly poly-disperse granular materials," Ultrasonics 48(6-7), pp. 498–505, 2008.

[18] J. C. Santamarina, K. A. Klein, and M. A. Fam, "Soils and Waves," Wiley, Hoboken, New Jersey, 2001.

[19] T. T. Dutta, M. Otsubo, R. Kuwano, and C. O'Sullivan, "Evolution of shear wave velocity during triaxial compression," Soils and Foundations 60 (6), 1357-1370, 2020.

Techno-Science Research Journal V13 (Special Issue) (2025) P 29-35

Content list available at ITC

Techno-Science Research Journal

Journal Homepage: www.ric.itc.edu.kh

Techno-Science Research Journal

Fossil and Depositional Environment Identification to study on Paleo-Environment at Phnom Thbeng Meanchey, Preah Vihear Province, Cambodia

Neang Sreynith[1*], Heng Muoy Yi[1,2], Lim Vanchan[2]

[1] *Faculty of Geo-Resources and Geotechnical Engineering, Institute of Technology of Cambodia, Russian Federation Blvd., P.O. Box 86, Phnom Penh, Cambodia*

[2]*Department Heritage Park, General Department of Local Community Ministry of Environment, Cambodia*

Received: 1 November 2024; Revised: 1 January 2025; Accepted: 20 June 2025; Available online: October 2025

Abstract: *The study of fossilized trees at Phnom Thbeng Meanchey, Cambodia is an important endeavor for scientists to have a better knowledge of the past and future climate change as well as understanding the depositional environment of fossil accumulations in this area. The present study delves into the relationship between paleo-environment and preserved fossil records, using petrography analysis (Thin section). According to the result obtained from the hand specimen and petrography indicate that sedimentary rock has medium-sized grains, subangular particles, and well-sorted grains. These characteristics of the sedimentary rock are dependent on the land depositional environment. Furthermore, the hand specimens demonstrate that petrified wood is dark gray to black in color. Some initial discoveries have showed that there are some parts of petrified wood that is not fully changed into rock but remains as coal. Research on the anatomical structure of the petrified tree using petrography has revealed features including resin canals, bordered pits, late and early wood tracheids, and ray that correspond to the division of the wood. Consequently, the division of the Coniferophyta, are determined by the similarities in wood anatomy between then and now. The among of mineral are silicate. Initial results indicate that lacustrine or fluvial environment are usually responsible for the formation of petrified wood. This research stresses on the need to understand Cambodia's geological history along with the importance of petrified tree in reconstructing past climate and environment conditions.*

Keywords: Petrified wood, Depositional environment, anatomy, and Subangular.

1. INTRODUCTION

The fossil had found so many areas in Cambodia mostly marine and also non-marine fossils, for non-marine fossil including animals and tree [1]. In 2020 local people saw a petrified tree was initially discovered in the Phnom Thbeng research area in the Preah Vihear region of Cambodia. The fossil tree found by the local people around this location in high elevation on the mountain ring of Phnom Thbeng. And fossilized tree was deposited on the mountain hence the way utilized to excavation is by the human strength to dig up the fossil. Fossil tree measuring 3.5 meters in length and 0.8 meters in diameter were discovered by the crew after they excavated 1.5 mater deep, 2 meters broad, and 6 meters long (Fig.1). Preah Vihear, a provincial town, is roughly 35 kilometers away from the research area.

Fig. 1. Fossil Site on Phnom Thbeng, Preah Vihear province.

* Corresponding author: Neang Sreynith
E-mail: *sreyneth8888168@gmail.com*

Additionally, it takes roughly 300 kilometers from Phnom Penh capital city of Cambodia.

Overall, the study area is under the jurisdiction of the Cambodia Ministry of Environment and collaboration with the Institute of Technology of Cambodia's Department of Geo-Resources and Geotechnical Engineering. To determine the kind of petrified tree and the fossil's original deposition habitat. The fossil was hidden by the mudstones and sandstone of Phnom Tbeng's mountain ring (Fig.2). Depend on the layer of sedimentary rock was deposited in Jurassic-Cretaceous era (251-65 million years) the layer that fossilized tree was formed that mean the tree also occurred in the Jurassic-Cretaceous era, too. On the condition layer of rock and environment at Phnom Thbeng related to the fluvial depositional environment, the majority of deposits found in fluvial are clastic, with grain sizes ranging from enormous boulders to the finest clay. Fluvial sediments and coal are frequently related. In sediment there are three conveyance types, only one type that related in this study is debris flows. The process of debris flows, when saturated with water, these poorly sorted masses of silt flow as a cohesive body.

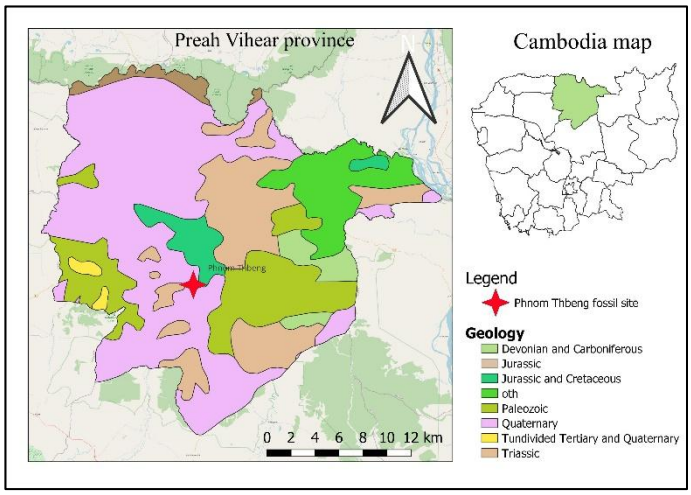

Fig. 2. Geological map of Preah Vihear Province.

For their commencement, a steep slope, a lot of clastic material, and a high discharge are necessary. These circumstances are typically met in semi-arid or dry regions, especially in areas where fire or logging activities had eliminated the plant cover. In these environments, clastic debris is produced by mechanical weathering processes and is washed away by sporadic flash floods. Debris flows are uncommon in humid climates because of vegetation and the existence of soil cover with its root network, which slows down rapid runoff. They are most typical of alluvial fans and typically stretch only a few km from a hilly source location into the alluvia plain [2]- [3]. The government of Cambodia designated Phnom Thbeng as a Natural Heritage Park. The park is home to important wood species, medicinal plants, and endangered creatures, and it is regarded as a crucial place for wildlife conservation. Additionally, the park serves as the upper watershed for the Stueng Saen River, a Tonle Sap tributary.

In order to present fresh scientific data on fossils plant found in Cambodia, this study presents the findings of its investigation into the paleoenvironment and identification of petrified wood. This will further our knowledge of the evolution and dissemination pathways of these plants in this area, offer proof for the preservation and development of fossil sites for tourism, and advance the nation's geological education.

1.1 Taxonomy and anatomy of vascular plants

a. Taxonomy

In the sub-kingdom of vascular plants for seeds producing devices into two class including, Gymnospermae (non-flowering) and Angiospermae (Flowering plants). For the class of Gymnospermae count into four extant divisions such as, Cycadophyta, Ginkgophyta, Gnetophyta, and Coniferophyta [4]-[5]. To the divisions of coniterophyta cover into seven families including, Pinaceae, Araucariaceae, Podocarpaceae, Sciadopityaceae, Taxaceae, Cephalotaxaceae, and Cupressaceae [6]. Most of conifers are evergreens, their leaves are staying green throughout the year. Conifers come in a variety of sizes, from yews and junipers to huge trees. They are found all across the planet, and they frequently favour high-elevation areas and colder climates over temperate ones. Conifers are most abundant in cool temperate and boreal regions, but they can also be found in warmer areas, including tropical mountains. Conifers also predominate in mid-latitude mountain systems, which have the richest north temperate conifer forests. Warm temperate climates are found at moderate elevations and lower latitudes. For the classification of the tree truck of Conifers have simple characteristics like a palm-like tree habit and an unbranched stem. The petrified wood has found only stem and truck in the mountain ring. The fossilized wood is around 3.5 meters in length and 0.8 meters in width. It may go deep into the conifer depending on the species and Southeast Asian weather.

b. Anatomy

Roots, stems, leaves, and reproductive structures are the four different organ types that make up plants. The cells content in the stem including xylem and phloem tissues. The food conducting tissue phloem and the water conducting tissue xylem serve as representations of the vascular tissue system. The main components of xylem tissue are tracheary elements, fibers, and parenchyma cells. Tracheids and vassel elements stand in for tracheary elements.

Vessels are an adaptation of blooming plants and have a larger diameter than tracheids. Sieve elements, parenchyma cells, and fibres make up the majority of phloem tissue. Members of sieve tubes and sieve cells are examples of sieve elements.

Parenchyma cells are closely related to both cell types. Members of sieve tubes are adapted from flowering plants and

have bigger pores. The food products of photosynthesis are transported throughout the plant by an interconnected system of tubes made up of sieve components [7].

2. METHODOLOGY

2.1 Petrography (Thin section)

The petrified wood sample was deriving out of Phnom Sruoch located at Phnom Thbeng as a Natural Heritage Park, Chamreoeun commune, Songkon tmey district, Preah Vihear province. There are two kinds of samples, petrified wood and sedimentary rock. The samples code: PTC-002-A1 and PTC1-001-A2 for petrified wood was excavated in the depth 1.5 meter in the layer 1 and layer 2 of sedimentary rock. The samples of sedimentary rock coeds: A2 excavated in the depth 1.2 meters in the layer one, A3 excavated 1.2 meters depth in layer two, and P2 located in the layer three in the deep 1.5 meters (Fig. 3).

The result from hand specimen showed the petrified wood gray to black in color. The sample silicified wood was cut in three sections. Radial, Traverse, and tangential sections and for sample of sedimentary rocks. The preparation for thin-section technique at the room 102D laboratory of department Ger-sources and Geotechnical at Institute of Technology of Cambodia.

Fig. 3. The depth of petrified wood in each layer in sedimentary rock.

The result of rock sample showed the propertied such as, mineral composition, texture include grain size, particle shape, grain sorting, and fabric. The fossilized tree was cut in three sections, tangential, transverse, and radial and clean up with water and broom to remove the dust and make the sample clear. The fossilized wood was polished using grinding with carborundum. During that time the anatomical structure was observed by microscope. In each slice of each sample silicified wood and sedimentary rock section, took approximately 20-25 minutes. Put samples on the hot plate the temperatures around 80 ºC about 8 hours, attached the sample with a glass slice by Petropoxy Resin 154 mixed with curing agent in 10:1 ratio respectively. After cut the sample and polished again until the specimen's anatomical structure was seen clearly. Pictures for macroscopical analysis were taken by microscopic camera (Nikon DIGITAL CAMERA D7100), all samples analysis under light microscope for detail anatomical structure were examined by PPL and XPL light microscope. The photographs from petrography show the wood cells, in each difference section of wood. All samples of wood had compared to the anatomy of softwood in the present, including resin canals, bordered pits, rays, and late and early wood tracheids. The photo of softwood in the reference page [8], verify with preparate of the divisions coniferphyta.

2.2 X-ray Fluorescence (XRF)

The method X-ray fluorescence used on sedimentary rock sample to capture the elements in the rock. To conformer the rock united. In order to ascertain the elemental compositions of rock elements, Energy Dispersive X-ray fluorescence (XRF) technology calibrations are highlighted in this work. There are three samples of sedimentary rocks had analysis with X-ray Fluorescence in differences layer, to verify the chemical propertied in each layer have differences or the same propertied.

Here are some activities for doing X-ray Fluorescence. First use a vibrating mill to grind the sample, after taking a sample from an iron mortar, place it in mortar machine sample containers and place the mortar machine sample containers in the grinding machine (Vibrating sample Mill), and run the machine for 6-9 minutes for limestone or longer depending on the hardness of the rock sample. For power diffraction, take 6.5 gram to 7 gram in each sample. The sample powder was obtained and forced into the ring for the powder diffraction sample. In the sample mixed with the binder to protect from the problematic, and use PVC rings. Use the pressing machine to press sample that has previously been produced. Record the mass and a little compaction to ensure for have a good sample for testing. Pressing thee sample with 10 KN for 2 minutes and 18 KN for 1 minute. After pressing, knock the sample to ensure that sample is suitable for processing in the machine. Prepared sample and placed it in cylinder dice to verify the sample. Pace the sample in the X-ray Fluorescence machine and ensure it plates.

3. RESULTS AND DISCUSSION

3.1 Petrography analysis of Anatomical

Numerous cell types, including tracheids, rays, pits, and resin canals, were kept in the truck of petrified wood sample in the Coniferophyta division that is still in existence. The transverse portion of the truck is often where the tracheids and resin canal

cells are located. The tangential and radial sections are often where the ray and pit are found.

a. Radial Section

In the radial section of the sample PTC1- 001-A2 the main cells are ray in the horizontal across the bordered pits, pits, and rays are around two layers and some parts is mostly seven layers of ray. On the bordered there are some large pits on the radial walls of the tracheids. Bordered pit in high 559µm-1000µm and 50µm-110µm in width. Pits in diameter round 85µm-200µm (Fig.4).

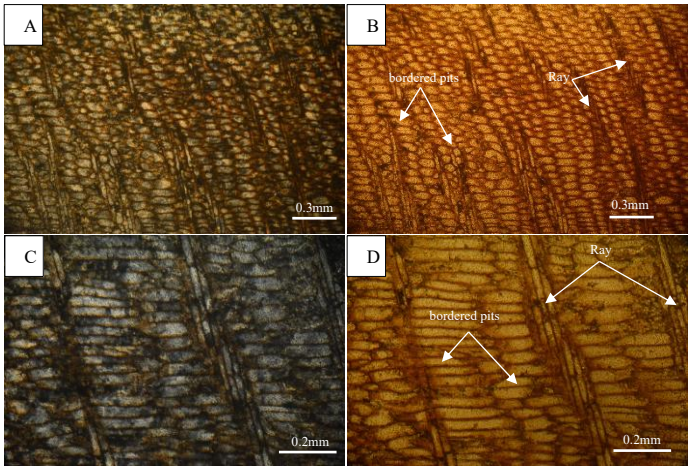

Fig. 4. A-D) Radial section- bordered pits, Ray, pits, and other cells, which A and C revealing in XPL, B and D revealing in PPL.

b. Transverse section

The transverse section of sample PTC1-002-A1 contains cells including, early and late wood tracheids, Parenchyma, and line of ray in the horizontal direction and risen canals. For early wood tracheids from 100µm in dimeter of the cell is big and the colour (light) and the latewood tracheids small in dimeter than the early wood the colour (dark).

For parenchyma on the transverse wall are smooth. The risen canals stay between the boundary of early and late wood, only vertical risen canals. The resin canal shape are ovals or circulars, in some part have resin canal 150-225µm in diameter.

There are no horizontal resin canals. Tracheid, axial and parenchyma, and resin canal epithelium are present in some family of division Coniferophyta. The grow ring boundary is absent and boundaries that are ambiguous, exhibit noticeable structural changes over time, or are not apparent. In the different climate condition tree from higher altitude tropical or subtropical climates may have growth ring boundaries that are more or less defined (Fig.5).

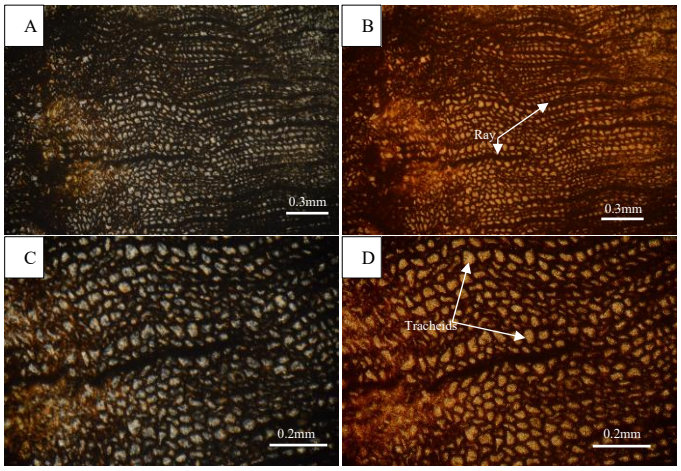

Fig. 5. A-D) Transverse section- wood tracheids, Ray, and other cells, which A and C revealing in XPL, B and D revealing in PPL.

c. Tangential section

On the tangential section of sample PTC1-001-A2 detail about the diameter on ray, make up from one to more than one layer of cell. Uniseriate rays can reach a height of more than 3 cell, however 3 cells are the most common height. Ray in high 225µm-749µm. On bordered pit have some pit present (Fig. 6).

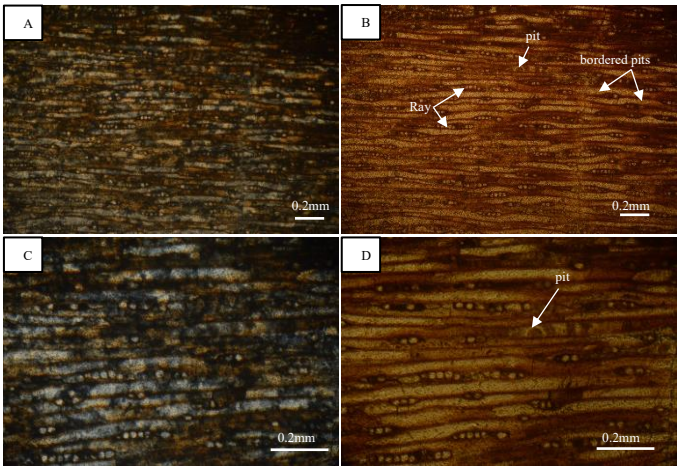

Fig. 6. A-D) Tangential section- Pit, Ray, bordered pit and other cells, which A and C revealing in XPL, B and D revealing in PPL.

d. Comparison of anatomy with the present wood

The major anatomical characteristics of the fossil wood are the mild rays, axial parenchyma, intercellular canals or resin canals, and wood tracheids. It's affinity for conifer wood, namely that of the Pinaceae family, is demonstrated by the xylotomical feature stated above. However, it may be further identified by the way the pit is arranged, with has led researchers to investigate the

ancient wood closer to the Pinaceae and Podocarpaceae families. The majority of the anatomical details of the fossil under study are identical to those of the Pinaceae family.

e. Petrography analysis of Sandstone

- *Sampel A2*

For sample A2 under microscope contain of quartz, lithic or rock fragment and matrix. Quartz in thin section is usually low relief to moderated, low birefringene, transparent in plain polarized light (PPL). The grain sorting is poorly sorted to well sorted, the particle shape is subangular low sphericity, that mean the sandstone deposited by high energy (Fig.7).

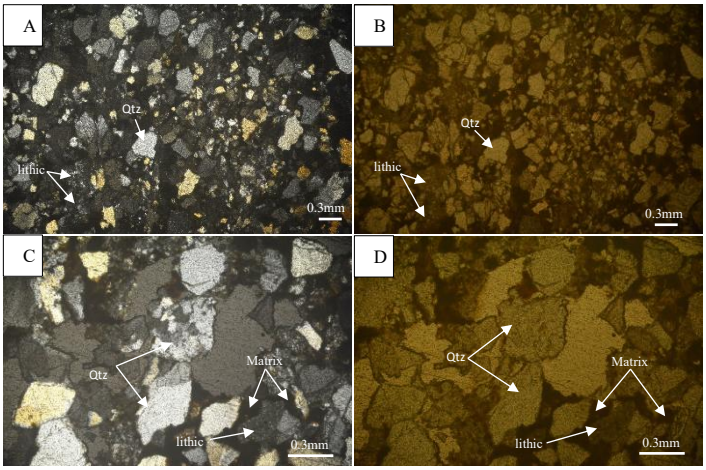

Fig. 7. A-D) Qtz=quartz, lithic or rock fragment, and matrix. These pictures A and C revealing in XPL, and pictures B and D has revealing in PPL.

- *Sample A3*

In the sample A3 under microscope contain of quartz, lithic or rock fragment and other compositions. Quartz in thin section is usually low relief to moderated, low birefringene, transparent in plain polarized light (PPL). Plagioclass is typically white and gray, it has twinning in cross polarized light (XPL). The grain sorting is poorly sorted to well sorted, the particle shape is subangular low sphericity, that mean the sandstone deposited by high energy (Fig.8).

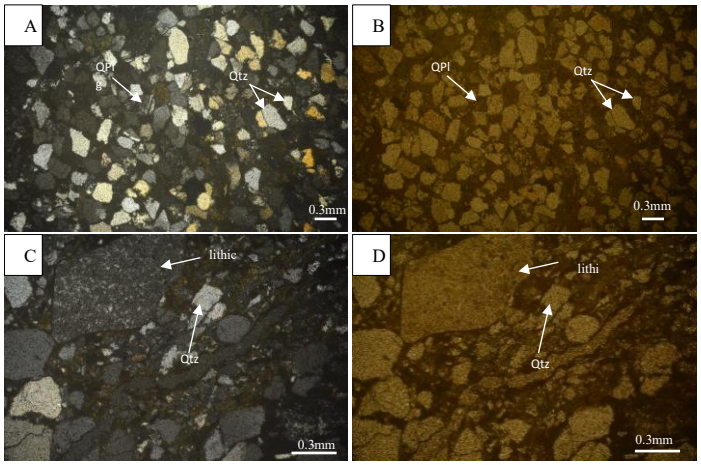

Fig. 8. A-D) Qtz=quartz, lithic or rock fragment, and Plg=plagioclase. These pictures A and C revealing in XPL, and pictures B and D has revealing in PPL.

- *Sample P2*

On the sample P2 under microscope contain of quartz, lithic or rock fragment, and Plagioclasse. Quartz in thin section is usually low relief to moderated, low birefringene, transparent in plain polarized light (PPL). Plagioclass is typically white and gray, it has twinning in cross polarized light (XPL). The grain sorting is poorly sorted to well sorted, the particle shape is subangular low sphericity, that mean the sandstone deposited by high energy (Fig. 9).

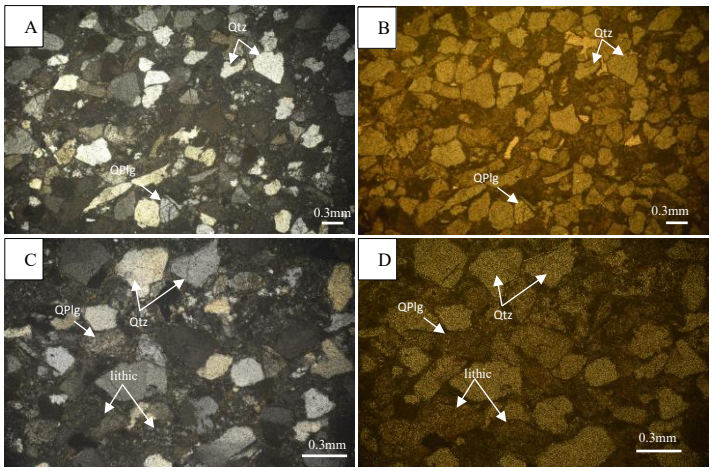

Fig. 9. A-D) Qtz=quartz, lithic or rock fragment, and Plg=plagioclase. These pictures A and C revealing in XPL, and pictures B and D has revealing in PPL.

The percentage of chemical and physical propertied varies in A2, A3, and P2 based on the result of petrography, physical properties, and XRF. This indicates that three sandstone samples remain in distinct layer.

a. X-ray Fluorescence

- *Chemical composition of the investigated sandstones*

By Binary of TiO_2, and Al_2O_3 typically, sandstones and mudstones are distinguished. By the data of X-ray fluorescence, Sample A_2 consists TiO_2 (0.3768wt%), and Al_2O_3 (11.702wt%). Sample A_3 consists TiO_2 (0.4900wt%), and Al_2O_3 (13.0795mass%). And Sample P_2 consists TiO_2 (0.1227wt%), and Al_2O_3 (14.6963wt%). For sample A_2 and A_3 showed clearly that samples are sandstone but the sample P_2 have difference levels of weathering and climatic change (Fig.10).

- *Depositional environment of sandstone*

The binary diagram of Fe_2O_3 versus MgO which characterizes and differentiates non-marine from marine and deltaic sandstones. By XRF results, sample A_2 consists MgO (0.5132wt%), and Fe_2O_3 (1.8420wt%), for sample A_3 obtained MgO (0.4907wt%), and Fe_2O_3 (2.7016wt%), and sample P_2 MgO (0.9954wt%), and Fe_2O_3 (1.5104wt%). Plotting the examined samples on this diagram, it shows clearly that all examined samples are non-marine and deltaic sandstone show in (Fig.11.)

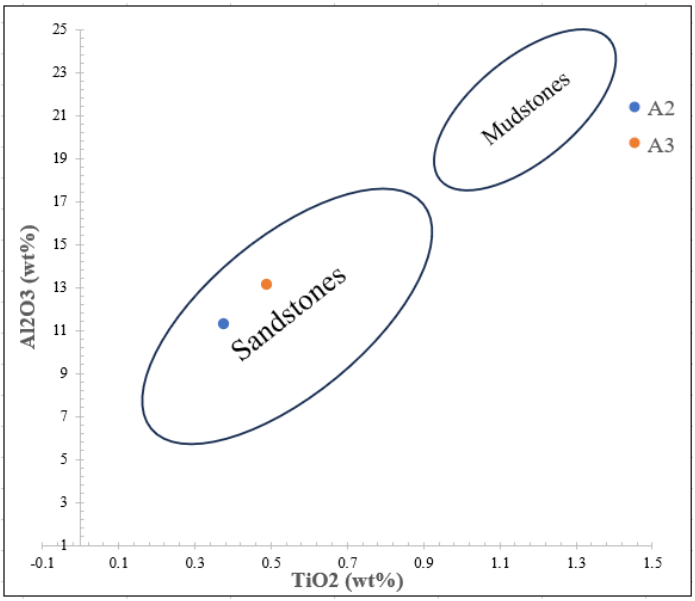

Fig.10. Chemical composition of the examined sandstones [9].

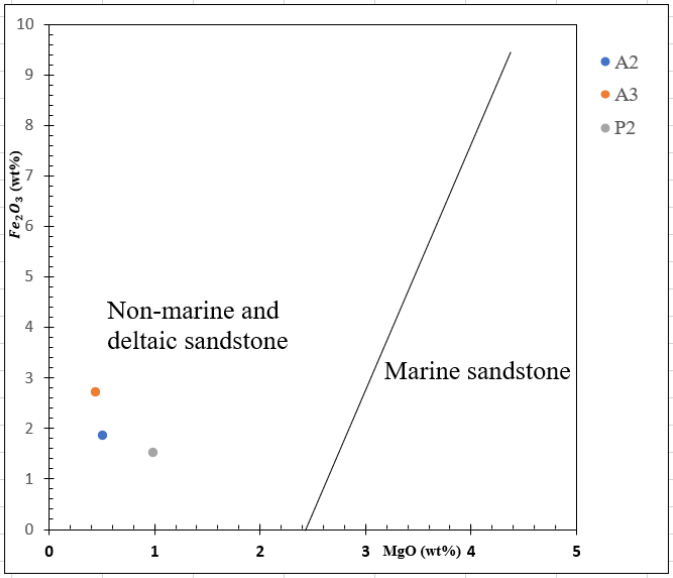

Fig.11. Depositional environment of the examined sandstones [9].

4. CONCLUSIONS

The wood fossils discovered on Phnom Sruoch, located on Phnom Thbeng, Preah Vihear province, belong to the softwood class and more closely resemble the divisions of coniterophyta. They are distinguished by their multiseriate ray line, diffuse early and latewood tracheids, ray lines in the horizontal plane, and resin canal arrangements in certain places, as seen in the transverse section. This wood fossil specimen has a pit in the tangential section that displays rays that, depending on their diameter, comprise one or more layers.

The depositional environment of fossil is cover by Alluvial fan deposits. It builds up at the foot of a mountain front or other upland area where a sediment body with a sloping surface that resembles a cone segment is deposited by rising mountain steam and the sandstone in deposited in the non-marine environment. The land depositional environment and low energy were used for the depositional environment of petrified wood.

ACKNOWLEDGMENTS

Firstly, I am extremely grateful to the lecturers Heng Mouy Yi and Mr. Lim Vanchan for giving us a change to study on the petrified wood and allowing some fossil samples from their work area to be analyzed. Secondly, I also thanks to Dean of the faculty of department of Geo-resources and Geotechnical Engineering for allowing us to use laboratory equipment in the reach and analysis the sample during research. Lastly, a big thank you to the senior who helped me with this research.

REFERENCES

[1] B. Eric , T. Haiyan , C. Lionel, L. Vanchan, L. Pich Sak and H. Muoy yi, "Fossil-bearing non-marine Mesozoic formation of south-western Cambodia," in *Proceeding of the 18th Regional Geoscience Conference of Southeast Asia*, Cambodia, 2024.

[2] D. Andrew, "Analysis of Fluvial Depositional Systems," in *American Association of Petroleum Geologists*, American, 1981.

[3] .. Tor H, "Alluvial Fan Deposits," in *Sandstone Depositional Environments*, 1982, 1982, pp. 49-86.

[4] C. R. Wu, "The New York Botanical Garaden," *Conifers and other Gymnosperms,* 1999.

[5] W. May Theilgaard, "A manual for the Idenitfication of Tree by Their Leaves," 1998.

[6] "BASIC BIOLOGY," May 21,2015.

[7] V. Mike , "The Anatomy of Arborescent Plant Life through Time," *Petrified wood,* 21 July 2015.

[8] IAWA, "IAWA List fo microscopic features for softwood identificatuib," *IAWA Journal,* vol. 25, pp. 1-70, 2004.

[9] A. Faisal and K. Mohammed, "Geochemical analysis for evaluating the paleoweathering, poleoclimate, and depositional environments of the siliciclastic Mioceene-Pliocene sequence at Ai-Rehaili area, Northern Jeddah, Saudi Arabia.," *Arabian Journal of Geosciences,* vol. 14, 2021.

[10] H. Waleed, S. Mohamed and M. Hussain, "Improving X-ray Fluorescence Factory Performance to Optimize Geological Samples Matrices," vol. 1, p. 1, 2023.

[11] F. Schweingruber, "Anatomie europaischer Holzer," 1990.

[12] G. E. LUIS and P. D. PALACIOS, "Comparative wood anatomy in Abietoideae (Pinaceae)," *Botanical Journal of the Linnean Society,* pp. 184-196, 2009.

[13] H. Nani , W. Sri, Erwin and B. S. Agus, "Identification of fossil Wood from Smarinda, East Borneo," *Advances in Biological Sciences Reaearch,* vol. 11, pp. 253-257, 2021.

Techno-Science Research Journal V13 (Special Issue) (2025) P 36-43

Content list available at ITC

Techno-Science Research Journal

Journal Homepage: www.ric.itc.edu.kh

Techno-Science Research Journal

Depositional Environment and Petrified wood Identification at Lom Phat district, Ratanakiri, Cambodia

Rattha DY[1*], Muoy Yi HENG[1,2], Vanchan Lim[2]

[1] *Faculty of Geo-Resources and Geotechnical Engineering, Institute of Technology of Cambodia, Russian Federation Blvd., P.O. Box 86, Phnom Penh, Cambodia*

[2]*Department Heritage Park, General Department of Local Community Ministry of Environment, Cambodia*

Received: 1 November 2024; Revised: 1 January 2025; Accepted: 20 June 2025; Available online: October 2025

Abstract: *The term "petrified wood" is preferred by paleobotanists over "permineralized wood" as it describes better the fossil wood where cellular tissues are replaced with minerals. Petrified woods typically form in two geological environments, trees transported by streams and rivers become buried in the fluvial sediments. The research was conducted in Lom Phat District, Ratanakiri province of northeastern Cambodia that lies approximately 588 kilometers from Phnom Penh. This research aimed to characterize petrified wood including depositional and paleoenvironmental contexts. Laboratory methods employed hand specimen descriptions and petrographic thin section. By physical properties investigation samples consisted of brownish, grayish and reddish color which was deposited fluvial (non-marine and deltaic environment) and high terrace sand. Petrographic analysis reveals that the wood is composed of crystalline quartz linings which formed during later stage diagenesis when silica content was sufficiently low to permit the growth of well-ordered lattices. Quartz crystals also occasionally replaced cells in the wood. It can form layers within the cells, eventually filling their internal spaces. Initially, the silica that adheres to the wood is in an amorphous state, but it gradually becomes more stable by crystallizing into more stable forms. This change involves ongoing polymerization and dehydration. The formation of higher-ordered opal through this process eventually results in the more thermodynamically stable mineral quartz. Distinct growth rings were observed, early wood had more than 60 cells with large cells having thin walls while late wood had three to eight rows of tangentially flattened, thick-walled cells, confiner it as Araucariaceae family, Agathis genera, formed in late Mesozoic period, Upper Jurassic to lower Cretaceous.*

Keywords: Petrified wood, Depositional Environment, Genera, Family

1. INTRODUCTION

The term "petrified wood" is preferred over "permineralized wood". Paleobotanists have traditionally used the latter term to describe fossilized wood, assuming that wood fossilization usually involves the filling of cellular tissues with mineral deposits. Petrified woods typically form in two geological environments. First, trees transported by streams and rivers become buried in the fluvial sediments of deltas and floodplains and the silica mobilization for infiltration must have originated from weathering and/or soil formation of silicate minerals and other silica dissolving controls. Second, ash from volcanic eruptions buries trees while felled or still upright [1]–[3]. This may involve co- and post-volcanic hydrothermal fluids, producing mainly quartz, sometimes with metastable silica polymorphs such as moganite. Although the general processes of petrified wood formation are relatively well understood, the mineralogical composition, diagenetic history, and tectonic significance of Mesozoic petrified wood from Cambodia and the broader Southeast Asian region remain insufficiently studied. Initial findings from Jurassic to Cretaceous stratigraphic units in northeastern Cambodia indicate possible connections to volcanism associated with a continental arc and active fluvial systems during the tectonic evolution of the Indochina Terrane. Nevertheless, comprehensive studies addressing the silica source, fossilization conditions, and geochemical characteristics are limited, which hinders deeper insight into the region's paleoecology and the development of its sedimentary basins [4]–[5]. This represents a significant research gap, as combining paleobotanical, mineralogical, and tectonic data from petrified wood could provide valuable contributions to our understanding

[*] Corresponding author: Dy Rattha
E-mail: *darothy10@gmail.com;* Tel: *+855 81 880 456*

of Mesozoic paleoenvironments and crustal dynamics in Southeast Asia.

1.1. Depositional environment

Therefore, the sediment is preserved in the rock record, the types of rocks that will form after lithification. Most of the time, it is possible to compare the environments associated with specific rock types or associations of rock types to their existing analogues. However, sediments were deposited over a longer period of geological time [6]. There are three major types of depositional environments they are Continental, Transitional, Marine. In continental deposits, it can be further classified into Alluvial, Fluvial and Lacustrine environment.

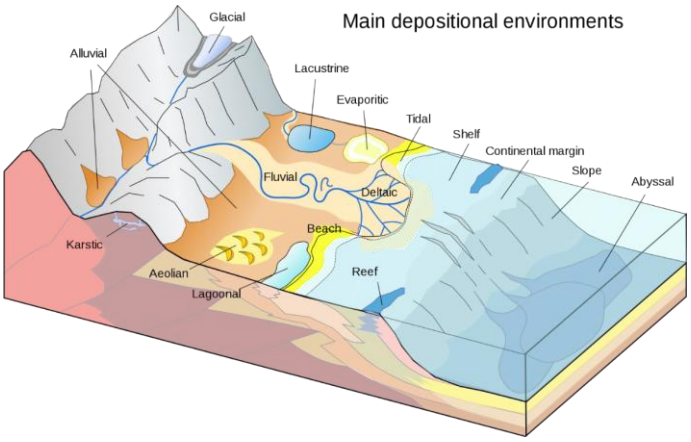

Fig. 1. Depositional Environment of sediments by [7].

Continental environments are those found on the landmasses of continents. These include alluvial fans, fluvial environments (rivers), lacustrine environments (lakes), aeolian or eolian environments (deserts), and paludal environments (swamps) [8]. Fluvial (river) environments are characterized by cross-bedded and rippled river sandstones, along with floodplain mudstones (siltstones and clay shales), which may be either parallel or cross-bedded [9]. Lacustrine (lake) environments feature sand deposits at river mouths where they flow into the lake, along the shoreline, and muddy sediments on the deep lake bottom [10]. Fluvial processes involve the movement of sediment and the erosion or deposition of material on the riverbed. When a river carries a significant amount of sediment, the particles can act as tools to erode the bed (abrasion), while the sediment itself becomes smaller and more rounded (attrition) [10]. Sediment in rivers is transported as bed load (larger particles moving near the bed) or suspended load (smaller particles carried in the water), with some material also dissolved in the flow [8]. Fluvial environments encompass braided and meandering river systems, which include sub-environments like river channels, bars, levees, and floodplains [9]. Channel deposits typically consist of coarse sediment, rounded gravel and sand, bars are composed of sand or gravel, levees are formed of fine sand or silt, and floodplains are covered with silt and clay [10].

1.2. Araucariaceae

The Araucariaceae is a family of ancient conifers that today includes three genera, Araucaria, Agathis, and Wollemia, with approximately 40 species. All genera are monophyletic with Wollemia interpreted as the most primitive living genus [11]. All extant species are evergreen and lack shoot dimorphism. Leaves may be helically arranged or opposite, linear or broad, and cones are typically large. There are only three genera and 41 species worldwide. Araucariaceae are large trees, generally from about 30 m to 90 m in height.

1.3. Taxonomy of vascular plants

In the sub-kingdom of vascular plants for seeds producing devices into two class including, Gymnospermae (non-flowering and cones) and Angiospermae (Flowering plants and seed). For the class of Gymnospermae count into four extant divisions such as, Cycadophyta, Ginkgophyta, Gnetophyta, and Coniferophyta. To the divisions of coniterophyta cover into seven families including, Pinaceae, Araucariaceae, Podocarpaceae, Sciadopityaceae, Taxaceae, Cephalotaxaceae, and Cupressaceae. Most of conifers are evergreens, their leaves are staying green throughout the year [12]. Conifers come in a variety of sizes, from yews and junipers to huge trees. They are found all across the planet, and they frequently favor high-elevation areas and colder climates over temperate ones. Conifers are most abundant in cool temperate and boreal regions, but they can also be found in warmer areas, including tropical mountains. Conifers also predominate in mid-latitude mountain systems, which have the richest north temperate conifer forests [12]. Warm temperate climates are found at moderate elevations and lower latitudes. For the classification of the tree truck of Conifers have simple characteristics like a palm-like tree habit and an unbranched stem. The petrified wood has found only stem and truck in the mountain ring. The fossilized wood is round 3.5 meters in length and 0.8 meters in width. It may go deep into the conifer depending on the species and Southeast Asian weather [12].

2. METHODOLOGY

2.1. *Fields investigation*

Field work was carried out in Lom phat district, Ratanakiri province. fossil wood taken from the 56 petrified wood excavation pits in Lom Phat area WGS1984(720755-1482844), The samples were labeled with number prefixed by Alphabet, arranged from A (1) to N (-3) in accordance with the excavation pits 1 to pits 56. Sample were collected from AC2, H1 and J3 pit.

Fig. 2. Petrified wood excavation site at Lom Phat area [13].

2.2. Petrography analysis (Thin section)

The result from hand specimen showed the petrified wood gray to black in color. The sample silicified wood was cut in three sections. Radial, Traverse, and tangential sections and for sample of sedimentary rocks. The preparation for thin-section technique at the room 102D laboratory of department Ger-sources and Geotechnical at Institute of Technology of Cambodia.

The result of rock sample showed the propertied such as, mineral composition, texture include grain size, particle shape, grain sorting, and fabric. The fossilized tree was cut in three sections, tangential, transverse, and radial and clean up with water and broom to remove the dust and make the sample clear. The fossilized wood was polished using grinding with carborundum. During that time the anatomical structure was observed by microscope. In each slice of each sample silicified wood and sedimentary rock section, took approximately 20-25 minutes. Put samples on the hot plate the temperatures around 80^{o}C about 8 hours, attached the sample with a glass slice by Petropoxy Resin 154 mixed with curing agent in 10:1 ratio respectively. After cut the sample and polished again until the specimen's anatomical structure was seen clearly. Pictures for macroscopical analysis were taken by microscopic camera (Nikon DIGITAL CAMERA D7100), all samples analysis under light microscope for detail anatomical structure were examined by PPL and XPL light microscope. The photographs from petrography show the wood cells, in each difference section of wood. All samples of wood had compared to the anatomy of softwood in the present, including resin canals, bordered pits, rays, and late and early wood tracheids.

2.3. Point counting

The point counting method is a widely used quantitative petrographic technique that involves identifying and recording the mineral phases at regular intervals across a thin section of a rock sample under a polarizing microscope. Typically, each point corresponding to a mineral grain intersected by a predefined grid. This process allows for the precise determination of the modal mineral composition, which is essential for the systematic classification of Sandstone.

In practice, after performing the point count, the percentages of Q, F, and R are normalized (Q+F+R = 100%) and plotted on the QFR ternary diagram [14].

2.4. X-ray Fluorescence (XRF)

The method X-ray fluorescence used on sedimentary rock sample to capture the elements in the rock. To conformer the rock united. In order to ascertain the elemental compositions of rock elements, Energy Dispersive X-ray fluorescence (XRF) technology calibrations are highlighted in this work. There are three samples of sedimentary rocks had analysis with X-ray Fluorescence in differences layer, to verify the chemical propertied in each layer have differences or the same propertied.

Here are some activities for doing X-ray Fluorescence. First use a vibrating mill to grind the sample, after taking a sample from an iron mortar, place it in mortar machine sample containers and place the mortar machine sample containers in the grinding machine (Vibrating sample Mill), and run the machine for 6-9 minutes for limestone or longer depending on the hardness of the rock sample. For power diffraction, take 6.5 gram to 7 gram in each sample. The sample powder was obtained and forced into the ring for the powder diffraction sample. In the sample mixed with the binder to protect from the problematic, and use PVC rings. Use the pressing machine to press sample that has previously been produced. Record the mass and a little compaction to ensure for have a good sample for testing. Pressing thee sample with 10 KN for 2 minutes and 18 KN for 1 minute. After pressing, knock the sample to ensure that sample is suitable for processing in the machine. Prepared sample and placed it in cylinder dice to verify the sample. Pace the sample in the X-ray Fluorescence machine and ensure it plates.

3. RESULTS AND DISCUSSION

3.1. Petrography analysis

Based on hand specimens and petrography analysis, were found out numerous types of minerals, including quartz, plagioclase, muscovite, feldspar, rock fragment (Lithic), micro quartz and textural of petrified wood.

3.1.1. Petrified wood analysis

Under microscopic observation, the tangential section of sample J3-C reveals a structure predominantly filled with quartz shown in (Fig. 3) Quartz appears transparent with low relief and low birefringence under plain polarized light (PPL) displays black, grey, and white interference colors under cross-polarized light (XPL). The wood tissue exhibits circular shaped cells, while dark inclusions interpreted as fibers are visible as black spots. Horizontal rays are also observed, extending from the cambium toward the center of the trunk, consistent with typical anatomical features of fossilized wood.

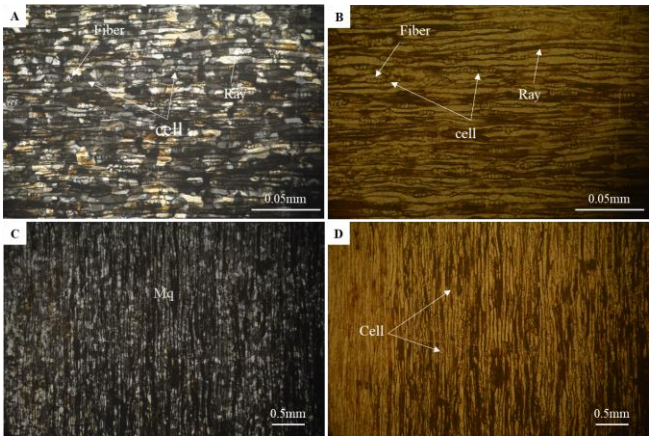

Fig. 3. A-D) tangential section- wood cell, elongate ray, fiber and Mq=microcrystalline quartz which A&C showing in XPL, B&D showing in PPL.

Under microscopic examination, the transverse section of sample J3-P is predominantly composed of quartz infilling within the cellular structures (Fig. 4). Quartz occurs as microcrystalline aggregates, characterized by low relief and low birefringence in plain polarized light (PPL), where it appears transparent. Under cross-polarized light (XPL), it displays interference colors ranging from black to white and grey. Rays are visible as horizontal linear structures. Resin ducts are present as elongated intercellular spaces lined with plastid-rich epithelial cells, which function in resin production and secretion into the duct lumen, where it is stored under pressure. Wood cells are generally circular in shape, consistent with typical gymnospermous anatomy. In the radial section of sample J3-K, the anatomical structure is well preserved show in (Fig. 5). Wood cells are circular in shape, and tracheid rays appear elongated and parallel to the radial direction. Ray-tracheids are found in the cross-fields and indicate intercellular communication by means of very small bordered pits where characterized feature of coniferous woods. Dark inclusions termed as fibers appear as black spots. Quartz again appears in microcrystalline form possesses the same optical properties as in sample J3-P is low relief, low birefringence, and transparency in PPL, while black, white, and grey interference colors under XPL.

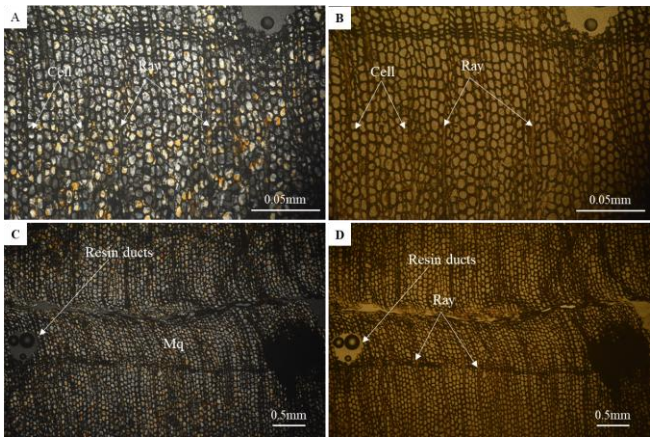

Fig. 4. A-D) Transverse section- Wood cell, Ray, Resin ducts and Mq= microcrystalline quartz, which A&C showing in XPL, B&D showing in PPL.

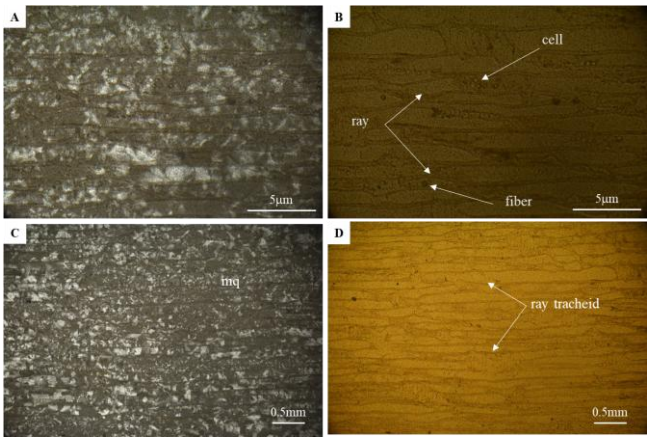

Fig. 5. A-D) Radial section- wood cell, Ray tracheid, fiber and Mq=Microcrystalline quartz, which A&C showing in XPL, B&D showing in PPL.

3.1.2. Depositional Environment by Sandstone analysis

Hand specimen analysis of sample H1 reveals a brownish-gray coloration with fine- to medium-grained texture. The rock exhibits moderate weathering and is characterized by poor sorting shown in (Fig. 6). Thin section analysis confirms the classification of the sample as a sandstone. The mineralogical composition is predominantly quartz, with subordinate amounts of K-feldspar, plagioclase, lithic fragments, and muscovite. The presence of matrix material is also noted, contributing to the overall framework of the rock.

Hand specimen observation of sample AC2 indicates a mixture of brown, grey, and reddish coloration, with a fine- to medium-grained texture. The rock shows moderate weathering and exhibits poor sorting of grains shown in (Fig. 7). Thin section analysis identifies the rock as a sandstone, primarily composed of quartz, K-feldspar, and plagioclase, with the

notable presence of iron oxide (hematite), which contributes to its reddish hue.

Under microscopic examination, sample H1 is composed primarily of quartz, plagioclase, and muscovite shown in (Fig. 8). Quartz appears with low relief and low birefringence in plain polarized light (PPL), where it is transparent, and displays interference colors in shades of black, white, and grey under cross-polarized light (XPL). Plagioclase is observed as colorless to white and grey, and is characterized by distinctive polysynthetic twinning visible under both PPL and XPL. Muscovite exhibits moderate relief and appears colorless in PPL, with a single prominent cleavage direction. Under XPL, it is anisotropic, showing high-order interference colors ranging from the third to fourth order.

Microscopic examination of sample AC2 reveals a mineral assemblage primarily consisting of quartz, plagioclase, and iron oxide (hematite) show in (Fig. 9). Plagioclase appears colorless to white and grey in thin section, exhibiting characteristic polysynthetic twinning visible under both plain polarized light (PPL) and cross-polarized light (XPL). Iron oxide minerals, such as limonite or hematite, are typically opaque under transmitted light. However, when thin enough, they may exhibit a deep red to brown coloration. Although their interference colors can be high, these are often obscured by the strong red-brown body color.

Based on point counting method, Sample H1 is primarily composed of quartz (17.82%), feldspar (25.58%), lithic fragments (43.80%), and matrix material (12.80%). Since the matrix content is below 15%, the sample plots within the arenite field on the sandstone classification diagram. Based on the relative proportions of feldspar and lithic fragments, it is classified as a feldspathic litharenite shown in (Fig. 10), Feldspathic litharenite is considered a subtype of lithic arenite, characterized by a feldspar content exceeding 5%, which distinguishes it from other lithic-rich sandstones.

Fig. 6. Hand specimen analysis of sample H1.

Fig. 7. Hand specimen analysis of sample AC2.

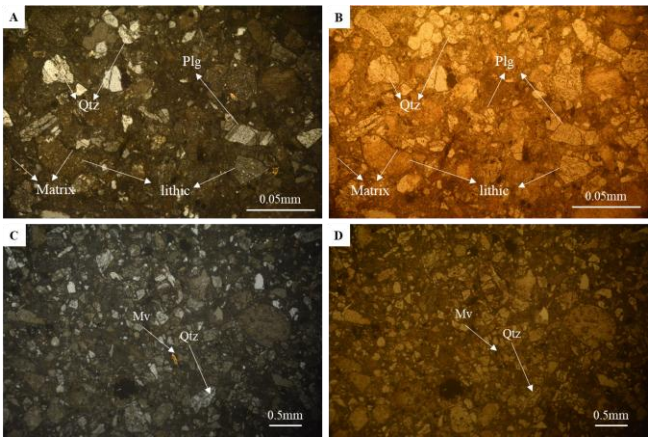

Fig. 8. A-D) Qtz=quartz, Plg=plagioclase, lithic or rock fragment, Mv=muscovite and matrix, which A&C showing in XPL, B&D showing in PPL.

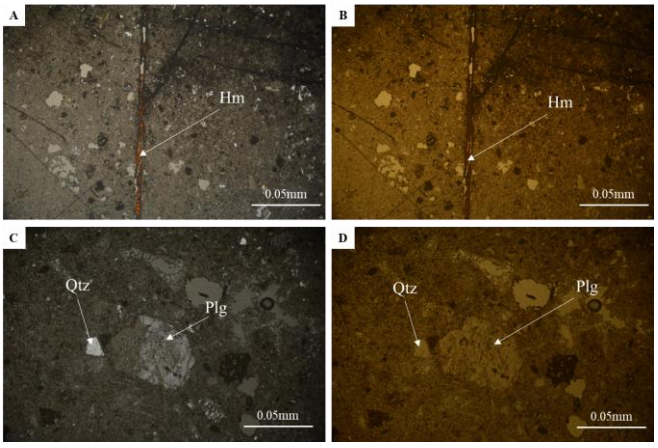

Fig. 9. A-D) Qtz=quartz, Plg=plagioclase, Hm= Hematite which A&C showing in XPL, B&D showing in PPL.

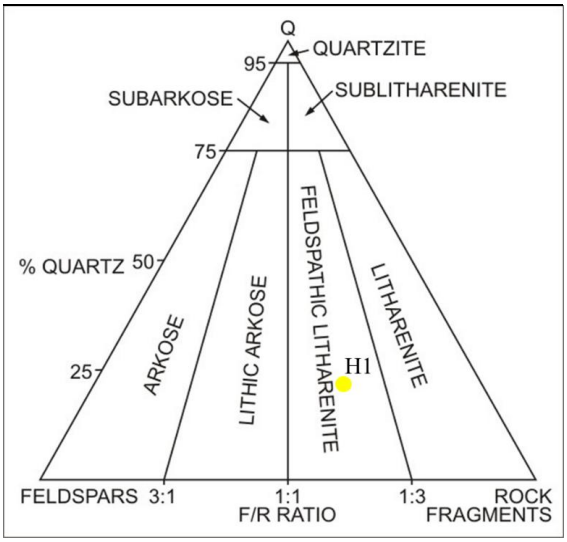

Fig. 10. Sandstone classification by [14].

3.2. X-ray fluorescence (XRF) analysis

Samples H1 and AC2 was selected for X-ray fluorescence's which obtained oxide element such as CaO, SiO_2, Fe_2O_3, Al_2O_3, MgO, K_2O, Na_2O, Ti_2O, (Table 1). According to chemical compositions from XRF were plotted into several diagrams. The binary plot of Al_2O_3 against TiO_2 is usually used to discriminate sandstones from mudstones. According to XRF results, sample H1 obtain Al_2O_3 (14.3287wt%) and TiO_2 (0.7086wt%), for sample AC2 contain Al_2O_3 (7.2621wt%) and TiO_2 (0.2928wt%). Plotting the examined samples on these plot shows that all samples are sandstone (Fig. 11). The binary diagram of Fe_2O_3 versus MgO which characterizes and differentiates marine from non-marine and deltaic sandstones. By XRF results, sample H1 consists Fe_2O_3 (3.4703wt%) and MgO (1.3142wt%), Hanse sample AC2 obtained Fe_2O_3 (7.9918wt%) and MgO (0.6935wt%). Plotting the examined samples on this diagram, it shows clearly that all examined samples are non-marine and deltaic sandstone (Fig. 12). The relation between log K_2O/Al_2O_3 versus log MgO/Al_2O_3 was used to discriminate marine from non-marine sandstones. According to XRF results, sample H1 composed K_2O (0.7554 wt%), Al_2O_3 (14.3287 wt%) and MgO (1.3142 wt%), Sample AC2 contain K_2O (0.2197 wt%), Al_2O_3 (0.6935 wt%) and MgO (1.3142 wt%) Applying this relation shows that most of the examined samples fall in non- marine field (Fig. 14).

Furthermore, the ternary diagram of MgO - Fe2O3 - (SiO2/Al2O3) categorizes and discriminates the marine from non-marine and deltaic sandstones. This plot confirms that all the examined samples fall in the field of non-marine and deltaic sandstones (Fig. 13).

Table 1. Summary percentages of oxide elements.

Sample ID	H1	AC2
Oxide Elements (wt.%)		
SiO_2	72.3333	81.3186
Al_2O_3	14.3287	11.2702
Na_2O	4.0230	0.0595
Fe_2O_3	3.4703	1.8420
K_2O	0.7554	2.1129
MgO	1.3142	0.5132
TiO_2	0.7086	0.3768
CaO	0.1575	0.0290
P_2O_5	0.1018	0.1024
SO_3	0.0963	0.0430
PbO	0.0838	0.0200
SrO	0.0346	0.0026
MnO	0.0192	0.0087
Loi-Flux	2.5246	2.2085

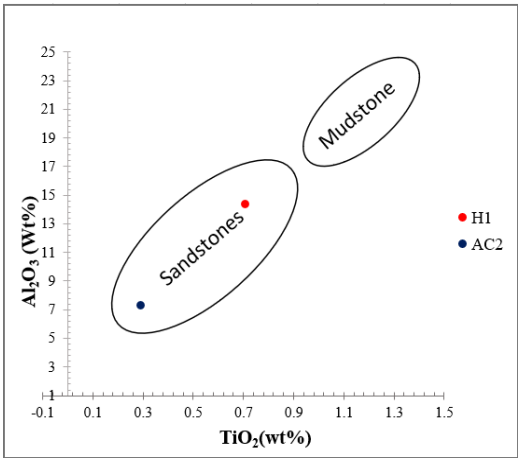

Fig. 11. Chemical composition of the examined sandstones by [15].

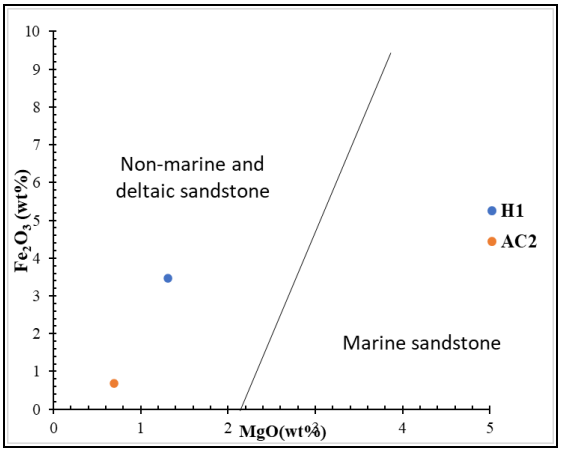

Fig. 12. Environments of deposition [16].

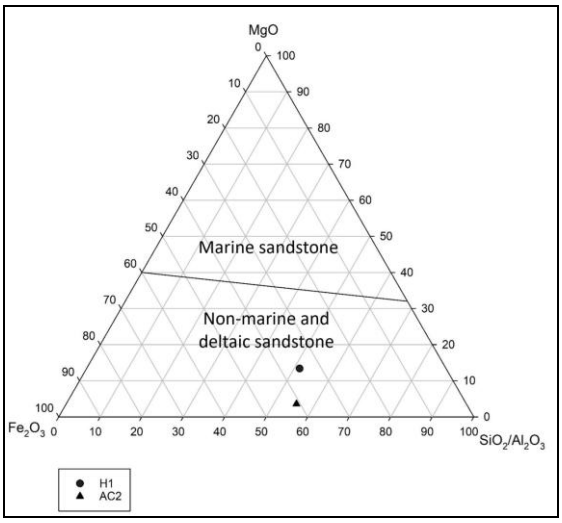

Fig. 13. Environments of deposition by [17].

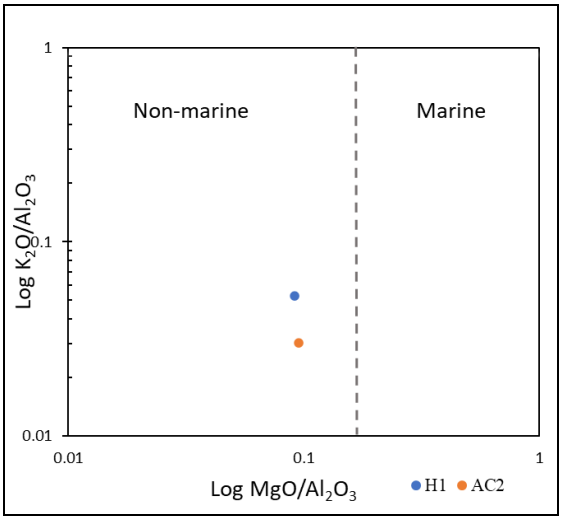

Fig. 14. depositional environment by [16].

4. CONCLUSIONS

The petrified wood located in Lom Phat District, Ratanakiri Province, belong to Araucaria genera, Araucariaceae family, Araucariales order, Pinospida class, coniterophyta division, Gymnospermae clade, Plantae kingdom. Where distinguished by diffuse early and latewood tracheid were composed silification filled, ray lines in the horizontal plane, wood cell, fiber and resin ducts arrangements in certain places, as seen in the transverse section.

The depositional setting of the fossil relates to alluvial fan deposits that typically aggrade at the front of mountain fronts or at high ground. These deposits form cone-shaped sediment bodies with sloping surfaces because of streams draining from mountainous terrain. The sandstone in the area was deposited under non-marine conditions. The wood was fossilized and deposited in a low-energy on-land depositional environment, which is favorable for the deposition and preservation of this organic material.

ACKNOWLEDGMENTS

First of all, I would like to express my deepest gratitude to my beloved parents and family, who always raise me well and supporting me. Secondly, am sincerely thank to Department Heritage Park, General Department of Local Community Ministry of Environment, Cambodia for supporting fund in this research. Furthermore, I also thanks to Dean of the faculty of department of Geo-resources and Geotechnical Engineering for allowing us to use laboratory equipment in the reach and analysis the sample during research. Lastly, a big thank you to the seniors and friends who helped me with this research.

REFERENCES

[1] K. J. Murata, “Volcanic ash as a source of silica for the silification of wood,” *American Journal of Science*, vol. 238, no. 8. pp. 586–596, 1940. doi: 10.2475/ajs.238.8.586.

[2] A. C. Sigleo, “Geochemistry of silicified wood and associated sediments, Petrified Forest National Park, Arizona,” *Chem. Geol.*, vol. 26, no. 1–2, pp. 151–163, 1979, doi: 10.1016/0009-2541(79)90036-6.

[3] K. Witke, J. Götze, R. Rößler, D. Dietrich, and G. ünter Marx, “Raman and cathodoluminescence spectroscopic investigations on Permian fossil wood from Chemnitz - A contribution to the study of the permineralisation process,” *Spectrochim. Acta - Part A Mol. Biomol. Spectrosc.*, vol. 60, no. 12, pp. 2903–2912, 2004, doi: 10.1016/j.saa.2003.12.045.

[4] K. Tanaka, K. Sato, and P. Chheng, "Jurassic stratigraphy and fossil woods in the northern Cambodian Basin," *J. Asian Earth Sci.*, vol. 162, pp. 121–135, 2018.

[5] P. Sok, S. Heng, and Y. Kobayashi, "Preliminary report

on petrified wood occurrences in the Phnom Nam Lyr area, eastern Cambodia," *Cambodian J. Earth Sci.*, vol. 5, no. 2, pp. 45–58, 2020.

[6] M. E. Tucker, *Sedimentary Rocks in the Field: A Practical Guide*, vol. 18, no. 4. 2012. doi: 10.2113/gseegeosci.18.4.401-b.

[7] M. Norton, "Main depositional environments [Diagram]," *Wikimedia Commons*, 2018. [Online]. Available: https://commons.wikimedia.org/wiki/File:Depositional_environment.jpg.

[8] G. Nichols, *Sedimentology and Stratigraphy*, 2nd ed. Oxford, UK: Wiley-Blackwell, 2009.

[9] H. G. Reading, Ed., *Sedimentary Environments: Processes, Facies and Stratigraphy*, 3rd ed. Oxford, UK: Blackwell Science, 1996.

[10] S. Boggs, *Principles of Sedimentology and Stratigraphy*, 5th ed. Boston, MA: Pearson Education, 2012.

[11] H. Setoguchi, T. A. Osawa, J. C. Pintaud, T. Jaffré, and J. M. Veillon, "Phylogenetic relationships within Araucariaceae based on rbcL gene sequences," *Am. J. Bot.*, vol. 85, no. 11, pp. 1507–1516, 1998, doi: 10.2307/2446478.

[12] Chao Rong Wu, Herbarium Intern (1999) The green New York Botanical Garden Conifers and Other Gymnosperms.

[13] Ranada N. and Vanchan L., *Excavation Report*. Department of Heritage Park, Ministry of Environment, 2020.

[14] R. L. Folk, *Petrology of Sedimentary Rocks*, 1st ed. Austin, TX: Hemphill Publishing, 1968, fig. 7A.

[15] Richard M. Moore, "The Skiddaw Group of Cumbria : early Ordovician Turbidite sedimentation and provenance on an evolving microcontinental margin," vol. 16, no. 1, pp. 1–23, 1992.

[16] Madukwe HY, Bassey CE (2015) Geochemistry of the Ogwashi-Asaba Formation, Anambra Basin, Nigeria: Implications for provenance, tectonic setting, source area weathering, classification and maturity. Inter J Sci Techno 4(7):312–327.

[17] Roaldest E (1978) Mineralogical and chemical changes during weathering, transportation and sedimentation in different environments with particular references to the distribution of Ytrium and lanthanide elements. Ph.D. Thesis, Geol. Inst., Univ. of Oslo, Norway.

Techno-Science Research Journal V13 (Special Issue) (2025) P 44-49

Content list available at ITC

Techno-Science Research Journal

Journal Homepage: www.ric.itc.edu.kh

Techno-Science Research Journal

A Comparative Study of Different Collectors in the Flotation of Rare Earth Mineral

Nadiah Adlin Muhamad Azman[1], Ku Esyra Hani Ku Ishak[1*]

[1] *Strategic Minerals Niche, School of Materials and Mineral Resources Engineering, Universiti Sains Malaysia, 14300 Nibong Tebal, Penang, Malaysia.*

Received: 1 November 2024; Revised: 1 January 2025; Accepted: 20 June 2025; Available online: October 2025

Abstract: *The application of rare earth elements (REE) in various fields has caused the demand for REE-bearing minerals (REM) to increase in recent years. Xenotime (YPO4), a source of yttrium (Y), is often sought because of its high-temperature superconductor properties and as an additive in alloys. Froth flotation is a fundamental method for processing complex minerals and is commonly applied for the beneficiation of rare-earth-bearing minerals. This study was designed to compare the effectiveness between two different collectors (octano-hydroxamic acid and sodium oleate) and its concentration on xenotime flotability. Samples were characterized using Particle Size Analysis (PSA), X-ray Diffraction (XRD), X-ray Fluorescence (XRF) and Scanning Electron Microscopy (SEM). It was found that in the absence of depressant, octano-hydroxamic acid shows better selectivity in the flotation of xenotime than sodium oleate. On the other hand, sodium oleate produces better grade of xenotime with the presence of depressant. Increases in concentration will improve xenotime grade but at higher concentration it can be detrimental. Optimum concentration for xenotime flotation was found at 0.001M. Overall, the addition of sodium silicate as depressant can significantly increase xenotime grade and successfully depress silica and alumina.*

Keywords: froth flotation, rare-earth, xenotime, collectors, depressant, bench flotation

1. INTRODUCTION

Rare earth elements (REEs) consist of 15 elements in the lanthanide group of the periodic table as well as yttrium and scandium, all of which exhibit similar chemical characteristics and behavior. These elements are frequently associated with rare earth oxides, with bastnaesite and monazite being the most common minerals. Separating pure elements from a material is the foremost concern for rare earth elements (REEs). As rare earth elements are more common than many other metals, such as gold, the name "rare" does not refer to their scarcity, but rather to the difficulty in obtaining a pure REE [1]. To date, the most common commercially extracted RE-bearing minerals are bastnaesite, monazite, xenotime and loparite [2].

REEs are commonly found in small amounts in REMs; thus, a highly selective extraction method needs to be adapted. There are a few popular methods for the beneficiation processes of REE-bearing ores; however, froth flotation, as shown in Figure 1, is more favorable owing to its ability to process a wide range of fine particle sizes and can be tailored to the mineralogy of a specific deposit. The process of mineral recovery by flotation from pulp comprises three mechanisms: (1) selective attachment to air bubbles (or "true flotation"), (2) entrainment in the water that passes through the froth, and (3) physical entrapment between particles in the froth attached to air bubbles.

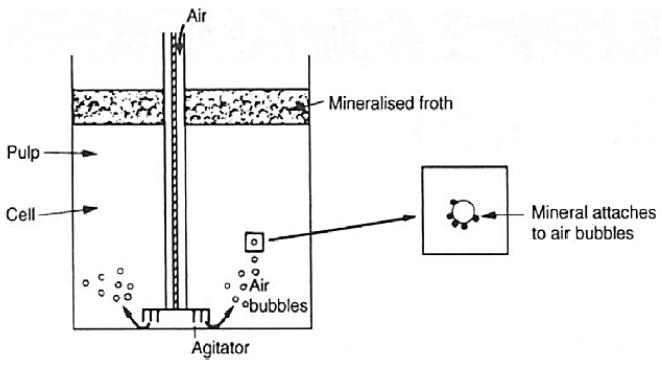

Fig. 1. Froth flotation (Wills et al., 2006).

* Corresponding author: Ku Esyra Hani Ku Ishak
E-mail: *kuesyrahani@usm.my*

In recent years, REE has gained enormous attention in public, economic, and scientific studies owing to their advancement in modern defense systems, electronic applications, and green technologies. The growing economic and strategic importance of these sectors, coupled with uncertainty in the global supply of REE from China, has led to concerns regarding the future availability of many of these metals [3]. Several countries such as the USA, the EU, and Canada have classified REE as a critical resource due to these supply concerns and increasing demand [4]. In Malaysia, samples came from the tin mine from northern part of Malaysia contain REM, which is the xenotime. The study of xenotime flotation from the gangue minerals had been done by some of the researchers by using sodium oleate and octano-hydroxamic acid as collectors and pentahydrate sodium silicate and ammonium lignosulfonate as a depressant [5]. Therefore, in this study, the samples obtained from the tin mine were characterized, and the flotation process was used to extract REM using different collectors.

2. METHODOLOGY

2.1 Materials

Samples were obtained from a tin mine in Kedah, and were characterized using X-ray diffraction (XRD), X-ray fluorescence (XRF), scanning electron microscopy (SEM), and particle size analysis (PSA). The chemicals involved in the flotation test were surfactants as collector, depressant, and pH modifier as shown in Table 1.

Table 1. Chemicals used in this study

Chemicals	Formula	Brand	State	Role
Sodium oleate	$C_{18}H_{33}NaO_2$	BDH	Granules	Collector
Octano-hydroxamic acid	$C_8H_{17}NO_2$	Biosynth® Carbosynth	Granules	Collector
Sodium silicate	Na_2SiO_3	Merck	Solution	Depressant
Sodium hydroxide	NaOH	Merck	Granules	pH modifier

2.2 Equipment and Procedure

Froth flotation of xenotime tests were conducted using a bench top Denver flotation machine equipped with cell. In each benchmarking (non-depressant) test, 100 g of representative feed sample sized -300 µm was added to 500 ml of collector (sodium oleate or octano-hydroxamic acid) at concentrations of 0.0005, 0.001, and 0.002M to achieve a solid concentration of 20 percent by weight and agitated for 15 min for conditioning. During conditioning, the pH of the slurry was adjusted using NaOH until a pH of 7 was achieved. The slurry was then transferred to the cell on the deck, and the flotation process was carried out for 5 min at 900 rpm. In each test with depressant addition, the same process was repeated; however, the sample was first conditioned with 100 ml 0.001M sodium silicate solution (depressant) for 5 min. Then, 15 min of conditioning was performed after the addition of 400 ml of the collector solution at concentrations of 0.0005, 0.001, and 0.002M. The froth concentrate was collected continuously for 5 min. The products were filtered, dried, weighed, and then ground and split to obtain the representative sample needed for characterization analysis.

3. RESULTS AND DISCUSSION

3.1 XRF analysis of the feed samples

10 g A representative powdered feed sample sizing -75µm was taken for XRF analysis. The results displayed in Table 2 show the mineral composition of the feed samples.

The compounds with the highest compositions were Al_2O_3 (42.5%), SiO_2 (42%), Fe_2O_3 (5.925%), K_2O (3.53%), and P_2O_5 (2.9%) in weight percent. The xenotime (present as Y_2O_3) concentration tested in this study was 1.955 wt%.

From the result, xenotime which is the focus for this research only made up a minor constituent of the sample. This condition mimics the real occurrence of rare earth elements, which are commonly found at low concentrations in other ore minerals.

Table 2. Feed sample composition (wt%)

Mineral	Formula	Weight percent
Alumina	Al_2O_3	42.5%
Silica	SiO_2	42%
Hematite	Fe_2O_3	5.925%
Potassium oxide	K_2O	3.53%
Phosphorite	P_2O_5	2.9%
Yttria	Y_2O_3	1.955%
Rutile	TiO_2	0.475%

3.2. Particle Shape Analysis of Feed Sample

The photomicrograph of the particle shape of the feed shows that it has an angular, irregular shape with some rounded and elongated shapes (Figure 2). Some particles display smooth edges and some show rough edges, which results in varying specific surface areas and has a significant effect on the adsorption of collectors on the surface. According to Zhang (2016), the surface area of a mineral determines the adsorption density of the collector on its surface. The larger the surface area of the mineral, the higher the consumption of collectors.

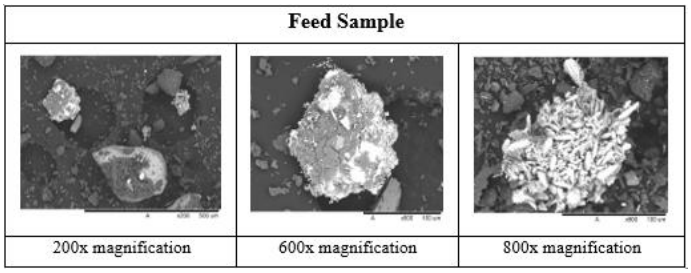

Fig. 2. Particle shape of feed sample in different degree of magnification

3.3 XRD Analysis of Feed Sample

From the diffractogram in Figure 3, the existence of xenotime in feed sample is proven. This analysis is to support the XRF data in Table 2 where xenotime concentration feed sample is found to be 1.955%.

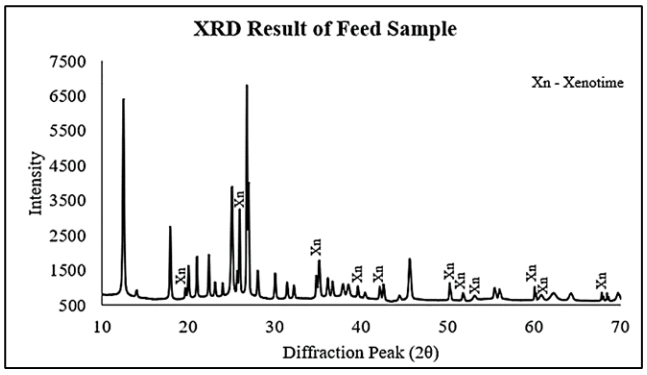

Fig. 3. The XRD pattern for feed sample

3.4 Particle Size Analysis of Feed Sample

The particle size distribution of the feed sample obtained using a laser particle analyzer (Malvern MS3000) is shown in Figure 4. From the analysis, it can be concluded that 10% of the samples are smaller than 4.98µm, 50% are smaller than 20 µm, and 90% are smaller than 82.6 µm. This result differ from Zhang who obtained the overall 80 percent passing (P_{80}) size of 125 µm for xenotime concentrate in 2016.

3.5 The Effect of Different Collectors to Flotation of Xenotime

Octano-hydroxamic acid (HXM) and sodium oleate (SOT) were tested at pH 7 at room temperature with a concentration of 0.0005M to observe the effect of different surfactants on the grade of the flotation products. The grade of xenotime and other major gangue minerals is tabulated in Figure 5.

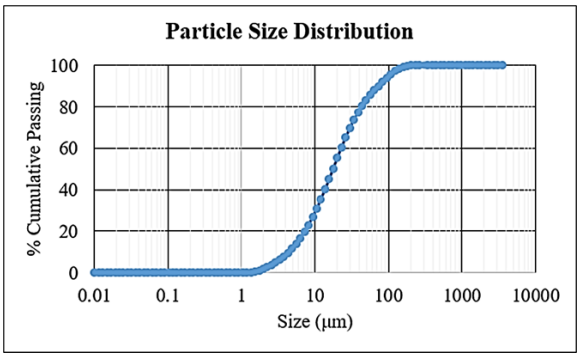

Fig. 4. Particle size distribution graph

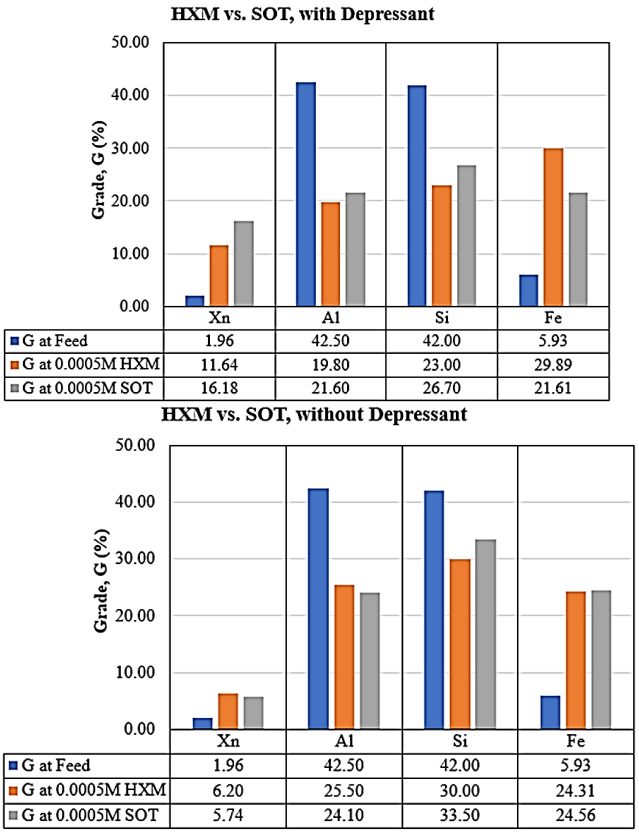

	Xn	Al	Si	Fe
G at Feed	1.96	42.50	42.00	5.93
G at 0.0005M HXM	11.64	19.80	23.00	29.89
G at 0.0005M SOT	16.18	21.60	26.70	21.61

	Xn	Al	Si	Fe
G at Feed	1.96	42.50	42.00	5.93
G at 0.0005M HXM	6.20	25.50	30.00	24.31
G at 0.0005M SOT	5.74	24.10	33.50	24.56

Fig. 5. Grade of xenotime and selected gangue minerals with 0.0005M HXM vs. 0.0005M SOT, without and with depressant

In the absence of a depressant, a better grade of xenotime (Xn) was noted when HXM was used as a collector compared to SOT. Pradip and Fuerstenau had also concluded that hydroxamate was more selective than sodium oleate in the flotation of bastnaesite from barite and calcite. Conversely, different results were recorded by Zhang (2016), who found that the grades of concentrate produced using sodium oleate were

much higher than those produced using octano-hydroxamic acid. In the presence of a depressant, SOT exhibited stronger selectivity than HXM in the flotation of xenotime from selected gangue minerals

3.6 The Effect of the Collector Concentration

The amount of collector plays a significant role in determining the effectiveness of separating the desired minerals from gangue minerals in the flotation process. If the concentration is too low, the minerals are not sufficiently hydrophobic. However, if the concentration is too high, it will also affect the flotation as two possibilities might occur: ineffective separation due to the collector rendering everything hydrophobic, causing high mass pull, low concentrate grades, and formation of micelles [6].

From the results in Figure 7 and 8, it can be concluded that the higher concentration of collectors will promote better flotation of xenotime. This is because more collector ions are available to adsorb onto the mineral surface, rendering the minerals hydrophobic. However, the plunge on xenotime grade from concentration 0.001M to 0.002M happened because of concentration of collectors is so high that micelles form rendering the xenotime hydrophilic. Figure 6 further illustrates the occurrence of this phenomenon.

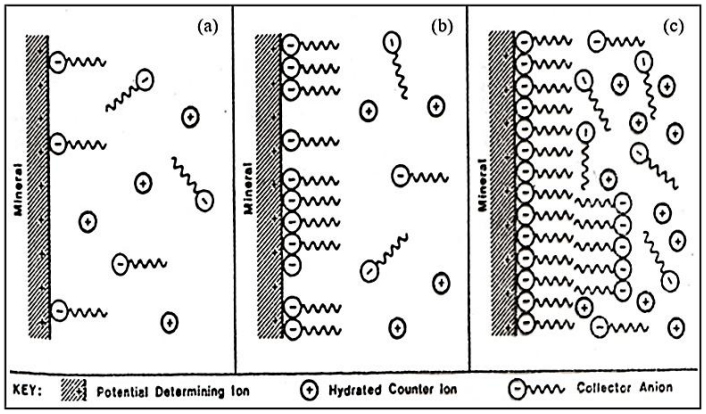

Fig. 6. Schematic representation of the mineral-solution interface in the presence of anionic collector

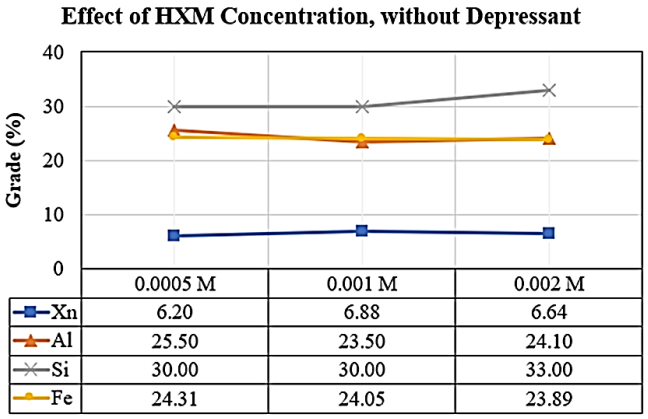

	0.0005 M	0.001 M	0.002 M
Xn	6.20	6.88	6.64
Al	25.50	23.50	24.10
Si	30.00	30.00	33.00
Fe	24.31	24.05	23.89

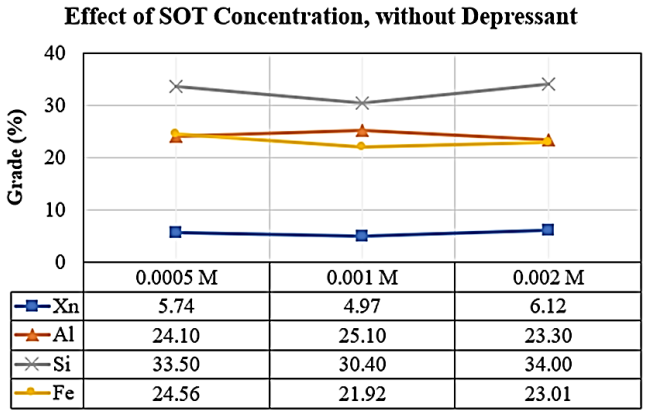

	0.0005 M	0.001 M	0.002 M
Xn	5.74	4.97	6.12
Al	24.10	25.10	23.30
Si	33.50	30.40	34.00
Fe	24.56	21.92	23.01

Fig. 7. Effect of SOT and HXM concentration on the minerals' grade without depressant

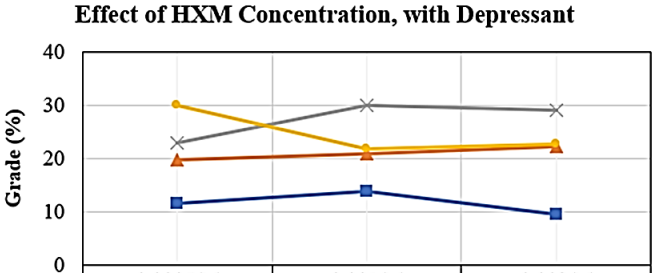

	0.0005 M	0.001 M	0.002 M
Xn	11.64	13.92	9.58
Al	19.80	20.80	22.20
Si	23.00	30.00	29.00
Fe	29.89	21.90	22.63

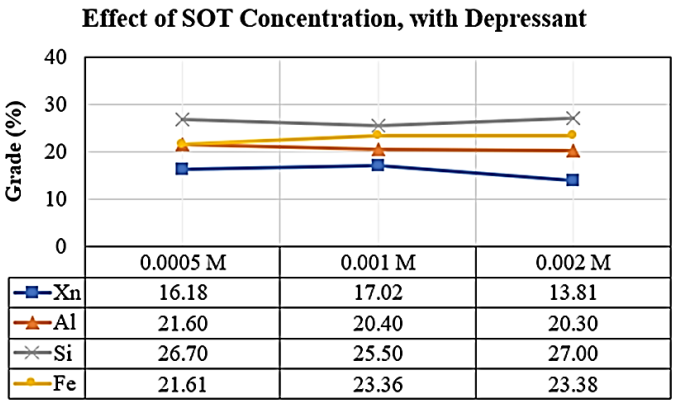

	0.0005 M	0.001 M	0.002 M
Xn	16.18	17.02	13.81
Al	21.60	20.40	20.30
Si	26.70	25.50	27.00
Fe	21.61	23.36	23.38

Fig. 8. Effect of HXM and SOT concentration on the minerals' grade with depressant

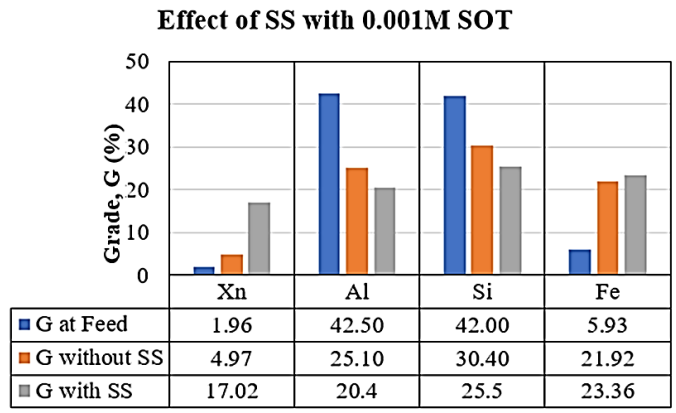

	Xn	Al	Si	Fe
G at Feed	1.96	42.50	42.00	5.93
G without SS	4.97	25.10	30.40	21.92
G with SS	17.02	20.4	25.5	23.36

Fig. 9. The effect of SS on the minerals' grade with 0.001M HXM and SOT

3.7 The Effect of Depressant

In further tests, sodium silicate (SS) was used in the flotation of the feed samples before the addition of octano-hydroxamate acid (HXM) or sodium oleate (SOT). Comparisons were made to investigate the effect of depressant to the grade of Xn and other selected minerals (Al, Si and Fe). From Figure 9, it can be concluded that SS increase the selectivity of both collectors towards xenotime. They also possess the ability to depress Si and Al. However, Fe was not affected by the depressant when it was applied together with the collector. This situation can be explained using Zhang's (2016) competition theory. He stated that siliceous ions must compete with the collector ions during the adsorption process on the surface of hematite. Since sodium silicate is not able to depress ilmenite, it indicates that active Fe2+ ions favor anionic collector ion species more than siliceous ion species. This is probably because the compound formed between Fe2+ on the surface of hematite and the anionic collector ions was more stable than that formed with silicate ions.

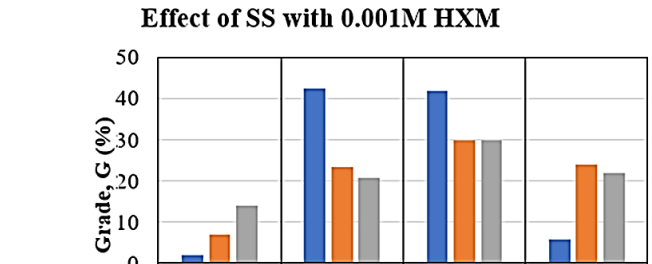

	Xn	Al	Si	Fe
G at Feed	1.96	42.50	42.00	5.93
G without SS	6.88	23.50	30.00	24.05
G with SS	13.92	20.80	30.00	21.90

4. CONCLUSIONS

Characterization of feed sample carried out is to analyze its composition, shape and particle size distribution The froth flotation of xenotime has been investigated, focusing on comparing the effectiveness between two collectors and how their concentration effects the floatability. The grades of the concentrate produced using sodium oleate were much higher than those produced using octano-hydroxamic acid. In the absence of a depressant, octanohydroxamic acid shows better selectivity in the flotation of xenotime from other gangue minerals; however, in the presence of a depressant, sodium oleate produces better grades of concentrate. Next, the concentration of collector influenced the grade of flotation products. A higher concentration of collectors will promote better flotation of xenotime. This is because more collector' ions are available to adsorb onto the surface of minerals and render the minerals hydrophobic. However, when the concentration of anionic collector is too high which in this study observed at 0.002M, the grade of xenotime will fluctuate. This is caused by the formation of micelles that will render the xenotime mineral hydrophilic and left sinking along with tailings. In the presence of depressant, the selectivity of both collectors significantly improved. However, combination between sodium oleate collector and sodium silicate depressant was found to be more favourable. In addition, sodium silicate shows no depressing power towards hematite as Fe2+ ions on the surface of hematite preferred anion collector species more than siliceous ion species, thus decreasing the amount of active area on the hematite surface for depressant to adsorb on. This further resulted in the hematite surface hydrophobic

ACKNOWLEDGMENTS

The authors would like to thank School of Materials and Mineral Resources Engineering for their support and contributions to this research.

REFERENCES

[1] N. Dushyantha, G. N. Kuruppu, C. J. Nanayakkara, and A. S. Ratnayake, "The Role of Permanent Magnets, Lighting Phosphors, and Nickel-Metal Hydride (NiMH) Batteries as a Future Source of Rare Earth Elements (REEs): Urban Mining Through Circular Economy," *Mining, Metallurgy and Exploration*. 2024, doi: 10.1007/s42461-023-00904-0.

[2] Z. M. Migaszewski, A. GaLuszka, and G. Zieliński, "REE-bearing minerals in sediment-hosted stratiform pyrite mineralization zones of the Wiśniówka area (Holy Cross Mts., Poland)," *Geol. Q.*, 2023, doi: 10.7306/gq.1687.

[3] H. Salim, O. Sahin, S. Elsawah, H. Turan, and R. A. Stewart, "A critical review on tackling complex rare earth supply security problem," *Resour. Policy*, 2022, doi: 10.1016/j.resourpol.2022.102697.

[4] S. E. Zhang, J. E. Bourdeau, G. T. Nwaila, and Y. Ghorbani, "Emerging criticality: Unraveling shifting dynamics of the EU's critical raw materials and their implications on Canada and South Africa," *Resour. Policy*, 2023, doi: 10.1016/j.resourpol.2023.104247.

[5] R. L. Martins, L. Magalhães, L. H. Santos, and G. Rodrigues da Silva, "The Use of Pracaxi Oil Collector in the Selective Flotation of Xenotime from Silicates," *SSRN Electron. J.*, 2022, doi: 10.2139/ssrn.4136247.

[6] Y. Gao *et al.*, "A quantitative innovation perspective on synergism and selectivity mechanism of mixed collectors in flotation," *Miner. Eng.*, 2024, doi: 10.1016/j.mineng.2023.108474.

Techno-Science Research Journal V13 (Special Issue) (2025) P 50-57

I.T.C

Content list available at ITC

Techno-Science Research Journal

Journal Homepage: www.ric.itc.edu.kh

Techno-Science Research Journal

A Review of Western Belt range of S-type granitoid with particular refer to Magnetite and Ilmenite-Series of Granitoid and An Experimental study of the Concentration of Valuable Minerals Analysis, Kampus Kejuruterran, Universiti Sains Malaysia (USM), Nibong Tebal, State of Pulau Pinang, Peninsular Northern Malaysia

Sokmeng Ni[1,2*], Muhammad Nasrul Amin Bin Mohd Zamzuri[2], Siti Fatimah Binti Rahim[2], Hashim Hussin[2], Ku Esrya Hani Ku Ishak[2], Azrul[2], Zulkunian[2]

[1] *Faculty of Geo-Resources and Geotechnical Engineering, Institute of Technology of Cambodia, Phnom Penh, Cambodia*
[2] *School of Materials and Mineral Resources Engineering, Kampus Kejuruteraan, Universiti Sains Malaysia, Nibong Tebal, Pulau Pinang, Malaysia*

Received: 1 November 2024; Revised: 1 January 2025; Accepted: 20 June 2025; Available online: October 2025

Abstract: *In the ilmenite-series of magma, tin maybe in the divalent state and has no suitable substitution site in the rock-forming minerals. Tin can accumulate in the residual. If the original magma in an apical part of the granitic magma. It considered that the presence of the ilmenite-series granitoids is a prerequisite in major tin fields. The ilmenite grains in both valleys are not homogeneous and are associated with other heavy minerals that include monazite, zircon, rutile, and cassiterite. Common textures of the ilmenite grains include replacement by leaching, intergrowths and exsolutions. Alluvial sample contaminated of Tin metal associated to Ilmenite mineralization of the study area located in between of main range belt of granite, Pulau Pinang state of Northern Malaysia. Concentration involves the separation of the valuable minerals from the other raw materials. Minerals that are economic value can classify as, metallic and non-metallic, denser or less dense which can extract for commercial use and it involved in the separation has its different properties with different advantages. These properties can be color or size (optical sorting or microscope), density (gravity separation), and magnetism (magnetic separation). The process starts with the coning and quartering method, to reduce the sample size without creating a systematic bias. Sieving method, to determine the particle size and liberate of each size. Spirals, involved in separate the particle according to its density. Magnetic separation, to separate the magnetic and non-magnetic minerals of magnetite and silica. XRF analysis reliable data on the elemental composition, the concentrates from the raw materials, spirals, and magnetic separation run by the grinding methods to achieve a smooth and uniform surface finish, which is essential for many applications. Through non-destructive analysis, these devices enable geologists and mining professionals to swiftly ascertain the percentages of various elements present in a sample. The recovery of spiral concentrator gives the result 86.12 % higher than magnetic separator, which was 64.30 %. The spiral concentrator effectively separates the denser ilmenite and Magnetite particles from the lighter gangue minerals based on gravity, ilmenite and magnetite have higher specific gravity which were 5.5 and 5.3 respectively compared to the silica or quartz has lower specific gravity which was 2.4. The separation between valuable and gangue minerals done easily causing the higher recovery percentage compared to the magnetic separator.*

Keywords: Ilmenite, Magnetite, Concentration, X-ray Florescence (XRF), Mineral Processing, Spiral Separator, Magnetic Separator, Particle Size Analysis (PSA), Microscopic and Petrographic Analysis, Magnetite and Ilmenite-Series Granitoid

1. INTRODUCTION

In the south-eastern Australia the importance of source rock composition and separation of melt and refractory residue in characterizing various suites led to "S" type granite classification. In this scheme, the S-type result from melting and residue of sedimentary or meta-sedimentary source material in which the source was taken to lie within continental crust. The western belt granite of peninsular Malaysia has been regarded to be constituted by exclusively "S" type granites in contrast to the eastern belt of granites which is dominated by "I" type with subordinate "S" type granites. The western belt granites of peninsular Malaysia is characterized by a huge mountain range extending from Malacca in the south to Thailand in the north. The classification by opaque phases mineral was based on the occurrence of Ilmenite and Magnetite

* Corresponding author: Ni Sokmeng
Email:*sokmeng584@gmail.com*

in granitic rock. In this classification, magnetite and ilmenite series can be distinguished by their different magnetic susceptibilities; rock of the magnetite series showing high values (more than 100 X 10 emu/g) while those ilmenite series showing lower than 100 X 10 emu/g.

In mineral processing, a major division in the science of Extractive Metallurgy. Extractive metallurgy has been defined as the science and art of extracting metals from their ores through several methods is majority's process to get high value of concentrate after the process. Concentration means the increase of the percentage of the valuable mineral in the concentrate. Within this research of the experimental study is concentration involves the separation of the valuable minerals from the other raw materials. Alluvial sample contaminated of Tin metal associated to Ilmenite mineralization of the study area located in between of main range belt of granite, Paulu Pinang state of Northern Malaysia.

To identify the recovery of valuable mineral from alluvial sample throughout several methods including mineral characterizations and based on physical processing of hand specimens, coning and quartering, humprey spiral separator, particle size distribution analysis, drying, ore microscope and petrography, magnetic separation, grinding and x-ray florescence (XRF) analysis.

The ilmenite grains in both valleys are not homogeneous and are associated with other heavy minerals that include monazite, zircon, rutile, and cassiterite. Common textures of the ilmenite grains include replacement by leaching, intergrowths and exsolutions.

2. GEOLOGICAL FRAMEWORK

2.1. Granitoid in Peninsular Malaysia

About ninety granitoids were examined by the magnetic susceptibility meter. Among three major intrusive belts of Permo-Triassic age, the main range granite belt of [1], almost all the Main Range Granites and Eastern belt are predominant in Peninsular Malaysia. Sporadically distributed magnetite-series ones in these belts are generally weakly magnetic, except for one pluton northwest of Malaca.

The magnetite-series granitoids seem to occur dorminantly in the Central intrusive belt, although the number of analyses is small (**Fig. 1**). As reported opaque oxide minerals higher than 0.2 vol.% on the Bukit Besar igneous complex, which should belong to the magnetite-series [2]. The retaceous pluton, such as Mount Ophir and Pulau Tioman, are also composed of the magnetite-series granitoids. Thus, aabundance of the magnetite-series or ilmenite-series granitoids in the Peninsular Malaysia is different among three geotectonic units of [1] and depending upon age of the granitoids.

Magnetite-bearing character of the Central Intrusion Belt is in harmony with its island arc nature [1], because typical island arc volcano-plutonic association has magnetite-bearing character [3]. The tendency that magnetite-free rocks predominate in the early Mesozoic Terrance but are scarce in the late Mesozoic one is the same as that found in the southern part of Korean Peninsula [4], which is different from the patterns observed in the Japanese island arc environment.

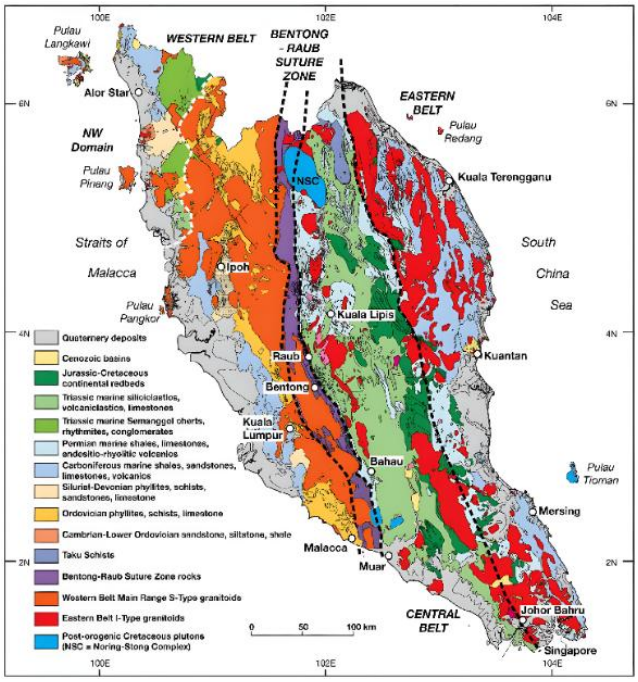

Fig.1. Distribution of the magnetite-series and Ilmenite-series granitoids of the Peninsular Malaysia. Map of the Peninsular Malaysia showing the Western Belt granite in relation to other granite batholiths.

2.2. S-type western belt granitoid

The S-type granite is characterized by restricted SiO2 content between 65% to 75%, which is characteristic of rocks derived from SiO2 rich sources. The granite are low in Na, Ca, and Sr, which are lost during the conversion of feldspar to clay mineral by weathering. High K2O/Na2O is the "S" type rocks is explained by the fact that potassium is incorporated into clay during the chemical weathering to produce sedimentary rocks, whereas sodium is removed in solution along with Ca, Sr, and Pb. The "S" type rocks are significantly lower than "I" type. As a result, of the lower Na and Ca, "S" types are always corundum normative or peraluminous and become more strongly so as the rocks become more primitive.

2.3. Magnetite and Ilmenite-series granitoid

The significance of opaque oxides of granitoids for tin mineralization was first pointed out by [5], who noted that granitoids accompanying tin deposits has little magnetite, less than 0.02 wt%, but "tin-barren granitoids" contain an average of 1.26 wt.% of magnetite. A similar conclusion was obtained indepently from studies of granitoids of W-Sn and Mo metallogenic provinces in southwest japan [6], and the genetic beqaring of magnetite in granitoids was discussed in terms of oxygen fugacity of the granitic magmas [3, 4].

Tin can have either tetravalent or divalent state in magmas

[7]. In the magnetite-series magma, tin can be tetravalent and is consumed in common rock-forming minerals, such as sphene, magnetite, ilmenite, epidote-group minerals and hornblende, in the early crystallization stage of magmatic differentiation. Thus, this type of magma cannot have a large concentration of tin in the residual.

In the ilmenite-series of magma, tin maybe in the divalent state and has no suitable substitution site in the rock-forming minerals. Tin can accumulated in the residual. If the original magma in an apical part of the granitic magma. It considered that the presence of the ilmenite-series granitoids is a prerequisite in major tin fields.

The magnetite-series and ilmenite-series granitoids can be identified easily in the field by magnetic susceptibility meter, assemblage of ferro-magnesian silicate, color of biotite and other method [3].

2.4. Relation of Tin mineralization

Three north-south belts characterize the Malay Peninsula: the Western, Central, and Eastern belts (**Fig. 2**). More than 90% of the plutonic rocks in Peninsular Malaysia are granitic. The granitoids can be divided into two belts, a West Malaya Main Range S-Type group of granitoids that yield Late Triassic to earliest Jurassic, and an eastern Malaya group of dominantly I-Type granitoids with a range of ages from early Middle Permian to early Late Triassic.

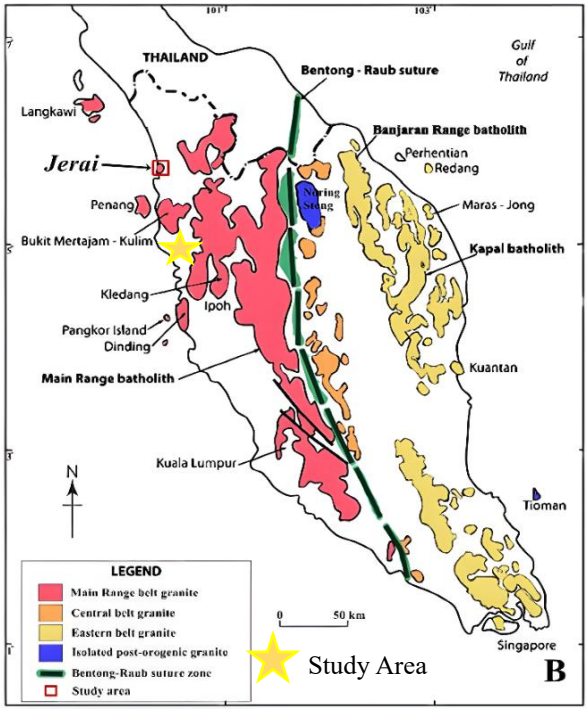

Fig.2. Location area of Ilmenite mineralization with alluvial deposit, northern part of Malaysia.

A significant Late Cretaceous tectono-thermal event affected the Peninsula with major faulting, granitoid intrusion, and re-setting of palaeomagnetic signatures [8].

The study area also falls within the Western Belt of Peninsular Malaysia with a main Range S-Type group of granitoids from the Late Triassic to earliest Jurassic periods. There are conjugate sets of brittle fractures affecting the surrounding plutons, one of which is parallel to the cleavage and may reflect the accommodation of deformation at two different structural depths [9]. Moreover, the geomorphology of the area consists of hilly terrains and undulating plateaus. The geology of the area mainly consists of Quaternary and Devonian granite. Distribution of tin placer deposits was shown in (**Fig. 2**). The tin deposits seem distributed around the ilmenite-series granitoids. The fact that ilmenite is the most predominant heavy mineral in these deposits supports the above conclusion.

3. METHODOLOGY

For this mineral processing experiment involve in several methods (**Fig. 3**) to liberate the valuable and non-valuable minerals from the alluvial feed and to estimate the recovery of the concentration inside the feed and the product.

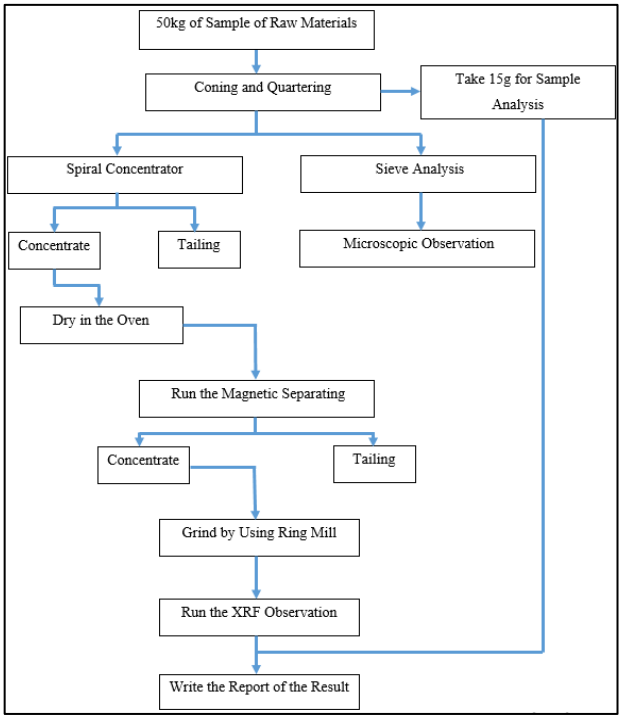

Fig.3. Research Flow Chart for Separation Methods.

After proceed with each method including Cone and Quartering, Humprey Spiral Separator to separate between Concetration; Middling; and Tailing, Dry process to extract the moisture, Magnetic Separator using magnetic to separate between Silica and Metallic, Particle Size Analysis (PSA), Ore microscopic and Petrography, Grinding in finer molecule, and X-Ray Fluorescence (XRF) analysis. To estimate the recovery of metallic valuable mineral with the formula calculation based

on Sieving (PSA).

3.1. Cone and Quartering

The reduction in size of a granular or powdered sample by forming a conical heap which is spread out into a circular, flat cake. The cake is divided radially into quarters and two opposite quarters are combined. The other two quarters are discarded. The process is repeated as many times as necessary to obtain the quantity desired for some final use (e.g. as the laboratory sample or as the test sample). If the process is performed only once, coning and quartering is no more efficient than taking alternate portions and discarding the others (PAC, 1990).

50 kg of the alluvial sample was given to students to do the experiment, Coning and Quartering is being involved in mixed the sample and after the process is done, 20kg of the sample was taken for the next experiment and the other was discharge.

3.2. Particle Size Analysis (PSA)

Particle size analysis, particle size measurement, or simply particle sizing, is the collective name of the technical procedures, or laboratory techniques which determines the size range, and/or the average, or mean size of the particles in a powder or liquid sample. Particle size analysis is part of particle science, and it is generally carried out in particle technology laboratories. The particle size measurement is typically achieved by means of devices, called Particle Size Analyzers (PSA), which are based on different technologies, such as high definition image processing, analysis of Brownian motion, gravitational settling of the particle and light scattering (Rayleigh and Mie scattering) of the particles.

The particle size can have considerable importance in a number of industries including the chemical, food, mining, forestry, agriculture, cosmetics, pharmaceutical, energy, and aggregate industries. However, Sieve analysis is a process used to separate the particle size in order and after spiral process, the left over piece of the sample of alluvial took to do PSA.

Sieving analysis, in order to separate the particle size of our sample such as 3.33mm; 2.8mm; 2.0mm; 1.0mm; 600 µm; 425 µm; 355 µm; 250 µm; 150 µm; 75 µm; and below 75 µm. After the particle size by using sieve-shaking monitor already, it needs to be measuring the sample weight from each tray and after measuring, keep it in a plastic bag and label per each.

3.3. Humprey Spiral Separator

The spiral concentrator is a modern high capacity and low-cost device. It developed for concentration of low-grade ores and industrial minerals in slurry form. It works on a combination of solid particle density and its hydrodynamic dragging properties. The spirals consist of a single or double helical conduit or sluice wrapped around a central collection column. The device has a wash water channel and a series of concentrate removal ports placed at regular intervals.

Separation achieved by stratification of material caused by a complex combined effect of centrifugal force, differential settling, and heavy particle migration through the bed to the inner part of the conduit. Extensive application is the treatment of heavy mineral beach sand consisting of monazite, ilmenite, rutile, zircon, garnet, and upgrade chromite concentrate. Two or more spirals were constructed around one central column to increase the amount of material that can be processed by a single integrated unit.

Before putting any sample into the spiral machine, students need to fill-up the reservoir with water below the spiral concentrator about 80-100liter and 20kg of the alluvial sample. A few minute later, the sample is mixed and it's time to separate the concentration, milling and tailing and after collected the concentration sample, student have to clean up the spiral's machine that contained the left-over of milling and tailing.

3.4. Drying Process

Drying of mineral processing products is the process in which the water content of mineral processing product is removed by thermophysical process. It is one of the ways to dehydrate mineral processing products. Usually the water content in materials is volatilized by heating. Alternatively, the water can be condensed and sublimated by temperature drop, depressurization, or other means of energy transfer, so as to remove the water content.

The concentration sample was taken to put in a metal plate and putted inside the oven for 24h until it removed all the moisture inside the sample.

3.5. Ore Microscopic and Petrography

The variety of commercially available reflected-light microscopes tends to mask the basic similarities between them in terms of the arrangement of light source, lenses, diaphragms, reflector, objectives, and oculars. Some of this variety is evident in (**Fig. 5**), which shows research and student model microscopes. Modern microscopes are deliberately designed to be "modular," and commonly both reflected-light and transmitted-light components combined in one instrument. Each manufacturer incorporates unique design features into the ore microscopes they produce, and it is necessary for the reader to refer to the instruction manual accompanying a particular microscope for the exact placement and employment of the components described below and for information regarding other accessories.

To analyst the type of the ore mineral, there are 6types of sieve sample that need to identify the ore and gangue mineral such as 425 µm, 355 µm, 250 µm, 150 µm, 75 µm and below 75 µm.

3.6. Magnetic Separator

Magnetic separation based on the differing degrees of attraction exerted on various minerals by magnetic fields. Success requires that the feed particles fall within a special size

spectrum (0.1 to 1 millimeter). With good results, strongly magnetic minerals such as magnetite, and ilmenite can be removed from gangue minerals by low-intensity magnetic separators. High-intensity devices can separate oxide iron ores as well as iron-bearing manganese, titanium, and tungsten ores and iron-bearing silicates.

After drying the sample in the oven from the spiral process, we took the sample to do the separation of concentration where it could possibly contained Milling and Tailing known as Gangue mineral.

3.7. Grinding Process

XRF analysis need powder sample to analyst, there are 3 samples of plastic bags were taken to do the grinding such as 1 sample from the raw feed (>15kg) and the other 2 samples are after magnetic separation (Concentration and Tailing within >15kg). The process won't take long around 10mn, all the grinding samples are done and need to confirm with the XRF.

3.8. X-Ray Fluorescence (XRF) analysis

XRF is a non-destructive elemental analysis method for solids and liquids. The phenomena are extensively used in element and chemical analysis. The purpose of an XRF analysis is to identify and determine the chemical compositions of recovery of the concentration in feed and concentrate of the product (**Table 3**).

The method is based on the energy properties of the atoms present in the samples. Atoms were ionized when they were subjected to short wavelength x-rays with energies greater than their ionization potential. The removal of one electron resulted in an unstable atomic structure that had to be compromised by electrons dropping from higher orbitals into lower orbitals. This falling produced energy in the form of a photon, equivalent to the energy difference between two orbitals.

4. RESULTS AND CALCULATION

4.1. Particle Size Analysis (PSA)

The data of the sieving process will accumulate in the table (**Table 1**) as shown. The values of percentage's cumulative passing, which are the diameters that correspond to the percentile of 25%, 50% and 75% respectively, can be determined from the grain-size distribution curve.

Table1. Sieve Data of Particle Size Analysis (PSA).

Particle Size, µm	Mesh size, µm	Mass, g	Percentage Retaine, %	Cumulative Percentage Retained, %	Cumulative Percentage Passing, %
-3350	3350	14.20	0.73	0.73	99.27
-2800+3350	2800	17.05	0.88	1.61	98.39
-2000+2800	2000	55.31	2.84	4.45	95.55
-1000+2000	1000	402.73	20.70	25.15	74.85
-425+1000	425	777.81	39.99	65.14	34.86
-355+425	355	120.38	6.19	71.33	28.67
-250+355	250	224.72	11.55	82.88	17.12
-150+250	150	240.30	12.35	95.23	4.77
-75+150	75	85.35	4.39	99.62	0.38
+75		7.40	0.38	100.00	0.00
Total		1945.25			

The grain-size distribution of the ore sample can be obtained by plotting the cumulative percentage passing against the particle size in the semi-log graph paper (**Fig. 4**), Three intersection lines were plotted to determine the particle size percentage and 25%, 50% and 75% respectively. From the (**Fig. 4**), as shown below:

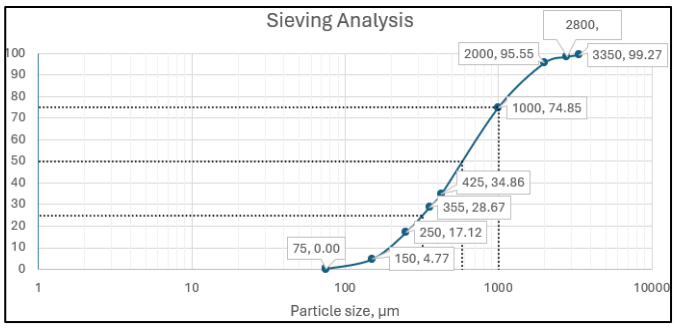

Fig.4. Grain Size Distribution Graph of Mesh size and Cumulative Passing percentage.

4.2. Microscopic observation and Petrographic Analysis

The samples were going to observed under microscope based on its size range. There are total 6 samples show the particles with size 425 µm, 355 µm, 250 µm, 150 µm, 75 µm and below than 75 µm (**Fig. 5**). There are three minerals had been found in the samples which were quartz, ilmenite and hematite. Based on the figure above there are three type of minerals presence in the samples which were hematite, ilmenite, and silica. The characterization of each minerals are shown in (**Table 2**) below:

Table 2. Mineralogy and Mineralization Properties

Mineral	Chemical Formula	Type of Mineral	Colour
Quartz	SiO_2	Gangue Mineral	White
Ilmenite	$FeTiO_3$	Valuable Mineral	Black
Magnetite	Fe_3O_4	Valuable Mineral	Metallic Grey

All the samples had been sieved before being observed under microscope. Based on the observation most of the valuable minerals are presence most at the size range of 355 µm and below. Then the particles size above 425 µm had being determine only a few valuable mineral's particle presence. Hence it can be concluded that, the sample which was from the alluvial deposit have the valuable minerals start to liberate from the size particles 355 µm and below.

4.3. Spiral Separation

The feed of the ore sample which has weight of 20 kg mixed with 80 litre of water in the reservoir of spiral concentrator give the percentage solid. By the equation of Percentage solid equal to mass of solid (20kg) multiple by 100% and divided by mass of solid (20kg) plus mass of water (80litre), where it equal 20% from its result.

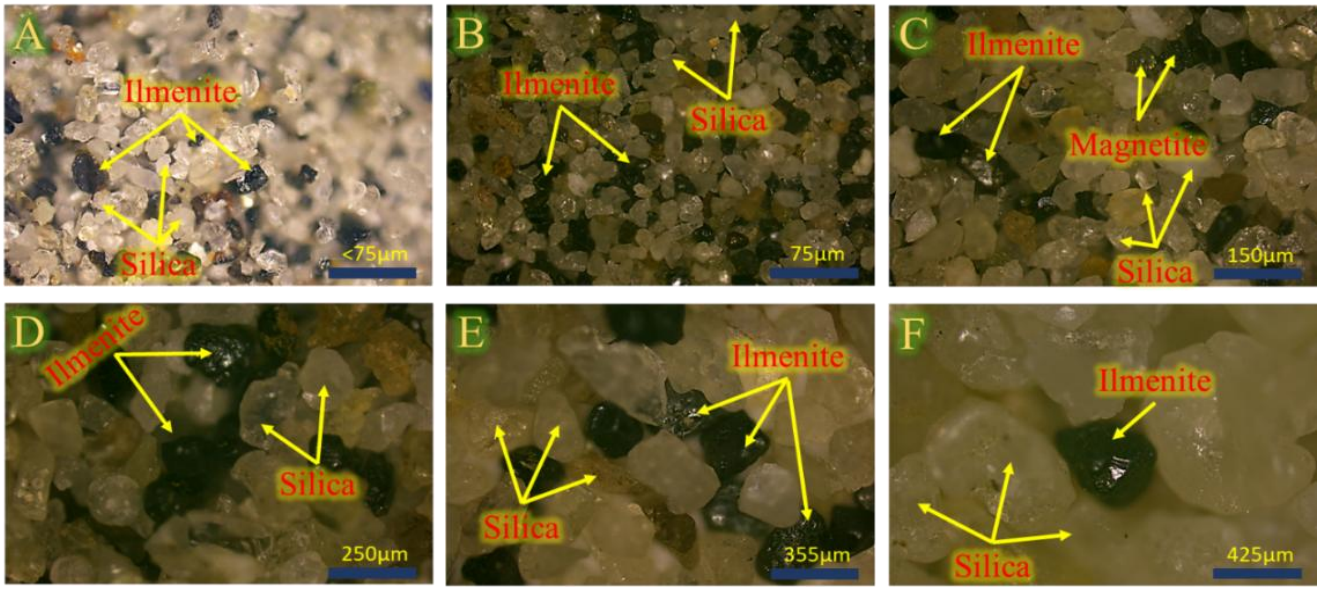

Fig. 5. Petrography Microscopic of representative in mineralogy of Silica and mineralization of Magnetite and Ilmenite inside the alluvial sample. Each of the different title represent for different range of sieve sizes A) below 75 µm, B) 75 µm, C) 150 µm, D) 250 µm, E) 355 µm, and F) 425 µm.

The spiral concentrator operates 20kg of feed in 1.5mn then, the equation formula of feed rate is equaled to mass of solid (20kg) divided by the time taken (1.5mn) equal to 13.33kg/mn. Based on the feed and concentrate take for 20second, the equation for the mass of feed is equaled to time (20sec) multiple by mass of solid (20kg) and divide by time taken of spiral (1.5mn=90sec) and we receive the number of mass of feed is about 4440g or 4.44kg.

From mass of concentration, we receive about 1052.53g after sieve analysis. Within the XRF analysis on (**Table 2**) below; the Grade of valuable mineral in feed's spiral concentrator = 4.95 + 10.66 = 15.61%. Grade of valuable mineral in concentrate's spiral concentrator = 23.00 + 33.71 = 56.71%

To determine the Recovery of the concentration, it is equal to mass of concentrate (C) 1052.53g multiply by grade of concentrate (c) 56.71% and 100%, divided by mass of feed (F) 4440g and grade of feed (f) 15.61%. The result for the recovery would be 86.12%.

4.4. Magnetic Separation

After the process of the separation by magnetic, the product from the operation, we receive the mass of feed's magnetic separator about 984g, Concentrate's magnetic separator 390g, Tailing's magnetic separator 558 g. Based on the XRF analysis (**Table 2**) below, Grade of valuable minerals from feed = 23.00 + 33.71 = 56.71%. Grade of valuable minerals from concentrate = 37.41 + 51.23 = 88.64%.

The equation of the recovery is equal Concentrate's magnetic separator 390g multiply by Grade of valuable minerals from concentrate about 88.64% and 100% divided by mass of feed's magnetic separator about 984g multiply by Grade of valuable minerals from feed 56.71%. The result of recovery from the magnetic separator equalled to 64.30%.

4.5. X-Ray Fluorescence (XRF) Analysis

The grade of the minerals content in the sample had been measured using XRF machine and type of minerals is set up as oxide minerals. In this analysis only major mineral presence in the samples that will be taken because of the XRF analysis which were silica/quartz, ilmenite and magnetite.

Table 3. Data Interpretation of Ilmenite and Magnetite Concentrate based on X-ray Florescence (XRF) Analysis

CHEMICAL COMPOSITION	SAMPLE RAW (WT %)	SPIRAL'S CONCENTRATE (WT %)	MAGNETIC SEPARATOR'S CONCENTRATE (WT %)
MgO	0.2145	0.0122	0.0045
Al_2O_3	8.0122	5.0113	1.4653
SiO_2	74.9722	37.3166	9.8121
P_2O_5	0.0000	0.0000	0.0000
SO_3	0.0091	0.0285	0.0137
K_2O	0.0290	0.0190	0.0190
CaO	0.7874	0.5274	0.0001
TiO_2	4.9534	23.0002	37.4143
Cr_2O_3	0.0973	0.0983	0.0012
MnO	0.1059	0.0406	0.0006
Fe_3O_4	10.6561	33.7121	51.2311
NiO	0.0221	0.0000	0.0000
ZnO	0.0012	0.1491	0.0000
SrO	0.0211	0.0215	0.0002
ZrO_2	0.0671	0.0611	0.0000
Nb_2O_5	0.0000	0.0000	0.0000
SnO_2	0.0000	0.0000	0.0000
PbO	0.0000	0.0000	0.0000
Total (%)	99.9486	99.9979	99.9621
Grade	15.6095	56.7123	88.6454

5. DISCUSSION

Based on the review the geological framework of western belt range of S-type with the magnetite and ilmenite-series granitoid by confirm with the XRF analysis and Petrography Microscopic Optical observation. We notice that the chemical composition of SiO_2 content is 74.9722% that is restrict between 65%-75%, where it considers as S-type Granitoid with the appearance of the Magnetite and Ilmenite mineralization observed in the microscopic.

Before concentrate the valuable from the ore sample, ore sampling method needs done by using coning and quartering sampling method. The ore sample needs to be sampling first to make sure that ore sampling is evenly mixing and to produce reference sample as this reference sample will be stored or being used to be analyst. If any accident occur this reference sample can be as a backup sample to replace the broke and contaminated sample.

Sieving Analysis useful to determine the particle size distribution, knowing the percentile of particle size range. 25 % and 75 % of sample are size below than 320 µm and 1010 µm respectively while the median is below than 580 µm. The particle size of ore sample are most medium size particles, only small percentage are course particles. It is because the ore sample itself are from alluvial deposit which had being weathered by the water in long time causing to reduce its diameter of particles. Sieving analysis are particularly useful to determine the type of the deposit based on the physical properties of ore sample. For example, we can determine this sample is a alluvial deposit or weathered ore deposit by looking at the size of the particles where most of the particles are medium to fine size of particles.

In mineral observation under microscope or petrography analysis there are three types of minerals had been identified which were quartz, ilmenite and magnetite. By observing its physical properties such as mineral's colour, the valuable minerals and gangue mineral can be identified more precisely. Ilmenite has black colour and metallic or submetallic luster. Other than that, hematite has steel-grey colour and metallic to dull luster. When the valuable mineral had being identified, the unit operation to concentrate valuable minerals can being decide which were spiral concentrator and magnetic separator. It is because both ilmenite and magnetite had similar characteristic which were heavy mineral where both have specific gravity of 5.5 and 5.3 respectively and magnetic particles where ilmenite has a magnetic characterization and magnetite has a strong magnetic characterization to separate from gangue mineral which was silica or quartz where it was a non-magnetic mineral. Other than that, by observe the ore sample under microscope based on its size range we can determine the liberation of ilmenite and magnetite in raw ore which later can affect recovery, as too small and too big size of valuable minerals can reduce the efficiency of concentrating operations.

The recovery of spiral concentrator gives the result 86.12 % higher than magnetic separator, which was 64.30 %. The spiral concentrator effectively separates the denser ilmenite and hematite particles from the lighter gangue minerals, which was silica or quartz based on gravity. It is because ilmenite and magnetite have higher specific gravity which were 5.5 and 5.3 respectively compared to the silica or quartz has lower specific gravity, which was 2.4. Due to the big difference of specific gravity between valuable minerals and gangue mineral in spiral concentrator operation, the separation between valuable and gangue minerals can done easily causing the higher recovery percentage compared to the magnetic separator. While magnetic separator further enriched the concentrate by exploiting the magnetic properties of ilmenite and magnetite. Since ilmenite are not too strong magnetic, separating the magnetic particles from non-magnetic particles will be quite difficult because ilmenite particles can be false separating as these particles can be escape from being attracted from the magnet even due to there is slightly obstacle or slightly mistakes occur during the operation.

There are some crucial factors need to take attention that might have influenced the result. Before putting the sample into the sieves, make sure that all sieves are clean. Brush the mesh using soft brush of iron brush to remove any particles stuck in the mesh as it can reduce the sieving's efficiency. Human error commonly can occur during doing microscope observation. Human eyes sometimes can mistakenly analysis the ore samples due to low skill in predicted the mineral based on the visual of the mineral. Other than that, the camera inside the camera can also affect, human prediction on the mineral under microscope because the camera cannot accurately capture and process the accurate picture and colour of the sample. Hence, it sometimes easily falsely interpret the picture of the sample. The camera setting such as exposure time, contrast and brightness need setting correctly to ensure that the camera are the correct picture and colour grading of the minerals. During gravity separation using spiral concentrator, gangue mineral can go into the concentrate fraction due to the mineral particles impede the gangue mineral to move to the outer spiral. The parameter of the spiral concentrator needs to set to ensure that it can separate the heavy mineral and light mineral more efficiency. For example, if the percent solid is higher, this operation will become harder for the spiral concentrator to separate the valuable minerals due to the lack of water to push the light mineral to the outer spiral. Other than that, the splitter outlet that control the mineral fraction of the concentrate, middling and tailing need to accurately adjusted to ensure that there is no valuable mineral enter to the tailing fraction. The splitter location offering the highest level of separation effectiveness (Mohanty, 2006)s. Lasty, the feed rate of magnetic separator cannot be too high because if there is high feed rate, there is some magnetic particles that will escape from being attract by the magnet to the concentrate fraction.

6. CONCLUSIONS

The "S" type granite classification in south-eastern Australia is based on source rock composition and separation of melt and refractory residue. This classification is dominated by the western belt granite of peninsular Malaysia, which is characterized by a large mountain range from Malacca to Thailand. The classification is based on the occurrence of Ilmenite and Magnetite in granitic rock, with magnetite series showing high values and ilmenite series showing lower values. This classification helps distinguish between different suites of granites.

Concentration is known as the process to separate the gangue from the valuable mineral in mining industrial. There are three minerals had been found in the samples which were quartz, ilmenite and hematite. Ilmenite is a valuable mineral that associated with the silica mineral know as gangue mineral. Ilmenite also seem to be a very small particle deposited in the alluvial and it contained with Titanium Dioxide (TiO2), where Titanium was one of the naturally metal product used in every industrial. The experiment for the concentration of valuable mineral involved with mineral characterizations based on physical processing of hand specimens, coning and quartering, humprey spiral, particle size analysis, drying, ore microscope and petrography, magnetic separation, grinding and x-ray florescence (XRF) analysis.

On the other hand, Spiral was seem to appeared with lot of gangue mineral more than magnetic separation process, where the amount recovery of grade ore in magnetic separation is higher than spiral process because it could extract more magnetic minerals from silica or gangue minerals. Both methods are suitable and connected to each other purpose, where spiral tends to separated silica from the concentrations in the first stage and magnetic separator is the last process.

AKNOWLEDGEMENTS

I would like to express my sincere gratitude and respect to all of the members of the SCHOOL OF MATERIALS AND MINERAL RESOURCES ENGINEERING, which is situated in the Engineering Campus of Universiti Sains Malaysia, including the doctors, technicians, and international friends, for the success of this experiment and research journal on mineral processing. for giving me this significant chance to participate in this project during my spring semester break in 2024 in order to enhance and expand my knowledge and abilities in mineral processing. In addition, I would want to express my gratitude to Prof. Dr. Eng Chandeoun, my dean faculty, for providing me with this amazing exchange program experience.

REFRENCES

[1] C. S. Hutchison, "Granite emplacement and tectonic subdivision of Peninsular Malaysia," 1977.
[2] B. Jaafar, "The geology and mineral resources of the Karak and Temerloh areas, Pahang," *Geological Survey of Malaysia,* vol. 15, p. 138, 1976.
[3] S. Ishihara and S. Terashima, "The tin content of the Japanese granitoids and its geological significance on the Cretaceous magmatism," *Jour. Geol. Soc. Japan,* vol. 83, pp. 657-664, 1977.
[4] S. Ishihara, "Metallogenesis in the Japanese island arc system," *Journal of the Geological Society,* vol. 135, no. 4, pp. 389-406, 1978.
[5] P. Aranyakanon, *The cassiterite deposit of Haad Som Pan, Ranong Province, Thailand*. Royal Department of Mines, 1962.
[6] S. Ishihara, "Modal and chemical composition of the granitic rocks related to the major molybdenum and tungsten deposits in the Inner Zone of Southwest Japan," *Jour. Geol. Soc. Japan,* vol. 77, pp. 441-452, 1971.
[7] H. Hamaguchi, R. Kuroda, N. Okuma, K. Kawabuchi, T. Mitsubayashi, and K. Hosohara, "The geochemistry of tin," *Geochimica et Cosmochimica Acta,* vol. 28, no. 7, pp. 1039-1053, 1964.
[8] I. Metcalfe, "Tectonic evolution of the Malay Peninsula," *Journal of Asian Earth Sciences,* vol. 76, pp. 195-213, 2013.
[9] B. Sautter *et al.*, "Late Paleogene rifting along the Malay Peninsula thickened crust," *Tectonophysics,* vol. 710, pp. 205-224, 2017.

Techno-Science Research Journal V13 (Special Issue) (2025) P 58-63

Content list available at ITC

Techno-Science Research Journal

Journal Homepage: http://techno-srj.itc.edu.kh/

Techno-Science Research Journal

A Review on Biodegradable Surfactants in Membrane Technology

Kyu Kyu Tin[1], Wirach Taweepreda[2]*

[1] *Environmental Management, Faculty of Environmental Management, Prince of Songkla University, Hat-Yai, Songkhla 90110, Thailand*

[2] *Polymer Science Program, Division of Physical Science, Faculty of Science, Prince of Songkla University, Hat-Yai, Songkhla 90110, Thailand*

Received: 1 November 2024; Revised: 1 January 2025; Accepted: 20 June 2025; Available online: October 2025

Abstract: *The integration of biodegradable surfactants in membrane technology represents a promising approach to increasing wastewater treatment processes while elevating environmental sustainability. This literature review mentions the types, mechanisms, applications and environmental impacts of biodegradable surfactants in various membrane processes, such as microfiltration, ultrafiltration, nanofiltration, reverse osmosis, and forward osmosis. Natural surfactants derived from microorganisms and plants, as well as synthetic biodegradable surfactants, are detected for their effectiveness in reducing membrane fouling, enhancing permeability, and improving overall performance. The environmental advantages of biodegradable surfactants, including reduced toxicity and elevated biodegradability, are mentioned, along with their potential to align with sustainable development goals. Case studies and comparative analyses show the benefits of biodegradable surfactants over conventional surfactants, emphasizing their sector in creating more efficient and eco-friendly membrane technologies. Despite current challenges, such as cost and performance variability, ongoing research and innovation give promise for the future development and widespread adoption of biodegradable surfactants in membrane technology.*

Keywords: Surfactants, Biodegradable surfactants, Membrane, Environmental sustainability.

1. INTRODUCTION

Membrane technology has mentioned as an essential role for wastewater treatment, sharing efficient separation and purification process. This technlolgy uses semi-permeable membranes that permit water molecules to pass through while rejecting dissolved solides, various pollutants and suspended particles. Membrane processes are faced for their ability to handle diverse wastewater streams, involving those from municipal, industrial and agricultural sources, creating them a versatile solution in the face of enhancing water contamination and scarcity challenges [1]. Membrane technology is used in various wastewater treatement processes, such as microfiltration, utltrafiltration, nanofiltration, and reverse osmosis. These methods are effective in discarding contaminants involving pathogens, inorganic chemicals, and organic matter. The advantage of membrane technology include smaller equipment size, decreased energy requiements, and reduce capital cost compared to traditional treatment techniques. Additionally, membranes are eco-friendly as they donot release toxic waste during operation, aligning with sustainable water treatement goals [2].

In membrane technology,Surface-active agents or surfactants, demonstrate a crucial sector by modifying the surface properties of membranes. They increase membrane performance in different ways. Surfactants decrase membrane fouling by protecting the accumulation of contaminants on the membrane surface, that helps maintains high filtration efficiency and belong the lifespan of the membranes. Plus, by altering the hydrophilicity or hydrophobicity of the membrane surface, surfactants increase water permeability and flux, heading to more efficient filtration mechanism. Furthermore, surfactants can modify the pore structure and surface charge membranes elevating their selectivity for specific contaminants

* Corresponding author: Wirach Taweepreda
E-mail: wirach.t@psu.ac.th; Tel: 0-7428-8007

[3].Conventioanl surfactants, while effective, often promote environmental concerns due to their potential toxicity and persistence. On the other hands, biodegradable surfactants offer a sustainable alternative , as they degrade into non-toxic byproducts, reducing its environmental impact. In wastewater applications,the utilization of biodegradable surfactant is crucial role for different reasons in membrane technology.It help environmental prevention by decreasing the risk of pollution and harm to aquatic life, making them a safer choice and they support meet regulatory compliance, as enhancing environmental regualtions and standards necessitate the utilization of eco-friendly chemical in industrial mechanisms, including wastewater treatment.Lastly, the adoption of biodegradable surfactants helps sustaianility by aligning with the global push towards green technologies, elevating long-term envrioemntal health and resource conservation. By focusing on biodegradable surfactants, researchers and industry professionlas can improve more sustainable membrenae processes that effectively treat wastewater while minimizing environmental impact [4].

2. Biodegradable surfactants in Membrane process

2.1 Types of Biodegradable Surfactants

Biodegradable surfactants both synthetic and natural , show a pivotal in increasing membrane technology for wastewater treatment (Table 1). Natural surfactants involve plant-based options like lecithin, saponins and alkyl polyglucosides(APGs). Lecithin, derived from sunflower and soybeans , serves as a natural emulsifier , reducing fouling and enhancing permeability. Saponins, observed in plants such as yucca, soapwort, and quillaja, belong excellent foaming and emulsifying properties, creating them suitable for membrane process [5]-[6]. APGs, came from fatty alcohols and sugars, are non-ionic biodegradable, and low in toxicity, applying them ideal for enviroementally friendly applications. Microbial surfactants, including sophorolipids from Candida bombicola, and mannosylerythritol lipids (MELs) produced by yeast, and rhamnolipids produced by Pseudomonas aeruginosa, are effective in reducing surface tension, have strong emulsifying properties, and are less toxic and biodegradable compared to synthetic surfactants [7]-[8].

Synthetic biodegradable surfactants involve polyhydroxyvalerate (PHV) and polyhydroxyalkanoates (PHAs) like polyhydroxybutyrate (PHB) , which are biodegradable polymers utilized to modify membrane surfaces, increasing hydrophicity and reducing fouling [9]-[10]. Synthetic APGs ensures consistent persistence and performance, making them suitable for membrane technology [11]. Biodegradable anionic surfactants, including sodium methyl cocoyl taurate, sodium lauryl sulfate (SLS), are designed to be less harmful to the environment whild maintain excellent cleansing and foaming properties [12]. Biodegradable non-ionic surfactants, such as polyethylene glycol (PEG) and ethoxylated alcohols derivatives, are synthesized to be biodegradable and low in toxicity, effectively reducing membrane fouling and enhancing permeability [13]. By focusing on these types fo biodegradable surfactants, membrane processes for wastewater treatement, reducing environmental impact and elevating long-term sustainability.

Table 1. Types of biodegradable surfactants

Types	Source	Examples	Applicationin Membrane Technology
Natural surfactants			
Plant-Based Surfactants(Desai & Banat, 1997; Marchant & Banat, 2012)	Plants	Saponins, Lecithin, APGs	Reduce fouling, improve permeability, enhance selectivity in microfiltration and ultrafiltration
Microbial Surfactants (Banat et al., 2010; Gautam & Tyagi, 2006).	Bacteria, Yeast	Bacteria, Yeast	Reduce fouling, improve flux, enhance selectivity in nanofiltration and reverse osmosis
Synthetic Biodegradable Surfactants			
Polyhydroxyalkanoates (PHAs) (Chen, 2010; Sudesh et al., 2000).	synthetic	PHB, PHV	Modify membrane surfaces, enhance hydrophilicity, reduce fouling in various membrane processes
Alkyl Polyglucosides APGs)(Hill et al.,2006).	synthetic	Synthetic APGs	Improve permeability, reduce fouling, enhance selectivity in microfiltration and ultrafiltration
Biodegradable Anionic Surfactants (Kralova & Sjoblom, 2009).	synthetic	Sodium Methyl Cocoyl Taurate	Reduce fouling, improve flux, enhance selectivity in reverse osmosis and forward osmosis
Biodegradable Non-Ionic Surfactants (Holmberg et al., 2002).	synthetic	Ethoxylated Alcohols, PEG Derivatives	Reduce fouling, improve permeability, enhance selectivity in nanofiltration and reverse osmosis

2.2 Mechanisms of action

Biodegradable surfactants increase membrane performance through various mechanisms. They absorb onto the membrane surface, forming a hydrophilic layer onto the membrane surface, forming a hydrophilic layer that attracts water molecules, reduces the contact angle, and elevates water flux. This enhanced hydrophilicity maintains higher permeability and reduces the adhesion of hydrophobic foulants [13]. Additionally, some biodegradable surfactants impart a charge to the membrane surface, including anionic surfactants providing a negative charge, which repels negatively charged foulants and increases membrane selectivity. Surfactants also impact pore size distribution by adsorbing onto pore walls, either reducing or enlarging pore sizes, thereby increasing permeability and selectivity. By filling in surface irregularities, surfactants smoothen the membrance surface, reducing foulant adhesion and accumulation. The hydrophilic layers created by surfactants serves as a barrier against hydrophobic foulants, whereas steric hinderance inhibit foulants from approaching the membrane surface, decreasing biofouling. In the feed solutions, surfactants form micelles , encapsulating hydrophobic foulants and hindering their disperse particulate foulants, aggregation, reducing inorganic fouling. By reducing surface tension and disrupting foulant adhesion, in cleaning solutions, making cleaning more effective and less frequent [7]. The reduces the requirement for harsh chemicals , making the cleaning process more enviromentlally friendly and less damaging to the membrane material and biodegradable surfactants significantly increase the efficiency and sustainability of membrane technology in wastewater treatment by leveraging these mechanisms [8].

3. APPLICATION IN MEMBRANE PROCESS

In water and wastewater treatment, microfilatration (MF) and Ultrafiltration(UF) are widely introduced, operating by discarding micororganisms and particles depends on size exclusion. The utilization of biodegradable surfactants can elevate membrane performance by decreasing fouling as a common issue. Biodegradable surfactants raise in cleaning the membrane more environmentally friendly, decreasing the ecological impact of the cleaning process [12]-[13].

For desalination and the removal of smaller contaminatns, Nanofiltration (NF) and Reverse Osmosis(RO) are efficiently applied, including dissolved salts and organic molecules and then is particularly in discaring specific ions and effective for water softening while reverse osmosis is attracting for creating high-purity water .Additionally, these process advantages from advancemnts in membrane technology , including enhancement of more robust and chosen membrane [14].

As an emerging technology, Forward Osmosis (FO) , applies a natural osmotic pressure gradient to stand water through a semi-permeable membrane.The potential of biodegradable surfactants in FO shows in their ability to reduce membrane fouling and increase water flux. This supports FO a promising technology for applications including desalination, and wastewater treatement, where sustainable and efficient processes are essential [15].

4. ENVIRONMENTAL IMPACT

Surfactants, widely applied in cosmetics, detergents, and industrial applications, vary significantly in their environmental impact and biodegradability. Conventioanl surfactants, can persist in the environment, heading to long-term ecological damage. In contrast, biodegradable surfactants such as those derived from natural sources like sugars and fatty acids, break down more readily, reducing theirenvironmental footprint[16]. Nevertheless, the toxicity of these biodegradable surfacatns is particularly lower compared to conventional ones. For instance, biosurfactants produced by microorganisms demonstrate lower toxicity to aquatic life and soil microorganisms. This makes them a more environmentally friendly option, as they decrease the bioaccumulation. Generally, the shift towards biodegradable surfactants display a positive step in mitigating the environmental impact of surfactants [17].

Biodegradable surfactants have shown significantlty lower envriomental impact compared to conventional surfactants (**Table 2**) [18]. They are more easily broken down and less toxic by natural processes, that reduces their persistence in the environment. Comparative studies have described that biodegradable surfactants can match or even surpass the performance of conventiaonl surfactants in specific applications. For instance, in membrane bioreactors, biodegradable surfactants like sophorolipids have shown to be effective in reducing membrane fouling than synthetic surfactants. Althoudhg the initital cos to of biodegradable surfactants may be higher, their long-term benefits, including lower environmental cleanup costs and increased system efficiency, often justify the investment. In addition, the lifecycle cost of applying biodegradable surfactants can be lower than that of conventioanal surfactants [19].

Table 2. Traditioanl versus biodegradable surfactants in membrane technology [18].

Aspect	Traditional Surfactants	Biodegradable Surfactants
Environmental Impact	Higher toxicity, persistent in the environment	Lower toxicity, easily broken down by natural processes
Performance	Effective but may cause more fouling	Effective in reducing membrane fouling (e.g., sophorolipids)

Cost	Lower initial cost, higher long-term costs	Higher initial cost, lower long-term costs
Efficiency	May require more frequent maintenance	Improved system efficiency

A type of biosurfactant, rhamnolipids, in a study observed by Nur liyana Ismail et al. (2022), were introduced in a membrane bioreactors for wastewater management which rhamnolipids effectively reduced membrane fouling and also biosurfactants elevated the overall efficiency of the treatment mechanism, creating it a viable solution for industrial wastewater treatement [20]. In the cleanup of oil spills, a review by Lidia Pinheiro and Celia Faustino (2017) mentioned the utilization fo amino acid-based surfactants in breaking down oil into smaller droplets, accelerating microbial degradation which is essential for preventing marine ecosystems and maintain water quality. The separation and purification of food products in the food industry, the study by Ismail et al.(2022) also noted the utilization of bio-based surfactants in maintain the quality and safetly of food by protecting contamination and enhancing the effiency of the separation process [22].

In environmental remediation,Biosurfactants are hilghly attractive, treating heavy metals in soils and water and hydrophobic organic pollutants with a removal efficiency of up to 96% making them ideal for cleaning up projects [22].
In the oil and gas industry,they are used for oil recovery,as disperants for oil spills, which aids in mobilizing trapped oil

Improving extraction efficiency. Plus, in agriculture, biosurfactants elevate soil health and plant growth by enhancing the bioavailability of nutrients and acting as natural pesticides , thereby protecting plants against diseases [23].

5. CHALLENGES AND FUTURE DIRECTIONS

One of the main challenges in utilizing biodegradable surfactants in membrane technology is their compatibility with existing membrane materials. Many biodegradable surfactants can react with membrane polymers, heading to reduced membrane performance and lifespan. Biodegradable surfactants may have lower stability under different operational conditions, including high temperatures, extreme pH levels, and the presence of oxidizing agents. This can limit their effectiveness and durability in membrane applications. The production of biodegradable surfactants is often more expensive than traditional surfactants. Scaling up production to fulfill industrial demands while maintaining cot-effectiveness remains a significant hurdle. Achieving the desire performance in terms of selectivity, permeability and antifouing properties is challenging. Biodegradable surfactants need to exceed or match the performance of traditional surfactants to be widely adopted [24].

Future research is required to enhance biodegradable surfactants which are compatible with a broad range of membrane materials without compromising their integrity and performance. In addition, under various operational situation, exploring ways to elevate the stability of biodegradable surfactant is essential and this include investigating new formulaitons and additives that can elevate their robustness. Afterwards, research should depend on optimizing production processes to release costs and this could involve utilizing alternative, sustainable feedstocks and improving fermentation and purification methods. More research are needed to accelerate the functional properties of biodegradable surfactants , involving its permeability, antifouling, and selectivity and also this will help create them more competitive with traditional surfactants.

Future development may include the creation of novel biodegradable surfactant formulations which share superior stability and performance and could be tailored for specific membrane applications, involving water treatment or gas separation. Advances in biotechnology, including genetic engineering and synthetic biology, could head to more efficient and sustainable production methods for biodegradable surfactants.

The combination of biodegradable surfactants with advanced membrane materials, such as bio-inspired or nanocomposites membranes, could show in hybrid systems with increased performance and enviroemntal benefits. Increase market incentives and regulatory support for environmentally friendly technologies could elevate the adoption of biodegradable surfactants in membrane technology. Growing public awareness of enviromentla issues and the demand for sustainable products could drive further research and development in this field, heading to more effective and innovative solutons. In membrane technology, biodegradable surfactants hold great promise, but addressing these challenges will need collaborative, efforts from researchers, regulatory bodied ,and industry.

Design thinking for biodegradable surfactants in membrane technology includes understanding the environmental need for eco-friendly solutions and specific performance requirements like stability and antifouling properties. It addresse challenges such as stability under various conditions, compatiiltiy with membrane materials, and cost-effectiveness. Solutons are generated through innovative formulations, hybrid systems and advanced biotechnology. Prototyping involves lab-scale experiments and pilot projects, while testing evalutes performance, environmental impact, and economic feasibility. Future prospects involve sustainable production methods, regulatory support, and enhanced public awarness driving demand for these sustainable solutions [25].

The integration of biodegradable surfactants in membrane technology helps various Sustainable Development Goals(SDGs) set by the United Nations, such as SDG 6 (Clean Water and Sanitation), SDG 9 (Industry, Innovation, and Infrastructure), SDG 12 (Responsible Consumption and

Production), and SDG 13 (Climate Action). By replacing conventional chemical surfactants, it can promote cleaner water systems and reduce environmental pollution. Using renewable feedstocks helps sustainable industrial practices and waste mangemnt. Advancing biotechnological techniques increases membrane process efficiency, fostering innovation and sustainable industrialization. Biodegradable surfactants are safer for human health , contributing to better working environment. Their adoption can stimulate economic growth by making job opportunities and new markets. Meeting enviormental regualtions supports industries avoid penalties and inelevates corporate social responsibility. These efforts contribute to a more environmentally friendly and sustainabl future.

6. CONCLUSIONS

In conclusion, the combination of biodegradable surfactants in membrane technology shows a promising pathway towards more sustainable and environmentally friendly industrial processes. By addressing main challenges including stability, compatibility and cost-effectiveness, and leveraging advanced biotechnology methods, it can enhance the adorption and performance of these alternatively eco-friendly alternatives. This shift not only helps different sustainable development goals, including cleaner water treatements, sustainable industrial best practices , and climate action, but also elevates safer increasing safer worker enviroments and stimulates economic growth. As research and innovation support to advance, the potential for biodegradable surfactants to revolutionize membrane technology and contribut to greener future becomes maximizing attainable. Collaborative bodies will be essential in overcoming existing barriers and realizing the full potential of these sustainable solutions.

ACKNOWLEDGMENTS

We would like to acknowledge and offer our affection to Prince of Songkla Univeristy, Thailand.

REFERENCES

[1] Singh, G., Yadav, P., Singh, S. K., Ranjan, N., Verma, H., Ferreira, L. F. R., & Kumar, A. (2024). Membrane processes for wastewater treatment. In A. Kumar, M. Bilal, & L. F. R. Ferreira (Eds.), Advances in Chemical Pollution, Environmental Management and Protection (Vol. 10, pp. 35-56). Elsevier. https:// doi.org/ 10.1016/ bs.apmp.2023.08.001

[2] Obotey Ezugbe E, Rathilal S. Membrane Technologies in Wastewater Treatment: A Review. Membranes. 2020; 10(5):89. https://doi.org/10.3390/membranes10050089

[3] Fung KCL, Dornelles HS, Varesche MBA, Gutierrez T. From Wastewater Treatment Plants to the Oceans: A Review on Synthetic Chemical Surfactants (SCSs) and Perspectives on Marine-Safe Biosurfactants. Sustainability. 2023; 15(14):11436. https://doi.org/10.3390/su151411436

[4] Lavanya, M., & Machado, A. A. (2024). Surfactants as biodegradable sustainable inhibitors for corrosion control in diverse media and conditions: A comprehensive review. Science of The Total Environment, 908, Article 168407. https://doi.org/10.1016/j.scitotenv.2023.168407

[5] Desai, J. D., & Banat, I. M. (1997). Microbial production of surfactants and their commercial potential. Microbiology and Molecular Biology Reviews, 61(1), 47-64.

[6] Marchant, R., & Banat, I. M. (2012). Biosurfactants: A sustainable replacement for chemical surfactants? Biotechnology Letters, 34(9), 1597-1605.

[7] Gautam, K. K., & Tyagi, V. K. (2006). Microbial surfactants: A review. Journal of Oleo Science, 55(4), 155-166.

[8] Banat, I. M., Makkar, R. S., & Cameotra, S. S. (2010). Potential commercial applications of microbial surfactants. Applied Microbiology and Biotechnology, 87(2), 427-444.

[9] Chen, G. Q. (2010). A microbial polyhydroxyalkanoates (PHA) based bio- and materials industry. Chemical Society Reviews, 39(8), 2580-2590.

[10] Sudesh, K., Abe, H., & Doi, Y. (2000). Synthesis, structure and properties of polyhydroxyalkanoates: Biological polyesters. Progress in Polymer Science, 25(10), 1503-1555.

[11] Hill, K., von Rybinski, W., & Stoll, G. (2006). Alkyl polyglycosides: Technology, properties and applications. VCH Verlagsgesellschaft mbH.

[12] Kralova, I., & Sjoblom, J. (2009). Surfactants used in food industry: A review. Journal of Dispersion Science and Technology, 30(9), 1363-1383.

[13] Holmberg, K., Jönsson, B., Kronberg, B., & Lindman, B. (2002). Biodegradable non-ionic surfactants. In Surfactants and Polymers in Aqueous Solution (2nd ed., pp. 485-512). John Wiley & Sons.

[12] Banerjee, P., Bhattacharya, S., Das, R., Das, P., & Mukhopadhyay, A. (2021). Microfiltration and ultrafiltration membranes for water purification. In R. Das (Ed.), Polymeric Membranes for Water Purification and Gas Separation (Vol. 113, pp. 33-68). Materials Research Forum. https://doi.org/10.21741/9781644901632-3

[13] Siddique TA, Dutta NK, Roy Choudhury N. Nanofiltration for Arsenic Removal: Challenges, Recent Developments, and Perspectives. Nanomaterials (Basel). 2020 Jul 6;10(7):1323. doi: 10.3390/nano10071323. PMID: 32640523; PMCID: PMC7407220.

[14] Tian J, Zhao X, Gao S, Wang X, Zhang R. Progress in Research and Application of Nanofiltration (NF) Technology for Brackish Water Treatment. Membranes. 2021; 11(9):662. https://doi.org/10.3390/membranes11090662

[15] Banerjee, P., Bhattacharya, S., Das, R., Das, P., & Mukhopadhyay, A. (2021). Forward osmosis for water purification. In R. Das (Ed.), Polymeric Membranes for

Water Purification and Gas Separation (Vol. 113, pp. 69-92). Materials Research Forum. https://doi.org/10.21741/9781644901632-3

[16] Badmus SO, Amusa HK, Oyehan TA, Saleh TA. Environmental risks and toxicity of surfactants: overview of analysis, assessment, and remediation techniques. Environ Sci Pollut Res Int. 2021 Nov;28(44):62085-62104. doi: 10.1007/s11356-021-16483-w. Epub 2021 Sep 29. PMID: 34590224; PMCID: PMC8480275.

[17] Nagtode VS, Cardoza C, Yasin HKA, Mali SN, Tambe SM, Roy P, Singh K, Goel A, Amin PD, Thorat BR, Cruz JN, Pratap AP. Green Surfactants (Biosurfactants): A Petroleum-Free Substitute for Sustainability-Comparison, Applications, Market, and Future Prospects. ACS Omega. 2023 Mar 24;8(13):11674-11699. doi: 10.1021/acsomega.3c00591. PMID: 37033812; PMCID: PMC10077441.

[18] Smith, J., & Brown, S. (2020). Innovations in Sustainable Chemistry: Biodegradable Surfactants and Their Applications. Green Chemistry Press.

[19] U.S. Environmental Protection Agency. (2021). Climate Change and Social Vulnerability in the United States: A Focus on Six Impacts. Retrieved from https://www.epa.gov/cira/social-vulnerability-report

[20] Ismail, N. L., Shahruddin, S., & Othman, J. (2022). Overview of bio-based surfactant – Recent development, industrial challenge, and future outlook. In A. K. Dutta (Ed.), Surfactants and Detergents - Updates and New Insights (pp. 69-92). IntechOpen. https://doi.org/10.5772/intechopen.100542

[21] Pinheiro, L., & Faustino, C. (2017). Amino acid-based surfactants for breaking down oil in marine ecosystems. Journal of Environmental Science and Technology, 45(3), 215-230. https://doi.org/10.1016/j.jenvsci.2017.03.015

[22] Ismail, N. L., Shahruddin, S., & Othman, J. (2022). Rhamnolipids in membrane bioreactors for wastewater treatment: Reducing fouling and enhancing efficiency. Journal of Environmental Management, 305, 114-123. https://doi.org/10.1016/j.jenvman.2022.114123

[22] Selva Filho, A. A. P., Converti, A., Soares da Silva, R. C. F., & Sarubbo, L. A. (2023). Biosurfactants as multifunctional remediation agents of environmental pollutants generated by the petroleum industry. Energies, 16(3), 1209. https://doi.org/10.3390/en16031209

[23] Patel, S., Homaei, A., Patil, S., & Daverey, A. (2019). Microbial biosurfactants for oil spill remediation: Pitfalls and potentials. Applied Microbiology and Biotechnology, 103(1), 27-37. https://doi.org/10.1007/s00253-018-9434-2

[24] Gupta, R. S., Samantaray, P. K., & Bose, S. (2023). Going beyond cellulose and chitosan: Synthetic biodegradable membranes for drinking water, wastewater, and oil-water remediation. ACS Omega, 8(24), 24695-24717. https://doi.org/10.1021/acsomega.3c01699

[25] Cevallos-Mendoza J, Amorim CG, Rodríguez-Díaz JM, Montenegro MDCBSM. Removal of Contaminants from Water by Membrane Filtration: A Review. Membranes (Basel). 2022 May 30;12(6):570. doi: 10.3390/membranes12060570. PMID: 35736277; PMCID: PMC9229562.

[26] UN-Water. (2018). SDG 6 Synthesis Report 2018 on Water and Sanitation. United Nations. Retrieved from https://sustainabledevelopment.un.org/content/documents/19901SDG6_SR2018_web_3.pdf

Techno-Science Research Journal V13 (Special Issue) (2025) P 64-71

Content list available at ITC

Techno-Science Research Journal

Journal Homepage: www.ric.itc.edu.kh

Techno-Science Research Journal

Integration of InSAR technique to enhance effectiveness of monitoring scheme on Tailings Storage Facility No.2, Chatree Gold Mine, Thailand

Chea Shanghai[1*], Pipat Laowattanabandit[1], Buth Chitra[1]

[1]*Department of Mining and Petroleum Engineering, Faculty of Engineering, Chulalongkorn University, Bangkok 10330, Thailand*

Received: 1 November 2024; Revised: 1 January 2025; Accepted: 20 June 2025; Available online: October 2025

Abstract: *Tailings storage facility (TSF) is a critical component of the mining industry, serving to safely contain waste generated during mineral extraction. The Chatree Gold Mine, large and only one gold mine in Thailand, currently operates Tailings Storage Facility No.2 (TSF No.2). It is designed to accommodate an annual 5 million tonnes of tailings approximately. Monitoring of TSF plays a critical role in hazard prevention and minimizing environmental impacts by ensuring compliance with standard and regulation. This study aims to enhance effectiveness of the monitoring scheme for detecting ground deformation within TSF No.2 by employing Interferometric Synthetic Aperture Radar (InSAR) technology. Despite traditional monitoring methods, such as in situ geodetic surveying, offering valuable insights, they may not provide timely warnings of potential instability and are costly when applied to large-scale areas. By utilizing Small Baseline Subset InSAR (SBAS-InSAR) time-series analysis, this study will assess the effectiveness of this advanced remote sensing technique in detecting subtle ground deformations by comparing its results with existing in situ geodetic data spanning from June 2016 to May 2019. The result of the study, reveals a strong correlation between the two datasets, indicating that both methods effectively capture similar phenomena. The findings are anticipated to make a significant contribution to the enhancement of monitoring practices and risk management strategies for tailings storage facilities (TSFs). It is a showcase the application of InSAR technology to monitor ground deformations in tailings storage facilities.*

Keywords: Chatree Gold Mine, Tailings storage facility, InSAR, Ground deformation

1. INTRODUCTION

Tailings storage facility play a critical role in the mining industry, serving as vital structures for the safe containment of waste materials generated during mineral extraction [1]. As mining operations yield valuable resources, they simultaneously produce tailings (finely ground materials resulted from processing) that can contain harmful substances. Proper management of these tailings is essential to mitigate environmental impacts and protect human health [1]. In certain projects, tailings embankments can reach heights of several hundred meters, while the impoundments can extend over several square kilometers.

Chatree Gold Mine is the largest gold mine in Thailand, it is located between the provinces of Phichit and Petchaboon, northen Thailand. The Chatree Gold Mine Project is currently operated by Akara Resources Public Company Limited, generating the output capacity 2 million tonnes per year (Mtpa) since its inception. The expansion was taking place since August 2011 to increase throughput to 5 Mtpa. The mining operation consists of open pits, waste dumps, a process plant and a tailings storage facility. Ore is sourced from a series of open pits and processed in crushing and milling circuits followed by a carbon-in-leach process to extract the gold. Tailings from the plant are being deposited into a purpose-designed storage facility, namely Tailing Storage Facility No.2 (TSF No.2), to ensure that the surrounding environment is not adversely impacted [2]. Tailing Storage Facility No. 2 (TSF No.2) was commissioned in October 2012 to serve as the primary tailings storage facility. Tailing Storage Facility No.2 construction comprises of 12 stages of embankments construction. The Stage 1 embankment was started to be constructed to reach a maximum height of approximately 10 m. Over the life time of the project, the embankments for TSF No.2 will be raised annually until the last stage (Stage 12), reaching a maximum height of 51.2 m, to store a projected 60 Mt of tailings. Currently, Stage 6 South, South-

[*] Corresponding author: Chea Shanghai
E-mail: *haichea526@gmail.com;* Tel: *+66 93 380 7464*

east and Western embankment were constructed with maximum height of approximately 37 m.

After finished each stage of the raising, several of prism base were installed at regular intervals along the upstream side of the TSF embankment crest. Each prism will be monitored for movement at regular intervals as outlined in the monitoring program. Once a month, in situ geodetic surveying is used to get the deformation results. Any displacement of the embankment which is considered excessive or ongoing may consider as an early warning or indicate embankment stability problems [2]. The monthly monitoring of prism bases along the TSF embankment, while essential for tracking deformation, may not provide timely early warnings of instability due to potential limitations in frequency of measurement. Furthermore, this approach may also miss critical movements occurring in other areas of the storage facility, such as the slopes or downstream toe, which could indicate stability issues.

Regarding the limitation of the above approach, several studies and techniques have been conducted to monitor and provide early warning for embankment stability problems because they are essential for timely and effective emergency response. Those techniques include Interferometric Synthetic Aperture Radar (InSAR). InSAR is an advanced remote sensing technique. InSAR has been utilized to detect and measure millimetric levels of ground deformation. InSAR refers to the processing chains of algorithms used to predict ground movement based on SAR acquisition phase differences, while SAR data refers to raw satellite data [3]. With the advantages of a wide monitoring range, high accuracy, and less measurement frequency, the satellite-based time-series InSAR technology has become an effective tool for monitoring the infrastructure [4]. Despite its advantages, InSAR faces several significant challenges that can impede accurate measurements. These challenges include atmospheric disturbances that introduce phase errors, temporal decorrelation arising from changes in land cover between radar acquisitions, and noise from urban environments that may obscure subtle deformation signals [5].

This work focuses on enhancing the effectiveness of (InSAR) technology in detecting and monitoring ground deformation associated with tailings storage facility no.2 of Chatree Gold Mine, Thailand by utilizing Small Baseline Subset InSAR (SBAS-InSAR) time-series analysis. The results of SBAS-InSAR time-series analysis and existing in situ geodetic data were evaluated, thereafter compared to validated the results and assess the characteristics of the ground deformation.

2. OVERVIEW OF THE TARGET GOLD MINE AND MEASUREMENT TECHNIQUES

2.1 Study Area

The project site is situated approximately 280 km north of Bangkok, Thailand. The location of the project site and the general layout of the site are illustrated in Fig. 1. In general, TSF No.2 is located to the west of the existing tailings facility, TSF No.1 and southwest of the plant site. The general topography slopes gently to the south-west with an overall average gradient of about 1%. There are no significant defined watercourses in the immediate vicinity of the site [2].

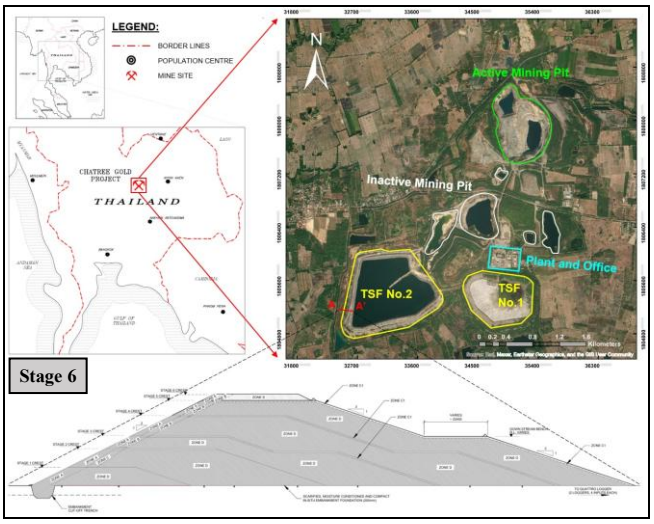

Fig. 1. Location and layout of the project site. The yellow box identifies the tailings storage facility. A-A' is a cross section of TSF No.2's embankment.

2.2 In Situ Geodetic Surveying

Accurate measurements of structural deformations are vital for assessing the safety and stability of a structure. Ground surveying is an effective technique for monitoring these deformations [6]. The precision and accuracy of measurements rely on the effectiveness of the surveying technique used. One precision method available is the reflector (or prism) total station. The 10 settlement pins were installed at regular intervals along the upstream side of the tailings storage facility (TSF) embankment crest to monitor the deformation of the Chatree Gold Mine's TSF No. 2 on a monthly basis, as shown in Fig. 2. These deformations represent the vertical displacements recorded on the top of the embankment's crest.

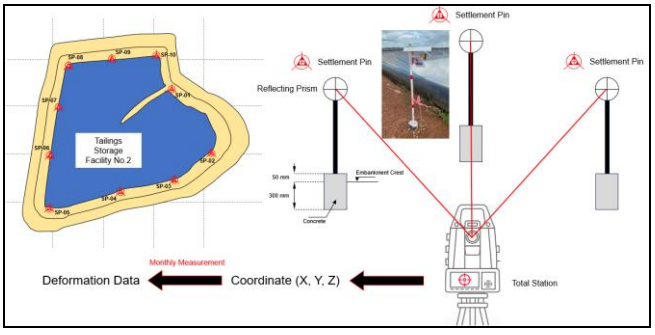

Fig. 2. Tailings storage facility no.2 deformation monitoring

2.3 Sentinel-1 SAR Dataset

This work utilizes unwrapped interferograms from the Sentinel-1 satellite's InSAR stack over the Chatree Gold Mine's TSF No.2. Launched on April 3, 2014, this satellite utilizes interferometric C-band SAR data, enhancing data acquisition capabilities and significantly boosting deformation monitoring potential. Sentinel-1 captures images over an area of 250 by 180 km with a standard revisit cycle of 12 days in its Interferometric Wide Swath mode. The data type used is Single Look Complex (SLC), with an Interferometric Wide (IW) data mode, VV+VH polarization, generated interferograms by using SBAS method, 300 m maximum spatial and 60 days temporal baselines, look resolution of 10x2 and a coherence mask threshold of 0.6 in the period from June 2016 until May 2019 were obtained from the following website https://search.asf.alaska.edu/#/.

This study preliminary collected 646 SAR images from June 1, 2016 to May 24, 2019. The images were acquired by the S1 ascending satellite, whose flight is from south to north. Time gap between each successive images are 12 and 60 days, respectively. All interferometric pairs have a perpendicular baseline 800 m, as shown in Fig. 3.

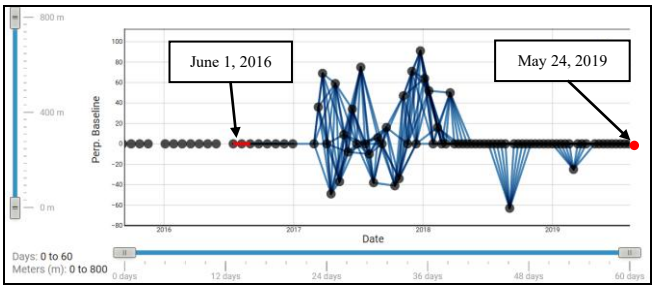

Fig. 3. Sentinel-1 SAR Dataset

2.4 Interferometric Synthetic Aperture Radar (InSAR)

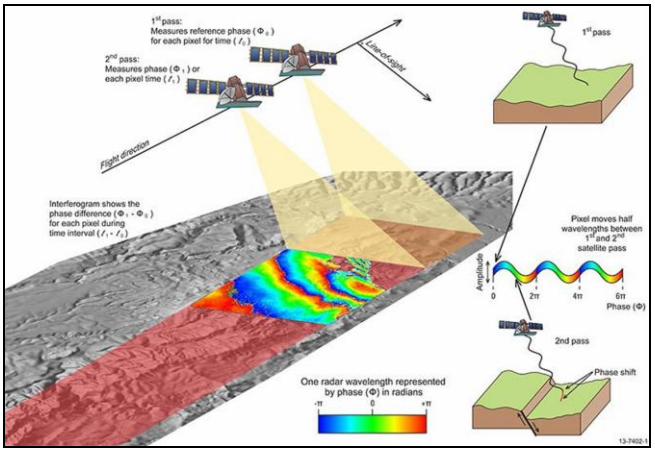

Fig. 4. Two SAR images of the same area are acquired at different times recording (www.ga.gov.au)

Interferometry is a technique that examines the interference patterns created by electromagnetic waves from two or more perspectives to gather information about the sources or the differences in their path lengths. In the context of InSAR, this involves generating an interference pattern from two complex SAR images and analyzing the phase difference between them, which can be collected from different positions or times, or a combination of both (Fig. 4) [5].

Interferometry is a technique that examines the interference patterns created by electromagnetic waves from two or more perspectives to gather information about the sources or the differences in their path lengths. In the context of InSAR, this involves generating an interference pattern from two complex SAR images and analyzing the phase difference between them, which can be collected from different positions or times, or a combination of both (Fig. 4) [5].

Before generating a SAR interferogram, various SAR images must undergo processing. In brief, this involves importing the raw data, eliminating unnecessary phase components, and coregistering the images to ensure that the pixels from one image align with those of the other. Instead of relying on only two images to detect surface displacement, it is now feasible to use a time series of multiple images over time, known as multi-interferometry.

2.4.1 Small Baseline Subset Interferometric Synthetic Aperture Radar (SBAS-InSAR)

Small Baseline Subset Interferometric Synthetic Aperture Radar (SBAS-InSAR) is one category of Time-series In-SAR method. Time-Series InSAR is an InSAR data analysis technique that takes a large number of InSAR data sets, which are obtained from collecting SAR images, and analyzes them to show the changes in the area over a period of time. For Small Baseline (SB), rather than using a single master scene as a reference for the interferograms; pairs of collected images produce multiple interferograms in a sequential manner. This approach focuses on averaging and comparing baseline interferograms instead of relying solely on point-wise coherent scatterers. It leverages a distributed scattering mechanism and is most effective in natural environments with limited strong scatter points [7].

SBAS-InSAR Algorithm

The original N+1 SAR images of a designated area produce (M) unwrapping interferograms under the assumption that the spatio-temporal baseline remains within a specific range. Points with an average phase coherence above a certain threshold are classified as high-coherence points. The unwrapped phase of a high-coherence points *(x,r)* in the *i-th* unwrapping interferogram corresponding to two moments t_1 and t_2 is represented as follows [8]:

$$\delta\phi_j(x,r) = \phi(t_2,x,r) - \phi(t_1,x,r) \approx \frac{4\pi}{\lambda}[d(t_2,x,r) - d(t_1,x,r)] \quad \text{(Eq. 1)}$$

where $\phi(t_2,x,r)$ and $\phi(t_1,x,r)$ represent as the phases of the two images involved in the interferogram generation and $d(t_2,x,r)$ and $d(t_1,x,r)$ represent the cumulative displacement of the radar line of sight (LOS) at t_1 and t_2 relative to the starting time. After eliminating the residual elevation phase, the phase is resolved to determine the velocity term. The parameters to be resolved are as follows:

$$v = \left[v_1 = \frac{\phi(t_1,x,r)}{t_1 - t_0}, \ldots . v_n = \frac{\phi(t_n,x,r) - \phi(t_{n-1},x,r)}{t_n - t_{n-1}}\right] \quad \text{(Eq. 2)}$$

The phase of the *i-th* unwrapping interferogram can be expressed as:

$$\sum_{t_{1,i+1}}^{t_2,j} (t_k - t_{k-1})v_k = \delta\phi_j \qquad \text{(Eq. 3)}$$

The phases of all interferograms are represented in the aforementioned equations. The aggregated expressions are shown in the error equation as:

$$Bv = \delta\phi \qquad \text{(Eq. 4)}$$

where B represents M x N matrix. In the case of a single interferogram subset, the least-squares approach can be employed to compute the deformation rate. However, when multiple interferogram subsets are established, the singular value decomposition method, along with minimum norm conditions, should be applied to derive the deformation rate.

3. METHODOLOGY

Small Baseline Subset Interferometric Synthetic Aperture Radar (SBAS-InSAR) time series analysis is used for this study (Fig. 5). The deformation rates (mm/year) obtained from the SBAS-InSAR time series are compared with results from in situ geodetic surveys, ensuring a thorough validation of the methodology. Sentinel-1 satellite interferograms, Global Atmospheric Models (GAMs), and Digital Elevation Models (DEMs) are among the data needed for this work.

3.1 Processing Workflow

The deformation velocity map is generated through the comprehensive workflow depicted in Fig. 5. This processing methodology, implemented in Python by utilizing the MintPy software (https://github.com/insarlab/MintPy).

The processing workflow consists of two main sections: (i) correction unwrapping errors and inversion for the time series' raw phases (blue rectangles in Fig. 5), and (ii) correction for phase causes from different sources to obtain the time-series displacement (green rectangles in Fig. 5) [9].

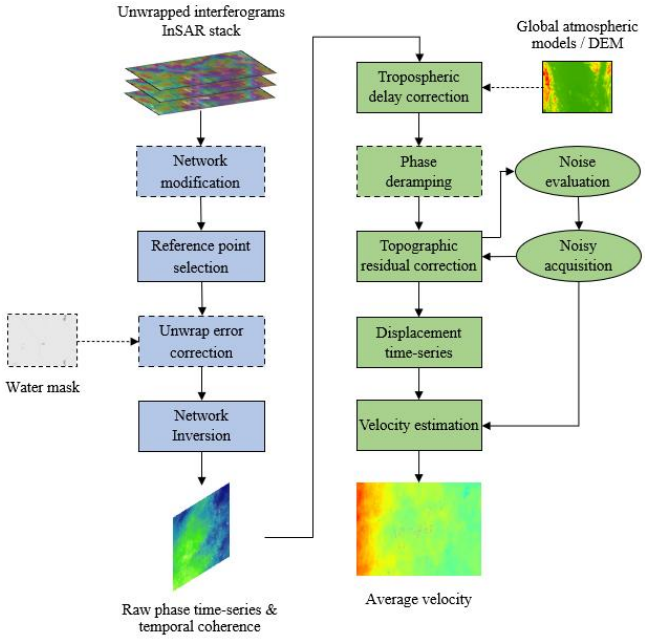

Fig. 5. SBAS-InSAR Processing workflow

3.1.1 Stack of unwrapped interferograms

A collection of phase-unwrapped interferograms, synchronized to a uniform SAR acquisition and adjusted for Earth's curvature and topography. In this process, interferograms created with GAMMA from the website https://search.asf.alaska.edu/#/ have been used.

3.1.2 Network modification

The software offers a network modification tool to eliminate outliers influenced by coherent pixels with unwrapping errors, excluding interferograms when the spatially averaged coherence in a specified area drops below a predetermined threshold. This method is similar to the approach outlined by [10].

3.1.3 Reference point selection

The reference pixel is typically selected either through random sampling in regions exhibiting high average spatial coherence (defaulting to 0.85) or based on prior knowledge of the study area. The selection process aims to ensure that the chosen pixel satisfies several key criteria: (i) it is located within a region of coherent spatial patterns, (ii) it avoids areas with significant atmospheric anomalies such as ionospheric streaks, and (iii) it is situated at a similar elevation to the region of

interest to minimize the effects of spatially correlated atmospheric delays.

3.1.4 Unwrapping error correction

Three distinct methodologies are commonly employed for the detection and correction of unwrapping errors within an interferogram stack. The first, bridging, is especially useful for errors in regions with islands or steep topography. The second method employs phase closure and is effective within a dense network of interferograms. Both methods operate efficiently at the regional scale. The third approach combines bridging and phase closure, addressing errors in both spatial and temporal domains.

3.1.5 Network inversion

This step involves inverting the network of interferograms to obtain the raw phase time-series. It is important to note that this raw phase time-series encompasses contributions from ground deformation, atmospheric delay, and residual topographic effects resulting from DEM errors. The following weighted least squares (WLS) inversion methods are available: Inverse of covariance, Finisher Information Matrix (FIM), Spatial coherence, and Uniform / no weighting.

3.1.6 Tropospheric delay correction

Tropospheric delay in InSAR occurs due to the propagation of radar signals through the Earth's atmosphere. As the radar waves travel, they are affected by changes in atmospheric pressure, temperature, and humidity, causing delays in the signal's travel time. The approach utilizes Global Atmospheric Models (GAMs) to derive estimations of tropospheric delay. This step ensures that the final displacement estimates are not influenced by atmospheric distortions.

3.1.7 Phase deramping

Phase ramps, which may result from residual tropospheric and ionospheric delays, along with some contribution from orbital inaccuracies, are commonly encountered in interferometric data. For deformation signals characterized by long spatial wavelengths, such as interseismic deformation, retaining these ramps is generally appropriate. In such cases, ionospheric delays can be addressed through physical and statistical correction methods [11]; [12]; [13] and measurement uncertainties can be assessed [14], [15]. However, for signals with short spatial wavelengths, as those associated with volcanic activity, landslides, or urban subsidence, it is typically recommended to estimate and remove linear/quadratic ramps from the displacement time series to ensure the reliability of the pixel-level measurements at each acquisition.

3.1.8 Topographic residual correction

The systematic topographic phase residual, which results from errors in the Digital Elevation Model (DEM), is estimated by its proportional relationship to the time-series of the perpendicular baseline [16]. Accurate matching of the processed DEM to the actual topography is essential.

3.1.9 Residual phase for noise evaluation

Calculating the Root Mean Square (RMS) for residual phase time-series for each acquisition is needed to exclude the identified noisy acquisitions automatically. Following that, it: (1) chooses the date with the lowest RMS value as the ideal reference date and (2) identifies the noisy acquisitions with RMS values exceeding the outlier detection threshold.

3.1.10 Average velocity estimation

The average velocity v is estimated as the slope and standard deviation of the line that best fits the displacement time series, as represented by:

$$\phi_{dis}^{i}.\lambda/(-4\pi) = v.t_i + c, i = 1, \dots, N_{,,} \quad \text{(Eq. 5)}$$

where c is an unknown constant offset. By default, noisy SAR acquisitions are excluded during the estimation process.

3.2 Validation with In Situ Geodetic Surveying

The deformation velocity map from SBAS-InSAR time-series is extracted via MATLAB software and using Open-Source Geographic Information System to displays the measurement points and makes it easy to retrieve information on where the significant deformation occurred. All measurement points were utilized in accordance with the locations of the prisms positioned around the embankment crest. Both InSAR and in situ measurement time-series shall be aligned. After ensuring both datasets are georeferenced to the same coordinate system and the same time-series, the deformation data can be statistically analyzed and visualized to assess relationships and discrepancies.

4. RESULTS AND DISCUSSION

The deformation velocity map presented in Fig. 6 illustrates the rate of surface deformation from June 2016 to May 2019, with values ranging from -63 mm/year to 28 mm/year. Negative values (-) indicate downward movement of the ground, while positive values (+) denote ground uplift. The deformation data, derived from SBAS-InSAR processing, provides insight into the spatial and temporal patterns of vertical deformation within the study area, particularly with regard to the movement of the TSF No.2.

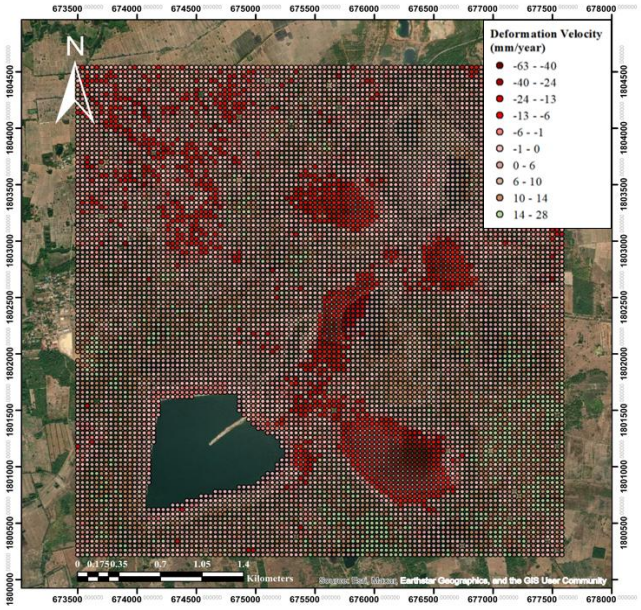

Fig. 6. Deformation velocity map from June 2016 to May 2019

We zoomed in on the location deformation at different rates in Fig. 7. As expected, varying degrees of ground deformation were observed within the area of TSF No. 2, particularly at the survey points. The data indicated that the ground experienced downward deformation at different rates.

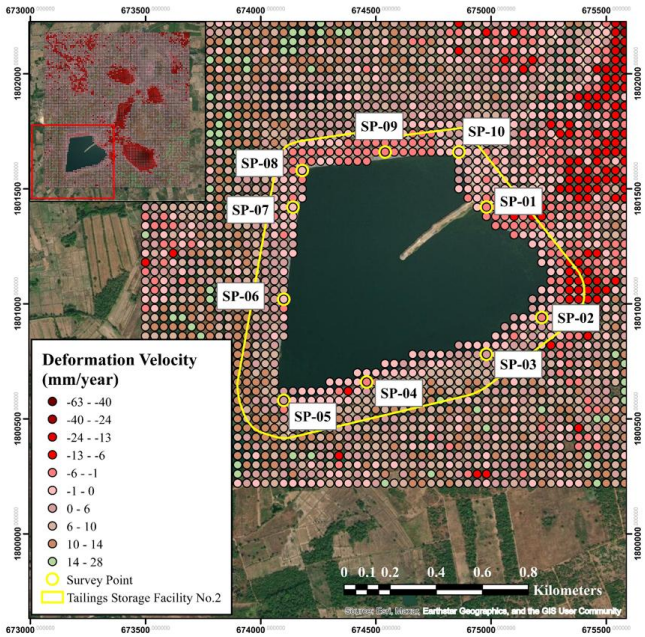

Fig. 7. Deformation velocity map showing SP-01, SP-01, SP-03, SP-04, SP-05, SP-06, SP-07, SP-08, SP-09, and SP-10's location

4.1 Validation of InSAR estimated vertical deformations

In estimating the time series of vertical deformation, the reference date was set as the starting point (value of 0 for Fig. 8(a) to (j)) for both InSAR and in situ geodetic measurements. This study compares results from SBAS-InSAR processing with in situ geodetic surveying data, including vertical deformation rates and time series for the ten selected survey points, to assess the reliability of the InSAR-derived measurements. As shown in Fig. 8(a) to (j), the vertical deformation times-series plot of InSAR and geodetic shows a good correlation. For a cross-comparison was conducted between InSAR and in situ geodetic data through linear regression analysis (Fig. 9). The deformation rates from both in situ geodetic and InSAR measurements demonstrate strong agreement, with an R^2 value of 0.7858 and root mean square (RMS) errors for InSAR measurements at the survey points from #01 to #10 at 11.98 mm. These results indicate that the SBAS-InSAR technique provides a reliable and effective method for extracting ground deformation information. Additionally, due to the relatively low observation frequency of geodetic surveys (conducted monthly), compared to the high temporal resolution of the spaceborne SAR system (with a 12-day revisit interval), it is not feasible to capture the detailed deformation process across the entire study period. Due restricting our capacity to do an equitable comparison across all methodologies, we recommend that future comparison exercises be conducted frequently, with precise specification of the time period, acquisition dates, and acquisition geometries in each instance.

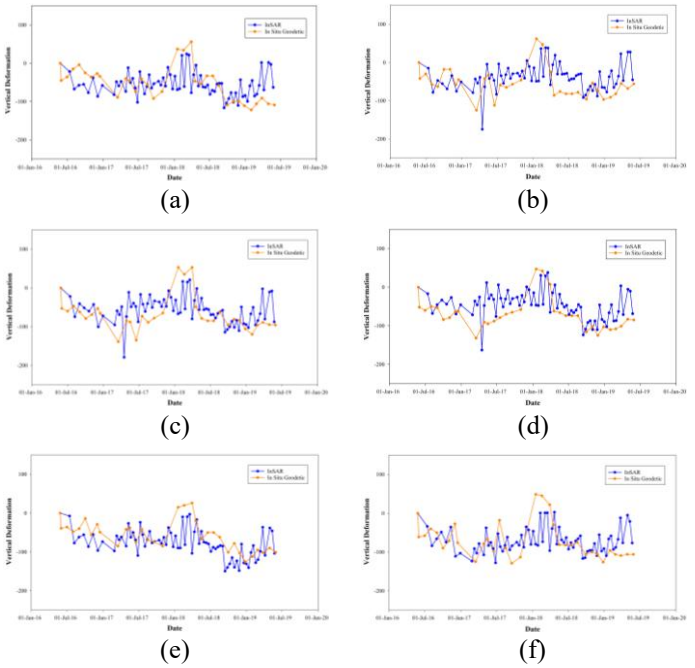

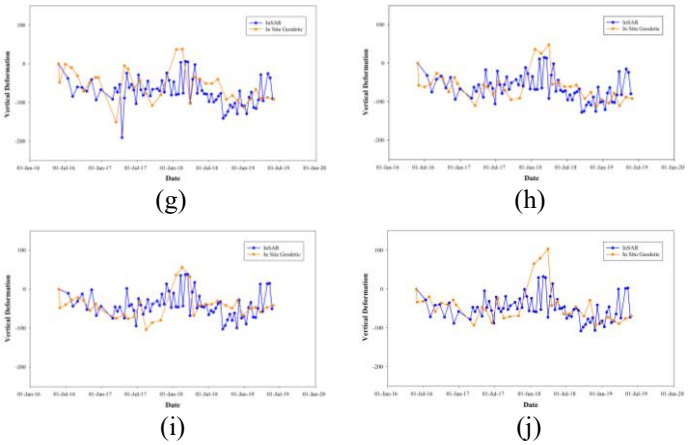

Fig. 8. Vertical deformation time series plot of ten InSAR and in situ geodetic points uses the first common date (01/June/2016) as a reference in time, (a) SP-01; (b) SP-02; (c) SP-03; (d) SP-04; (e) SP-05; (f) SP-06; (g) SP-07; (h) SP-08; (i) SP-09; (j) SP-10

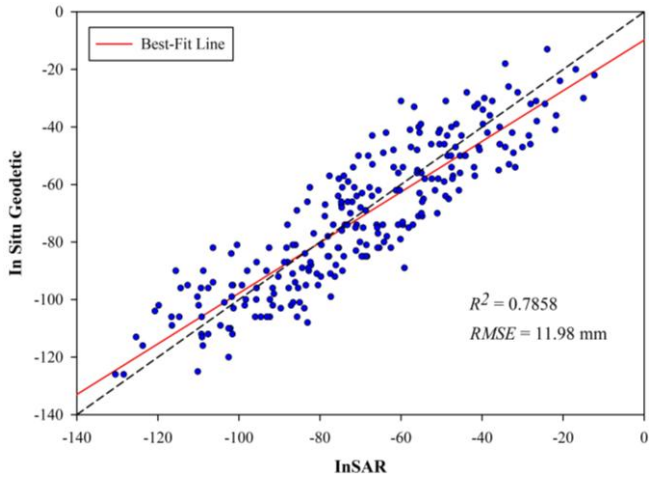

Fig. 9. Comparison between InSAR and In Situ Geodetic using representative data from all ten points

5. CONCLUSIONS

This study provides a comprehensive assessment of the surface deformation patterns at Tailings Storage Facility (TSF) No. 2 from June 2016 to May 2019, utilizing SBAS-InSAR processing to track vertical ground deformation. The deformation velocity map revealed a range of deformation rates from -63 mm/year (indicating settlement) to +28 mm/year (indicating uplift), with significant variation observed across the facility. Comparison between InSAR and in situ geodetic surveying data demonstrated good correlation and agreement, with an R^2 value of 0.7858 and a root mean square (RMS) error of 11.98 mm, confirming the reliability and effectiveness of the SBAS-InSAR technique in tailings storage facility monitoring deformation. The findings are anticipated to make a significant contribution to the enhancement of monitoring practices and risk management strategies for tailings storage facilities (TSFs). We also offered some recommendations derived from our comparison results that may be valuable for future InSAR applications and validation processes.

Considering that deformation may continue as long as operations are ongoing, regular inspections and maintenance of the facility are crucial for identifying early signs of issues such as cracks, leaks, and erosion. If left unaddressed, these issues could lead to more significant deformation over time.

In the future research, integrating Finite Element Modeling (FEM) with InSAR data should be focused to predict the mechanical behavior of the Tailings Storage Facility (TSF). This integration would create more accurate models to understand TSF responses to material properties, loading, and external forces, helping identify potential failure points and refine risk assessments. Additionally, long-term monitoring beyond the 2016-2019 period should be conducted to provide insights into how deformation evolves capturing seasonal variations and the cumulative effects of mining operation, weather, and other factors on TSF stability.

ACKNOWLEDGMENTS

The authors would like to thank the financial support from the scholarship program for ASEAN or Non–ASEAN Countries supported by Chulalongkorn University. Also, the authors would like to acknowledge the Alaska Satellite Facility (ASF) for providing the InSAR Sentinel-1 product, the Copernicus Climate Data Store (CDS) for providing ERA5 data, and Akara Resources Public Company Limited for providing the in situ geodetic surveying data.

REFERENCES

[1] Akara Mine, "Environmental impact Assessment Chatree Gold project," Document 1999, vol. 2.

[2] Knight Piésold Pty Limited, "CHATREE GOLD PROJECT: TAILINGS STORAGE FACILITY No. 2 FINAL DESIGN," 2011.

[3] M. Bayaraa, B. Sheil, and C. Rossi, "InSAR and numerical modelling for tailings dam monitoring – the Cadia failure case study," *Géotechnique,* vol. 74, no. 10, pp. 985-1003, 2024, doi: 10.1680/jgeot.21.00399.

[4] L. Clarkson, D. Williams, and J. Seppälä, "Real-time monitoring of tailings dams," *Georisk: Assessment and Management of Risk for Engineered Systems and Geohazards,* vol. 15, no. 2, pp. 113-127, 2021/04/03 2021, doi: 10.1080/17499518.2020.1740280.

[5] M. Simons and P. Rosen, "Interferometric Synthetic Aperture Radar Geodesy," *Treatise on Geophysics,* pp. 339-385, 2015.

[6] Z. Zeidan, A. A. E. Beshr, and S. M. Sameh, "Precision Comparison and Analysis of Reflector-less Total Station Observations," *MEJ-Mansoura Engineering Journal,* vol. 40, no. 5, pp. 86-97, 2021.

[7] A. Ferretti, A. Rucci, A. Tamburini, S. Del Conte, and S. Cespa, "Advanced InSAR for reservoir geomechanical analysis," in *EAGE Workshop on Geomechanics in the Oil and Gas Industry*, 2014: European Association of Geoscientists & Engineers, pp. cp-397-00016.

[8] P. Berardino, G. Fornaro, R. Lanari, and E. Sansosti, "A new algorithm for surface deformation monitoring based on small baseline differential SAR interferograms," *IEEE Transactions on geoscience and remote sensing,* vol. 40, no. 11, pp. 2375-2383, 2002.

[9] Z. Yunjun, H. Fattahi, and F. Amelung, "Small baseline InSAR time series analysis: Unwrapping error correction and noise reduction," *Computers & Geosciences,* vol. 133, p. 104331, 2019.

[10] E. Chaussard *et al.*, "Potential for larger earthquakes in the East San Francisco Bay Area due to the direct connection between the Hayward and Calaveras Faults," *Geophysical Research Letters,* vol. 42, no. 8, pp. 2734-2741, 2015.

[11] H. Fattahi, M. Simons, and P. Agram, "InSAR time-series estimation of the ionospheric phase delay: An extension of the split range-spectrum technique," *IEEE Transactions on Geoscience and Remote Sensing,* vol. 55, no. 10, pp. 5984-5996, 2017.

[12] G. Gomba, A. Parizzi, F. De Zan, M. Eineder, and R. Bamler, "Toward operational compensation of ionospheric effects in SAR interferograms: The split-spectrum method," *IEEE Transactions on Geoscience and Remote Sensing,* vol. 54, no. 3, pp. 1446-1461, 2015.

[13] C. Liang, Z. Liu, E. J. Fielding, and R. Bürgmann, "InSAR time series analysis of L-band wide-swath SAR data acquired by ALOS-2," *IEEE Transactions on Geoscience and Remote Sensing,* vol. 56, no. 8, pp. 4492-4506, 2018.

[14] H. Fattahi and F. Amelung, "InSAR uncertainty due to orbital errors," *Geophysical Journal International,* vol. 199, no. 1, pp. 549-560, 2014, doi: 10.1093/gji/ggu276.

[15] H. Fattahi and F. Amelung, "InSAR bias and uncertainty due to the systematic and stochastic tropospheric delay," *Journal of Geophysical Research: Solid Earth,* vol. 120, no. 12, pp. 8758-8773, 2015.

[16] H. Fattahi and F. Amelung, "DEM error correction in InSAR time series," *IEEE Transactions on Geoscience and Remote Sensing,* vol. 51, no. 7, pp. 4249-4259, 2013.

Techno-Science Research Journal V13 (Special Issue) (2025) P 72-76

Content list available at ITC

Techno-Science Research Journal

Journal Homepage: www.ric.itc.edu.kh

Techno-Science Research Journal

The Characteristics of Radon Migration in Overburden of Gob Mine with Spontaneous Combustion

Zhiyu Zhang[1,*], Hemeng Zhang[1,2,3], Pengcheng Wang[1], Xiaoying Liu[1,2,3], Yongjun Wang[1,2,3]

[1] *College of Safety Science and Engineering, Liaoning Technical University, Huludao, China*
[2] *Key Laboratory of Mine Thermodynamic Disasters and Control of Ministry of Education, Huludao, China*
[3] *Institute of Engineering and Environment, Huludao 125105, China*

Received: 1 November 2024; Revised: 1 January 2025; Accepted: 20 June 2025; Available online: October 2025

Abstract: *Coal spontaneous combustion in underground coal mines is difficult to detect. Surface radon detection has the advantages of simple operation and low cost. It is necessary to study the mechanism of radon generation from spontaneous combustion of loose coal and the migration law, which can provide a theoretical basis for retrieving the range of underground fire zones. In this study, the closed radon accumulation test (CRAT) is built to investigate the radon generation characteristics under different constant temperatures and combined with numerical simulation to study the radon migration of underground coal fire. CRAT was conducted under different thermostatic conditions, and the wavelet analysis was applied to get the accumulation function of radon concentration and the radon release rate. It was found that temperature is positively correlated with the radon generation rate. Then, construct the radon migration model of spontaneous coal combustion in the 2D mining area, exploring the effect of coal combustion temperature on the radon migration and surface response. The results show that the higher the fissure thickness, the higher the radon concentration at the surface.*

Keywords: Coal spontaneous combustion; Numerical simulation; Radon migration; Radon generation

1. INTRODUCTION

Spontaneous coal combustion in underground coal mines and shallow buried coal seams is characterized by strong concealment, high danger and difficulty in extinguishing fires. Especially, the location of the fire source cannot be accurately determined, which will increase the difficulty and complexity of the prevention and control of spontaneous coal combustion. Therefore, the key to managing spontaneous coal combustion lies in the accurate detection of the location of the fire source[1].

In recent years, surface radon detection has been widely used to detect underground coal fires. Liu[2] built a simulation experiment system of coal spontaneous combustion in the leftover coal mining area and analyzed the influence law of radon generation and migration in different overlying mining area states and different factors of the airspace above the mining area. Fei et al[3] clarified the location and scope of the coal-fire zone in the Liujiaxuan coal mine, using the radon method. The results show that there are 14 abnormal areas of radon gas concentration in the detection area. Zhou et al[4]took a small abandoned coal mine in Shanxi Province as the research object and used the surface isotope radon method to identify the spontaneous combustion zone, verified by the detection results with the drilling temperature measurement.

In this study, taking the loose coal pile as the research object, the radon generation and migration mechanism theories are investigated through the closed radon accumulation test and numerical simulation. 8 levels of temperature were applied in the test to study the effect of temperature on radon generation. The numerical simulation was applied to explore the radon migration law of underground coal fire. This study makes the surface isotope radon detection technology more accurate. It is expected to provide some help for the safety of the coal mine production.

2. RADON GENERATION EXPERIMENT

2.1 Materials and method

[*] Corresponding author: Zhang Zhiyu
E-mail:*zzy63992023@163.com;* Tel*: +86 13204246399*

To explore the law of radon generation during different temperatures, the closed radon accumulation test (CRAT) was designed (Figure 1), which consists of a temperature control cabinet, reaction tank, condenser, drying pipe, hot oven, flowmeter, Rad7 radon detector, and preheating pipe.

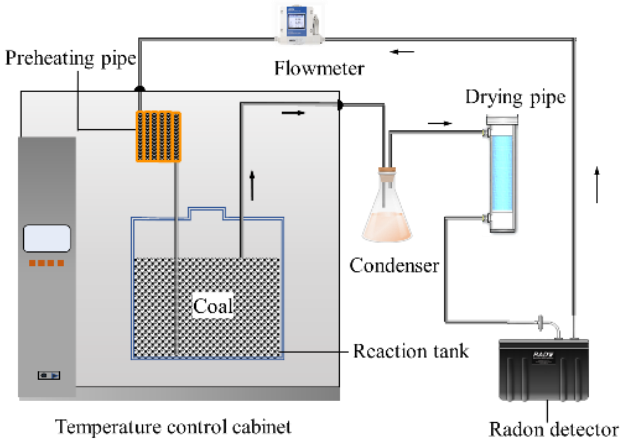

Fig 1 Experimental device of closed radon accumulation test (CRAT)

The coal sample with a mass of 2000 g was placed in the reaction tank, which was then placed in a constant temperature oven. Set the temperature of the hot oven at 30 ℃. Once it reaches the setting temperature, run the radon detector to check the radon concentration. The RAD7 radon detector has a built-in air pump. The circulating gas flow rate is adjusted to 120 ml/min by controlling the flowmeter. During the measurement, the RAD7 radon meter was set to Sniff mode for 60 cycles of continuous monitoring (5 min for each cycle), amounting to 300 min. CRATs were repeated by adjusting the oven temperatures to 60 ℃, 90 ℃, 120 ℃, 150 ℃, 180 ℃, 230 ℃, and 280 ℃, respectively. The curves between radon concentration and time were obtained for later analysis.

2.2 Experimental results

Figure 2 shows the curves of radon concentration under different temperatures (30 ℃, 60 ℃, 90 ℃, 120 ℃, 150 ℃, 180 ℃, 230 ℃, 280 ℃). It can be found that the variation of radon concentration at the same temperature fluctuates over a wide range. It is due to the influences of radioactive decay and noise interference. However, it can still be seen that when the ambient temperature is ≤230 ℃, the cumulative concentration of radon gas shows a tendency to increase and then keep stable.

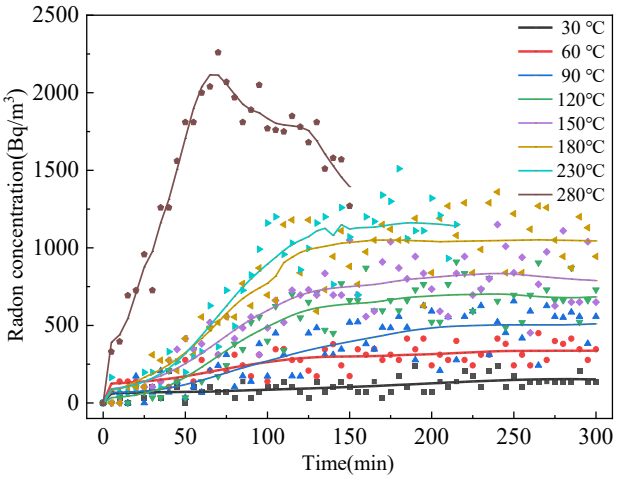

Fig 2 The curves of radon concentration under different constant temperature conditions

However, when the oven temperature is 280 ℃, the cumulative radon gas concentration shows a tendency of increasing and then decrease. Compared with the measured radon concentration curves, the radon concentration curve after noise reduction treatment has less fluctuation and presents a more obvious pattern.

In order to characterize the radon generation rate from the coal under different temperatures, the phase of linear increase of radon concentration with time is generally taken as the object. Equation (1) was applied to fit the data in Figure 2:

$$\alpha = \frac{V}{Mt}(C - C_0) \quad (1)$$

Where:

V = experimental system space volume (m^3)
M =sample quantity (kg)
t = cumulative time (s)
C = radon accumulation concentration (Bq/m^3)
C_0 = radon concentration in the tank, when t=0 (Bq/m^3)

The radon generation rate of coal at different temperatures was thus calculated by the fitting curve. The radon generation rate change curves under different temperatures conditions are shown in Figure 3. It can be seen in the figure that the radon generation rate of coal samples exponentially increased with the increase of temperature. It is because the coal is broken due to the increase in temperature, and radon gas escapes from the closed pores. The exponential fitting formula in Figure 3 can be applied to the radon generation source term in subsequent simulations, S in Equation (7)

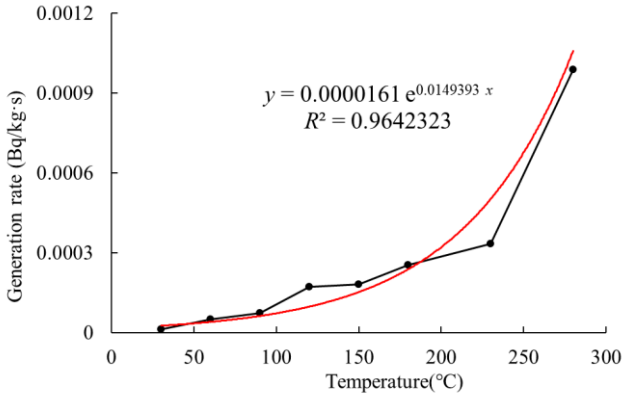

Fig 3 Changes of radon generation rate of different temperatures

3. MODEL OF RADON MIGRATION

3.1 Governing equations

In the numerical simulation, the parameters are solved by establishing the control equations, imposing the boundary and initial conditions, and applying the finite element method. Continuity equation:

$$\frac{\partial \rho}{\partial t} + \nabla \cdot (\rho v) = 0 \tag{2}$$

Continuity equations in coal, rock, soil, and fissure:

$$\frac{\partial}{\partial t}(\varepsilon \rho) + \nabla \cdot (\rho u) = 0 \tag{3}$$

$$d_f \frac{\partial}{\partial t}(\varepsilon_f \rho) + \nabla \cdot (d_f \rho u) = 0 \tag{4}$$

According to Darcy's law, momentum equation:

$$u = -\frac{k}{\mu}\nabla p \tag{5}$$

where:k is the permeability of fissures in rock, coal seams, collapse zones, fracture zones, flexural zones, soils, and fissures. Fissure permeability(k_f) is considered by the following equation:

$$k_f = \frac{d_f^2}{12} \tag{6}$$

Species mass transfer conservation equation

$$\frac{\partial(\varepsilon c)}{\partial t} + u\nabla c = \nabla(D_e \nabla c) + S \tag{7}$$

Species mass transfer conservation equation in fissure

$$d_f \frac{\partial(\varepsilon_f c)}{\partial t} + d_f u\nabla c = \nabla(d_f D_e \nabla c) + d_f S \tag{8}$$

D_e is the effective diffusion coefficient which can be calculated by Equation (9)

$$D_e = \frac{\varepsilon}{\tau} D \tag{9}$$

Where:
C = radon concentration (Bq/m^3)
ρ = density (kg/m^3)
v = speed (m/s)
u = is darcy speed (m/s)
d_f = is fissure thickness (m)
p = is pressure (Pa)
μ = dynamic viscosity coefficient (Pa·s)
k = permeability (m^2)
S = gas source (mol/(m^2·s))
D = diffusion coefficient of gas (m^2/s)
ε = porosity
τ = tortuosity

3.2 Physical model

As shown in Figure 4, the gob (width L=160 m, height H_1=3 m) is located in the middle area at the bottom of the geometric model. The overlying medium of the extraction zone consists of four zones: collapse zone (H_2=20 m), fracture zone (H_3=50 m), bending zone (H_4=40 m), and soil layer (H_5=5 m). Five vertical fissures connected to the surface are set up above the extraction zone (the thickness of the fissure is d_f, and the height is H=H_2+H_3+H_4+H_5). The surrounding rock and soil layers (30 m in width), which were not affected by mining, were placed on both sides of the zone.

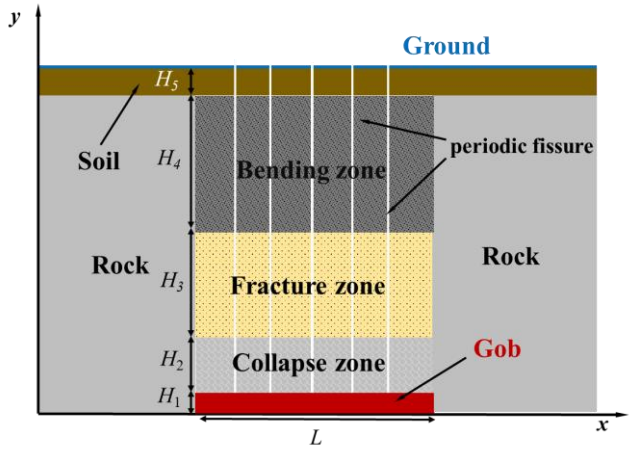

Fig 4 Physical model schematic

The fire-wind pressure generated by the high temperature of coal combustion drives the radon gas upward migration. Based on equation (10), the bottom boundary of the extraction zone is set as the pressure inlet, and the surface is the open boundary; the remaining boundary condition is the no-flux boundary. The initial seepage velocity within the model is 0, and the initial radon gas concentration is 0. The fire-wind pressure can be expressed as,

$$\Delta p = H(\rho_0 - \rho_s)g \quad (10)$$

Where:
ρ_0 = average density of the gas before spontaneous combustion (kg/m^3)
ρ_s = average density of the gas after spontaneous combustion (kg/m^3)
g = is the gravitational acceleration (m/s^2)

4. RESULTS AND ANALYSIS

4.1 Fissure thickness effects on radon migration in the gob

Figures 5, 6, and 7 show the radon distribution, surface radon concentration, and the seepage velocity in the middle fissure under different fissure thicknesses, respectively. In order to investigate the influence of the fissure thickness of the gob on radon migration, four different thicknesses (df=0.7 mm, 1 mm, 1.2 mm, 1.5 mm) are selected. The influence of fissure thickness on radon transport is mainly reflected in the following: the larger the fissure thickness is, the larger the fissure porosity and permeability are, and the smaller the gas flow resistance is compared with other regions of the model. The high-temperature environment is generated by spontaneous combustion of coal. The increase in the temperature also creates a significant pressure gradient between the gob and the surface, prompting rapid airflow in the vertical direction. The typical characteristics resulting in the thermal buoyancy (fire-wind pressure), and radon gas are firstly surged along the fissure to the ground surface under the drive of the pressure gradient.

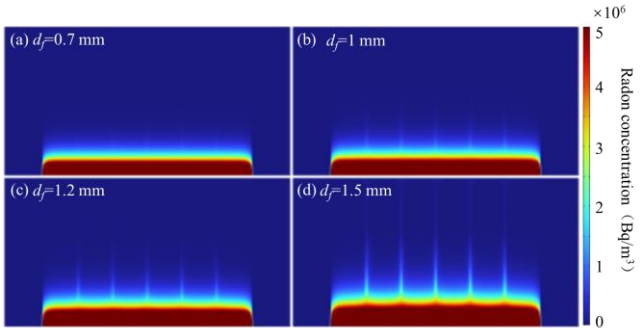

Fig 5 Radon distribution under different fissure thickness

As shown in Figure 5, the radon concentration in the area around the fissure is much higher than that in the area away from the fissure, and the radon gas concentration increases gradually as the thickness of the fissure increases. With the increase of the fissure thickness, the porosity and permeability of the fissure increase, which leads to an increase in the seepage rate. Therefore the high concentration of radon gas formed in the gob migrates to the surface along the fissure through convection. The maximum surface radon concentration values occurred in the center fissure, the maximum surface radon gas values of df=0.7 mm, 1 mm, 1.2 mm, 1.5 mm fissures are 10.926, 590.53, 5145, and 62007 Bq/m3, respectively. According to the data, there is a positive correlation between the thickness of the fissure and the maximum radon concentration at the surface, and when the thickness of the fissure is greater than 1.2 mm, the radon concentration at the surface will increase rapidly.

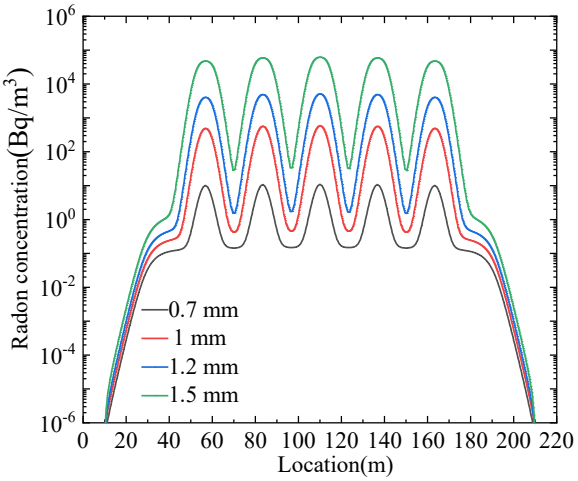

Fig 6 Surface radon distribution (logarithm)

As shown in Figure. 7, the average seepage velocities in the central fissure of the overlying rock layer in the mining zone with fissure thickness of df=0.7 mm, 1 mm, 1.2 mm, and 1.5 mm are 0.0195, 0.0397, 0.0572 and 0.0894 m/s, respectively, and there is a linear positive correlation between the average seepage velocities and the thickness of the fissures. Therefore, high concentrations of radon gas are evident around the fissure. When convection is dominant, the time for radon gas to be migrated from the underground fire zone to the surface is much smaller than the time required due to attenuation. It can be seen that the loss of radon gas caused by radioactive decay is almost negligible. However, in low-permeability areas, convection is weak, diffusion superior, radon gas migration time is long and radon gas concentration will be reduced by radioactive decay. This results in low radon concentration in non-fissure areas. The formation of the ‘peak shape’ is observed in Figures 5 and 6.

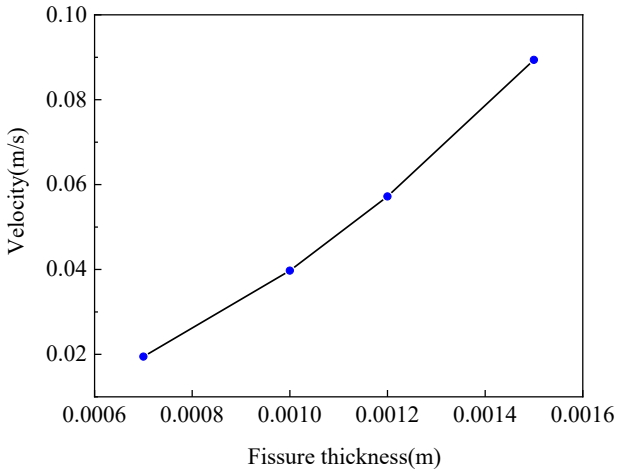

Fig 7 Seepage velocity in the middle fissure

5. CONCLUSIONS

The experimental system was built to test the radon gas accumulation concentration under different constant temperature conditions. The rate of radon generation from coal is exponentially positively correlated with temperature.

A 2D underground coal fire with a radon generation and migration model was constructed to study the effects of fissure thickness on radon response. The surface radon concentration is positively correlated with the fissure thickness, the larger the thickness, the more favorable to the migration of radon.

REFERENCES

[1] Z. Lu et al., “Study on the formation mechanism of a radon source during coal spontaneous combustion in a goaf,” Fuel, vol. 336, p. 127135, 2023.

[2] Liu B. (2022). Experimental simulation on radon precipitation law during spontaneous combustion of coal in goaf. Inner Mongolia: Inner Mongolia University of Science and Technology; 2022

[3] Fei J, Wen, H, et.al, Application of radon method in detection of fire area in the shallow coal seam,” Journal of Xi’an University of Science and Technology, vol. 38, no. 1, pp. 6–10, 2018.

[4] B. Zhou, J. Wu, J. Wang, and Y. Wu, “Surface-based radon detection to identify spontaneous combustion areas in small abandoned coal mine gobs Case study of a small coal mine in China,” Process Saf. Environ. Prot., vol. 119, pp. 223–232, 2018.

.

Techno-Science Research Journal V13 (Special Issue) (2025) P 77-83

Content list available at ITC

Techno-Science Research Journal

Journal Homepage: www.ric.itc.edu.kh

Techno-Science Research Journal

Evaluation of shear strength of porous volcanic soils in Hokkaido, Japan by in-situ cyclic direct shear tests

Akira Sato[1*], Hiroyuki Hashimoto[1], Kuwano Reiko[2]

[1] *Department of Civil Engineering, Graduate School of Engineering, The University of Tokyo, Japan*
[2] *Institute of Industrial Science, The University of Tokyo, Japan*

Received: 1 November 2024; Revised: 1 January 2025; Accepted: 20 June 2025; Available online: October 2025

Abstract: *Volcanic pumice soils are widely distributed in many countries. Mechanical properties of those need to be characterized since seismic ground motions can cause serious hazards such as large-scale slope failures and long-distance debris flows. Since volcanic pumice generally retains extremely high porosity and has a sensitive structure. The natural soil structure is easily broken during sampling or transportation. Therefore, it is preferable to conduct in-situ tests without disturbing the original structure of the soil. In this study, an in-situ cyclic direct shear test apparatus was developed and in-situ cyclic direct shear tests of volcanic pumice (Ta-d) were conducted. This pumice soils are considered to be the main cause of the slope failure of the thermocline caused by the 2018 Hokkaido earthquake. Laboratory cyclic direct shear tests were also conducted on Intact samples taken from the site.*

The results revealed that soil structure and the cyclic displacement have a significant effect on the cyclic shear strength and the transition of peak strength during cyclic shear. In order to evaluate the mechanical behavior of such susceptible soils, it is crucial to use specimens with as less disturbance as possible. We measured the cyclic shear strength of a highly susceptible volcanic pumice soil using a newly developed in-situ cyclic direct shear test apparatus.

Keywords: cyclic direct shear test, volcanic pumice soils, in-situ test

1. INTRODUCTION

Volcanic pumice soils are distributed in Japan and around the world and are known to cause large-scale slope failures [3]. For example, the 2018 Hokkaido earthquake caused numerous landslides on gentle slopes of pumice fall deposits, resulting in dozens of casualties [7]. The 2009 Padang earthquake in Sumatra, Indonesia, caused rapidly moving landslides in many locations occurred, killing hundreds of people [4,8]. However, the characteristics of volcanic pumice soils are not yet fully understood. Volcanic soils are generally composed of delicate, porous particles with a loose structure. Due to the nature of this soil structure, it can be easily damaged during sampling and transport, making it difficult to reproduce the original structure. Therefore, it is desirable to conduct the tests with the original soil structure intact.

In this study, a lightweight and compact cyclic direct shear test apparatus was developed and in-situ tests were conducted on volcanic pumice soils. The apparatus can be used for testing in areas inaccessible to vehicles and large heavy machinery. Using this apparatus, repeated direct shear tests were conducted at a slope failure site where volcanic pumice soils are believed to be the primary cause.

In this paper, we report on the relationship between the strength of the soil and the displacement amplitude of the cyclic direct shear test, and the amount of crushing by the direct shear test.

2. METHODOLOGY

2.1 In-situ direct shear test device

Fig. 1. shows a photograph of the in-situ cyclic direct shear test apparatus, which is a modified version of the in-situ shear test apparatus developed by Hashimoto et al. 2023 [10]. This apparatus was reported in A. Sato et al [11] and is intended to

[*] Corresponding author: *Akira Sato*
E-mail: sato-akira1225@g.ecc.u-tokyo.ac.jp; Tel: +81 90 3445 1516

reproduce in the field a direct shear test performed in the laboratory. Since it is not a common apparatus, a description of the apparatus is quoted below.

2.1.1 Components

The apparatus comprises a rigid frame that houses the specimen, a top lid, a jack for applying shear stress, a displacement transducer, a load cell, and a microcomputer unit. The frame is square with a base of 120 mm per side and is designed to enclose a specimen of 60 mm height. The fixture was 3D printed to simplify construction and reduce its weight. The device weighs around 7 kg and can be manually carried to the site of a slope failure in mountainous terrain. It is equipped with one displacement transducer and two load cells to measure horizontal displacement, horizontal load, and vertical load, respectively. The digital data is obtained and stored in real-time by a micro-controller unit. However, measuring vertical displacements is not possible due to the structure of the device.

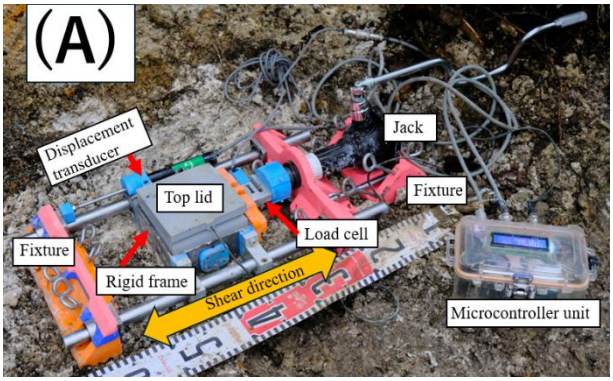

Fig. 1. In-situ test apparatus

2.1.2 Testing procedures

The procedure for in-situ direct shear tests is described below. First, the slope is excavated horizontally and a frame is installed on the shaped specimen. After the frame is installed, other parts are attached.

Vertical stress is applied by placing a weight on top of the specimen. It should be noted that vertical stress at the bottom of the specimen cannot be measured due to the structure of the equipment.

Shear stress is applied by manually rotating a rotary jack. The shear rate was 10 mm/min and data were recorded at 10 Hz.

After shearing, the crushed surface is checked to ensure that there are no large gravels on the crushed surface that could affect the test results. To compare the grain sizes, soil samples were taken from the soil near the shear surface and from soil that was at the same height as the shear surface but not involved in the shearing process.

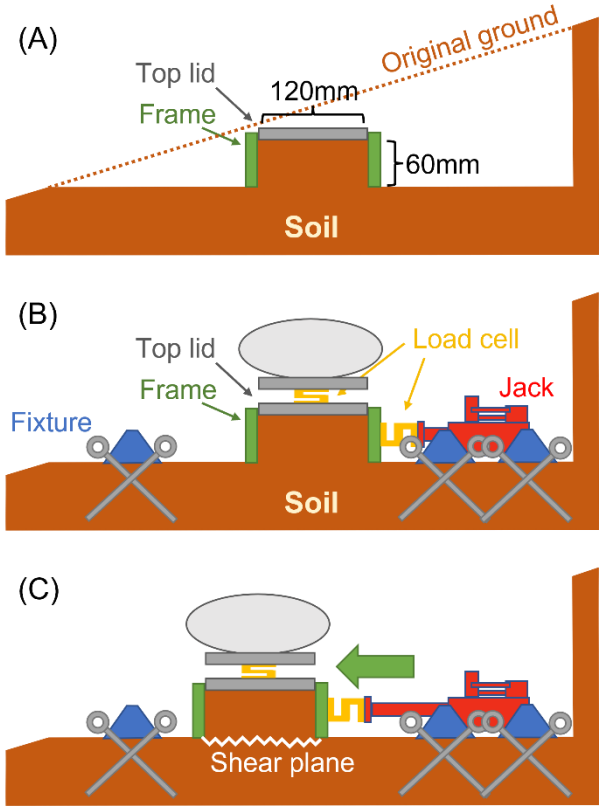

Fig.2. Testing procedures of the in-situ direct shear test. (A) Shear box installation, (B) loading and measuring devices installation and (C) shearing. [10]

2.2 Laboratory direct shear tests

A direct shear test was also conducted in a room. Intact specimens were prepared to ensure that the original soil structure was maintained. The intact specimens were transported with minimal soil disturbance by fitting them into shear boxes created by a 3D printer (Fig.3.).

Fig.3. Field sampling of intact specimens

2.3 Measurement of particle breakage volume

2.3.1 Sieve analysis

After the direct shear test, the particle size distribution was examined to determine the degree of comminution of the pumice. Normally, samples are oven dried and sieved, but fragile volcanic pumice can be crushed during the sieving process. To prevent this, the pumice was sieved while being rinsed with water. Grain sizes ranging from 0.075 mm to 6.7 mm were used for the convenience of the test facility.

2.3.2 Particle breakage index

The relative crush volume Br proposed by Hardin [1] was used to quantify particle breakage. This is an index that can be calculated from the ratio of the areas of the particle size additive curves and can only be obtained by sieving. The definition is shown in Fig.4.

Since it is difficult to sieve the particles before shearing in the in-situ test, the shear zone after the direct shear test was used as the post-crushed sample, and the original soil at the same level as the shear zone was used as the intact sample. In the laboratory tests, the shear zone soil and other intact soils were separated and the shear zone sample was compared as the post crushed sample and the other soil as the intact sample.

2.4 Sample

2.4.1 Tarumae d pumice (Ta-d pumice)

On September 6, 2018, an earthquake occurred in the Iburi region of Hokkaido, Japan [9]. The city of Atsuma, near the epicenter, experienced strong seismic shaking, which triggered numerous landslides [6]. The figure shows the reddish-brown pumice soil exposed in the study area. This Ta-d layer is believed to have played a major role in the present slope failure [7]. Table 1 shows the physical properties of this pumice.

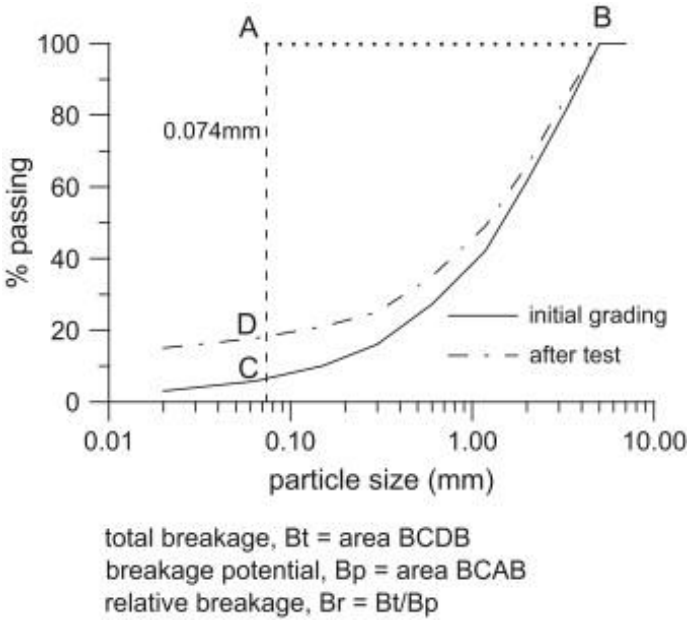

Fig.4. Figure showing the definition of the relative crushing volume Br. [1,5]

Fig.5. Ta-d pumice

Table 1. Physical properties of Ta-d pumice soil

ρ_s	ρ_d	W_n	e	D_{50} (mm)	W_P (%)	W_L (%)	I_p
2.68	0.30	219	7.93	2.5	151	206	55

ρ_s: Soil particle density, ρ_d: Dry density, w_n: Water content in natural condition, e: Void ratio, D_{50}: Mean particle diameter, w_p: Plastic limit, w_L: Liquid limit, I_p: Plasticity index

2.4.2 White pumice in Ontake

A slope failure occurred on the Ontake Plateau as a result of an earthquake in the western part of Nagano Prefecture in 1984. A field survey conducted immediately after the slope failure revealed a layer of white pumice exposed on the slope, which is believed to be the main cause of the slope failure [2].

Fig.6. White pumice in Ontake

Table 2. Physical properties of white pumice soil

ρ_s	ρ_d	W_n	e	D_{50} (mm)	W_P (%)	W_L (%)	I_p
2.65	0.55	86.5	3.83	0.15	53.2	78.7	25.5

ρ_s: Soil particle density, ρ_d: Dry density, w_n: Water content in natural condition, e: Void ratio, D_{50}: Mean particle diameter, w_p: Plastic limit, w_L: Liquid limit, I_p: Plasticity index

3. RESULTS AND DISCUSSION

3.1 Results of Ta-d pumice

The test conditions for the in-situ direct shear test of Ta-d are shown in Table 3. The displacement amplitude in Case 4 was 7 mm for the first 10 cycles and 14 mm for the latter 10 cycles.

Table 3. Test conditions for in-situ direct shear tests of Ta-d

Case ID	Horizontal loading mode	Normal stress σ (kPa)	Displacement amplitude (mm)	N Number of repetition
Case 1	Monotonic	35	-	-
Case 2	Monotonic	20	-	-
Case 3	Cyclic	10	14	10
Case 4	Cyclic	10	7→14	20

Shear rate: 10mm/min

Fig. 7 shows the results of Cases 1 and 2 [11]. The point of maximum shear stress is marked with a marker. The relationship between shear stress and horizontal displacement from the direct shear test is shown. The maximum shear stress was observed at a displacement of approximately 13 mm.

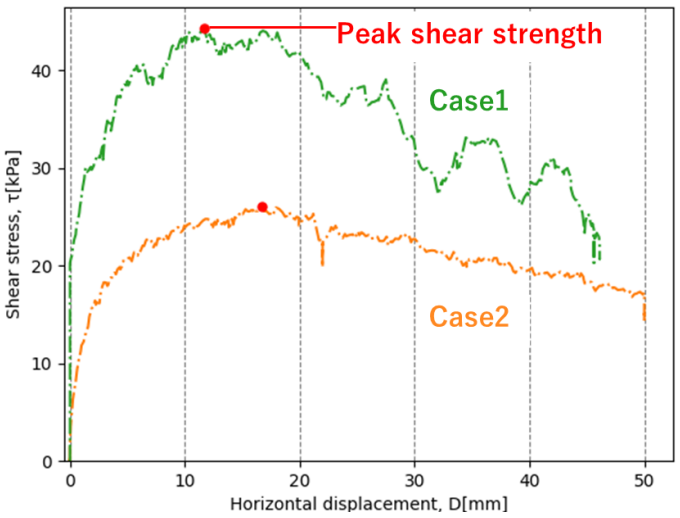

Fig.7. Results of in-situ monotonic direct shear tests of Ta-d

Fig. 8. shows the results of repeated loading tests on Ta-d, i.e., Cases 3 and 4. The upper graph shows that the shear stress decreases as the number of cycles increases. In particular, the change from the first to the second iteration is remarkable. In the lower graph, Case 4, the area with a displacement amplitude of 7 mm is colored blue and the area with a displacement amplitude of 14 mm is colored orange. 7 mm indicates that the shear stress decreases from the first to the second amplitude, but the change is not significant when the amplitude is increased after that. It is noteworthy that when the amplitude is set to 14 mm, the maximum shear stress is similar to that at 7 mm, indicating that after the change to 14 mm, the shear stress decreases with each additional iteration.

Fig. 9. shows Case 3 and 4 with the horizontal axis changed to cumulative displacement. As mentioned above, in Case 3, the shear stress decreases as the number of iterations increases. On the other hand, in Case 4, there is no significant decrease when the displacement amplitude is 7 mm, and the shear stress decreases after the displacement amplitude is increased.

The intact samples were also run in the laboratory under the test conditions shown in Table 3.

Table 3. Test conditions for in-situ direct shear tests of Ta-d
Shear rate: 3mm/min

Case ID	Horizontal loading mode	Normal stress σ (kPa)	Displacement amplitude (mm)	N Number of repetitions
Case 5	Cyclic	10	14	15
Case 6	Cyclic	10	7	15

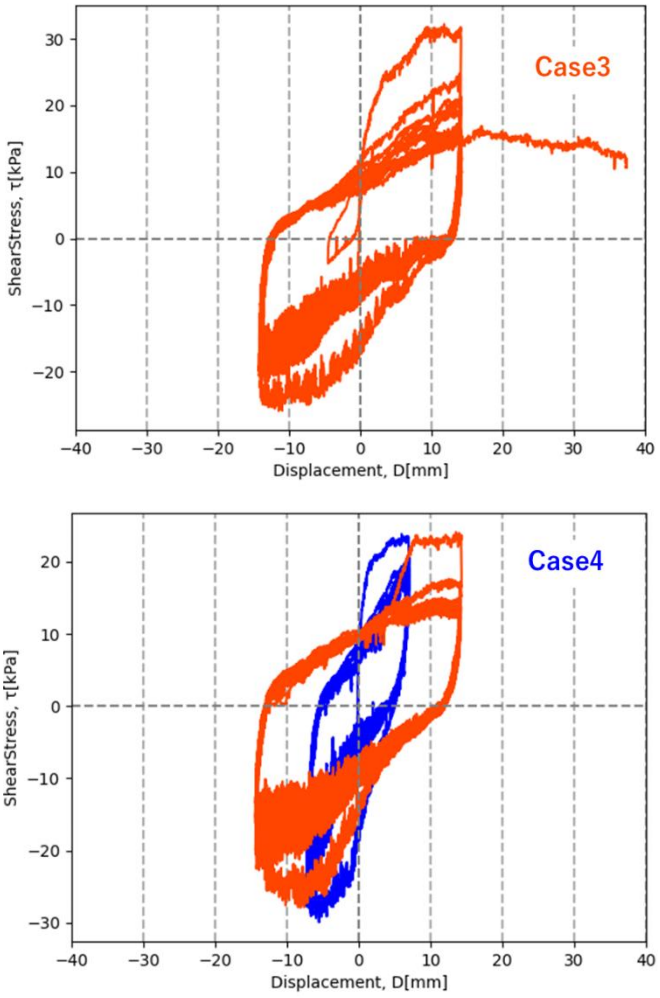

Fig.8. Results of in-situ cyclic direct shear tests of Ta-d

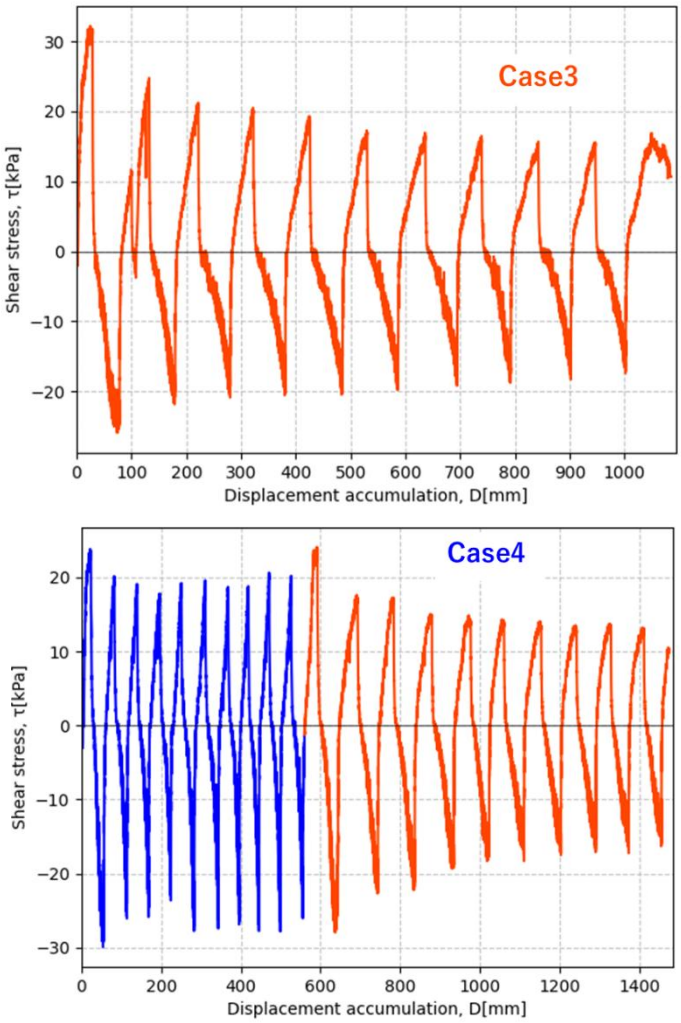

Fig.9. Relationship between accumulated displacement and shear stress in in-situ direct sheear tests at Ta-d

Fig. 10. plots the results of direct shear tests of an intact specimen, with the horizontal axis representing the cumulative displacement and the vertical axis representing the shear stress. In Case 5, where the displacement amplitude is large, the shear stress decreases as the number of cycles increases. On the other hand, in Case 6, where the displacement amplitude is as small as 7 mm, the shear stress does not decrease as the number of iterations increases.

These results indicate that shear stress does not change when the displacement amplitude is smaller than the displacement that produces peak stress, and that shear stress decreases as the number of repetitions increases when the displacement amplitude is larger than the displacement that produces peak stress. This is expected to be due to the fact that the original soil structure is not significantly destroyed until the displacement that causes peak stress is exceeded, while the soil structure is destroyed when the displacement that causes peak stress is exceeded.

Table 4 shows the relative amount of crushing for each case. Comparing Cases 3 and 4 of the same in-situ test, Case 4, with a higher number of repetitions, has a higher relative crushing volume. Case 6, which was tested with a small displacement amplitude, shows a smaller relative crushing volume than the other cases. This suggests that small displacements do not cause significant failure of the structure.

Table 4. Relative crushing volume by direct shear test of Ta-d

Case ID	Relative breakage
Case 3	0.020
Case 4	0.115
Case 5	0.014
Case 6	0.009

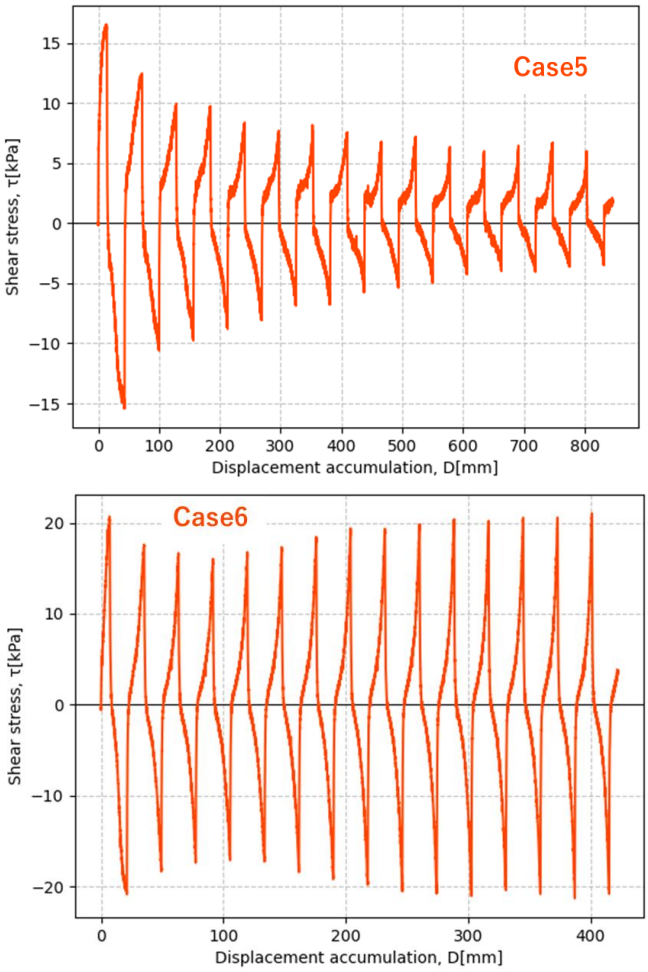

Fig.10. Relationship between accumulated displacement and shear stress in direct sheear tests at Ta-d intact sample

3.2 Results of white pumice in Ontake

The test conditions for in-situ direct shear tests on white pumice at Ontake, Nagano, Japan are shown in Table 1. In Case 8, the displacement amplitude was set to 2 mm and the shear rate was set to 10 mm/min.

Table 4. Test conditions for in-situ direct shear tests in Ontake

Case ID	Horizontal loading mode	Displacement amplitude (mm)	N Number of repetition
Case 7	Monotonic	-	-
Case 8	Cyclic	2	5
Case 9	Cyclic	14	4

Normal stress:35kPa, Shear rate: 10mm/min

Fig. 11. shows the results of in-situ direct shear tests on white pumice. The upper figure shows the simple displacement on the horizontal axis and the lower figure shows the cumulative displacement on the horizontal axis. The shear stress is maximum when the displacement is 12.7 mm.

Cases 8 and 9 show the results with repetitive displacement amplitude. In the large displacement amplitude case, the shear stress decreases as the number of iterations increases. On the other hand, in the small displacement amplitude case, the shear stress does not decrease as the number of iterations increases.

This indicates that, as with Ta-d, the shear stress does not decrease when the displacement is less than the peak stress, while the shear stress decreases when the displacement is greater than the peak stress. This indicates that the displacement must be greater than the displacement at the peak stress for the soil structure to fail.

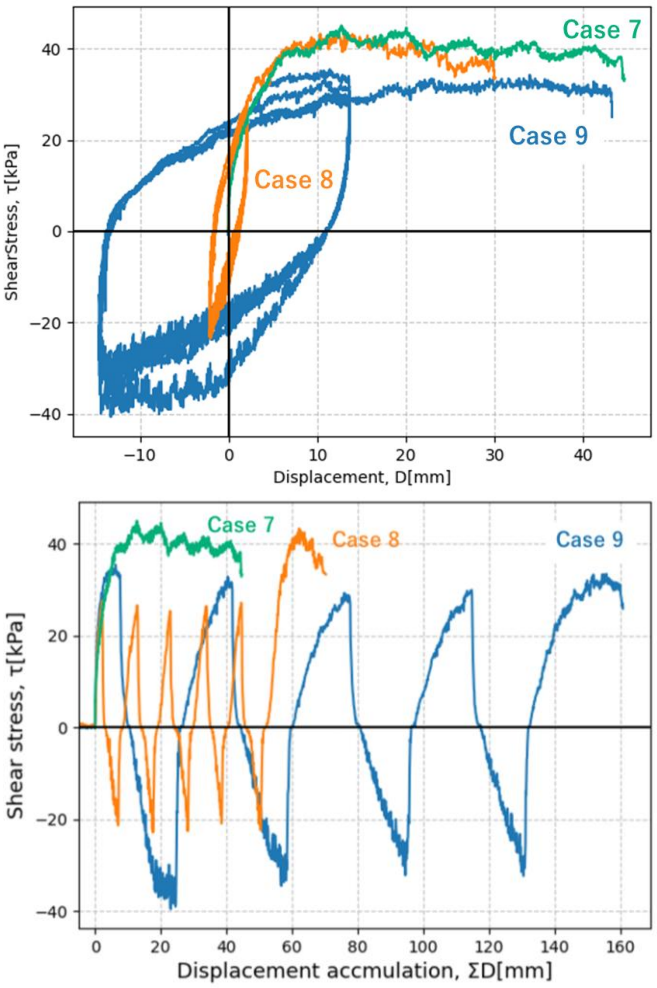

Fig.11. Results of in-situ cyclic direct shear tests of white pumice

4. CONCLUSIONS

In-situ tests were conducted on volcanic pumice that had caused slope failures in the past, and the following points were discussed.

The direct shear test was performed repeatedly by changing the displacement amplitude. The shear stress did not decrease with repeated shearing below the displacement at which the peak stress was reached under monotonic loading. On the other hand, the shear stress decreased with repetition when the displacement exceeded the displacement at which the peak stress was reached. This suggests that displacement in excess of the peak stress is important for breaking the soil structure.

The relative crushing volume based on Hardin's results also showed that the relative crushing volume was small when small displacement amplitudes were applied, suggesting that large displacement amplitudes are required to fracture a structure to the point where its strength is reduced.

ACKNOWLEDGMENTS

Mr. Kuno of the Institute of Industrial Science, the University of Tokyo, continued to provide invaluable assistance in the development of the in-situ direct shear test apparatus and in the preparation of the in-situ tests.

REFERENCES

[1] Bobby O. Hardin, “Crushing of soil particles,” Journal of geotechnical engineering, Vol. 111, No. 10, 1985, pp. 1177–1192.

[2] K. Ishihara, Hai-Lung Hsu, I. Nakazumi, K. Sato. “Analysis of Landslides during the 1984 Naganoken-Seibu Earthquake”, 1986.

[3] Bommer, J. J., Rolo, R., Mitroulia, A., and Berdousis, P., “Geotechnical properties and seismic slope stability of volcanic soils”, In Proceedings of the 12th European Conference on Earthquake Engineering, London, UK, 2002.

[4] Bothara, J., Beetham, D., Brunsdon, D., Stannard, M., Brown, R.,Hyland, C., Lewis, W., Miller, S., Sanders, R., Sulistio, Y, “General observations of effects of the 30th september 2009 PadangEarthquake,” Indonesia. Bulletin of the New Zealand Society forEarthquake Engineering, 2010, pp. 143–173.

[5] G. Vilhar, V. Jovičić, and M.R. Coop, “The role of particle breakage in the mechanics of a non-plasticsilty sand,” Soils and Foundations, 2013, Vol. 53, No. 1, pp. 91–104.

[6] Ministry of Land, Infrastructure, Transport and Tourism (MLIT), “Comparison of collapsed area at the 2018 Hokkaido Eastern Iburi Earthquake and past earthquake disasters” (in Japanese), [online] Available at: https://www.mlit.go.jp/river/sabo/h30_iburitobu/210526_sediment_volume.pdf , accessed: 5/2/2024.

[7] Kawamura, S., Kawajiri, S., Hirose, W., and Watanabe, T. “Slope failures/landslides over a wide area in the 2018 Hokkaido Eastern Iburi earthquake”, Soils and Foundations, 2019, 59(6), pp. 2376-2395.

[8] Hosobuchi, N. M., Chigira, M., Lim, C., Komoo, I. “Geological history controlling the debris avalanches of pyroclasticfall deposits induced by the 2009 Padang earthquake,” Indonesia:The sequential influences of pumice fall, weathering, and slopeundercut. Engineering Geology, 2021, 287, 106104.

[9] Ishikawa, T., Yoshimi, M., Isobe, K., Yokohama, S. “Reconnaissance report on geotechnical damage caused by 2018 Hokkaido Eastern Iburi earthquake with JMA seismic intensity 7”, Soils and foundations, 2021, 61(4), pp. 1151-1171.

[10] Hashimoto, H., Kuno, M., Sato, A., and Kuwano, R. “Soil Structure in Volcanic Pumice Soil of Dozou-sawa River Evaluated from In Situ and Laboratory Tests”, Geotechnical Testing Journal, 46(6), 2023.

[11] A. Sato, H. Hashimoto and R. Kuwano, “In-Situ Cyclic Direct Shear Tests on Volcanic Soil in the Site of Landslide Due to Earthquake”, in: ISC2024, 2024.

Techno-Science Research Journal V13 (Special Issue) (2025) P 84-94

Content list available at ITC

Techno-Science Research Journal

Journal Homepage: www.ric.itc.edu.kh

Techno-Science Research Journal

Foundation Analysis following Eurocode 7 Standard

Khihok Ing*

Geotechnical Engineer, Inros Lackner (Cambodia), Co., Ltd, Street 588, Boeung Kak II, Toul Kork, 12152 Phnom Penh, Cambodia

Received: 1 November 2024; Revised: 1 January 2025; Accepted: 20 June 2025; Available online: October 2025

Abstract: *Eurocode Standard has been widely used for structural and geotechnical design in European countries and other countries. The basic concept is the design effect (E_d) must be equal to or less than the design resistance (R_d). In Cambodia, the standard has been adopted as the design reference. However, the study of geotechnical design following Eurocode 7 Standard in Cambodia is rather limited. In this paper, the analysis of shallow and pile foundations in the Phnom Penh area following Eurocode 7 will be presented. The design pile capacity will be calculated following the empirical formulas presented by Tomlinson and Woodward (2015). It will be evaluated by the static load test in the fields. The design shallow foundation will be conducted following the formula presented in the Eurocode 7 Standard. The settlement analysis and safety factor obtained from the analysis will also be discussed.*

Keywords: Eurocode Standard, Pile foundation, Shallow foundation, Safety factor and Foundation settlement.

List of Symbols

A'	design effective foundation area
A_b	cross-sectional area of pile toe
A_c	nominal pile cross section
a_d	design value of geometrical data
A_s	nominal cross-sectional area of reinforcement
$A_{s,i}$	area of pile shaft
ASD	allowable stress design
B	footing width
B'	effective foundation width
b_c, b_q, b_γ	factors of inclination of the foundation
c'	effective cohesion
c_u	undrainded shear strength
d	equivalent diameter
DA	design approach
d_{crit}	critical depth
E_d	design effects of action
E_m	design value of the modulus of elasticity
EN	Eurocode standard
E_u	undrained dormation modulus
F	length factor
f	settlement coefficient
$F_{c,d}$	design axial compression load
f_{ck}	characteristic compressive cylinder strength of concrete at 28 days
F_k	allowable load
F_{rep}	representative value of an action
G	permanent loads
GL	soil shear modulus at the level of the pile base
H	thickness of the soil layer
i_c, i_q, i_γ	factors of inclination of the load
I_f	Fox's reduction factor
I_p	influence factor
L	embedded length
$LRFD$	load resistance factor design
m_v	modulus of volume compressibility
N_c, N_q, N_γ	factors of bearing resistance
N_{Rd}	design resistance of pile material
p	the bearing pressure, linearly distributed on the base of the foundation
P_t	total compression load on pile head
Q	imposed or variable loads
q	overburden or surcharge pressure at the level of the foundation base
q_{all}	allowable stress
$q_{c;I;mean}$	mean cone penetration resistance from pile base level to the critical depth (d_{crit})
$q_{c;II;mean}$	mean of the lowest cone penetration resistance values over the depth going upwards from d_{crit} to the pile base

* Corresponding author: Khihok Ing
E-mail: *ingkhihok@gmail.com;* Tel: *+855 96 456 2877*

$q_{c;III;mean}$ mean of cone penetration resistance values between pile base level to a level of 8 times of the pile base diameter above the pile base.
$q_{c;z;a,I}$ cut-off value of cone penetration resistance at depth z
q_d design capacity
q_n net foundation pressure
q_u ultimate capacity
R resistance
R_b base or toe resistance
$R_{b,k}$ resistance characteristics of pile toe
$R_{c,k}$ total resistance characteristics of pile in compression
$R_{c;mean}$ average of compressive resistance of piles
$R_{c;min}$ minimum of compressive resistance of piles
R_d design resistance
R_s shaft resistance
$R_{s,k}$ resistance characteristics of pile shaft
R_t total compression resistance
s shape factor of pile base
s_0 immediate settlement
s_1 settlement caused by consolidation
s_2 settlement caused by creep
s_b settlement of the pile toe due to the load on the pile
s_c, s_q, s_γ factors of shape of the foundation
s_{el} elastic shortening caused by compression
SF safety factor
SLT static load test
s_{total} total settlement
V_d design actions including the weight of the foundation, the weight of any backfill material and all earth pressure
w_t pile head settlement
X_k characteristic value of a material property
α_{cc} coefficient taking account of long-term effects on the compressive strength and of unfavourable effects resulting from the way the load is applied
α_p peak adhesion factor
α_p pile class factor (for CPT test)
$\alpha_{s,i}$ factor of shaft resistance
$\alpha_{s,I}$ factor of shaft resistance
β factor of shape of the pile point
γ' design effective weight density of soil
γ_b partial factor of the base resistance
γ_c partial safety factor for concrete
γ_E partial factor of the effects of actions
γ_F partial factor on action
γ_M partial factor for soil parameters
γ_s partial factor for reinforcement
γ_s partial factor of the shaft resistance
γ_t partial factor of total resistance
ζ measure of radius of influence of pile
η ratio of underream for underreamed piles
λ pile-soil stiffness ratio
μ_d depth factor
μ_g geological factor
μL measure of pile compressibility
ν Poisson's ratio
ξ ratio of end-bearing for end-bearing piles
ξ_1, ξ_2 correlation factors to evaluate the results of static pile load tests
ξ_3, ξ_4 correlation factors to derive the pile resistance from ground investigation results
ξ_5, ξ_6 correlation factors to derive the pile resistance from dynamic impact tests
σ'_{v0} effective vertical stress
σ_z average effective vertical stress imposed on the soil layer due to the net foundation pressure at the base of the equivalent raft foundation
φ' effective friction angle of soils

1. INTRODUCTION

The allowable stress design (ASD) or working stress design is a simple method that has been applied in civil engineering design especailly geotechnical design. The principal concept is that the ratio of the resistance (R) and the load assumptions is equal to or greater than the recommended value which is called "Safety Factor" or "SF". The SF-values can be in the range of 1.50 to 4.00 depending on the uncertainties in the selected design parameters and the degree of structural failure [1]. The SF-values for foundation design are commonly greater than 2.00 when the minimum value of siding and overturning or retaining walls is 1.50. Currently, another design method, called Load Resistance Factor Design or LRFD, has been widely used in civil engineering design. Eurocode (EN) Standard is one of many design standards that selected LRFD as the basic concept. EN Standard has been published by the European Committee for Standardization (CEN) in order to provide a common approach for structural and geotechnical design in European countries. The concept is that the design effects of actions (E_d) must be equal to or less than the design resistances (R_d). The effects include the internal forces, moments, stresses and strains within the structural members, plus any deflection or rotation of the structure as a whole [2]. The design resistance depends on material properties and the dimension of the structural element. The standard has been fully or partially adopted by other countries such as Singapore, Malaysia, Canada and Australia and was recently adopted as the design reference in Cambodia. However, the study of geotechnical design in Cambodia especially following the EN Standard is rather limited. Due to the availability of geotechnical data, the study of foundation design comprising shallow and pile foundations will be conducted following the EN Standard. The empirical formulas presented by Tomlinson and Woodward (2015) [3] will be used to calculate pile foundaions when the formulas given in the Eurocode 7 Standard – Part 1 (EN 1997-1) [4] will be used for the analysis of shallow foundation. The design pile capacity will be compared to the results of static load tests (SLT) from the fields. The safety factors obtained from the analytical solutions

and SLT will be discussed. The load-settlement analysis is also included in this study.

2. GEOLOGICAL CONDITIONS OF THE GREATER PHNOM PENH AREA

All selected foundation designs in this study are located in Phnom Penh City, the capital city of Cambodia. The city is located at the confluences of Mekong River, Bassac River and Tonlé Sap River. The subsoil conditions of this area are significantly affected by the river flood. The previous studies of the geological conditions of the greater Phnom Penh area indicated the complex of sandy and clayey soils along the depths [5], [6]. Touch et al. (2014) [6] classified the subsoil condition of this area into three categories: western, central and eastern regions. The soil profiles of the western region are typically the existing old soil comprising made ground underlaid by medium stiff to very stiff clay approximately 6.0-7.0 m thick. The deeper depth is medium dense to very dense sand. The profile of the central region of the area is made ground of approximately 2.0 m followed by a complex of subsoil layers such as very soft to soft clay, medium stiff clay, very loose to loose sand, stiff to very stiff clay, hard silt, medium dense to very dense sand. The profile of eastern region is very soft clay and silt down to a depth of 12.0 m underlaid by medium dense to very dense sand to a depth of 25.0 m.

3. LITERATURE REVIEW

3.1 Analytical solutions of shallow foundations

A shallow foundation is a type of foundation in which the embedded depth is less than or equal to its width. The concept of shallow foundation design was first presented by Terzaghi (1943) [7]. The concept has been then modified by including several design factors such as shape factors, depth factors, load inclination factors and bearing capacity factors [8]. EN 1997-1 [4] recommended the plasticity theory and experimental results for analysis of the design vertical bearing capacity. The ultimate bearing capacity can be calculated in two conditions: undrained conditions and drained conditions. For the traditional method, the allowable stress can be determined as follows:

$$q_{all} = (q_u - \sigma'_{v0}) / SF + \sigma'_{v0} \quad \text{(Eq. 1)}$$

where:
q_{all} = allowable stress (kPa)
q_u = ultimate capacity (kPa)
σ'_{v0} = effective vertical stress at pile base (kPa)
SF = safety factor (-)

3.1.1 Undrained conditions

The bearing capacity for undrained conditions can be expressed as follows:

$$R/A' = (\pi + 2)c_u b_c s_c i_c + q \quad \text{(Eq. 2)}$$

where:
R = the bearing resistance (kN)
A' = design effective foundation area (m^2)
c_u = undrainded shear strength (kPa)
q = overburden or surcharge pressure at the level of the foundation base (kPa)

The bearing capacity factors including factor of inclination of the foundation base (b_c), factor of shape of the foundation (s_c) and factor of inclination of the load (i_c) are presented in Annex D of EN 1997-1 (2004) [4].

3.1.2 Drained conditions

The bearing capacity for drained conditions can be calculated in functions of effective cohesion (c') and effective friction angle (φ') at foundation base as follows:

$$R/A' = c'N_c b_c s_c i_c + q'N_q b_q s_q i_q + 0.5\gamma'B'N_\gamma b_\gamma s_\gamma i_\gamma \quad \text{(Eq. 3)}$$

where:
q' = design effective overburden pressure at the level of the foundation base (kPa)
B' = effective foundation width
γ' = design effective weight density of soil below foundation.

The factors of bearing resistance (N_c, N_q, N_γ), of inclination of the foundation (b_c, b_q, b_γ), of shape of foundation (s_c, s_q, s_γ), of inclination of the load (i_c, i_q, i_γ) are presented in Annex D of EN 1997-1 (2004) [4].

3.1.3 Settlement of shallow foundations

The foundation settlement comprises immediate and delayed settlement [4]. Three components of settlement that should be considered for partially or fully saturated soils are immediate settlement (s_0), settlement caused by consolidation (s_1) and settlement caused by creep (s_2). The total settlement of foundations on cohesive and cohesionless soils can be determined by elasticity theory as:

$$s = p \times B \times f / E_m \quad \text{(Eq. 4)}$$

where:
p = the bearing pressure, linearly distributed on the base of the foundation (kPa)
B = footing width (m)
f = settlement coefficient (-)
E_m = design value of the modulus of elasticity (kPa)

The net immediate settlement of foundations on clays can be estimated as follows [3]:

$$s_0 = q_n \times B \times (1 - \nu^2) \times I_p / E_u \quad \text{(Eq. 5)}$$

where:

q_n = net foundation pressure (kPa)
ν = Poisson's ratio (-)
E_u = undrained dormation modulus (kPa).

The influence factor (I_p) is calculated following the formulas of Steinbrenner (1934) [9]. The embedded depth also affects the foundation settlement [1]. An additional reduction factor (I_f) proposed by Fox (1948) [10] is therefore included in the analysis for foundations embedded at any depth below the ground surface. The E_u–value can be determined from plate bearing tests, drained triaxial compression tests on good-quality samples, oedometer tests and pressuremeters [3]. The relations of E_u/C_u presented by Jamiolkowski et al. (1979) [11] can be used in the absence of the available testing results. The settlement is calculated to a depth at which vertical stress caused by the net pressure at the foundation level is equal to 20% of effective vertical stress (σ'_v). The consolidation settlement (s_1) of clay is calculated as:

$$s_1 = \mu_g \times \mu_d \times m_v \times \sigma_z \times H \qquad \text{(Eq. 6)}$$

where:

μ_g = geological factor (-)

μ_d = depth factor (-)

m_v = modulus of volume compressibility (m^2/kN)

σ_z = average effective vertical stress imposed on the soil layer due to the net foundation pressure at the base of the equivalent raft foundation (kPa)

H = thickness of the soil layer (m).

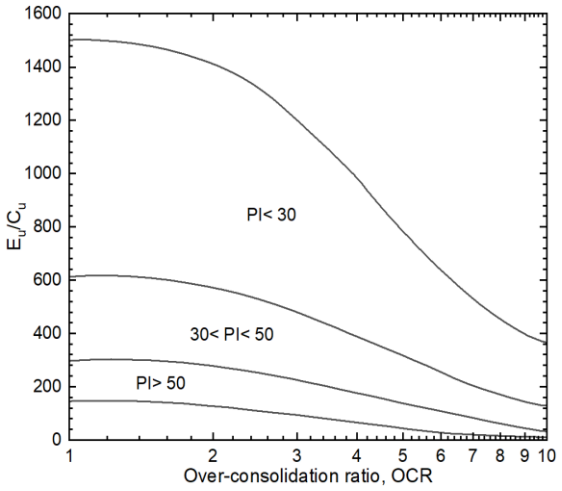

Fig. 1. Relationship between E_u/C_u for clays with plasticitiy index (PI) and degree of over-consolidation (OCR) [11]

3.2 Analytical solutions of pile foundation

Pile foundations are types of foundations in which the ratio of the embedded length and diameter is equal to or greater than 5. The ultimate pile bearing capacity is the summation of shaft and toe resistances. The shaft resistance can be estimated by the α–method for the short term and the β–method for the long term. The toe bearing capacity can be calculated following the empirical formulas proposed by previous researchers. The pile capacity for this study will be derived following the empirical formulas presented by Tomlinson and Woodward (2015) [3].

3.2.1 Pile in cohesive soils

The ultimate pile bearing capacity (Q_{ult}) in cohesive soils can be determined as follows:

$$Q_{ult} = N_c C_{u,b} A_b + \Sigma_i F \alpha_p C_{u,i} A_{s,i} \qquad \text{(Eq. 7)}$$

where:
$C_{u,b}$ = undrained shear strength at pile toe (kPa)
$C_{u,i}$ = undrained shear strength along pile shaft (kPa)
A_b = cross-sectional area of pile toe (m^2)
$A_{s,i}$ = area of pile shaft (m^2)

The toe bearing capacity factor (N_c) is equal to 9.0 for the embedded length at least 5 times of diameter. The length factor (F) and peak adhesion factor (α_p) can be determined in function of the ratio of undrained shear strength and effective overburden pressure (C_u/σ'_v) and the ratio of embedded length and width ratio of pile (L/B), respectively, as shown in Fig. 2.

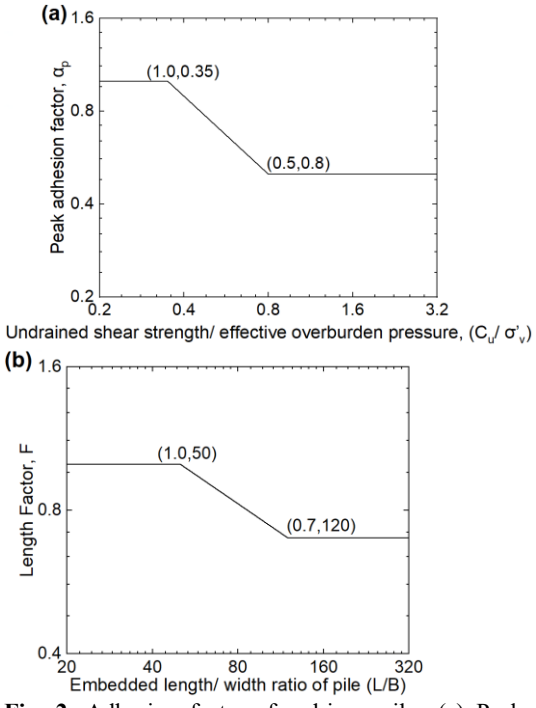

Fig. 2. Adhesion factors for driven piles (a) Peak adhesion factor versus undrained shear strength/effective vertical pressure and (b) Length factor versus embedded length/ width ratio of pile [3]

3.2.2 Analysis of pile settlement

The pile settlement is the summation of the elastic shortening of the shaft and the settlement of the pile toe [3]. Tomlinson and Woodward (2015) [3] proposed a mathematical equation for the prediction of pile head settlement. However, the load distributions of the pile shaft and toe are nonlinear. The axial loads contributed by toe resistance is one of several factors which significantly affect the estimation. Thus, the elastic continuum model was recommended for the analysis of the pile settlement. Tomlinson and Woodward (2015) [3] then adopted the semi-analytical method of Fleming et al. (2009) [12] for the estimation of pile head settlement. The settlement of a single pile in compression can be calculated in function of several factors as follows [12]:

$$P_t/w_t dG_L = f(\eta,\ \nu, \xi, \zeta, \mu L, \lambda, L/d) \quad \text{(Eq. 8)}$$

Where:
P_t = total compression load on pile head (kN)
w_t = pile head settlement (mm)
G_L = soil shear modulus at the level of the pile base (kPa)
η = ratio of underream for underreamed piles (-)
ν = Poisson's ratio (-)
ξ = ratio of end-bearing for end-bearing piles (-)
ζ = measure of radius of influence of pile (-)
μL = measure of pile compressibility (-)
λ = pile-soil stiffness ratio (-)
L/d = ratio of pile length and equivalent diameter (-)

The equivalent pile diameter (D_{eq}) can be determined by assuming the gross cross-sectional area of the actual pile equal to the area of circular pile or $\pi(D_{eq})^2/4$. Thus, the equivalent diameter of the circular piles is equal to the nominal diameter while it is equal to 1.13 of edge for square piles.

3.2.3 Analysis of pile capacity from CPT test

The design pile capacity from the cone penetration test (CPT) can be determined by different methods. Tomlinson and Woodward (2015) [3] adopted the Netherlands method to predict the pile capacity in coarse-grained soils. The detailed design was presented in Annex D of EN 1997-2 (2007) [13]. The total compression resistance of a single pile (R_t) is:

$$R_t = R_b + R_s \quad \text{(Eq. 9)}$$

$$R_b = 0.5\alpha_p\beta s\{(q_{c;I;mean} + q_{c;II;mean}) / 2 + q_{c;III;mean}\} \quad \text{(Eq. 10)}$$

$$R_s = \Sigma_i\ \alpha_{s,i} q_{c;z;a,i} A_{s,i} \quad \text{(Eq. 11)}$$

where:

R_b = base resistance (kN)

R_s = shaft resistance (kN)

α_p = pile class factor (-)

β = factor of shape of the pile point (-)

s = factor of shape of pile base (-)

$\alpha_{s,i}$ = factor of shaft resistance (-)

$q_{c;z;a,i}$ = cut-off value of cone penetration resistance at depth z (MPa)

$A_{s,i}$ = area of pile shaft (m^2)

$q_{c;I;mean}$ = mean cone penetration resistance from pile base level to the critical depth (d_{crit}) (MPa)

$q_{c;II;mean}$ = mean of the lowest cone penetration resistance values over the depth going upwards from d_{crit} to the pile base (MPa)

$q_{c;III;mean}$ = mean of cone penetration resistance values between pile base level to a level of 8 times of the pile base diameter above the pile base.

The critical depth (d_{crit}) ranges between 0.7 to 4.0 times of equivalent pile base diameter. The α_p-value and α_s-value are presented in Tables D.5 and D.6 of Annex D of EN 1997-2 (2007) [13]. The s-value is equal to 1.0 for square or circular piles. The detail of the β-value is presented in Annex D of EN 1997-2 (2007) [13]. The pile head settlement is the summation of the pile toe due to the load on the pile (s_b) and elastic shortening caused by compression (s_{el}) [14], [15]. The s_b– value is determined with Fig. 3 and Fig. 4.

4. EUROCODE 7 STANDARD

Eurocode 7 Standard has adopted the LRFD method for geotechnical design. In this case, the geotechnical design can be verified if and only if the design value of the effect of action (E_d) is less than the design value of the resistance (R_d). The value of E_d is calculated by applying the partial factors on actions either to the action themselves (F_{rep}) or to their effects (E). The partial factors on resistance (γ_R) may be applied either to ground properties (X) or resistance (R) and sometimes both. The general equations of E_d and R_d can be expressed as:

$$E_d = E\{\gamma_F F_{rep};\ X_k/\gamma_M;\ a_d\}$$

$$\text{or } E_d = \gamma_E E\{F_{rep};\ X_k/\gamma_M;\ a_d\} \quad \text{(Eq. 12)}$$

$$R_d = R\{\gamma_F F_{rep};\ X_k/\gamma_M;\ a_d\}$$

$$\text{or } R_d = R\{F_{rep};\ X_k;\ a_d\}/\gamma_R$$

$$\text{or } R_d = R\{\gamma_F F_{rep};\ X_k/\gamma_M;\ a_d\}/\gamma_R \quad \text{(Eq. 13)}$$

According to EN 1997-1 [4], the equation for bearing resistance of spread or shallow foundation can be expressed as:

$$V_d \leq R_d \quad \text{(Eq. 14)}$$

where:
V_d = design actions including the weight of the foundation, the weight of any backfill material and all earth pressure (kN)
R_d = design resistance (kN).

The design pile foundation in compression is verified if:

$$F_{c,d} \leq R_{c,d} \text{ or } F_k \leq R_{c,d}/\gamma_F \quad \text{(Eq. 15)}$$

The design resistance of pile foundation in compression ($R_{c,d}$) can be derived as follows:

$$R_{c,d} = R_{b,k}/\gamma_b + R_{s,k}/\gamma_s = R_{c,k}/\gamma_t \quad \text{(Eq. 16)}$$

where:
$R_{b,k}$ = resistance characteristics of pile toe (kN)
$R_{s,k}$ = resistance characteristics of pile shaft (kN)
$R_{c,k}$ = total resistance characteristics of pile (kN)
$F_{c,d}$ = design action (kN)
F_k = allowable load (kN)

γ_b, γ_s and γ_t are partial factors of the base, shaft and total resistance, respectively. The partial factor on action (γ_F) is presented in Table 1. The characteristic compressive resistance (R_k) is taken as the lesser value of:

- static load tests

$$R_k = \text{Min}\{R_{c;mean}/\xi_1 \; ; \; R_{c;min}/\xi_2\} \quad \text{(Eq. 17)}$$

- ground test results

$$R_k = \text{Min}\{R_{c;mean}/\xi_3 \; ; \; R_{c;min}/\xi_4\} \quad \text{(Eq. 18)}$$

- dynamic load results

$$R_k = \text{Min}\{R_{c;mean}/\xi_5 \; ; \; R_{c;min}/\xi_6\} \quad \text{(Eq. 19)}$$

where:
$R_{c;mean}$ = average of compressive resistance of piles (kN)
$R_{c;min}$ = minimum of compressive resistance of piles (kN)
ξ = correlation factors depending on number of tests (-)

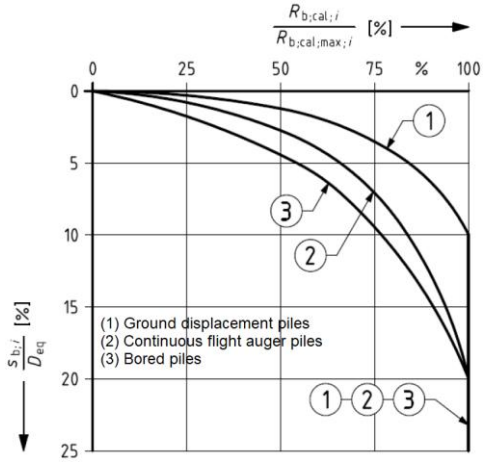

Fig. 3. Relationship between ratio load contributed by pile base to maximum toe resistane and ratio of toe settlement to equivalent diameter [14]

The design resistance of a pile from static load tests, ground tests or dynamic load tests cannot be greater than the design resistance of pile material. The design resistance of pile material for driven piles can be determined as:

$$N_{Rd} = A_c\alpha_{cc}f_{ck}/\gamma_{cc} + A_sf_{yk}/\gamma_s \quad \text{(Eq. 20)}$$

where:
N_{Rd} = design resistance of pile material (kN)
A_c = nominal pile cross section (m^2)
f_{ck} = characteristic compressive cylinder strength of concrete at 28 days (MPa)
α_{cc} = coefficient taking account of long-term effects on the compressive strength and of unfavourable effects resulting from the way the load is applied (-)
γ_c = partial safety factor for concrete (-)
A_s = nominal cross-sectional area of reinforcement (m^2)
f_{ck} = characteristic yield strength of reinforcement (MPa)
γ_s = partial factor for reinforcement (-)

The α_{cc}-value ranges between 0.8 to 1.0 and α_{cc}= 0.85 is the recommended value. The values of γ_c and γ_s are 1.5 and 1.15, respectively [16]. Eurocode 7 Standard separated three different design approaches, Design Approach 1 (DA1), Design Approach 2 (DA2) and Design Approach 3 (DA3), for the combination of the partial factors on effects and resistances. The DA1 is separated into two different combinations: Combination 1 (DA1-1) and Combination 2 (DA1-2). The details of the design approach are presented as follows:
Design Approach 1 or DA1 (except for axial pile and anchors)
DA1-1: A1 + M1 + R1
DA1-2: A2 + M2 + R1
Design Approach 1 or DA1 (for axial pile and anchors)
DA1-1: A1 + M1 + R1
DA1-2: A2 + (M1 or M2)* + R4
Design Approach 2 or DA2: A1 + M1 + R2
Design Approach 3 or DA3: (A1 or A2)** + M2 + R3

"A" refers to partial factors on actions (γ_F) or the effects of actions (γ_E), "M" is partial factors for soil parameters (γ_M) and "R" is partial factors for resistance. For the design of axial piles and anchors, M1 of DA1-2 is used for calculating the resistance of piles or anchors while M2 is used for calculating unfavorable actions on piles. For DA3, A1 is applied on structural actions and A2 is applied on geotechnical actions.

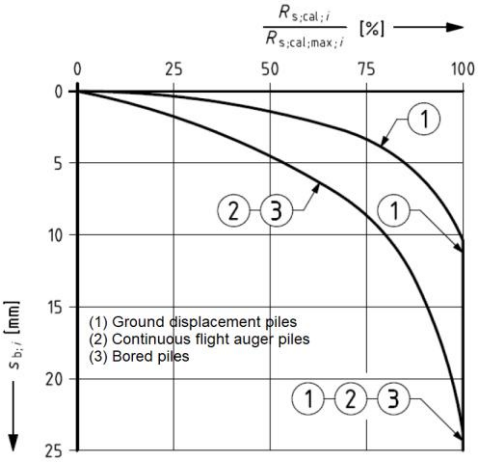

Fig. 4. Relationship between ratio load contributed by pile shaft to maximum shaft resistane and toe settlement [14]

Table 1. Partial factors on action (γ_F) or the effects of action (γ_E) [4]

Action		Symbol	Set	
			A1	A2
Permanent	Unfavourable	γ_G	1.35	1.00
	Favourable		1.00	1.00
Variable	Unfavourable	γ_Q	1.50	1.30
	Favourable		0.00	0.00

Table 2. Partial factors for soil parameters (γ_M) [4]

Soil parameter	Symbol	Set	
		M1	M2
Angle of shearing resistance*	$\gamma_{\varphi'}$	1.00	1.25
Effective cohesion	$\gamma_{c'}$	1.00	1.25
Undrained shear strength	γ_{cu}	1.00	1.40
Unconfined strength	γ_{qu}	1.00	1.40
Note: This factor is applied for tan φ'.			

Table 3. Partial factors for spread foundations (γ_R) [4]

Resistance	Symbol	Set		
		R1	R2	R3
Bearing	$\gamma_{R,v}$	1.00	1.40	1.00
Sliding	$\gamma_{R,h}$	1.00	1.10	1.00

Table 4. Partial factors for driven pile (γ_R) [4]

Resistance	Symbol	Set			
		R1	R2	R3	R4
Base	γ_b	1.00	1.10	1.00	1.30
Shaft (compression)	γ_s	1.00	1.10	1.00	1.30
Total/combined (compresssion)	γ_t	1.00	1.10	1.00	1.30
Shaft in tension	$\gamma_{s;t}$	1.25	1.15	1.10	1.60

Table 5. Correlation factors ξ for static pile load tests [4]

	Number of tests				
	1	2	3	4	≥5
ξ_1	1.40	1.30	1.20	1.10	1.00
ξ_2	1.40	1.20	1.05	1.00	1.00

Table 6. Correlation factors ξ for ground test results [4]

	Number of tests						
	1	2	3	4	5	7	10
ξ_3	1.40	1.35	1.33	1.31	1.29	1.27	1.25
ξ_4	1.40	1.27	1.23	1.20	1.15	1.12	1.08

5. CASE STUDIES

5.1 Shallow foundation on clayey soil

The first study is the design shallow foundation 0.6 x 0.6 x 0.3 m for supporting a structural frame. The footing was embedded 1.0 m into the ground surface. The soil condition of the footing base was medium stiff to stiff lean clay underlaid by medium dense clayey sand and medium dense to dense silty sand, as shown in Fig. 5. The correlation of deformation modulus of Jamiolkowski et al. (1979) [11] was applied for calculating the footing settlement. Based on Touch et al. (2014) [6], the over-consolidated ratio (OCR) of Phnom Penh clay for depths less than 5.0 m ranges between 2.0 to 10.0. Assuming that OCR =5.0 and plasticity index PI<30%, the E_u/C_u–value ranges between 314 to 776. Thus, E_u/C_u= 350 is selected for settlement design.

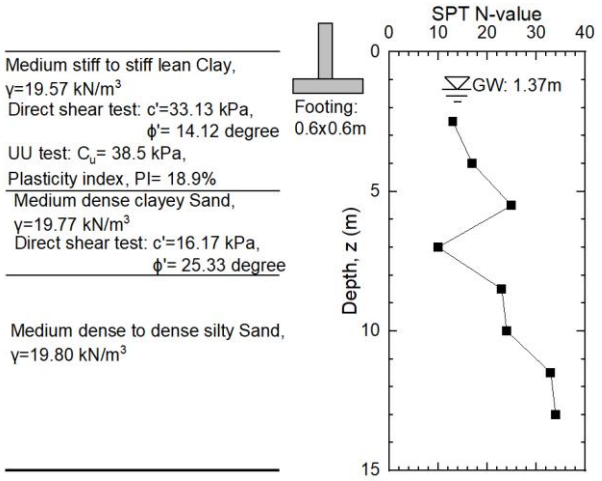

Fig. 5. Soil profile of site 1

The capacities of footing in undrained and drained conditions were calculated following Eq. 2 and Eq. 3. The net ultimate bearing capacities for undrained and drained conditions were 285 kPa and 359 kPa, respectively. The allowable stress on footing was calculated by assuming that the total permanent loads equal to 60% of the total vertical load. The μ_g–value was assumed to be 0.6. The design capacity of footing (q_d), allowable stress (q_{all}), safety factor (SF), immediate settlement for allowable stress (s_0), consolidation settlement (s_1) and total settlement (s_{total}) are summarized as follows:

For undrained condition

Design approach	q_d (kPa)	q_{all} (kPa)	SF	s_0 (mm)	s_1 (mm)	s_{total} (mm)
DA1-1	258	175	1.47	9.70	2.64	12.34
DA1-2	190	159	1.62	8.81	2.40	11.21
DA2	258	119	2.18	5.40	1.74	7.15
DA3	190	123	2.10	5.61	1.81	7.42

For drained condition

Design approach	q_d (kPa)	q_{all} (kPa)	SF	s_0 (mm)	s_1 (mm)	s_{total} (mm)
DA1-1	579	403	1.44	44.00	6.49	50.49
DA1-2	396	342	1.69	33.52	5.46	38.99
DA2	413	281	2.06	24.42	4.44	28.86
DA3	396	269	2.15	20.42	4.19	24.60

The analysis indicates that the s_{total}-values for the undrained condition were less than the allowable settlement ($s_{total} \leq$ 25 mm), but the s_{total}-values for drained condition are greater than the allowable value. The back-calculated safety factors for DA1 are less than the minimum recommended value (SF=2.00) when the SF-values of other design approaches are slightly greater than 2.00. The back-analysis indicates that the design resistances for all cases seem unsafe for foundation design. Thus, an additional bearing capacity factor is recommended for the shallow foundation design following Eurocode 7. The French National Annex (NF EN 1997-1, 2005) [17] provided the additional factors ($\gamma_{R;d;v}$) depending on design methods. The model factors ($\gamma_{R;d;v}$) equal to 2.00 are used in the drained condition and 1.20 in the case of the undrained condition, pressuremeter method and static penetrometer tests [18]. An additional bearing capacity factor of at least 1.40 is recommended for this analysis to obtain SF$\geq$ 2.00.

5.2 Driven pile on clayey soil

Another study is the design of a driven pile in clayey soil. The field study is located in the downtown area of Phnom Penh city. The geotechnical investigation was conducted and the driven piles 0.3x0.3m were then selected as the foundation systems of the building. Fig. 6 shows the geological conditions of the fields and the dimensions of the testing pile. The design resistance of the pile was calculated following the EN 1997-1 Standard [4]. The base and shaft resistances of the pile are summarized in Table 7. The calculation of design resistance ($R_{c,d}$), allowable load (F_k) and safety factor (SF) is presented in Table 8. The allowable load is calculated by assuming that the ratio of the dead load is 60% of the total load. $\xi_3 = \xi_4 = 1.40$ is used for a number of ground test results, n= 1 [4].

Except for DA1-1 whose safety factor (SF) is equal to 1.97, the SF-value of other design approaches is greater than 2.00. Smith (2014) [2] recommended that the correlation factors (ξ) and resistance factors (γ_R) for foundation design must be calculated following the National Annex, rather than the values recommended in Eurocode documents. The UK National Annex is one of many National Annexes which has been widely used for design practice. The UK National Annex has revised the correlation factors and resistance factors from the Eurocode Standard to follow the design practice in the country. This is because they are concerned that the EN 1997-1 Standard might provide conservative or unsafe bearing capacity [19]. The revisions of the factors have also been conducted in other countries in order to provide suitable safety factors for design practices in each country.

The analysis of bearing capacity in this case was verified by the static load test in the fields. The maximum applied load was 200% of the working load. In Cambodia, the safety factor for static pile load test is generally equal to 2.00. Thus, the design pile capacity can be verified if the piles do not reach the ultimate capacity before 200% of the working load. Fig. 7 shows the actual settlement of the static load test (SLT) from the fields. The settlement of the pile head that reaches 10% of the pile base diameter should be considered as the "failure" criterion [4]. Thus, the pile load test did not reach the ultimate capacity. The extrapolation methods including the Mazurkiewicz method [20] and Chin-Kondner Method [21] were applied to determine ultimate capacity, as shown in Fig. 8. The ultimate capacity from the Mazurkiewicz method and Chin-Kondner Method was 440 and 461 kN, respectively. The results seem to be slightly greater than the predicted pile capacity for without partial factor of soil parameters (R_c= 406 kN). It must be noted that the design resistance of the pile from the analytical solution and static load test cannot be greater than the design resistance of pile material. Assuming that the concrete strength of pile materials f_{ck}= 40 MPa, the design resistance of the driven pile is N_{Rd}= 2,040 kN. The analysis indicates that the design resistance is less than the resistance of the pile material.

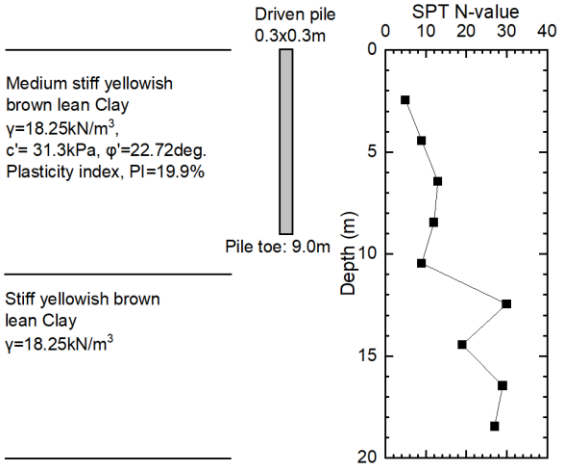

Fig. 6. Soil profile and dimension of pile test for site 2

Table 7. Summary results of estimated pile capacity

Resistance	Partial factor of soil parameters	
	M1	M2
R_b (kN)	60	43
R_s (kN)	347	248
R_c (kN)	406	290
$R_{c,k}$ (kN)	290	207

The average extrapolation value (R_c= 450 kN) was used to design pile capacity from a static load test. According to EN 1997-1 (2004) [4], $\xi_1 = \xi_2 = 1.40$ is used for a number of static

load tests, n= 1. The back-calculated safety factors from the static load test are the same as the ground testing results. However, it cannot be applied to DA3 because DA3 consists of a partial factor of soil parameters (γ_M) which is impractical for the static load test. The pile settlement was estimated following the formula of Fleming et al. (2009) [12]. The modulus of the clayey soil of the shaft and pile toe was estimated following the correlation of Jamiolkowski et al. (1979) [11]. Assuming that the OCR-value of soils along the shaft and pile toe was 2.0, the E_u/C_u-values therefore range between 574 and 1,416. The comparison between the estimated pile settlement seems to be a good agreement with the actual pile settlement for E_u/C_u= 700.

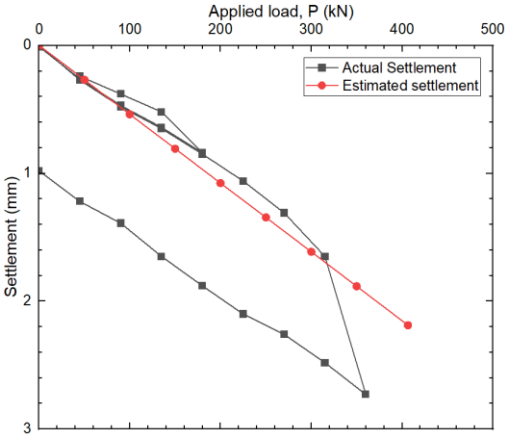

Fig. 7. Comparison between actual pile settlement and estimation following Fleming et al. (2009)

Table 8. Summary results for driven pile in site 2 (Ground test result)

Symbol	DA1-1	DA1-2	DA2	DA3
$R_{c,k}$ (kN)	290	290	290	207
γ_t	1.00	1.30	1.10	1.00
$R_{c,d}$ (kN)	290	223	264	207
γ_F	1.41	1.12	1.41	1.41
F_k (kN)	206	199	187	147
SF	1.97	2.04	2.17	2.76

Table 9. Summary results for driven pile in site 2 (Static load test)

Symbol	DA1-1	DA1-2	DA2	DA3
$R_{c,k}$ (kN)	321	321	321	N/A
γ_t	1.00	1.30	1.10	N/A
$R_{c,d}$ (kN)	321	247	292	N/A
γ_F	1.41	1.12	1.41	N/A
F_k (kN)	228	221	207	N/A
SF	1.97	2.04	2.17	N/A

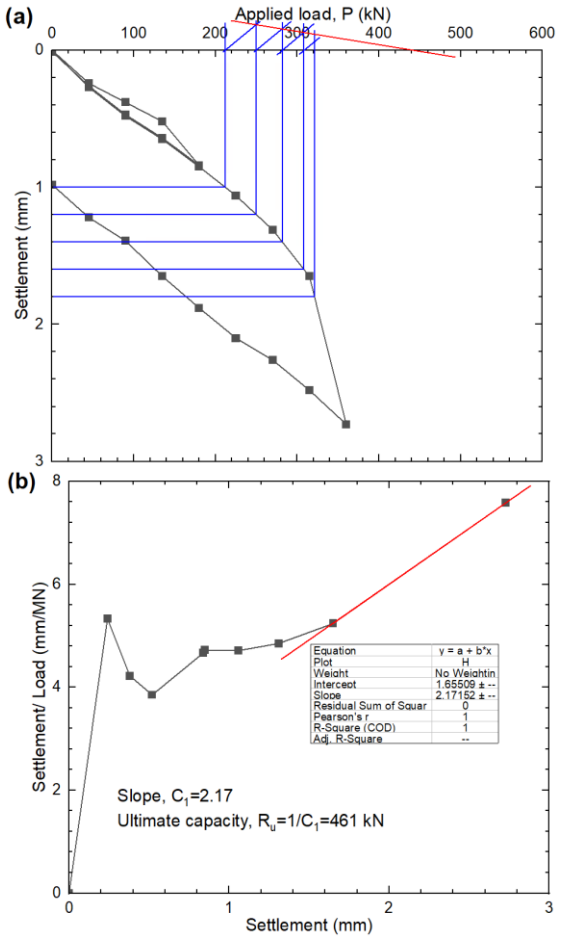

Fig. 8. Interpretation of ultimate capacity for site 2 following (a) Mazurkiewicz Method and (b) Chin-Kondner Method

5.2 Driven pile on silty sand and sandy silt

This case is an analysis of the bearing capacity of a driven pile of genset buildings. There are two available piezocone penetration tests (CPTu) in the fields. The design resistance of the pile was calculated following the Netherlands method presented previously. The level of cone resistance for the analysis must be at least 4 times of equivalent diameter deeper than the embedded depth of the pile. Thus, the minimum required data for analysis of driven pile 0.3x0.3 m embedded 8.00 m into the ground surface must be at least 9.36 m. One of them, namely CPTu2, was therefore omitted from the analysis due to insufficient available data. The soil profile of CPTu1 was determined using CPeT-IT software. The capacity analysis indicates that the toe and shaft resistances of the pile for M1 were 664 and 476 kN, respectively. It cannot be analyzed for M2 because EN Standard does not have any partial factors of soil parameters for CPT analysis. Thus, a design pile cannot be carried out for DA3. The calculations of $R_{c,d}$, F_k and SF are summarized in Table 10 by assuming that the ratio of dead load is the same as the case 1. ξ_3= ξ_4= 1.40 has been used for a

number of available ground test results, n= 1. The back-calculated FS-value are the same as the results of case 2.

One static load test was conducted on the fields for the verification of the analysis. The extrapolation methods presented in the previous case were applied to determine the ultimate capacity. The ultimate capacities from the Mazurkiewicz method and Chin-Kondner Method were 1,060 and 1,126 kN, respectively. The results seem to be comparable with the total capacity from the analytical solution. The average value from the extrapolations was used to calculate $R_{c,d}$, F_k and SF values, as shown in Table 11. As discussed in the previous case, the SF-values of the DA1-1 from the analytical solution and SLT were lower than 2.00 when SF-values from the DA1-2 and DA2 were greater than 2.00. Fig. 10 shows the comparisons between the actual and the predicted pile settlement following the NEN 9997-1 Standard [14]. The predicted result seems to be comparable with the actual value.

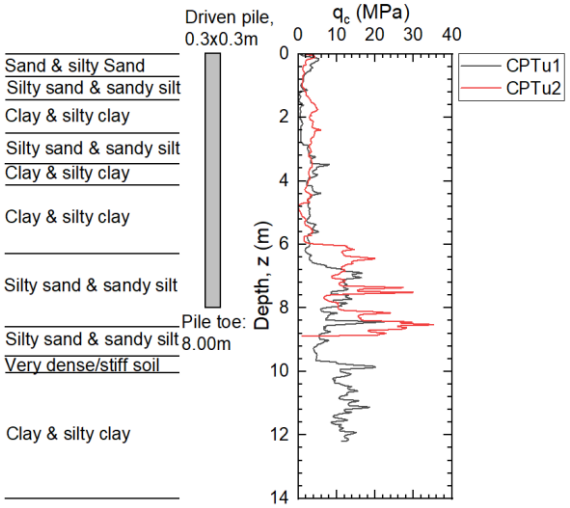

Fig. 9. Soil profile and dimension of pile test for site 3

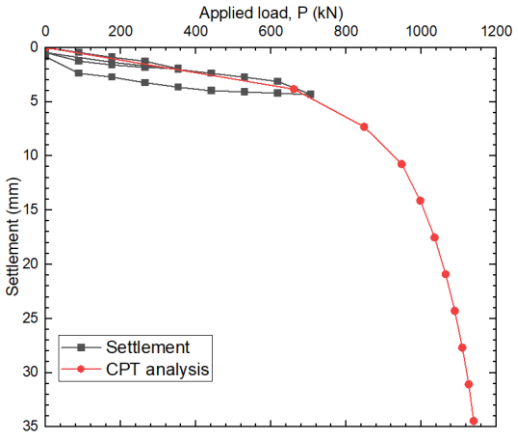

Fig. 10. Comparison between actual pile settlement and estimation following NEN 9997-1

Table 10. Summary results for driven pile in site 3 (CPT result)

Symbol	DA1-1	DA1-2	DA2	DA3
$R_{c,k}$ (kN)	814	814	814	N/A
γ_t	1.00	1.30	1.10	N/A
$R_{c,d}$ (kN)	814	626	740	N/A
γ_F	1.41	1.12	1.41	N/A
F_k (kN)	577	559	525	N/A
SF	1.97	2.04	2.17	N/A

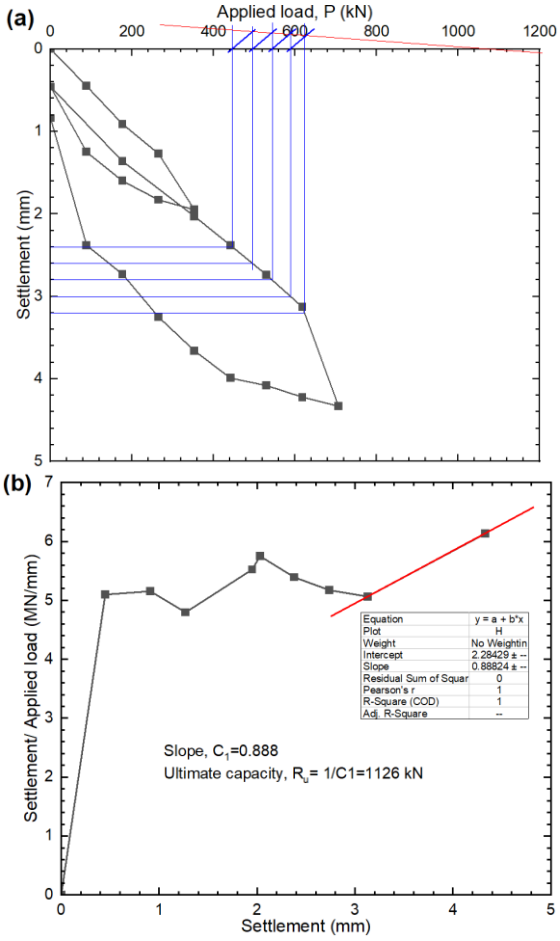

Fig. 11. Interpretation of ultimate capacity for site 3 following (a) Mazurkiewicz Method and (b) Chin-Kondner Method

Table 11. Summary results for driven pile in site 3 (Static load test)

Symbol	DA1-1	DA1-2	DA2	DA3
$R_{c,k}$ (kN)	781	781	781	N/A
γ_t	1.00	1.30	1.10	N/A
$R_{c,d}$ (kN)	781	601	710	N/A
γ_F	1.41	1.12	1.41	N/A
F_k (kN)	554	536	530	N/A
SF	1.97	2.04	2.17	N/A

6. CONCLUSIONS

The concept of Load Resistance Factor Design (LRFD) is that the design effects of actions (E_d) must be equal to or less than the design resistances (R_d). Eurocode 7 (EN 1997) Standard has adopted the LRFD method for the geotechnical design. According to EN 1997-1, the values of E_d and R_d are obtained by applying partial factors to them. The partial factors can be determined following the recommended values from EN Standard or National Annexes. The understanding and selection of proper partial factors are extremely important for design practice. The analysis of shallow foundations following EN 1997-1 indicates that the safety factors (SF) for DA1 are less than 2.0 when the SF-values of other design approaches are slightly greater than 2.00. The back-calculation seems to be unsafe when the total settlements for drained condition are greater than the allowable settlement. For pile foundation design, the estimated pile capacities are comparable to the extrapolation results from the static load tests. The safety factor (SF) from the analytical solutions and static load tests are greater than 2.0 except DA1-1 in which SF= 1.97. The analysis of pile settlement was also conducted and compared with the results from the static load tests. As a result, the empirical formulas of Fleming et al. (2009) [12] and the NEN 9997-1 Standard [14] can be applied to the estimation.

In design practice, the partial factors for the analysis of shallow and pile foundations are recommended to follow the National Annexes rather than the recommended values of EN Standard. This is because the EN Standard might provide conservative or unsafe bearing capacity. The analysis of foundation settlement is also essential for structural stability. The analysis depends on several parameters which can be determined in the laboratory or in the fields. The understanding of some parameters especially the deformation modulus of soils can lead to calculate accurately the foundation settlement.

REFERENCES

[1] B. M. Das, and N. Sivakugan, *Principles of foundation engineering (9ed)*, Boston: US: Cengage Learning, Inc., 2019.

[2] I. Smith, *Smith's element os soil mechanics (9ed)*, West Sussex: UK: John Wiley & Sons, Ltd, 2014.

[3] M. Tomlinson, and H. Woodward, *Pile design and construction practice (6 ed.)*, Florida: USA: CRC Press, 2015.

[4] *Eurocode 7: Geotechnical design – Part 1: General rules*, EN 1997-1, European Committee for Standardization, rue de Stassart, 36 B-1050 Brussels, November 2004.

[5] S. Kubo (2008), "Geomorphological Features and Subsurface Geology of the Lower Mekong Plain around Phnom Penh City, Cambodia (Southeast Asia),". *Revista Geográfica Acadêmica*, vol. 2, no. 1, pp. 20-32.

[6] S. Touch, S. Likitlersuang, and T. Pipatpongsa, "3D Geological Modelling and Geotechnical Characteristics of Phnom Penh Subsoils in Cambodia," *Engineering Geology*, vol. 178, pp. 58–69, Accessed: June 19 2014.

[7] K. Terzaghi, *Theoretical Soil Mechanics*, New York: USA: John Wiley & Sons, 1943.

[8] G. G. Meyerhof, "Some recent research on the bearing capacity of foundations," *Canadian Geotechnical Journal*, vol. 1, no. 1, pp. 16-26, Sep., 1963. Accessed: Sep., 1963. doi: doi.org/10.1139/t63-003. [Online].

[9] W. Steinbrenner (1934). "Tafeln zur Setzungsberechnung," *Die Strasse*, Vol. 1, pp. 121–124.

[10] E. N. Fox (1948). "The Mean Elastic Settlement of a Uniformly Loaded Area at a Depth below the Ground Surface," *Proceedings, 2nd International Conference on Soil Mechanics and Foundation Engineering*, Rotterdam, Vol. 1, pp. 129–132.

[11] M. Jamiolkowski, R. Lancellotta, S. Marchetti, R. Nova, and E. Pasqualini, "Design Parameters for Soft Clays," in Proceedings of the Seventh European Conference on Soil Mechanics, Brighton, UK, 1979, pp. 21–57.

[12] K. Fleming, A. Weltman, M. Randolph, and K. Elson, *Piling Engineering (3 ed.)*, Taylor & Francis, 2009.

[13] *Eurocode 7: Geotechnical design – Part 2: Ground investigation and testing*, EN 1997-2, European Committee for Standardization, 36 B-1050 Brussels, March 2007.

[14] *Geotechnical design of structures - Part 1: General rules*, NEN 9997-1, the Royal Netherlands Standardization Institute (NEN), Netherlands, 2012.

[15] K. Reinders, A. V. Seters and M. Korff, "Design of piles according to Eurocode 7-Dutch practice,", in *Procceeding of International Symposium on Design of Piles in Europe*, in Design of Piles in Europe How did Eurocode 7 Change daily practice?, vol. 2, April 2016, pp. 75-100.

[16] *Eurocode 2: Design of concrete structures- Part 1-1: General rules and rules for buildings*, EN 1992-1-1, European Committee for Standardization, Avenue Marnix 17, B-1000 Brussels, December 2004.

[17] *Eurocode 7 - Calcul géotechnique - Partie 1 : regles générales (indice de classement P94-251-1)*, NF EN 1997-1, Afnor, 2005.

[18] B. Hubert, B. Philipponnat, O. Payant, and M. Zerhouni, *Foundations et Ouvrages en terre: Manuel professional de géotechnique du BTP*, Paris: France: Eyrolles, 2019.

[19] A. Bond, and A. Harris, *Decoding Eurocode 7*, Oxon: UK: Taylor & Francis, 2008.

[20] B. K. Mazurkiewicz, "Test loading of piles according to polish regulations,". Preliminary Report No. 35, Commission on Pile Research, Royal Swedish Academy of Engineering Service, Stockholm, 1972.

[21] F. K. Chin, "Estimation of the ultimate load of piles from tests not carried to failure," in *Proceedings of Second Southeast Asian Conference on Soil Engineering*, Singapore, 11-15 June 1970, pp. 81-92.

Techno-Science Research Journal V13 (Special Issue) (2025) P 95-101

Content list available at ITC

Techno-Science Research Journal

Journal Homepage: www.ric.itc.edu.kh

Techno-Science Research Journal

Geological Investigation of Gold Mineralization in Taungni Area, Madaya Township, Mandalay Region, Myanmar

Moe Min Soe[1*]

[1] *Department of Geology, Sittway University, Myanmar*

Received: 1 November 2024; Revised: 1 January 2025; Accepted: 20 June 2025; Available online: October 2025

Abstract: *The investigated area is situated in Madaya Township, Mandalay Region, Myanmar. It is about 45 km northeast of Mandalay town. Physiographically, this area lies on the margin of the Shan Scarp Fault.Geologically,the area lies within the Mogok Metamorphic Belt (MMB), bounded by the Shan Scarp Fault on the east and by the Sagaing Fault on the west. The purpose of the current research work is to increase the minerals resources inventory of the country, with the geological and geochemical data acquired contributing to future exploration efforts. Stratigraphically, the investigated area is mainly composed of two stratigraphic units:Precambrian Unit and Cambrian Unit. The Precambrian Unit of the Chaungmagyi Group is entirely composed of low-grade regional metamorphic rocks of phyllite,slate and quartzite. The Cambrian Unit of Kyaukkwe orthoquartzite is exposed in the southern part of the area. The presence of major fault is signified by the straight alignment of stream courses and topographic expression. The methods of investigation are field investigation and laboratory investigation. Laboratory investigation include microscopic study and rocks geochemical analysis by atomic absorption spectrophotometer(AAS).Geochemical assayed value of the rock chip samples gave mean value(X) of Au(<4ppm),Ag(<5ppm),Cu(<100ppm),Fe(<8200ppm)and As(<60ppm)pointed to mineralization in the area. Gold mineralization is characterized by an increase in sulfide content with a notable abundance of hematite. In reflected light irregular patches of gold occurs within hematite matrix. Gold grains range from 0.002mm to 0.5mm in size.Silicification,pyritization and hematitiztion assemblages have been recognized at the area. The northeast-southwest trending sigmoidal fault, Phayaung Taung Fault structures and Chaungmagyi Group rocks are controlled of mineralization in the area. The stratigraphic, lithologic, structural and geochemical guides were important in exploration of the gold mineralization in the investigated area.*

Keywords: Mogok Metamorphic Belt (MMB),Shan Scarp Fault, Sagaing Fault,Phayaung Taung Fault

1. INTRODUCTION

The investigated area is situated in Madaya Township, Mandalay Region, Myanmar.It is about 45 km northeast of Mandalay town. The area is bounded by latitude 22 ᵈ 5′ 00″ N and longitude 96 ᵈ 13′ 00″ E. This area is covered by Myanmar Survey Map no. 93B/8 on a scale 1 inch to 1 mile (1:63360) **Fig.1**.

The area is easily accessible from Mandalay town by using the Mandalay-Mogok motor road. Physiographically, this area lies on the margin of the Shan Scarp Fault region. The annual rainfall is more than 150cm and the temperature ranges from 21 ᵈC to 40 ᵈC. The investigated area is extremely hot in the summer.

The purpose of the current research work is to increase the minerals resources inventory of the country. With the acquired geological and geochemical data that would aid exploration in the future.

Geologically, the investigated area lies within the Mogok Metamorphic Belt (MMB). It is bounded by the Shan Scarp Fault on the east and by the Sagaing Fault on the west. Topographically, the general elevation in the area is about 500m above mean sea level. The stream and tributaries draining this area generally show the dendritic pattern. This area is bounded by On-hlut stream in the north and Ye-cho stream in the south. Most of the tributaries flow from east to west.

Stratigraphically, the investigated area is mainly composed of two stratigraphic rock units. The two stratigraphic rock units from oldest to youngest are Precambrian Unit and Cambrian Unit.

* Corresponding author: Moe Min Soe
E-mail: *moemins893@gmail.com;* Tel: *+9595170496*

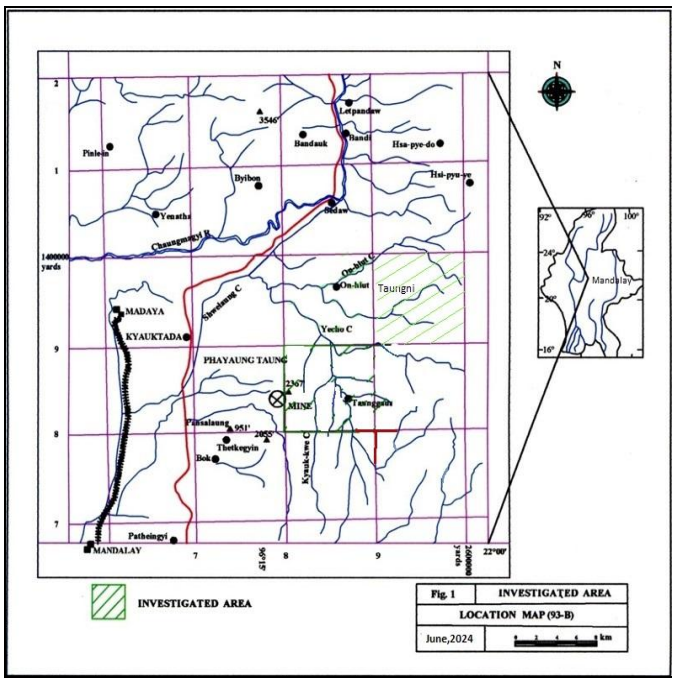

Fig.1. Location map of the investigation area

1.1 Precambrian Unit

The Precambrian unit of the Chaungmagyi Group is widely distributed in this area. The Chaungmagyi Group covers half of the research area. It is entirely composed of low-grade regional metamorphic rocks of phyllite, slate and quartzite.

There are four rock units of the Chaungmagyi Group. They are in ascending order; Nyaung Chaung Chloritic Phyllite, Kin Sandy Phyllite, Graphitic-garnet-biotite schist and Maukkaw Quartzite.

1.2 Cambrian Unit

The Cambrian Unit of Kyaukkwe Orthoquartzite is exposed in the southern part of the area. This orthoquartzite is white to pinkish, friable to compact and thick bedded. This unit trends nearly N-S and the beds usually dip30-40 degrees eastward but have higher dip angles in the fault zone. In the present area, the Kyaukkwe orthoquartzite unit comes against the Chaungmagyi Group with a faulted contact.

1.3 Structure

The present investigated region lies on the eastern fringe of the Mogok Metamorphic Belt (MMB) occupied by epimetasediment of the Chaungmagyi Group and on the western margin of the Shan Plateau **Fig.2**.

Gold mineralization in the Mogok Metamorphic Belt (MMB) has followed the sequence of tectonic history during metamorphism. The tectonism and metamorphism cause by the collision of the India and Asia plates during the Cenozoic [1].

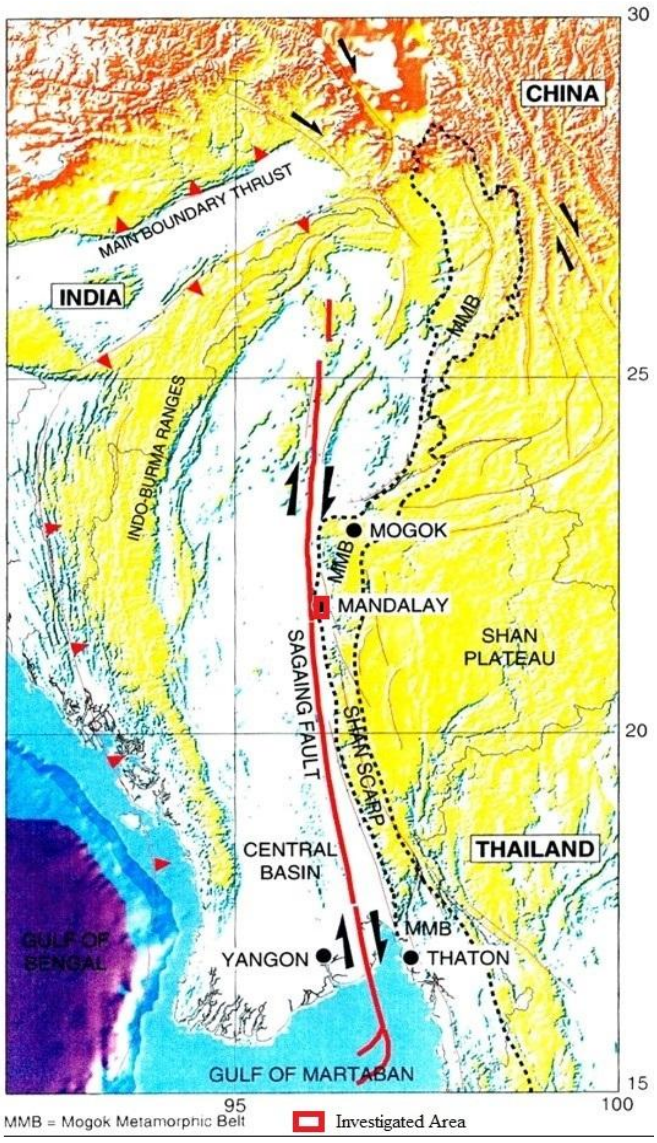

Fig.2. Physiographic features of Myanmar (Modified after [1])

The presence of major fault is signified by the straight alignment of stream courses and topographic expression. There are two major faults system; one trend N-S and the other trends NE-SW.Tight folds and drag folds are developed mostly in the Chaungmagyi Group and broad open folds occurs in Kyaukkwe orthoquartzite.

In the present area, all of the joints are tectonic joints. They have resulted from folding and three sets of joints are recognized; strike joints, dip joints and conjugated joints. Joints in the Chaungmagyi Group are of great importance in this area

because gold mineralization is in fractures, joints and weak planes occupying the crest of the anticline.[2]

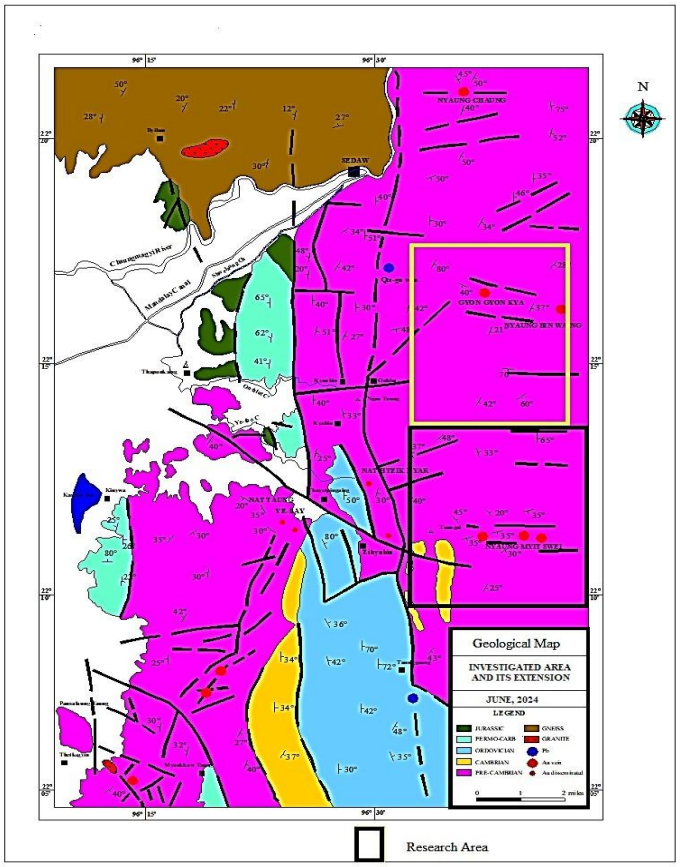

Fig.3. Geological map of the investigated area

2. METHODOLOGY

2.1 Area Selection

The area for the study was chosen based on the previous knowledge of geology and mineralization. The mineralization have been controlled by the northeast-southwest trending sigmoidal fault, Phayaung Taung Fault.[2] Toward the south of fault zone is concealed below younger rocks and alluvium. It was decided to cover the northeastern part of Phayaung Taung fault zone and where the metasediment of the Chaungmagyi Group is well exposed. The area covered during the current research work was 9 square kilometers.

2.1 Field Investigation

Geological investigation was carried out in the study area during the summer and winter of the year. The topographic map of 93B/8 is used for the preliminary studies. Geochemical sampling of rocks was collected at random and mineralized vein samples was taken that samples were collected from each rock unit present in the area. The structural features of this area and approximate boundaries of some major units were identified on the aerial photographs and satellite photos.

2.2 Laboratory Investigation

Petrographic thin-sections and polished sections were prepared from representative samples collected from all the distinctive rock types and ore specimens were made for the identification of gold and other opaque minerals. Rock samples were assayed for gold, copper, silver, iron and arsenic by using atomic absorption spectrophotometer(AAS) in the geochemical laboratory of the Applied Geology Department at Yangon University.

3. RESULTS AND DISCUSSION

3.1 Geochemical Investigation

Rock samples were collected from the Taungni area. These samples were packed and analyzed in the Applied Geology Department of Yangon University. In the laboratory, the 80 mesh size fraction of the samples was digested with aqua-regia. The element analysis was done by an atomic absorption spectrophotometer. The data obtained from geochemical analysis of rock samples have been treated statistically by computer using“ SPSS” software. This was done by calculating the value of mean (X) and standard deviation (S). The normal background values for the mean (X) and threshold value were taken as (X+S).

A total of 20 rock samples were assayed. The concentration of gold, silver and copper are expressed as geochemical dot maps. The large solid circles indicate higher concentration values. Rock chip assays when plotted indicated anomalous gold area within the research area. The Au, Ag and Cu anomalies apparently coincides at the Nyaung Myit Swei area, east of the Taungni area.

Table 1. Distribution of Elements in Rock Samples

Element	Mean (X)ppm	Standard Deviation (S)ppm	Threshold (X+S)ppm
Au	2.49	4.22	6.71
Ag	4.29	3.97	8.26
Cu	97.30	74.30	171.60
Fe	8141.00	1110.42	9251.42
As	56.20	12.63	68.83

3.1.1 Distribution of Gold (Au)

The concentration of gold in rock samples ranges from 0.02 ppm to 9.28 ppm. The mean value (X) is 2.49 ppm and the threshold value (X+S) is 6.71 ppm. Geochemical dot map shows that the high gold values coincide with high copper and silver values. The concentration of gold in rock sample from the research area is shown in **Fig.4**.

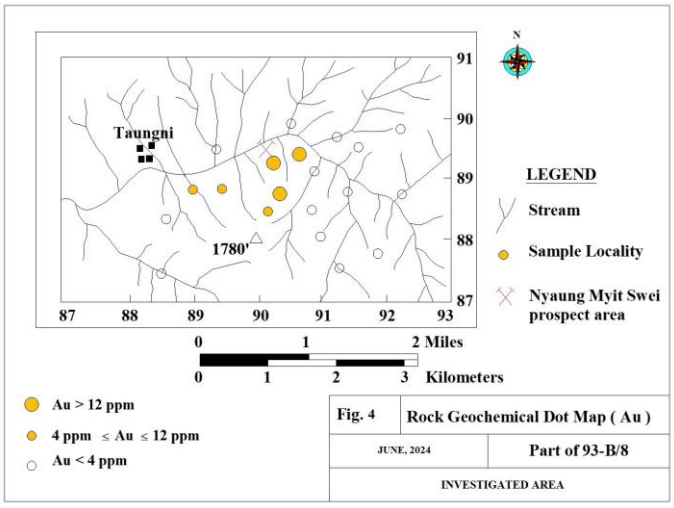

Fig.4. Geochemical dot map of gold (Au) in rocks

3.1.2 Distribution of Silver (Ag)

The concentration of silver in rock samples ranges from 0.25 ppm to 10.58 ppm. The mean value (X) is 4.29 ppm and the threshold value (X+S) is 8.26 ppm. Geochemical dot map shows that the high silver values coincide with high gold and copper values. The concentration of silver in rock sample from the research area is shown in **Fig.5**.

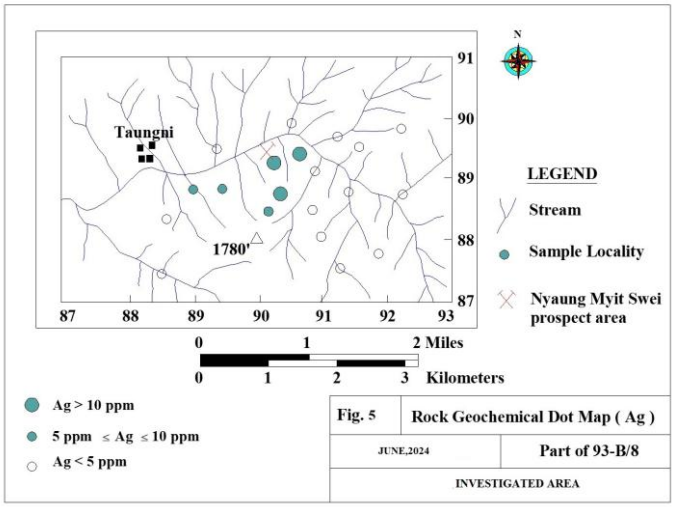

Fig.5. Geochemical dot map of silver (Ag) in rocks

3.1.3 Distribution of Copper (Cu)

The concentration of copper in rock samples ranges from 20 ppm to 225 ppm. The mean value (X) is 97.30 ppm and the threshold value (X+S) is 171.60 ppm.Geochemical dot map shows that the high copper values coincide with high gold and silver values. The concentration of copper in rock sample from the research area is shown in **Fig.6**.

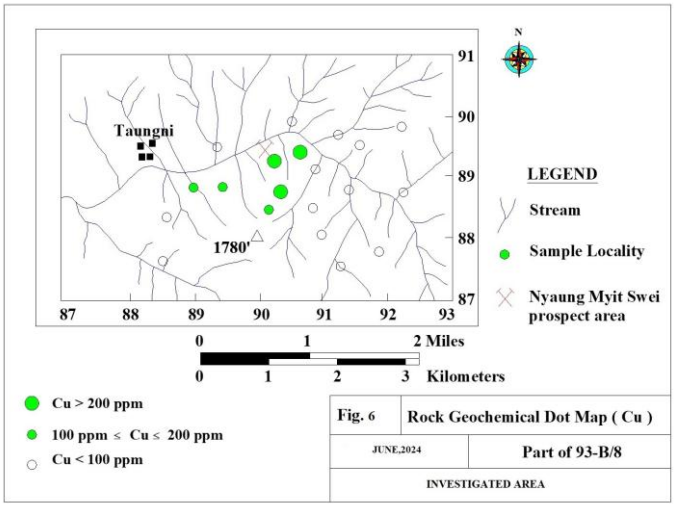

Fig.6. Geochemical dot map of copper (Cu) in rocks

3.1.4 Distribution of Iron (Fe)

The concentration of iron in rock samples ranges from 6420 ppm to 9890 ppm. The mean value (X) is 8141.00 ppm and the threshold value (X+S) is 9251.42 ppm.

3.1.5 Distribution of Arsenic (As)

The concentration of arsenic in rock samples ranges from 38 ppm to 85 ppm. The mean value (X) is 56.20 ppm and the threshold value (X+S) is 68.83 ppm.

3.2 Mineralization

In the research area, gold mineralization is characterized by an increase in sulfide (pyrite) content with a striking feature being the abundance of hematite(specularite). It can be inferred that mineralization was probably deposited in an oxidizing environment.[3] Gold dispersion is found in the wallrocks as disseminated grains accompanied by pyrite and hematite. In the Taungni area the dispersion zone extend up to 2 meters from the vein.

3.3 Host Lithology

Chaungmagyi Group rocks of Kin Sandy Phyllite and Maukkaw Quartzite have an important bearing of the gold mineralization in the research area.

3.4 Ore Mineralogy

Microscopic studies of ore specimens were conducted to identify of gold and other opaque minerals with associated with mineralization.

Under reflected light, gold occurs irregular patches within hematite matrix. Gold grains ranges from 0.002 mm to 0.5 mm in size. Gold grain is characterized by their bright golden yellow color ,very high reflectance, softness and extinction properties.[4]

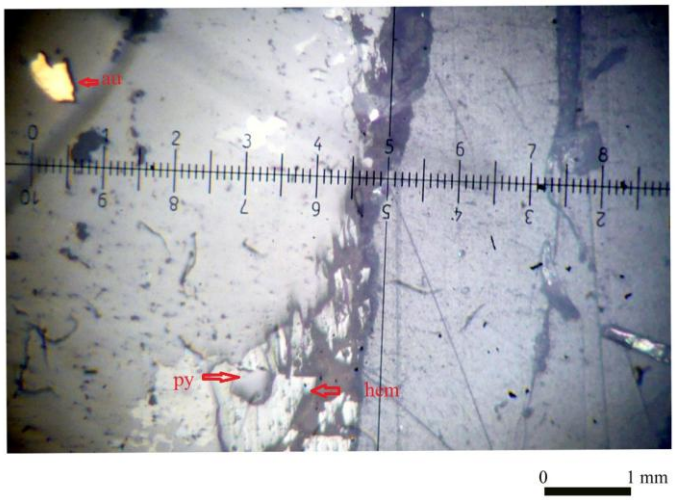

Fig,7. Irregular patches of gold (bright golden yellow) and pyrite(light grey) in hematite matrix (Reflected Light)

Silver minerals occurs as anhedral mass. The reflection color appears bright silver white within the quartz matrix. The size of silver minerals ranges from 0.5mm to 1mm.Numerous scratches developed on the surface of silver minerals numerous during polishing. [5]

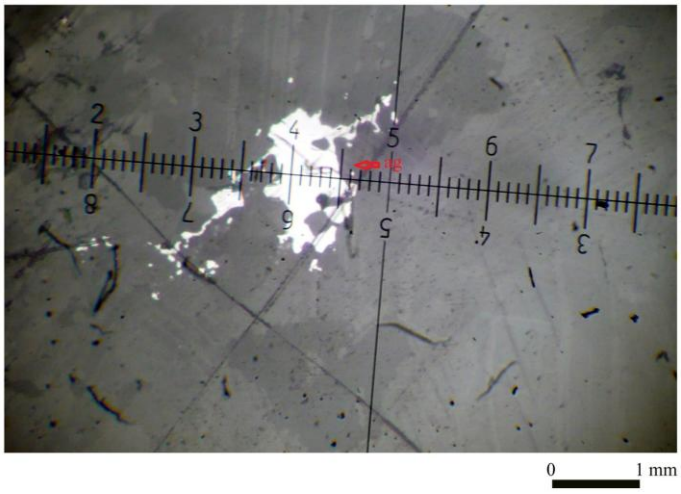

Fig.8. Anhedral silver (white) in quartz matrix (Reflected Light)

Pyrite occurs as euhedral to subhedral crystalline masses often associated with chalcopyrite and hematite. The individual grain size from 0.5 mm to 3 mm.A few pyrite grains show a skeleton-like texture. Pyrite is distinguished from chalcopyrite by its color (white) and greater hardness.

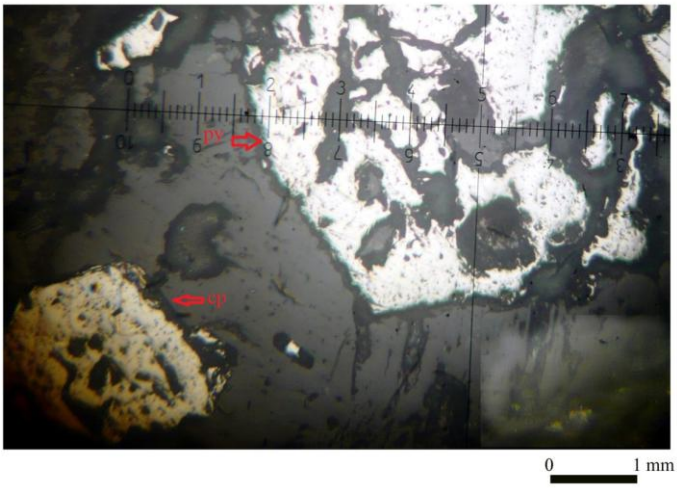

Fig.9. A skeleton-like pyrite (white) as a result of hematite replacement and chalcopyrite (yellow) in matrix (Reflected Light)

3.5 Alteration

Silicification, pyritization and hematitization assemblages have been recognized in the research area. The host rocks have undergone considerable silicification, with quartz being the primary constituent of the gold veins.

Pyritization occurs near the gold-quartz veins, which typically contain a high concentration of pyrite. Hematitization

results in the formation of red iron oxides near the gold-bearing veins, serving as an indicator of possible mineralization.

The alteration assemblages were formed during the premineralization stage and the hydrothermal fluids are as are concentrated,weakly dissociated, alkali chloride-rich electrolyte solution. These hydrothermal fluids followed the channel ways later used by gold transporting fluids.[6]

3.6 Controls of Mineralization

In the research area, controls of mineralization are rocks of Chaungmagyi Group and Phayaung Taung Fault structures. Detailed studies of the mineralized veins reveal two parallel fractures linked by shattered broken ground. This pattern is commonly referred to as a dilational jog and a symoid loop. The linking fracture is considered to form via stress field building up at the main fracture tips which are ultimately relieved via brittle semi-oriented rupture. The reason for stress concentration could be either directly tectonic or a fluid pressure build up associated with metamorphism.[7]

Gold mineralization is hosted within the metamorphic rocks of Chaungmagyi Group, formed through the precipitation gold transported by metamorphic fluids generated during metamorphism. Subsequently, an S-type plutonic intrusion occurred.[8] These events took place during the period of collision between India and Asia Plates the extension of the metamorphic belt, the formation of major strike slip faults.[1] Fault structures provided pathways for the fluid flow and played a crucial role controlling the mineralization.[2]

The belt of metasediments composed of phyllite and quartzite of Chaungmagyi Group serves as a regional guide to gold mineralization of the area. The two regional faults, the Sagaing Fault and the Shan Scarp Fault probably played a significant role in the tectonics of the region.

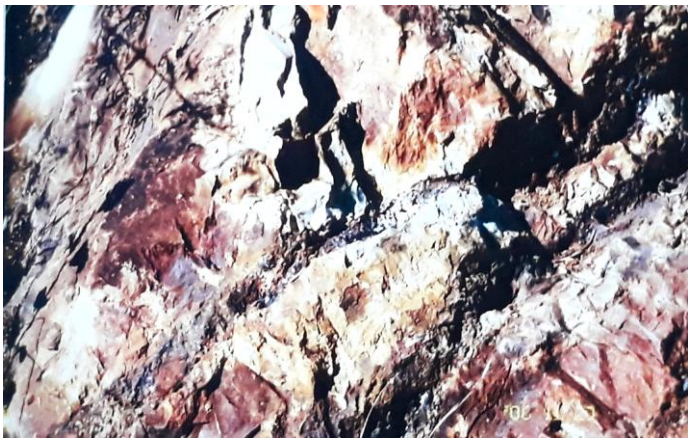

Fig.10. Photograph showing dilational jog of Au+pyrite-specularite vein in phyllite,Chaungmagyi Group

Fig.11. Photograph showing Au+pyrite mineralization in quartz vein, Chaungmagyi Group

3.7 Style of Mineralization

The style of mineralization is characterized by the dissemination of gold associated with bleached quartzite. It is inferred that mineralization has been derived from the hydrothermal fluids and the fissures veins of openings in Chaungmagyi Group rocks that may serve as receptacles for ore or permit the movement of solution on their constituents through the rocks and rock alteration openings play an important role in formation of epigenetic mineral deposits [6].

3.8 Ore Paragenesis

The microtextures and microstructures are used to decide the order of mineral deposition. The study of polished sections across the area has established a general sequence of minerals deposition. The open-space texture indicated that fine- grained minerals on the walls of a cavity with coarser minerals in the center. The earliest formed minerals that form along the sides of an open vein are usually fine-grained, probably because of heat loss to the wall rocks and consequent rapid crystallization. The later form minerals that form in the centers of veins are inclined to be coarse and probably form from more dilute, cooler solutions late in the vein history.[6] These evidences indicated that pyrite and hematite were precipitated first The formation of chalcopyrite before silver and gold. Gold is late in paragenetic sequence.

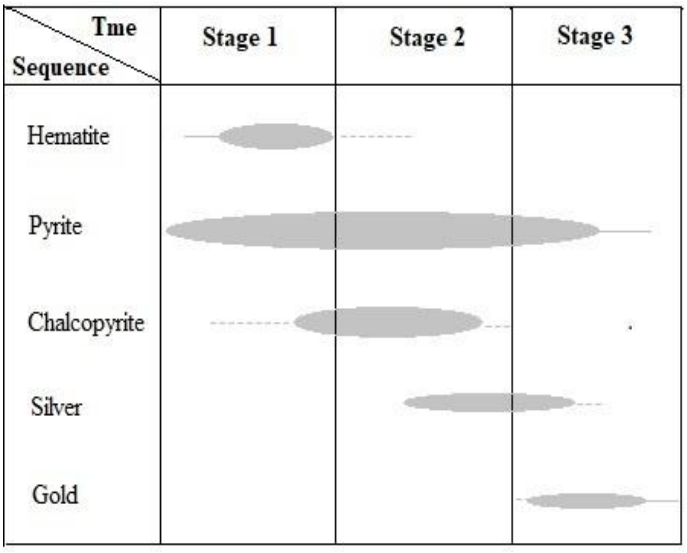

Fig.12. Paragenetic sequence diagram of the investigated area

4. CONCLUSIONS

In the research area, gold mineralization was found in phyllites and quartzites units of the Chaungmagyi Group. Geochemical surveys using rock chip samples were useful tool in location of mineralization. At Taungni area, the rock chip samples with mean value (X) of Au (<4ppm), Ag (<5ppm) and Cu (<100ppm) pointed to mineralization. The stratigraphic, lithologic, structural and geochemical factors were important exploration guides of the gold mineralization in the research area. Evidence of structures and textures shows that mineralization has been derived from the hydrothermal fluids, with deposition occurring in an epigenetic origin.

ACKNOWLEDGMENTS

I wish to express my sincere gratitude to Chairman and all committee members of EraGET2024 for allowing me to submit this research paper.

REFERENCES

[1] GIAC Project, " Geodynamic of India-Asia collision and tectonics of Myanmar",2001

[2] Moe Min Soe, " Geology and Geochemistry of the Phayaung Taung Gold Mineralization Extension Area, Mandalay Division" PhD dissertation, Dept. Geol., Yangon Uni., Myanmar,MA,2009.

[3] Mead L. Jensen and Alan M.Bateman " Economic Mineral Deposits" 3rd edition, John Wiley & Sons, New York, 1981.pp.239-250

[4] Dan Marshall ,et al, " Ore Mineral Altas " Geological Association of Canada, Mineral Deposits Division, Canada, 2004, pp.24-92

[5] Bernhard Pracejus," The Ore Minerals Under the Microscope " An Optical Guide, 1th edition, Elsevier, The Netherlands Linacre House, Jordan Hill, Oxford OX2 8DP,UK,2008, pp 4-190

[6] John M.Guilbert and Charles F. Park,Jr " The Geology of Ore Deposits " 5th printing, W.H Freeman and Company, New York,1996,pp 25-162

[7] Roger Taylor, " Ore Texture" Recognition and Interpretation , Springer Dodrecht Heidelberg London, New York ,2009,pp 163-218

[8] Khin Zaw, "Geological, petrological and geochemical characteristics of the granitoid rocks in Burma with special reference to W-Sn mineralization" Southeast Asia Earth Science Journal, vol.4, No.4,1990

Techno-Science Research Journal V13 (Special Issue) (2025) P 102-109

Content list available at ITC

Techno-Science Research Journal

Journal Homepage: http://techno-srj.itc.edu.kh/

Techno-Science Research Journal

The Thae Phyu Chaung gold deposit in Kyaikhto District, Southern Myanmar: hydrothermal alteration zones and mineralogical characteristics

Myo Kyaw Hlaing[1*], Kotaro Yonezu[2], Koichiro Watanabe[2]

[1] *Department of Geology, University of Yangon, Yangon, Kamayut 11041, Myanmar*
[2] *Department of Earth Resources Engineering, Faculty of Engineering, Kyushu University, Fukuoka 819-0395, Japan*

Received: 1 November 2024; Revised: 1 January 2025; Accepted: 20 June 2025; Available online: October 2025

Abstract: *The Thae Phyu Chaung deposit, located in the Kyaikhto gold district of the Mergui belt, is a newly discovered gold deposit in Myanmar. The present research investigates gold deposits utilizing petrography, ore microscopy, and X-ray diffraction to better understand their mineralogy, alteration, and formation conditions. Gold mineralization is found in metasedimentary rocks (mainly of the Carboniferous age) that contain black slate and slaty phyllite. There is a trending N-S comprising brittle-ductile shear zones, which are mainly hosted by slate and slaty phyllite, that are metamorphosed into sub-greenschist to greenschist facies. Four distinctive alteration styles consist of muscovite/sericite + chlorite ± pyrite I ± quartz in stage I, muscovite/sericite + chlorite ± pyrite II ± quartz in stage II, muscovite/sericite + chlorite + kaolinite ± illite/semectite ± pyrite II ± quartz in stage III, and kaolinite + illite/semectite ± hematite ± magnetite in stage IV. Stages I and II are typical of the deeper parts of the hydrothermal system, and these types have provided clues to stages III and IV developed at shallower crustal depths, locally close to the surface. Stages III and IV of alterations are probably to be late-stage, shallow-level conditions. The amount of gold is associated with sulfide minerals (pyrite, chalcopyrite, sphalerite, and galena) and disseminated along the fractures. Based on mineralogical investigations, ore occurrences are considered the product of low- to moderate-temperature hydrothermal processes.*

Keywords: Alteration, Greenschist facies, Thae Phyu Chaung Gold Deposit, southern Myanmar

1. INTRODUCTION

The Thae Phyu Chaung deposit (TPC) is located in the southern part of the Mergui Belt. The belt is one of the best–known metallogenic provinces in Myanmar with orogenic gold deposits (e.g., Modi Taung), tin and tungsten deposits (e.g., Mawchi), antimony deposits (e.g., Kaw Hket–Taunggalay–Htimiwa) and copper deposits (e.g., Meyon) (Fig.1). Hydrothermal alteration is possibly associated with numerous precious and base metal deposits, such as orogenic gold deposits, volcanogenic massive sulfide (VMS) deposits, porphyries and intrusion–related deposits and Archean greenstone belts. These deposits are the results of magma to hydrothermal processes, which require alteration of thin halos (centimeters) to extensive halos (hundreds of kilometers) beyond mineralization [1–6].

Various studies show that the key characteristics of geochemical dispersion can be used to determine orogenic gold exploration targets, including chemical and mineral changes in rock [5, 10–14]. The same term applies to metamorphism. However, the chemical changes caused by metamorphism are usually less intense than those found in altered rocks. The distinguishing of these processes is implicit, where deposits consist of metamorphic fluids, such as orogenic gold deposits [6, 15]. The genesis of many of the world's largest gold deposits has included metamorphic processes, including gold in slate belts, South Africa's Witwatersrand goldfields, Nevada's Carlin deposits, and gold in Archaean greenstone belts [16].

Controls on the formation or lack of formation of hydrothermal alteration zones throughout orogenic gold deposits

*Corresponding author: Myo Kyaw Hlaing
E-mail: myokyawhlaing@uy.edu.mm; Tel: +959-776-571-577; Fax:+95 (0)1 510721.

are often confused and although there are several unification models in the formation of orogenic gold deposits, the characteristics of the related alterations are less well reported [17–21]. This study will focus on chemical and mineralogical changes caused by moderate to high temperature mineralizing fluids (300–400°C for orogenic gold deposits) influenced by hydrothermal alteration [6, 15]. This paper was carried out as an attempt to investigate the alteration mineralogy and chemistry of the orogenic gold deposit by the application of petrography, ore microscopy and X–ray diffraction analysis.

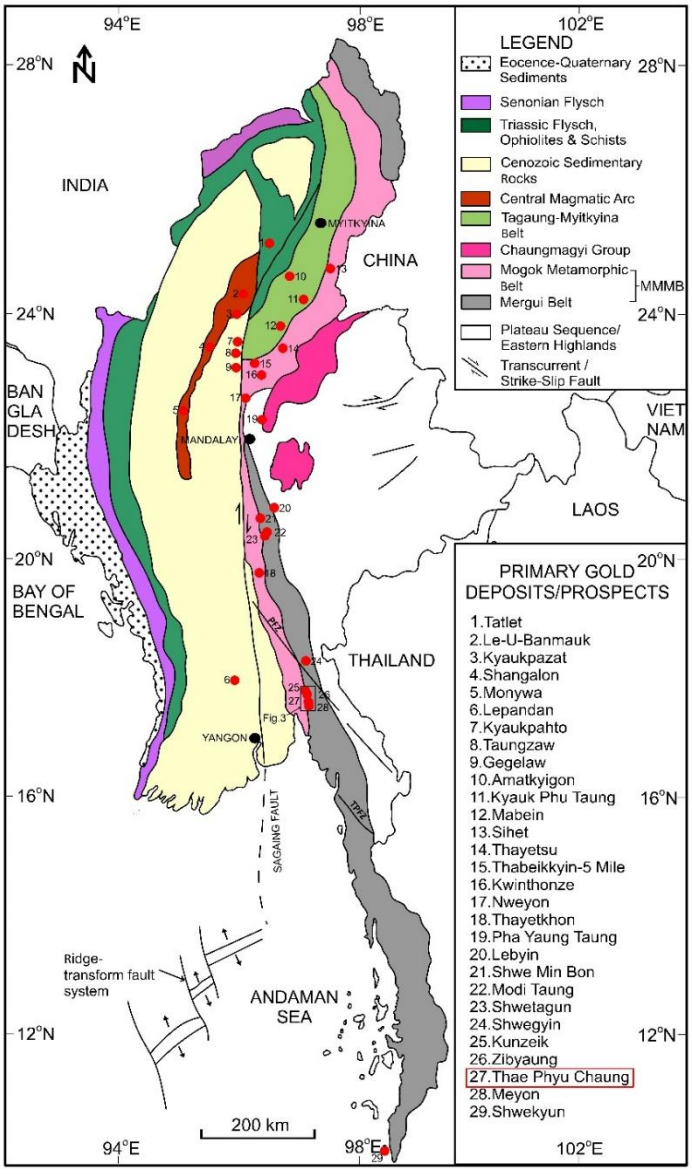

Fig. 1. Major structural belts, and gold occurrences in Myanmar (Modified after [7–9], PFZ, Papun Fault Zone; TPFZ, Three Pagodas Pass Fault Zone; MMMB, Mogok–Mandalay–Mergui Belt).

2. GEOLOGIC SETTING AND DEPOSIT GEOLOGY

Numerous gold deposits and prospects emerge along the Mergui Belt, some of which are currently being mined for gold, such as the Modi Taung and Thae Phyu Chaung deposits. The Mergui Belt comprises variably–reworked in any type of supracrustal rocks or in the vicinity of regional, crustal–scale deformation zones with a brittle to ductile type of deformation at sub–greenschist to greenschist facies that were subsequently intruded by Cretaceous and Eocene granitoids ([22–28]; (Fig. 1)). The Mergui Belt consists mostly of upper Carboniferous to lower Permian metasedimentary rocks that were metamorphosed and exhumed in the lower Jurassic, coexisting or unexpectedly accompanied by mineralization that all hosts numerous orogenic gold occurrences [7-9].

The Thae Phyu Chaung deposit of the Kyaikhto gold district, situated in the Mergui Belt between Mogok Metamophic Belt and Sibumasu, is the eastern part of the Burma Plate. The rocks in the surroundings of Thae Phyu Chaung mainly consists of metasedimentary rock sequences of slate, slaty phyllite, schist and granitic rocks (Fig. 2). Thae Phyu Chaung is spatially associated with N–S, NNE–NNW trending and hosted by back slate and slaty phyllite (Fig. 3). Black slate and slaty phyllite are mostly slightly laminated to thickly bedded, with foliation ranging from 2 mm to 3 cm thick (Fig. 4 a, c). Black slate with a blocky form in outcrop is a very fine–grained rock with a dark grey to black in color. Black slate is strongly altered (silicified, chloritized and sericitized). Gold–bearing quartz veins are usually massive or laminated and milky–white in reddish or greenish color (Fig. 4 a, b). They typically contain vugs, which are sometimes filled with iron oxides, clays and sometimes with fragments of the host rocks (Fig. 4 a–d). Even so, Thae Phyu Chaung is structurally controlled by fault and fracture zones that cross the metasedimentary rocks. Hydrothermal alteration was controlled by the fracture system, the foliation, and a shear fabric. However, the gold mineralization is not ubiquitous throughout the altered shear zones but is rather confined to alteration zones primarily composed of chlorite, muscovite/sericite, and pyrite. There is no direct genetic association between the orogenic gold deposits and the igneous intrusions in the Mergui Belt [7, 27–29].

3. MAPPING, SAMPLING AND ANALYTICAL METHODS

Field work involves mapping, alteration and mineralization of surface geology, as well as sampling of representative types of rocks, altered rocks and gold–bearing quartz veins. The alteration was mapped according to the white greyish color, the silky luster and altered lamination of the slate and slaty phyllite, and oxidized and silicified nature of the altered rocks (claystone) (Fig. 3). As the deposit is heavily metamorphosed and hydrothermally altered, preference was given to those types of hydrothermal alteration samples.

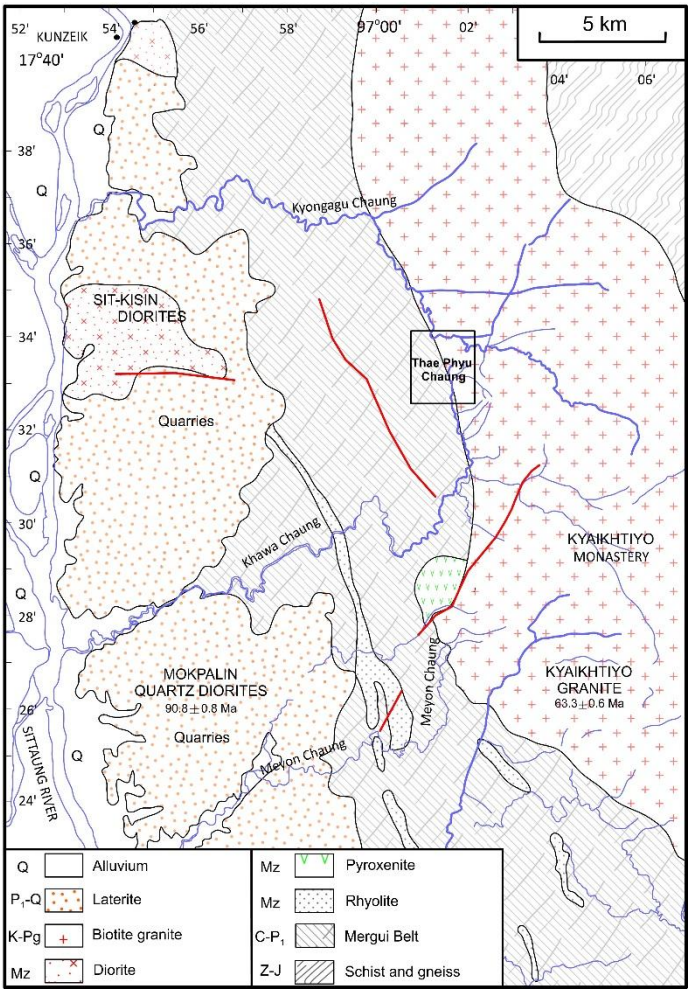

Fig. 2. Geological map of the Kyaikhto Gold District. Red lines are faults (Modified after [9, 26, 30]). Abbreviations: Q = Quaternary, P1-Q = Lower Pliocene to Quaternary, K-Pg = Cretaceous to Paleogene, Mz = Mesozoic, C-P1= Carboniferous to Lower Permian, ZJ = Late Proterozoic to partly Jurassic.

Laboratory work comprises petrographic analysis of the thin section and ore microscopy for polished section and XRD (X–ray diffraction) analysis. A systematic petrographic analysis was carried out on thirty–five representative thin sections of Thae Phyu Chaung. Hydrothermal alteration minerals were determined by X–ray diffraction (XRD) following hydraulic elutriation. Altered host rocks and claystone were gently crushed in stainless steel mortars. Clay fractions (<2 μm) from the fine-grained metasedimentary rocks separated by the sedimentation method were analyzed as usual (air dried at 25 °C for 16 h), hydrochloric acid (HCL), ethylene glycolated—EG (remained in a desiccator at 60 °C for 16 h). Mineral separate was put in thin sections and air-dried for XRD analysis. The oriented samples were analyzed using the Rigaku Ultima IV X–ray diffractometer, which operates at 40kV and 20mA with a CuKα range of 2.0–65.0 (2θ). Semi-quantitative abundances of rock–forming minerals have been identified using [31] external standard method. In addition, the relative abundance of clay minerals was obtained using their basal reflections and the mineral intensity factors defined by [32]. The different mixed–layer mineral phases were classified using [32]. Mineral abbreviations were used after [33]. All analyzes were conducted at the Department of Earth Resources Engineering, Kyushu University.

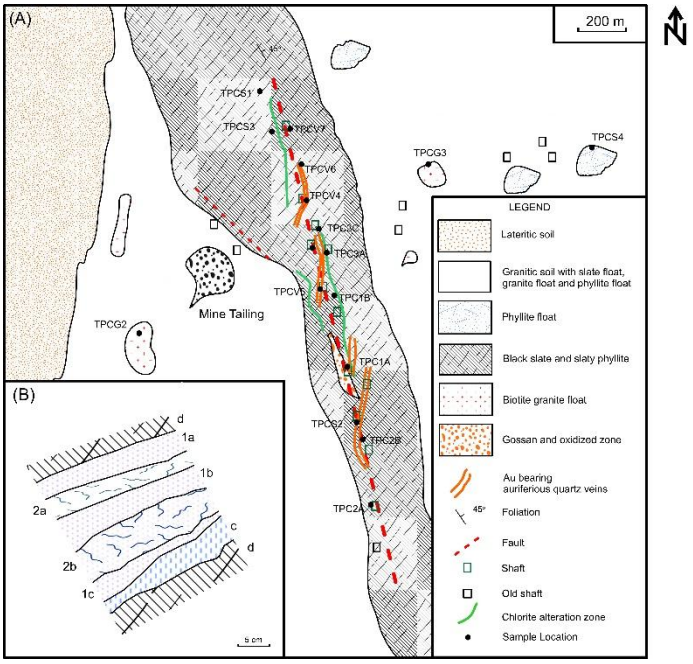

Fig. 3. (A) Mineralization map of Thae Phyu Chaung. (B) Mineralized vein textures in the black slate and slaty phyllite (1a), (1b), and (1c) the massive auriferous quartz veins (2a) and (2b) the laminated auriferous quartz veins (c) the chlorite alteration with quartz veinlets, and (d) the host rocks.

4. RESULTS

4.1 Mineral Paragenesis

The gold–bearing quartz veins formed in slate and slaty phyllite contact would have controlled the early hydrothermal circulation. The hydrothermal ore–forming process of these veins can be divided into four ore stages by considering the relationship between the observed minerals and the timing of their crystallization. (Fig. 5). The main ore minerals of Thae Phyu Chaung are pyrite, chalcopyrite, sphalerite, galena, native gold, electrum and telluride–bearing minerals, which include hessite, tellurobismuthite, hedleyite, altaite, cervelleite, tetradymite, and petzite.

Stage I began with an intense silicification that affected the wall rocks (slate and slaty phyllite), and marked the beginning of the formation of a quartz vein system. Subsequently, quartz (Q1), muscovite, epidote, chlorite, pyrite I, chalcopyrite, sphalerite, galena, pyrrhotite, arsenopyrite and native gold minerals were deposited. Quartz (Q1) occurs as deformed anhedral aggregates. Alteration assemblages in all host rocks appear mostly composed of chlorite, muscovite, and epidote. These mineral assemblages represent those common between sub–greenschist and greenschist facies within orogenic and regional metamorphism. In Thae Phyu Chaung, gold is the only significant native metal found. Gold typically occurs in a disseminated form as anhedral grains surrounded by silicates and fractured muscovite/sericite and chlorite grains and the epidote is a regional metamorphic mineral in slate and slaty phyllite (Fig. 6a–f). Hydrothermal processes that eventually contributed to the formation of Thae Phyu Chaung were then initiated early in the formation of the main fault system under late metamorphic conditions.

The stage II is characterized by the mineral paragenesis of base metal group (chalcopyrite, sphalerite, galena). Textural relationships show that pyrite II, famatinite, tellurobismuthite, petzite, altaite, hessite with quartz (Q2) formed throughout the entire in this stage (Fig. 6a–i). Native gold and electrum appear to be coexistent with sulphides, muscovite/sericite and chlorite minerals.

The stage III is the hydrothermal occurrence and the main episode of gold mineralization that was responsible for the dissolution of muscovite/sericite, chlorite, kaolinite, illite/semectite and pyrite and for the substitution of transparent microstructure quartz (Q3) minerals. This stage is characterized by the deposition of paragenesis, consisting of chalcopyrite, bismuth, hedleyite and galena, in intergranular pores and microcracks in preformed minerals (Fig. 6a–i), resulting in the formation of gold–bearing sulphide minerals (e.g., pyrite II, chalcopyrite, sphalerite and galena), native minerals (e.g., native bismuth, native silver). Gold exists mainly as native particles that are easily identified by light microscopy in microcracks that cross early sulphides (e.g., pyrite II, chalcopyrite).

The stage IV is marked by a late hydrothermal circulation and secondary pore space (fractures and breccias). This stage is also associated with recrystallized kaolinite, illite/semectite-hematite and magnetite. Significant sulfide mineralogical variations include compositional modifications (e.g., pyrite→ hematite and magnetite), exsolution of less compatible substitute elements during recrystallization of unnamed minerals (e.g., gold→ Au+Sb) (Fig. 5), and changes in temperature dependence during metamorphism in the composition of pyrrhotite, sphalerite, and arsenopyrite [34].

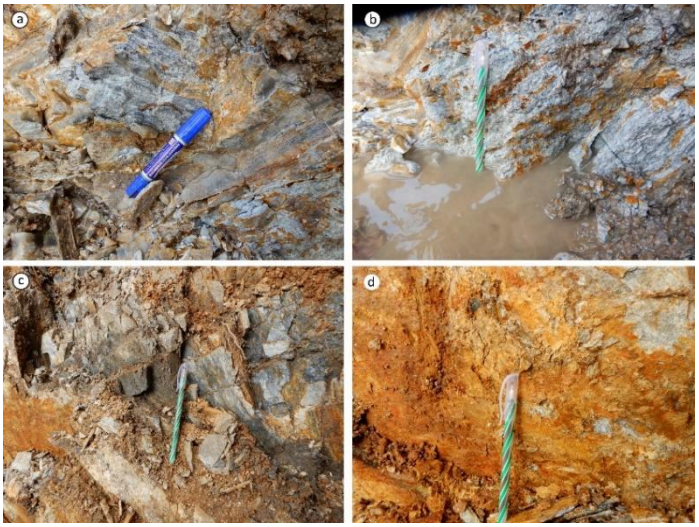

Fig. 4. Photographs showing the nature of the gold-bearing quartz vein hosted by black slate and slaty phyllite with an altered zone at Shafts I and II of Thae Phyu Chaung (a) and (b) of the laminated and sheeted gold-bearing quartz vein with chlorite alteration at Shaft I, (c) slaty phyllite at Shaft II, and (d) an oxidized zone at Shaft II.

4.2 Hydrothermal Veins and Alteration Mineralogy

4.2.1 Clay mineralogy

X–ray diffraction analyses identify the presence of quartz, chlorite, illite, kaolinite and smectite in claystone (Fig.7a–d). Chlorite includes peaks at 14.12 and 3.54 Å, and kaolinite sharp peaks at 7.23–7.14 and 3.57–3.59 Å which are unaffected by ethylene-glycol treatment (Fig. 8a, b). The term illite was used instead of sericite based on reports that roentgenographically determined illite corresponds to optically determined sericite [35]. Illite was classified by reflections at 10.0 and 5.0 Å, is not affected by the ethylene-glycol treatment (Fig.8a–d). The existence of mixed–layer illite/smectite minerals is inferred from the width of the 17 Å peak (ethylene glycolated) and the lack of rational d spacing for the remaining basal reflections. Quartz was described by peaks at 4.26 and 3.34 Å (Fig. 8a–d). Smectite was estimated by a peak at 14.93 Å which was extended to 17.01 Å following ethylene–glycolation. At the Thae Phyu Chaung, clay mineral assemblages are defined as illite (Fig. 8a–d); illite/smectite + chlorite/smectite + chlorite ± kaolinite (Fig. 8a–d). Abundant quartz–illite alteration is identified in the gold–bearing quartz veins of Thae Phyu Chaung.

From the proximal to the distal zone, illite was changed to regular and irregular interstratified illite/smectite (Fig. 8a–d). Chlorite was followed by illite and illite/smectite. Kaolinite was detected at the distal zone together with smectite and illite in claystone of Thae Phyu Chaung. The clay mineralogy from the proximal zone to distal zone of the ore horizon constitutes of

chlorite, illite, smectite and kaolinite. In some of these cases, chlorite and illite are closely related to gold mineralization.

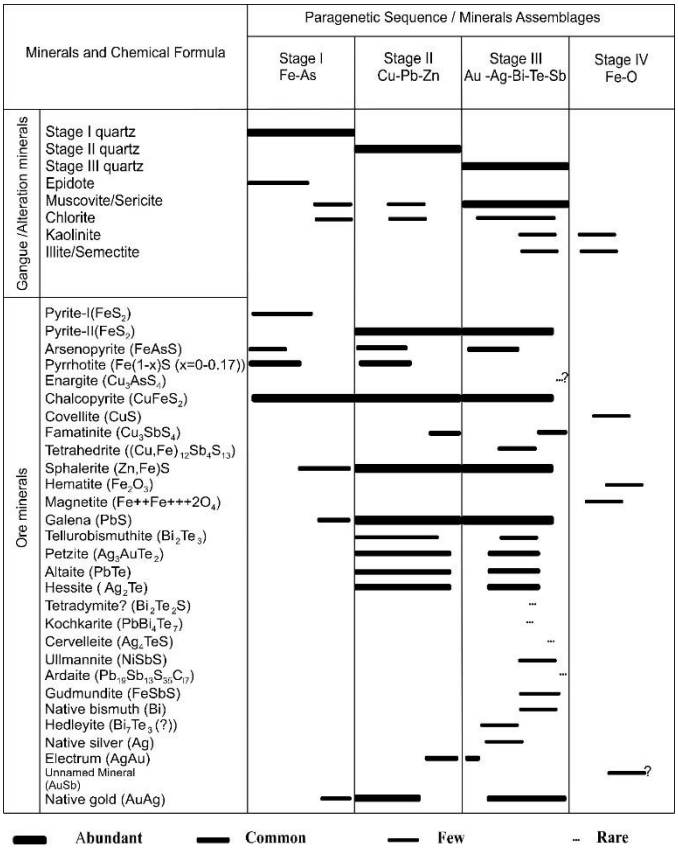

Fig. 5. Schematic summary of the paragenetic sequence of mineral assemblages and alteration of gold-bearing quartz veins in host greenschist facies rocks

Based on field and mineralogical data suggests at least four hydrothermal alteration assemblages. The entire sequence was strongly affected by hydrothermal circulation, observed by different types of hydrothermal veins and related alterations. The following main types of veins (older to younger) have been defined on the basis of petrography and cross-cutting relationships:

Stage I is the early alteration at Thae Phyu Chaung and is characterized by epidote ± muscovite/sericite + chlorite ± pyrite I ± chalcopyrite ± arsenopyrite ± pyrrhotite ± quartz (Fig. 5). Stage I alteration is common but not common in all samples. This assemblage represents the complete replacement of epidote by muscovite/sericite, chlorite and quartz. The mineral assemblage epidote ± muscovite/sericite + chlorite + quartz characterizes the distal alteration of the underlying gold ore bodies and is possibly associated with pre-metamorphic exhalation activity (Figure 5).

Stage II alteration is marked by persistent infilling of fractures and partial replacement of minerals. The mineral assemblage within this stage consists of muscovite/sericite + chlorite ± quartz and pyrite II. Within this stage, there is a gradual transition from sericite + chlorite assemblage to quartz + pyrite II ± chalcopyrite ± arsenopyrite ± pyrrhotite ± native gold ± electrum ± galena ± sphalerite.

Stage III commonly includes Stage II minerals. Adjacent dehydration and mineral assemblage of muscovite/sericite + chlorite + chlorite/smectite + kaolinite ± illite/semectite ± pyrite II ± quartz is differentiated by the proximal and most intense alteration zones (Fig. 5). Mixed layer chlorite/smectite is the first phase of precipitation in fractures during Stage III (Fig. 8a, b). The terminology " mixed layer chlorite/smectite " is used in current communication without clear interpretation of ordering between layers [36]. The first appearance of kaolinite and illite/semectite is the outer boundary of the transitional alteration zone. This assemblage is the result of the replacement of kaolinite and illite to muscovite (sericitization).

The latest alteration at Thae Phyu Chaung (stage IV) occurs in fractures representing the mineral assemblage: kaolinite + illite/semectite ± hematite ± magnetite in stage IV. This evident temperature decrease during stage IV may indicate the diffusion of the heat flow associated with the crystallization of gold–bearing quartz veins.

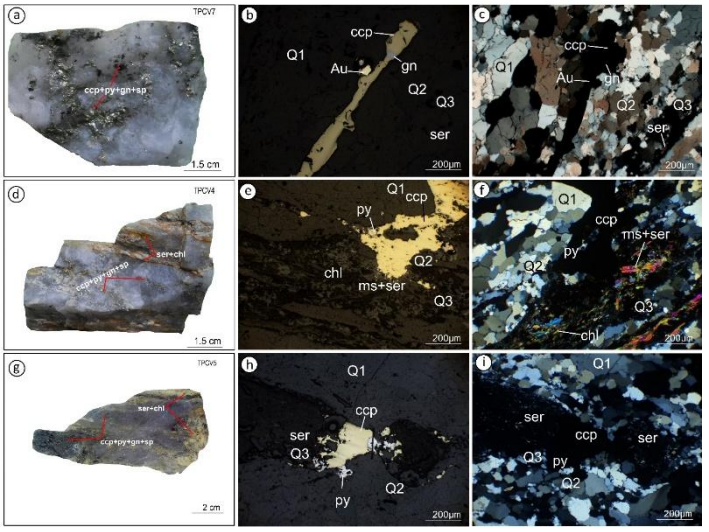

Fig. 6. (a, d, and g) hand specimen in paragenetic stage I–III of gold-bearing quartz veins. Photomicrograph showing (b and c) native gold (Au) associated with paragenetic stage I (Q1),II (Q2), and III (Q3) quartz, galena (gn), chalcopyrite (ccp), chlorite (chl), and sericite (ser) of gold-bearing quartz vein, (e and f) chalcopyrite (ccp) associated with paragenetic stage I (Q1),II (Q2), and III (Q3) quartz, pyrite (py), chlorite (chl), and sericite (ser) and muscovite (ms) in gold-bearing quartz vein, (h and i) chalcopyrite (ccp) associated with paragenetic stage I (Q1),II (Q2), and III (Q3) quartz, pyrite (py), chlorite (chl), and sericite (ser) of gold-bearing quartz vein.

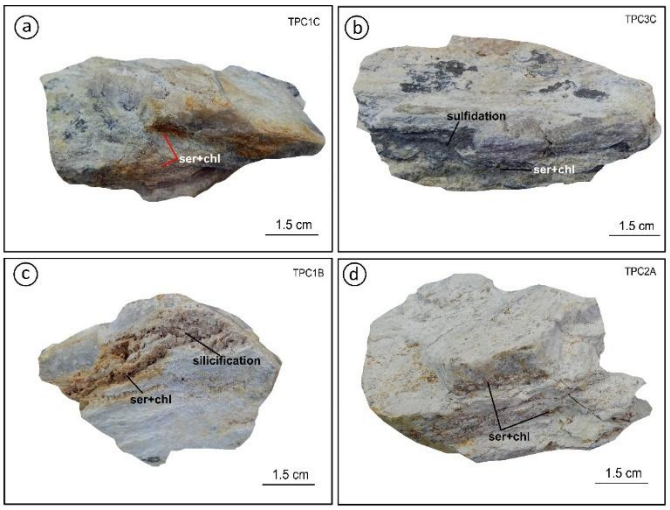

Fig.7. (a) (a) Photograph showing claystone in shear zone from Shaft I; (b) sulfidation with sericite and chlorite alterations in shear zone from Shaft I; (c) sericite and chlorite alterations with silicification in altered zone from Shaft II; (d) sericite and chlorite alterations in altered zone from Shaft II. Abbreviations: qz = quartz ser=sericite and chl = chlorite

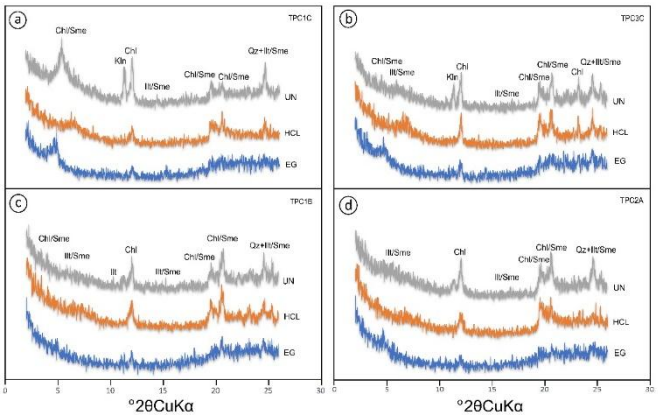

Fig. 8. XRD patterns of oriented clay fractions from Thae Phyu Chaung under untreated (UN), ethylene glycolated (EG), and hydrochloric acid (HCL) (Ilt, illite; Chl, chlorite; Kln, kaolinite; Sme, smectite; Qz, quartz; Chl/Sme, mixed layer chlorite/smectite; Ilt/Sme, mixed layer illite/smectite).

5. DISCUSSION AND CONCLUSIONS

The mineral parageneses observed at Thae Phyu Chaung and other low–grade metasedimentary rocks localities often result from multiple stages of alteration that can be difficult to differentiate. Some orogenic deposits have a fluid flow controlled by microshears and alterations similar to metamorphic processes [15, 16, 37, 38], while others are strongly controlled by open fracture permeability [19–21]. The fluid source is uncertain, but it is possible that the heat metamorphic pile is deeply circulating dehydration fluids and/or meteoric water [15, 16, 21, 39]. Hydrothermal alteration and related mineralization happened under lower greenschist facies conditions (300–400 °C; 10–15-km depth) and epidote + muscovite/sericite + chlorite ± pyrite ± arsenopyrite ± pyrrhotite ± quartz mineral assemblages are comparable to the sub–greenschist–greenschist facies conditions of Thae Phyu Chaung [15,16]. The alteration zones indicate that epidote + muscovite/sericite + chlorite ± pyrite ± arsenopyrite ± pyrrhotite ± quartz in stage I, muscovite/sericite + chlorite ± pyrite ± quartz in stage II, muscovite/sericite + chlorite + kaolinite ± illite/semectite ± quartz in stage III, and kaolinite + illite/semectite ± magnetite in stage IV. The mineral assemblages referred to above, formed not only in the alteration zone but also in the quartz vein, indicate that the ore–forming fluids of Thae Phyu Chaung are almost neutral to weakly acidic conditions (pH=5.2–6.8) and are controlled by fault and fracture systems [40–42]. Gold-bearing quartz veins occur in the pseudomorph of the modified muscovite/sericite or chlorite, which indicates that this alteration is a precedent for gold deposition. The possible mineral reactions proposed by the equations in the metamorphic alteration zones are as follows [6, 21]:

(muscovite) $2KAl_3Si_3O_{10}(OH)_2$ + (fluid) $3H_4SiO_4 + 9Fe^{2+} + 6Mg^{2+} + 18H_2O$ = (chlorite) $3Mg_2Fe3Al_2Si_3O_{10}(OH)_8$ + (fluid) $2K^{+}+ 28H^{+}$ → (1)

(muscovite) 2FeO(silicates) + (chlorite) H_3AsO_3(aq) + (arsenate) $0.5H_2 + 3H_2S$ = (pyrite) FeS_2 + (arsenopyrite) FeAsS + $5H_2O$ → (2)

These two reactions dominated the mineralization in diverse lithologies at Thae Phyu Chaung. The alteration patterns and ore formation at Thae Phyu Chaung were formed by hydrothermal fluids, a hybrid of meteoric water, and resulting from the dehydration reactions of metamorphic fluids. It can either derive from deep metamorphic fluids or mantle fluids similar to other worldwide orogenic gold deposits [15, 16, 42]. The alteration zones appear above the main dehydration zone in the Mergui Belt, where new rocks are constantly inserted at plate tectonic rates, while the dehydrated rocks are exhumed and removed by erosion from the orogen [21]. However, orogenic gold deposits are mostly generated by metamorphogenic processes that are closely comparable [43]. The gold metallogeny in the Kyaikhto District is related to the world-wide metallogenic event of lower Cretaceous to Oligocene age which is responsible for important orogenic gold ores formation with the subduction of India–Burma plate (e.g., [27–29, 42]).

ACKNOWLEDGMENTS

This research is part of the PhD thesis of the first author and has been financially sponsored by the Japan International Cooperation Agency (JICA) SHIGEN NO KIZUNA's PhD scholarship program, which is warmly appreciated.

REFERENCES

[1] Sumail, N. Thébaud, Q. Masurel, C.M. Fisher, R.H. Smithies, and R. Schreefel, "Temporal constraints on gold mineralisation at the world-class Jundee deposit: Insights into the episodic nature of orogenic gold mineralisation in the Neoarchean Yilgarn craton," Precambrian Research, v. 410, 2024, article 107479.

[2] R.J. Goldfarb, and I. Pitcairn, "Orogenic gold: Is a genetic association with magmatism realistic?" Mineralium Deposita, v. 58, 2023, p. 5–35.

[3] D.I. Groves, M. Santosh, J. Deng, Q. Wang, L. Yang, and L. Zhang, "A holistic model for the origin of orogenic gold deposits and its implications for exploration," Mineralium Deposita, Vol.55, 2019, pp. 275–292.

[4] T. C. Mccuaig, and R. Kerrich, "P–T–t–deformation–fluid characteristics of lode gold deposits: evidence from alteration systematics," Ore Geology Reviews, Vol.12, 1998, pp.381–453.

[5] P. Eilu, E.J. Mikucki, and A.L. Dugdale, "Alteration zoning and primary geochemical dispersion at the Bronzewing lode gold deposit, Western Australia," Mineralium Deposita, Vol. 36, 2001, pp.13–31.

[6] L. Mathieu, "Quantifying hydrothermal alteration: a review of methods," Geosciences, Vol.8:245, 2018. https://doi.org/10.3390/geosciences8070245

[7] A.H.G. Mitchell, C. Ausa, L. Deiparine, T. Hlaing, N. Htay, and A. Khine, "The Modi Taung-Nankwe gold district, Slate Belt, central Myanmar: mesothermal veins in a Mesozoic orogen," Journal of Asian Earth Sciences, Vol.23, 2004, pp.321–341.

[8] Myo Kyaw Hlaing, K. Yonezu, Khin Zaw, Aung Zaw Myint, May Thwe Aye, and K. Watanabe, "Origin and characteristics of the shwetagun deposit, modi taung-nankwe gold district and the kunzeik and zibyaung deposits, kyaikhto gold district in mergui belt, Myanmar:implications for fluid source and orogenic gold mineralization," Frontiers in Earth Science, Vol 9, 2021, 772083. http://doi:10.3389/feart.2021.772083

[9] Myo Kyaw Hlaing, Aung Zaw Myint, T. Tindell, May Thwe Aye, Gold mineralization in the Kyaikhto District, Mon State, southern Myanmar, Open Journal of Geology, Vol. 9, 2019, pp.29–42. http://www.scirp.org/journal/ojg

[10] R. Schreefe, S. G. Hagemann, C.Davy's, J. A. Robinson, N. Thébaud, C. M. Fisher, M.P. Roberts, L.A.J.Martin, L.E. Schoneveld, and R. A. Creaser, "Granitoid-Hosted Orogenic Gold Mineralization: Genetic Constraints on the 7.4 Moz Archean Gruyere Gold Deposit, Yilgarn Craton, Western Australia," Economic Geology, Vol.120, no. 1, 2025, pp. 171–203.

[11] T. J. Smith, and S. E. Kesler, "Relation of fluid inclusion geochemistry to wall rock alteration and lithogeochemical zonation at the Hollinger McIntyre gold deposit," Timmins, Ontario, Canada, Canadian Institute of Mining and Metallurgy Bulletin, Vol. 78, 1985, pp.35–46.

[12] A. Kishida, and R. Kerrich, "Hydrothermal alteration zoning and gold concentration at the Kerr-Addison Archean lode gold deposit," Kirkland Lake, Ontario," Economic Geology, Vol. 82, 1987, pp. 649–690.

[13] H. Li, Q. Wang, L.Yang, C. Dong, W. Weng, J. Deng, "Alteration and mineralization patterns in orogenic gold deposits: Constraints from deposit observation and thermodynamic modeling," Chemical Geology, 607, 2022, 121012. https://doi.org/10.1016/j.chemgeo.2022.121012

[14] P. Eilu, and E.J. Mikucki, "Alteration and primary geochemical dispersion associated with the Bulletin lode-gold deposit, Wiluna, Western Australia," Journal of Geochemical Exploration, Vol.63, 1998, pp. 73–103.

[15] G.N. Phillips, and R. Powell, "Formation of gold deposits: a metamorphic devolatilization model," Journal of Metamorphic Petrology, Vol. 28, 2010, pp. 689–718.

[16] G. N. Phillips, and R. Powell, "Formation of gold deposits: review and evaluation of the continuum model," Earth Sciences Reviews, Vol.94, 2009, pp.1–21.

[17] S.G. Hagemann, G. Gebre-Mariam, and D.I. Groves, Surface–water influx in shallow-level Archean lode-gold deposits in Western Australia, Geology, Vol.22, 1994, pp. 1067–1070.

[18] D.I. Groves, R.J. Goldfarb, M. Gebre–Mariam, S.G. Hagemann, and F. Robert, "Orogenic gold deposits: a proposed classification in the context of their crustal distribution and relationship to other gold deposit types," Ore Geology Reviews, Vol.13, 1998, pp. 7–27.

[19] D.I. Groves, M. Santosh, and L. Zhang, "A scale-integrated exploration model for orogenic gold deposits based on a mineral system approach. Geoscience Frontiers, Vol. 11, 2020, pp. 719–738.

[20] R. J. Goldfarb, T. Baker, B. Dube, D.I. Groves, C. J. R. Hart, and P. Gosselin, "Distribution, character, and genesis of gold deposits in metamorphic terranes. In Hedenquist, J. W., Thompson, J. F. H., Goldfarb, R. J. and Richards, J. P. (Eds.) Economic Geology 100th Anniversary Volume, Society of Economic Geologists Inc., Littleton, 2005, pp.407–450.

[21] D. Craw, P. Upton, and D.J. Mackenzie,"Hydrothermal alteration styles in ancient and modern orogenic gold deposits, New Zealand," New Zealand Journal of Geology

and Geophysics, Vol. 52, 2009, 11–26. https://doi.org/10.1080/00288300909509874

[22] Khin Zaw, "Geological, petrological and geochemical characteristics of granitoid rocks in Burma: with special reference to the associated W–Sn mineralization and their tectonic setting," Journal of Asian Earth Sciences, Vol.4, 1990, pp. 293–335.

[23] E.J. Cobbing, P. Pitfield, D. Darbyshire, and D. Mallick, "The Granites of the Southeast Asian Tin Belt," Overseas Memoirs of the British Geological Survey 10, London, 1992.

[24] M.E. Barley, M.G. Doyle, Khin Zaw, A.L. Pickard, and P. Rak, "Jurassic–Miocene magmatism and metamorphism in the Mogok Metamorphic Belt and the India-Eurasia collision in Myanmar," Tectonics, Vol. 22, 2003, pp.1–11.

[25] M.P. Searle, S.R. Noble, J.M. Cottle, D.J. Waters, A.H.G. Mitchell, Tin Hlaing, and M.S.A. Horstwood, "Tectonic evolution of the Mogok metamorphic belt, Burma (Myanmar) constrained by U–Th–Pb dating of metamorphic and magmatic rocks," Tectonics 26, 2007.

[26] A.H.G. Mitchell, S.L.Chung, T.Oo, T.H. Lin, and C.H .Hung, "Zircon U–Pb ages in Myanmar: Magmatic–metamorphic events and the closure of a neo–Tethys ocean?," Journal of Asian Earth Sciences, Vol. 56, 2012, pp. 1–23. https://doi.org/10.1016/j.jseaes.2012.04.019

[27] N.J. Gardiner, M.P. Searle, L.J. Robb, and C.K. Morley Neo–Tethyan magmatism and metallogeny in Myanmar – An Andean analogue?," Journal of Asian Earth Sciences,Vol.106, 2015, pp.197–215.

[28] N. J. Gardiner, M. P. Searle, C. K. Morley, L. J. Robb, M. J. Whitehouse, N. M. Roberts, C.L. Kirkland, and C. J. Spencer, "The crustal architecture of Myanmar imaged through zircon U-Pb, Lu-Hf and O isotopes: Tectonic and metallogenic implications," Precambrian Research, Vol. 62, 2018, pp. 27-60. https://doi.org/10.1016/j.gr.2018.02.008

[29] A.H.G. Mitchell, "Geological belts, plate boundaries, and mineral deposits in Myanmar," Elsevier, Oxford, 509 p, 2018.

[30] M.J. Mackenzie, "Report on the exploration progress in block 3/13 for the period January 1998 to December 1998, Palmer Resources Ltd. Myanmar (Burma) Project," (Unpublished), pp.1–67, 1999.

[31] G.W. Brindley, "Quantitative X-ray mineral analysis of clays. In: Brindley, G.W., Brown, G.C. (Eds.), Crystal Structures of Clay Minerals and Their X-ray Identification," Mineralogical Society, Monograph No. 5, 1980, pp. 411–438.

[32] D.M. Moore, and R.C. Jr. Reynolds, "X–Ray Diffraction and the Identification and Analysis of Clay Minerals, Oxford University Press, Oxford, pp.332, 1997.

[33] D.L. Whitney, and B.W. Evans, "Abbreviations for names of rock forming minerals," American Mineralogist, Vol. 95, 2010, pp.185–187.

[34] F. Vokes, "Ores and metamorphism: introduction and historical perspectives. Metamorphosed and metamorphogenic ore deposits, Reviews in Economic Geology, Vol.11, 2000, pp. 1–18.

[35] J. Środoń, and D.D. Eberl, "Illite. In: Bailey SW (Ed) Micas. Reviews in mineralogy 13," Mineralogical Society of America, Washington, DC, 1984, pp. 495–544.

[36] R. C. J. Reynolds, "Interstratified clay minerals, in Brindley, G. W., and Brown, G., editors, Crystal Structures of Clay Minerals and Their X–ray Identification," London, Mineralogical Society, 1988, pp. 249–304.

[37] S.F. Cox, V.J. Wall, M.A. Etheridge, and T.F. Potter, "Deformation and metamorphic processes in the formation of mesothermal vein–hosted gold deposits: examples from the Lachlan Fold Belt in central Victoria, Australia, Ore Geology Reviews, Vol.6, 1991, pp.391–423.

[38] A.G. Tomkins, On the source of orogenic gold. Geology, Vol. 41, 2013, 1255–1256.

[39] R.J. Goldfarb, D.I. Groves, and S. Gardoll, "Orogenic gold and geologic time: a global synthesis," Ore Geology Reviews, Vol.18, 2001, pp.1–75.

[40] D. Gaboury, "Parameters for the formation of orogenic gold deposits, Applied Earth Science, Vol.128 (3), 2019, pp.124–133.

[41] A.G. Tomkins, "Windows of metamorphic sulfur liberation in the crust: implications for gold deposit genesis," Geochimica et Cosmochimica Acta, Vol.74, 2010, pp.3246–3259.

[42] D.I. Groves, M. Santosh, Q. Wang, L. Zhang, H. Zhao, "The Boring Billion: A key to resolving controversy on ore-fluid source models for orogenic gold deposits?" Mineralium Deposita Vol.59, 2024, 435–444.

[43] B.W.D. Yardley, and J.S. Cleverley, "The role of metamorphic fluids in the formation of ore deposits," Geological Society, London, Special Publications, Vol.393, 2015, pp.117–134. http://doi.org/10.1144/sp393.5.

Techno-Science Research Journal V13 (Special Issue) (2025) P 110-117

I.T.C

Content list available at ITC

Techno-Science Research Journal

Journal Homepage: www.ric.itc.edu.kh

Techno-Science Research Journal

Lithology, Alteration, Mineralization, and Quartz Textures of Epithermal-Porphyry Transition Systems at Phnom Srongam Prospect, Chhouk District, Kampot Province

Jolsa Heng [1], Sirisokha Seang[1,2*], Kakda Kret[1,2], Kotaro Yonezu[3], Koichiro Watanabe[4], Panhavong Ly[5], Potheanaram Nhim[5] ,Samnang Kong[6]

[1]*Faculty of Geo-Resources and Geotechnical Engineering, Institute of Technology of Cambodia, Russian Federation Blvd., P.O. Box 86, Phnom Penh, Cambodia*

[2]*Research and Innovation Center, Institute of Technology of Cambodia, Russian Federation Blvd., P.O. Box 86, Phnom Penh, Cambodia*

[3]*Department of Earth Resources Engineering, Faculty of Engineering, Kyushu University,744 Motooka, Nishi-ku Fukuoka 819-0395 Japan*

[4]*Jica Senior Advisor at Japan International Cooperation Agency, 2 Chome-49-5 Nishihara, Shibuya City, Tokyo 151-0066, Japan*

[5]*Geologist exploration at Renaissance Minerals (Cambodia) Limited, Chong Phlah, Okvau, Keo Seima, Phumi Chhung, Cambodia*

[6]*Samnag Angkor Development Ltd, Phnom Penh, Cambodia*

Received: 1 November 2024; Revised: 1 January 2025; Accepted: 20 June 2025; Available online: October 2025

Abstract: *Phanom Srongam is a favorable area for gold and copper exploration and potential for mining development. It is located in located in Kampot Province, Southwestern Cambodia, within the Loei Fold Belt. Hand specimen descriptions, petrographic thin sections, petrographic polished section, X-ray fluorescence (XRF), and X-ray diffraction (XRD) were conducted in this study to obtain mineral composition, alteration minerals, quartz textures and mineralization. As results from petrography and X-ray fluorescence analysis, lithologies of drill hole ZK-40 are granodiorite and dacite. The alteration minerals assemblages can be categorized into an advanced argillic zone and phllic alteration zone. Advanced argillic contains quartz, and alunite, which formed under acidic conditions at temperatures ranging from approximately 100˚C to 300˚C and phyllic alteration zone consists of quartz, sericite, and chlorite, which formed under moderately acidic fluids at temperatures between 250˚C to 350˚C. The mineralization in this area consists of pyrite, chalcopyrite, sphalerite, covellite, and arsenopyrite, occurring in veins, veinlets, and disseminations. Based on hand specimen observations and petrographic analysis, quartz textures are identified as crustiform, colloform, comb, and zonal. These textures are common in epithermal systems and are potentially associated with precious metal mineralization, such as gold and silver. A comprehensive understanding of the lithological units, hydrothermal alteration, ore mineralization, and quartz textures is essential for effectively targeting prospective areas for gold and copper mining.*

Keywords: Ore mineralization, Quartz Texture, Kampot, Cambodia.

1. INTRODUCTION

Cambodia, located on the Indochinese mainland of Southeast Asia, has a wealth of mineral resources that could significantly benefit the economy. These resources include iron ore, copper, and gold, which are abundant in various deposits across the country. The Indochina Terrane is the largest tectonic unit in SE Asia which hosts mineralization belts such as the Truong Son Fold (TSFB), Loei Fold Belt (LFB), and Dalat-Kratie Belt (DKB). In SW Cambodia, the Phom Sro Ngam area corresponds to the Loei fold belt which lies along the western periphery of the Indochina Terrane and is bounded by Sukhothai Terrane at the west along with the Jinghong-Nan-Sra Kaeo Suture The Loei fold belt spans from northern Laos through Loei and Phetchabun provinces in central Thailand, extending to Sra Kaeo in southeastern Thailand and into western Cambodia [1]. The Loei fold belt predominantly consists of Late Permian

* Corresponding author: Sirisokha Seang
E-mail: seangsirisokha@itc.eud.kh, Tel: +855-16308415

to Triassic andesitic-rhyolitic volcanic formations, although recent reports indicate the presence of older Devonian-Carboniferous and Silurian magmatic rocks[1]. This belt serves as a host to various mineral deposits, including Cu-Au skarn deposits, Au skarn deposits, epithermal Au deposits, and epithermal Sb-Au deposits in regions encompassing Loei, Lobburi, Phentchabun, Nakhon Sawan, and Chachoengsao provinces [1].

Recently, Samnang Angkor Development, a mining exploration company,obtended exploration permits in the Chhouk district of Kampot province, targeting gold and copper deposits. The project encompasses dintinct areas, but this study focuses on Area 1. The Cambodian Development Council (CDC) has issued an exploratory license to Samnang Angkor Development Limited for resource investigation. This study area is situated in Phnom Sro Ngam tenement, Taken commune, Chhouk District, Kampot Province, Cambodia.

1.1 Regional Geology and Ore Deposit

Cambodia occupies the south-central region of the Indochina Peninsula, which covers a total area of 181,035 km^2 between the Northing coordinates of 1100000N and 1600000N and Easting of 200000E and 800000E. The country is bordered by Thailand in the north and west, the Lao People's Democratic Republic in the north, and Vietnam in the southeast and south [2]. The Tonle Sap-Mekong Plain divides Cambodia into two regions: northeast and southwest. The North-East and South-West regions consist of metamorphic, sedimentary, volcanic, and intrusive rocks. The low altitude of the pond leads to silt erosion, but the southwestern and northwestern regions have high-level terrain. The Quaternary unit covers most of Cambodia's surface geology from the border with Thailand to Tonle Sab Lake and the lower Mekong River. The South-West region has Triassic-Cretaceous Mesozoic sedimentary rock units, with Anticlinorial and Synclinorial zones in Indosinian fold belts. Mesozoic sedimentary formations, including granites and high-grade metamorphic, are found in the northeast. Cambodia is part of the Indochina Terrane within mainland Southeast Asia, which separated northward from Gondwana during the Middle Devonian. Southeast Asia includes several Gondwana-derived terranes, with Indochina being the largest, bordered by the South China Terrane to the north and the Truong Son Fold Belt to the northeast, containing Paleozoic volcanic formations and Early Permian–Triassic granitoids. The southwestern region of Cambodia connects to the Loei fold belt, which stretches from Laos through Thailand into western Cambodia. This belt, rich in Late Permian to Triassic volcanic rocks, hosts various mineral deposits, including gold (Au) and copper-gold (Cu-Au) skarns, and notable deposits in Cambodia's Preah Vihear province [1].

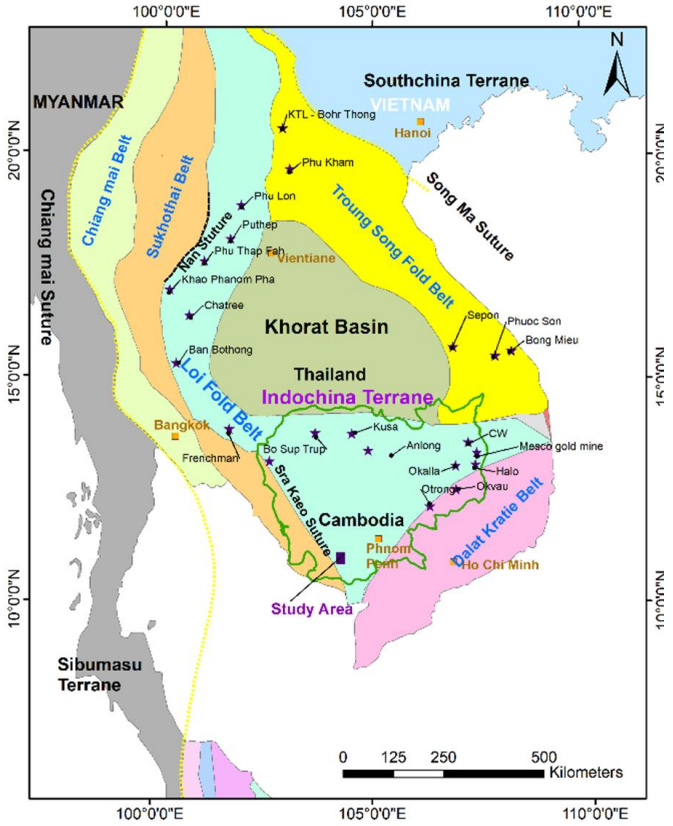

Fig. 1. Tectonic divisions mapping of the Indochina Terrane as well as mineralization belts modified after [1]

1.2 Geology of Study area

Phnom Sro Ngam, located in the southwest of Cambodia in Kampot province, is situated within the Loei fold belt (LFB), which is a promising area for the exploration of porphyry, epithermal, and skarn-related gold deposits (Fig. 1). The geological surface of Phnom Sro Ngam is primarily covered by Cambrian to Silurian metamorphic rocks such as quartzite, metasandstone, phyllite, and schist, with the presence of limestone and carbonaceous sandstone. The area also contains multiple intrusions, some of which are buried and have caused mineralization as indicated by shallow diggings. However, detailed mapping of most lithologic units has not been conducted. The gold-bearing veins at Phnom Sro Ngam are found within quartzite and other invaded metamorphic units that have been affected by auriferous, sulfide-bearing fluids derived from magmatic sources. The gold mineralization is associated with NW and WNW trending quartz veins and massive sulfides, mainly pyrite minor chalcopyrite, and galena. Sericitization and silicification halos are apparent around these striking NW and WNW vein structures, with the width of the quartz veins ranging from a few centimeters to a meter.

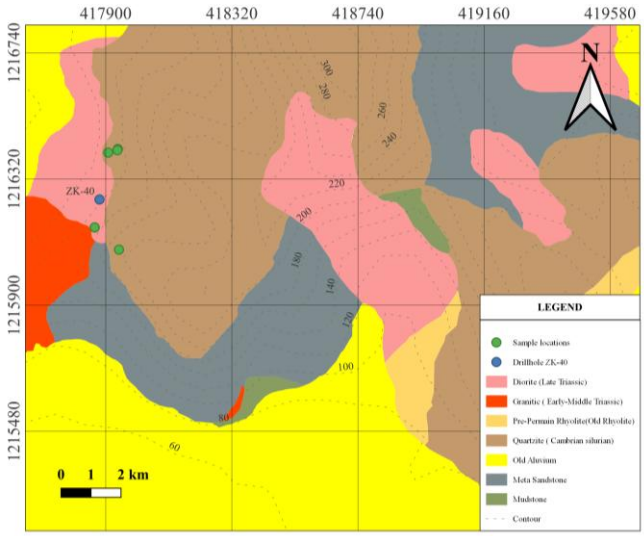

Fig. 2. Lithology of study area with drill hole location (modified [3])

2. METHODOLOGY

Seven petrography thin sections, three samples of petrography polish sections were conducted to determine the characteristics of alteration minerals, ore mineralization, and their textures under microscope. Additionaly, eight drill core samples were analyzed using X-ray fluorescence (XRF) to determine the chemical composition of the rocks.All analyses were conducted in the Faculty of Geo-resources and Geotechnical Engineering, Institute of Technology of Cambodia. Alteration minerals were further examined using using X-ray diffraction (XRD) in combination with hand specimen observations. XRD analyses were performed using Rigaku Ultima IV X-Ray Diffractometer at Kyushu University, Japan.

3. RESULTS AND DISCUSSION

3.1.Lithology

Based on the hand-specimen and microscopic observations, granodiorite is white to grayish in color, exhibiting a medium to coarse-grained phaneritic texture and a high percentage of plagioclase felspar. The rock primary consists of quartz, alkali felspar, plagioclase, and biotite. Under microscope, plagioclase feldspar was partially altered to sericite (Fig. 3). Dacite is grey to dark grey in color, and exhibiting a fine to medium-grained. Under microscope, the rock primarily consists of quartz, plagioclase and alkali-feldspars. Both alkali felspar and plagioclase were partially altered to sericite (Fig. 4).

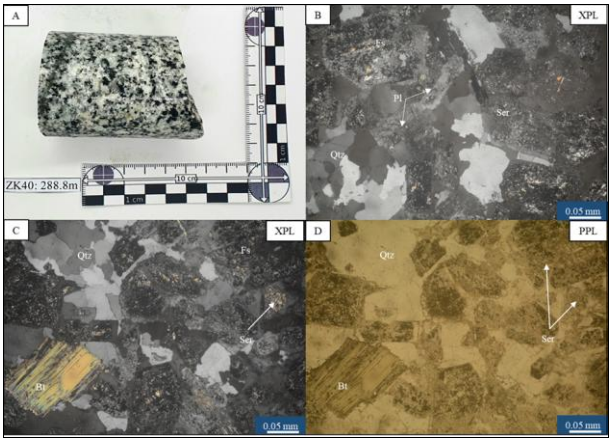

Fig. 3. (A) Photographs of granodiorite rock in depth 288.80m. (B),(C) the appearance of cross-polarized under microscope. (D) the appearance of plane-polarized light under microscope Abbreviation: Qtz: quartz, Pl: Plagioclase, Ser: Sericite, Bt: Biotite, Fs: Feldspar.

Fig. 4. (A) Photograph of dacite . (B),(C) the appearance of cross-polarized under microscope. (D) the appearance of plane-polarized light under microscope Abbreviation: Qtz: Quartz, Pl: Plagioclase, Ser: Sericite Fs: Feldspar, Bt: Biotite.

The weight percentage of SiO_2, NaO_2, and K_2O are present in Table 1. The intrusive rocks are classified as granodiorite (Fig. 5), based on whole-rock composition in terms of Na_2O + K_2O and SiO_2 contents [4]. According to Total alkalis versus silica (TAS) diagram [5] indicates that volcanic rocks are classified as dacite (Fig. 6)

Table 1. Summary results XRF

Sample ID	SiO_2 (mass%)	Na_2O+K_2O (mass%)	Rock type
ZK-40:28m	63.91	5.48	Granodiorite
ZK-40:30m	70.20	4.47	Granodiorite
ZK-40:103m	64.96	4.10	Granodiorite

ZK-40:127.3m	64.44	6.12	Granodiorite
ZK-40:153m	65.86	5.63	Dacite
ZK-40:208m	67.24	5.60	Dacite
ZK-40:288.8m	68.63	6.38	Granodiorite
ZK-40:315m	64.76	5.62	Granodiorite

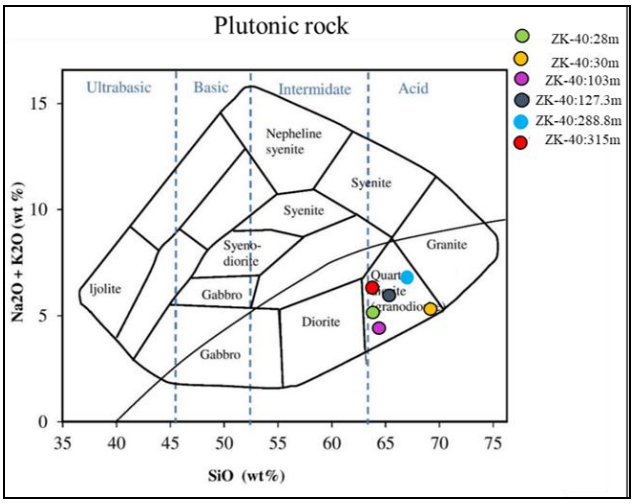

Fig. 5. Diagrams showing the magma composition of intrusive rocks [4]

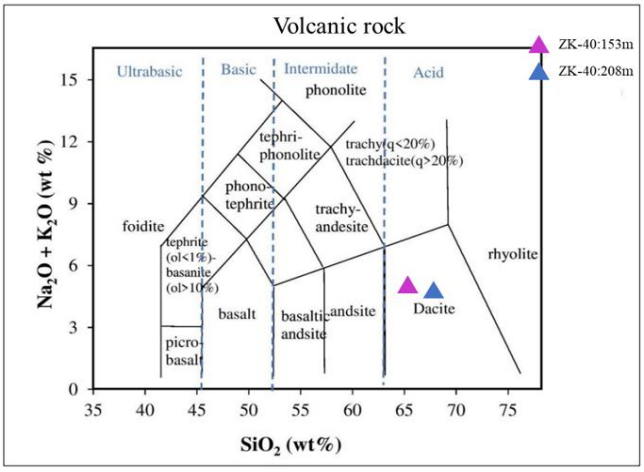

Fig. 6. TAS diagram for Volcanic rocks after [5]

Based on core logging, petrographic thin sections and rock classification using $Na_2O + K_2O$ and SiO_2 , the lithology in drillhole ZK-40 includes granodiorite and dacite, as shown in Fig. 7.

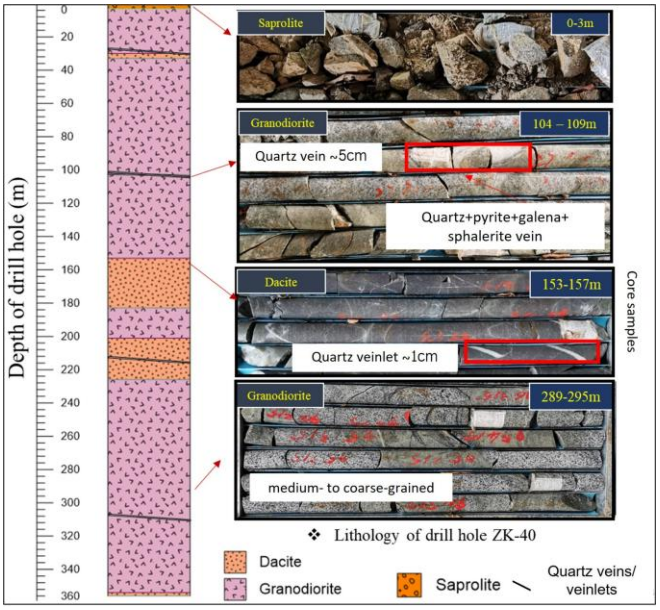

Fig. 7. Lithology of drillhole ZK-40

3.2. Hydrothermal alteration

Based on petrography analysis, alteration minerals include alunite, chlorite, and sericite. Allunite occurs as fine to medium grained, subhedral to anedral crystal and replacing plagioclase and associated with quartz. Sericite appears as fine-grained, fibrous flakes replacing felspar. Chlorite appears as greenish, platy to fibrous aggragates (Fig. 8).

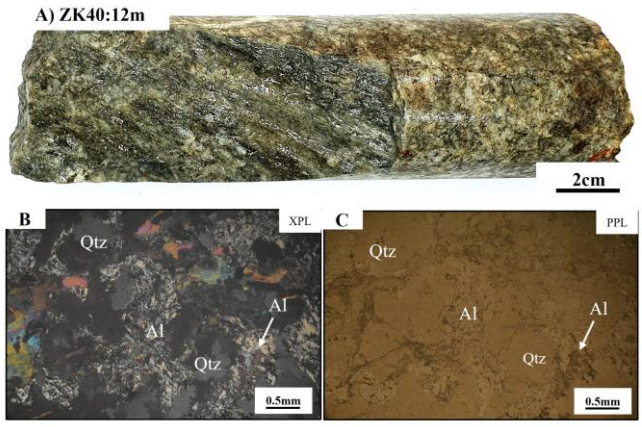

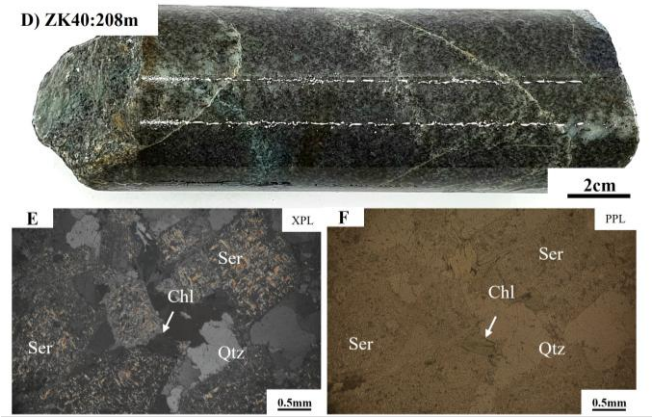

Fig. 8. (A) and (D) Photographs of hand specimens of samples from ZK40:12m and ZK40:208m. (B,C,E,and F). Photomicrographs shwing alteration minerals : alunite, sericite and chlorite alteration. Abbreviations: Al= alunite, Qtz= Quartz (B). Dacite, Ser= sericite

Based on X-ray diffraction analysis, samples ZK-40:30 m and ZK-40:47 m consist of quartz, alunite, and plagioclase (Fig. 9).

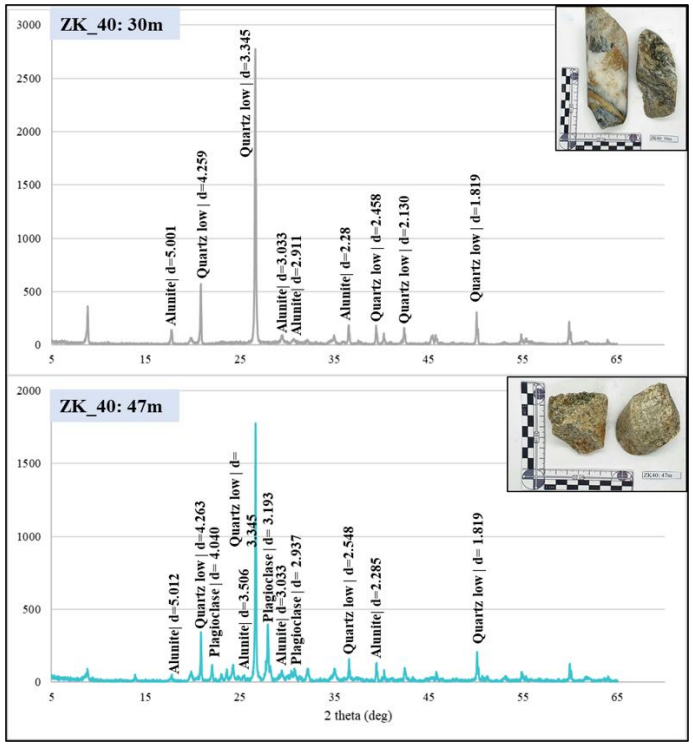

Fig. 9. Representative of samples show quartz, alunite, plagioclase by X-ray diffraction.

Table 1. Sumarry of alteration minerals.

Sample ID	Type of sample	Alteration Minerals
ZK_40: 12m	Granodiorite	Quartz+ alunite
ZK_40: 30m	Granodiorite	Quartz+ alunite
ZK_40: 47m	Granodiorite	Quartz+ alunite
ZK_40: 208m	Granodiorite	Quartz+ sericite+chlorite

The alteration minerals at Phnom Srongam include quartz, alunite, sericite and chlorite. The presence of alunite and quartz indicate formation temperatures ranging from approximately 100-300 °C under neutral pH conditions (Fig. 10), and characteristic of the advanced argillic zone. The zone forms in the upper levels of hydrothermal of system where magmatic vapor condensation and mixing with meteoric water produce low-pH fluid enriched SO_2 and H_2S [6], and [7].

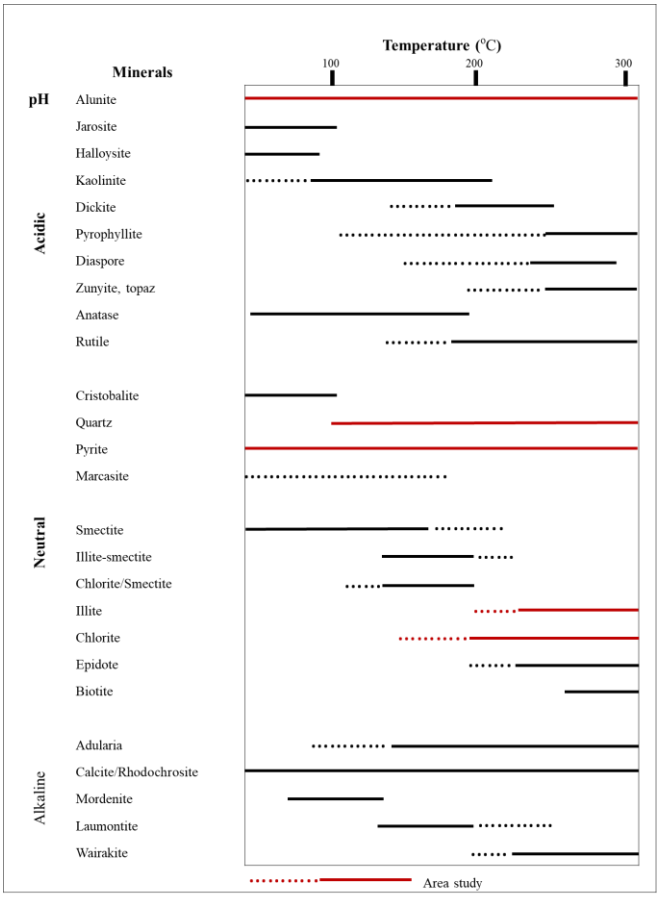

Fig. 10. Mineral stability under varying temperature and pH conditions at epithermal deposition [7]

Alunite is a key mineral indicator of this environment and is often spatially associated with potential precious metal mineralization in high-sulfidation systems[8]. Phyllic alteration consists of quartz, sericite, and chlorite, typically forms in acidic condition (pH 4.5-7) and temperature 250˚C to 350˚C [9]. These alteration type suggest that the hydrothermal system at Phnom Sro Ngam experienced multiple fluid pulses, likely transitioning from a high-sulfidation epithermal environment in the upper parts to a porphyry-related system at depth [10].

3.3. Ore Mineralization

Based on petrographic analysis, ore mineralization include pyrite, arsenopyrite, sphalerite, covellite, and bornite. The common ore minerals occur as both vein-type and disseminated assemblages. Vein styles consist of quartz + pyrite vein, quartz + pyrite + chalcopyrite + arsenopyrite vein, quartz + sphalerite + arsenopyrite + covellite vein, pyrite + chalcopyrite + arsenopyrite + sphalerite + covellite + galena vein, quartz + pyrite + arsenopyrite + sphalerite + covellite + bornite vein, quartz + arsenopyrite vein. Arsenopyrite is typically associated with high-temperature system and is a common host or pathfinder for gold mineralization. It is also associated with galena, sphalerite and chalcopyrite[11]. The observed mineralological zoning reflects a telescoped hydrothermal system, wherein early high-temperature fluid deposited pyrite and arsenopyrite, followed by main mineralizing phase with chalcopyrite, sphalerite, galena, and bornite. Subsequent near-surface oxidation and enrichment led to the formation of secondary mineral such as covellite and malachite. This telescoping is characteristic of epithermal-porphyry transition zones or zoned intermediate-sulfidation systems, particularly in subduction related volcanic arc [10],[12].

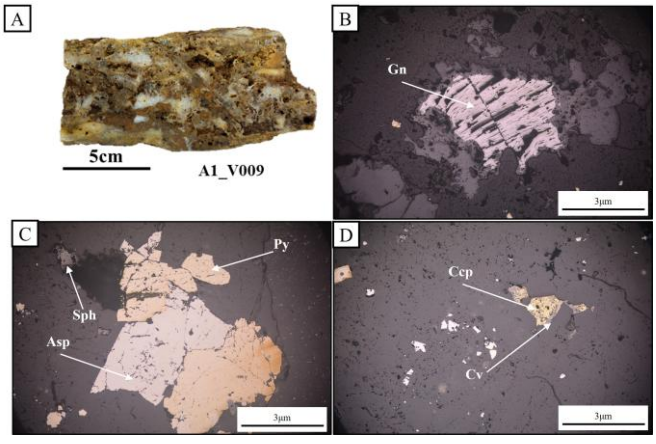

Fig. 11. (A) Hand specimen of sample A1_V009 showing quartz vein with iron oxide staining. (B,C,and D) Photomicrographs of arsenopyrite, sphalerite, chalcopyrite, covellite, pyrite, and galena. Abbreviations: Asp=arsenopyrite, Sph=Sphalerite, Cv=covellite, Gn=Galena, Ccp=Chalcopyrite**.**

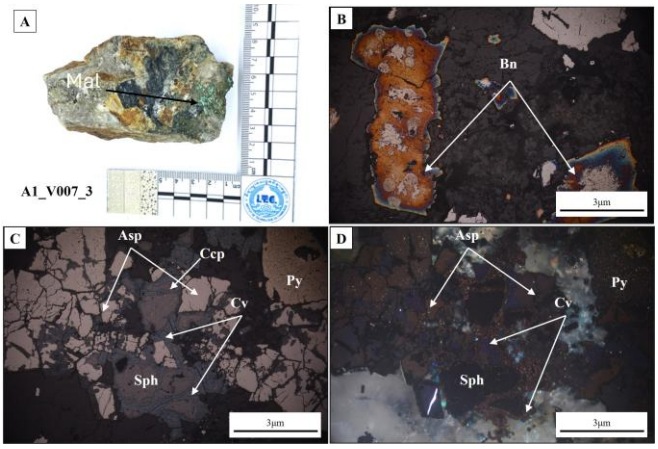

Fig. 12. (A) Hand specimen sample A1_V007_3 showing malachite staining, (B, C, D) Photomicrographs of arsenopyrite, sphalerite, covellite and bornite. Abbreviations: Asp=Arsenopyrite, Sph=Sphalerite, Cv=covellite, Mal=malachite, Bn=bornite, Py=pyrite and Ccp=chalcopyrite.

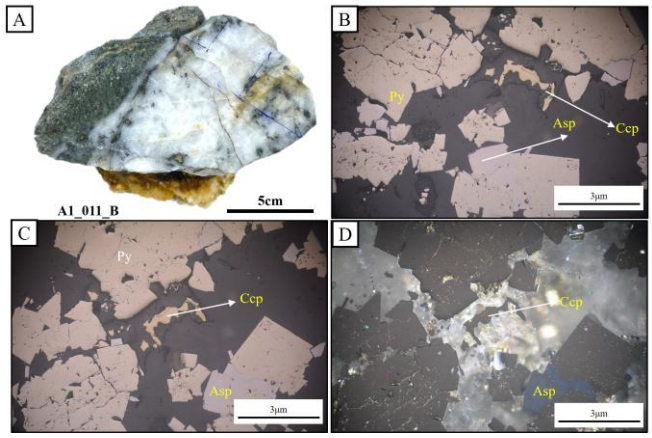

Fig. 13. (A) Hand specimen sample A1_011_B showing quartz with minor sulfide staning. (B,C, and D) Photomicrographs of arsenopyrite associated with pyrite and chalcopyrite. Abbreviations: Asp=arsenopyrite, Ccp=chalcopyrite, Py=pyrite.

3.1 Quartz textures

A comprehensive petrographic analysis of quartz textures and the presence of sulfides in the quartz veins from surface of Phnom Srongam reveals that the quartz exhibits a colloform banded, crustiform, zonal, and comb texture (Fig. 14). A group of quartz crystals with the same orientation is often referred to as exhibiting comb texture, while a banded arrangement of mineral aggregates with distinct textures and compositions is referred to as having crustiform texture. The colloform-crustiform and zonal are mostly associated with mineralization such as pyrite, chalcopyrite, and arsenopyrite. In simplified terms, all quartz textures are associated with epithermal deposits[13], [14]. There is a positive association between gold mineralization and boiling in epithermal conditions, and certain

textures of quartz have been identified as useful indicators of boiling. And crustiform texture and comb textures are known to form under epithermal deposit [15].

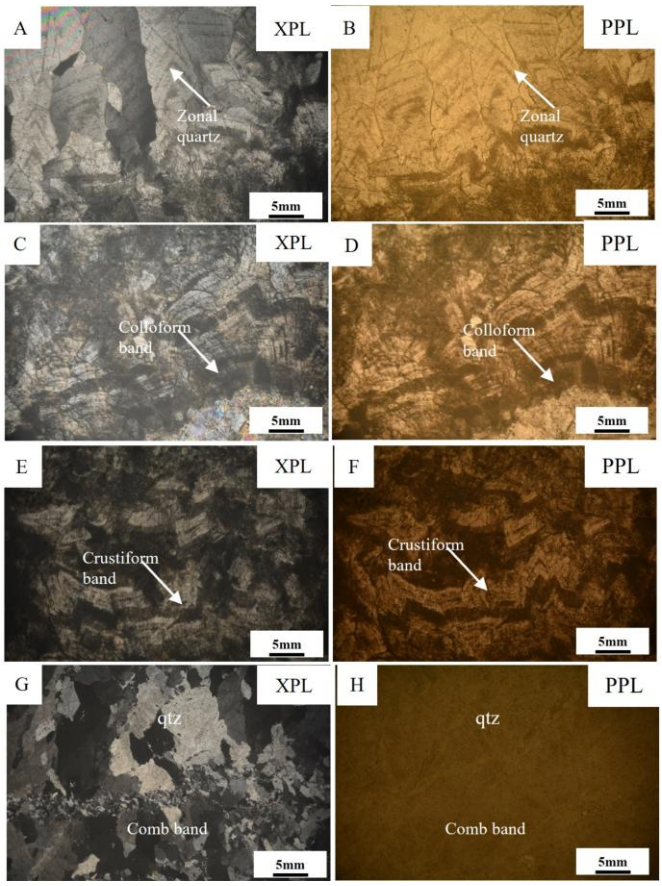

Fig. 14. Various quartz textures observed in vein samples from Phnom Srongam, Kampot, Cambodia. A and B: Zonal texture; C and D: Colloform texture; E and F: Crustiform texture; G and H: Comb texture. Images A, C, E, and G were taken under cross-polarized light

4. CONCLUSIONS

Based on results from field observations and laboratory analysis, the following data was gathered in the study area:

1. The rock units in this study area are granodiorite, dacite.
2. Alteration minerals are classified into advanced argillic and phyllic zones. The advanced argillic zone, with quartz and alunite, formed under acidic conditions (100–300 °C), while the phyllic zone, containing quartz, sericite, and chlorite, developed under moderately acidic conditions (250–350 °C).
3. The mineralization consists of pyrite, arsenopyrite, sphalerite, covellite, and bornite. The common ore minerals which are formed as veins, veinlets and disseminated assemblages.
4. The presence of crustiform and comb textures in the quartz veins suggests hydrothermal fluid activity consistent with epithermal systems.
5. The integration of lithology, alteration mineralization and quartz textures at Phnom Srongam supports a model of a telescoped hydrothermal system, with epithermal-porphyry transition system. This geological setting is highly favorable for gold and copper mineralization.

ACKNOWLEDGMENTS

We sincerely thank the Institute of Technology of Cambodia (ITC), the Department of Geology in the Ministry of Mines and Energy of Cambodia, and the Project for Strengthening Engineering Education and Research for Industrial Development in Cambodia for their support of Laboratory-Based Education (LBE). We would like to sincerely thank His Excellency Mr. Kong Samnang, Chairman of Samnang Angkor Development Co. Ltd., for approving and providing support for the fieldwork in the Cambodian province of Phnom Sro Ngam, Chhouk District.

REFERENCES

[1] K. Zaw et al., “Tectonics and metallogeny of mainland Southeast Asia - A review and contribution,” Gondwana Res., vol. 26, no. 1, pp. 5–30, 2014, doi: 10.1016/j.gr.2013.10.010.

[2] S. Tum, M. L. Puotinen, and D. B. Copeman, “A geographic information systems model for mapping risk of fasciolosis in cattle and buffaloes in Cambodia,” *Vet. Parasitol.*, vol. 122, no. 2, pp. 141–149, 2004, doi: 10.1016/j.vetpar.2004.03.016.

[3] Ly, P., Seang, S., Kret, K., Oy, K., Yonezu, K., Watanabe, K., Sreu, T., 2022,. Lithology, 478 hydrothermal alteration, and ore characteristics of Area-1 in Koh Sla, Chhouk district, 479 Kampot Province, southern Cambodia. Proceedings of the International Symposium on 480 Earth Science and Technology, Japan.

[4] Cox, K.G., et al. (1979) The Interpretation of Igneous Rocks. Allen and Unwin, London, 450 p. http://dx.doi.org/10.1007/978-94-017-3373-1.

[5] Le Bas, M.J., Le Maitre, R.W., Streckeisen, A. and Zanettin, B. (1986) A Chemical Classification of Volcanic Rocks Based on the Total Alkali-Silica Diagram. Journal of Petrology, 27, 745-750. https://doi.org/10.1093/petrology/27.3.745.

[6] J. W. Hedenquist and A. Arribas, “Epithermal ore deposits: First-order features relevant to exploration and assessment,” SGA Bienn. Meet., no. August, pp. 47–50, 2017, [Online]. Available: https://www.researchgate.net/publication/319272359

[7] N. C. White and J. W. Hedenquist, “Epithermal gold

deposits: Styles, Characteristics, and Exploration: Resource Geology Special Publication," SEG Newsl., no. 23, pp. 9–13, 1995.

[8] Arribas, A. (1995) Characteristics of High-Sulfidation Epithermal Deposits, and Their Relation to Magmatic Fluids. Mineralogical Association of Canada Short Course Series: Magmatic, Fluids, and Ore Deposits, 23, 419-454.

[9] Lowell, J. D., & Guilbert, J. M. (1970). Lateral and vertical alteration-mineralization zoning in porphyry ore deposits. Economic geology, 65(4), 373-408

[10] Sillitoe, R. H. (1999). Styles of high-sulfidation epithermal mineralization: Implications for exploration. Reviews in Economic Geology, 11, 221–244

[11] J. I. Kim and S. H. Choi, "Petrogenesis and tectonic implications of the late Paleoproterozoic (ca. 1.7 Ga) post-collisional magmatism in the southwestern Gyeonggi Massif at Garorim Bay, South Korea," J. Asian Earth Sci. X, vol. 5, p. 100050, 2021, doi: 10.1016/j.jaesx.2021.100050.

[12] Corbett, Greg J., and Leach, Terry M (1998).Southwest Pacific Rim Gold-Copper Systems: Structure, Alteration, and Mineralization

[13] K. Dowling and G. Morrison, "Application of quartz textures to the classification of gold deposits using North Queensland examples," Econ. Geol. Monogr. 6 Geol. Gold Depos. Perspect. 1988; Econ. Geol. Publ. Company., no. 1983, pp. 342–355, 1988.

[14] J. R. Vearncombe, "Quartz vein morphology and implications for formation depth and classification of Archaean gold-vein deposits," Ore Geol. Rev., vol. 8, no. 5, pp. 407–424, 1993, doi: 10.1016/0169-1368(93)90036-X.

[15] G. Dong, G. Morrison, and S. Jaireth, "Quartz textures in epithermal veins, Queensland-Classification, Origin, and implicationIn hand specimens , the usual ! y has," Econ. Geol., vol. 90, pp. 1841–1856, 1995.

Techno-Science Research Journal V13 (Special Issue) (2025) P 118-125

I.T.C

Content list available at ITC

Techno-Science Research Journal

Journal Homepage: www.ric.itc.edu.kh

Techno-Science Research Journal

Preliminary Study on Petrography and Geochemistry of Basaltic Rock in Ratanakiri Province, Northeast Cambodia

Chan Virak[1], Sirisokha Seang[1,2]*, Kakda Kret[1,3], Kotaro Yonezu[4], Koichiro Watanabe[5]

[1] *Faculty of Geo-Resources and Geotechnical Engineering Institute of Technology of Cambodia, Russian Federation Blvd, P.O. Box 86, Phnom Penh120404, Cambodia*

[2] *Materials Science and Structure Unit, Research and Innovation Center, Institute of Technology of Cambodia, Russian Federation Blvd, P.O. Box 86, Phnom Penh120404, Cambodia*

[3] *Energy Technology and Management Unit, Research and Innovation Center, Institute of Technology of Cambodia, Russian Federation Blvd, P.O. Box 86, Phnom Penh 120404, Cambodia*

[4] *Department of Earth Resources Engineering, Faculty of Engineering, Kyushu University,744 Motooka, Nishi-ku Fukuoka 819-0395 Japan*

[5] *Jica Senior Advisor at Japan International Cooperation Agency, 2 Chome-49-5 Nishihara, Shibuya City, Tokyo 151-0066, Japan*

Received: 1 November 2024; Revised: 1 January 2025; Accepted: 20 June 2025; Available online: October 2025

Abstract: *The investigation of basalt occurrence holds significant importance in Ratanakiri, northeastern Cambodia. Basalt in some parts of the area has not been well characterized and classified. This research aims to identify the type and composition of basalt in the study area by applying petrography, X-ray diffraction, and X-ray fluorescence analysis. Nine basalts were selected to represent distinct physical properties associated with diverse mineral compositions within the study area. Based on petrographic thin section, the prevalent minerals in the basaltic rocks within the study area comprise plagioclase, olivine, iddingsite, orthopyroxene, and, clinopyroxene. There are three types of basalts including plagioclase-olivine basalt, plagioclase-orthopyroxene-olivine basalt, and plagioclase-clinopyroxene-olivine basalt. Based on geochemical characteristics, the basaltic samples show Fe_2O_3 contents of 11.62–14.62 wt.%, TiO_2 of 1.64–2.16 wt.%, and SiO_2 of 44.12–49.37 wt.%. Alkali contents vary, with Na_2O at 0.47–1.48 wt.% and K_2O at 0.93–1.62 wt.%. The ratio of Zr/TiO_2 and Nb/Y of samples are classified as alkali basalt. That is generated from the same alkaline magma series. Most of basalts in Ratanakiri are plotted in the transition between Tholeiitic and Calc-alkaline* series *on (Na_2O + K_2O – MgO - FeO total) diagram. The majority of the basaltic rocks in the study area are similar to those in southern Vietnam, they predominantly tholeiitic, with a small quantity of alkaline basalts. The samples plot on the within-plate basalt (WPB), as shown by the Nb* 2-Zr/4-Y triangle and Zr/Y with Zr diagrams.*

Keywords: Volcanic Rock, Basalt, Geochemistry, Petrography, Within-plate basalt.

1. INTRODUCTION

All gem corundum and zircon deposits in Southeast Asia are linked to intraplate alkaline basaltic volcanic activity from the late Cenozoic period (< 30 Ma) [1]. Zircon crystals are occasionally found in alluvial deposits created by weathering Cenozoic (Neogene-Quaternary) basaltic rocks in Ratanakirir .Cenozoic basalt magmatism transitioned from early tholeiitic flood basalts to dispersed alkaline volcanic cones . Zircon in Ratanakiri was hosted in Alkali basaltic rocks [2].

Basalt is a type of mafic volcanic rock, that primarily consists of up of plagioclase and pyroxene, alternatively consisting of other mafic minerals (olivine, magnetite) and apatite and volcanic glass .These minerals may be altered to a variety of phyllosilicates, such as clay minerals, serpentine, montmorillonite, chlorite, etc [3].

This paper documents petrography and geochemical data to determine the type and composition of the basalts in the Ratanakiri province, which represents the research area. The basalts also have varying mineral compositions, indicating varying origins and genes, such as magma formation conditions, eruption processes, and the evolution of the Earth's mantle and crust.

* Corresponding author: Sirisokha Seang
E-mail: seangsirisokha@itc.eud.kh, Tel: +855-16308415

1.1 Regional Geology

Cambodia is located in the Indochina Terrane of Southeast Asia, which drifted northward from northwestern margin of the Gondwana supercontinent during the Middle Devonian period [4, 5]. It share border with Thailand to the west, Laos to the north, Vietnam to the southest, and the Gulf of the Thaialand to the southwest (Fig. 1). The Neogrne to Quaternary basaltic rocks are mostly represented in the northeastern and southwertern regions of Cambodia (Fig. 2 [6,7,8]).

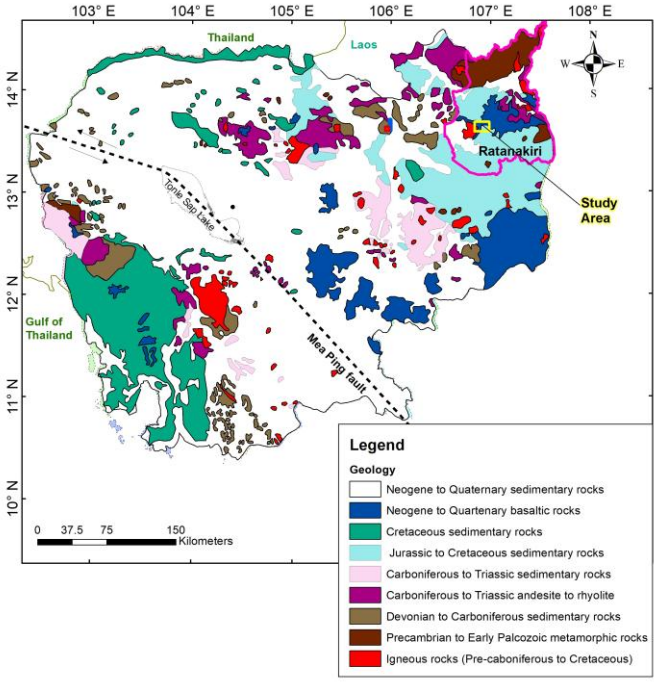

Fig. 1. Geological map of Cambodia showing Ratanakiri Province (outlined in pink), located in northeastern Cambodia [6,7].

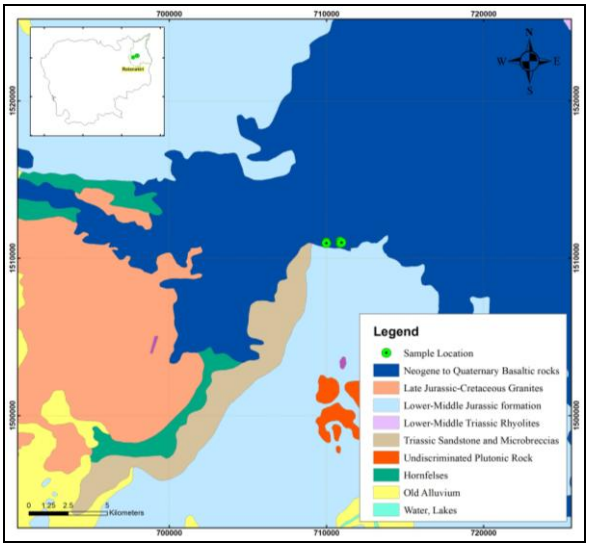

Fig. 2. Location of Study area [8].

2. METHODOLOGY

Nine samples were prepared as petrographic thin sections to examine the rocks' textural characteristics and mineral composition. These sections were observed using a Nikon Eclipse E600 POL microscope equipped with an AdvanCam-U3II camera. Twelve rock samples were analyzed by analyzed by X-ray fluorescence (XRF) spectroscopy to obtain whole-rock major element oxides. All experiments were conducted at the Faculty of Geo-Resources and Geotechnical Engineering, Institute of Technology of Cambodia. Ten samples were analyzed by using Rigaku Ultima IV X-Ray Diffractometer to determine their mineral composition. The samples were ground into a powder, mounted, and then examined by XRD at Kyushu University in Japan.

3. RESULTS AND DISCUSSION

3.1 Petrography and Mineralogy

The petrographic thin sections were used to identify the textural, primary, and secondary mineral compositions of basalt.

The current study classifies the basaltic rocks into three types: plagioclase-olivine basalt, plagioclase-orthopyroxene-olivine basalt, and plagioclase -clinopyroxene-olivine basalt.

Sample B1 contains euhedral plagioclase crystals ranging from 0.15 to 0.5 mm, subhedral to anhedral olivine crystals from 0.01 to 0.1 mm, and iddingsite (altered from olivine) reaching up to 0.5 mm (Fig. 3B). Sample B3 contains euhedral plagioclase crystals ranging from 0.1 to 0.3 mm, subhedral to anhedral olivine crystals ranging from 0.01 to 0.1 mm, orthopyroxene crystals ranging from 0.01 to 0.2 mm, and iddingsit up to 0.4 mm (Fig. 3D). Sample B4 contains euhedral plagioclase crystals ranging from 0.1 to 0.4 mm, subhedral to anhedral olivine crystals from 0.01 to 0.1 mm, and clinopyroxene crystals ranging from 0.01 to 0.15 mm (Fig. 3F). Sample B5a consists of a groundmass of plagioclase with crystal sizes varying from 0.01 to 1 mm, along with subhedral to anhedral olivine crystals up to 0.2 mm (Fig. 3H). Sample B5b contains plagioclase crystals surrounding or enclosed by olivine minerals measuring less than 0.15 mm, along with subhedral to anhedral olivine crystals up to 0.3 mm (Fig. 3J). Sample B7 contains plagioclase crystals ranging up to 0.2 mm, along with subhedral to anhedral olivine crystals up to 0.2 mm (Fig. 3L). Samples B1, B5a, B5b, and B7 are classified as plagioclase-olivine basalt. Sample B3 is classified as plagioclase-orthopyroxene-olivine basalt. Sample B4 is classified as plagioclase-clinopyroxene-olivine basalt.

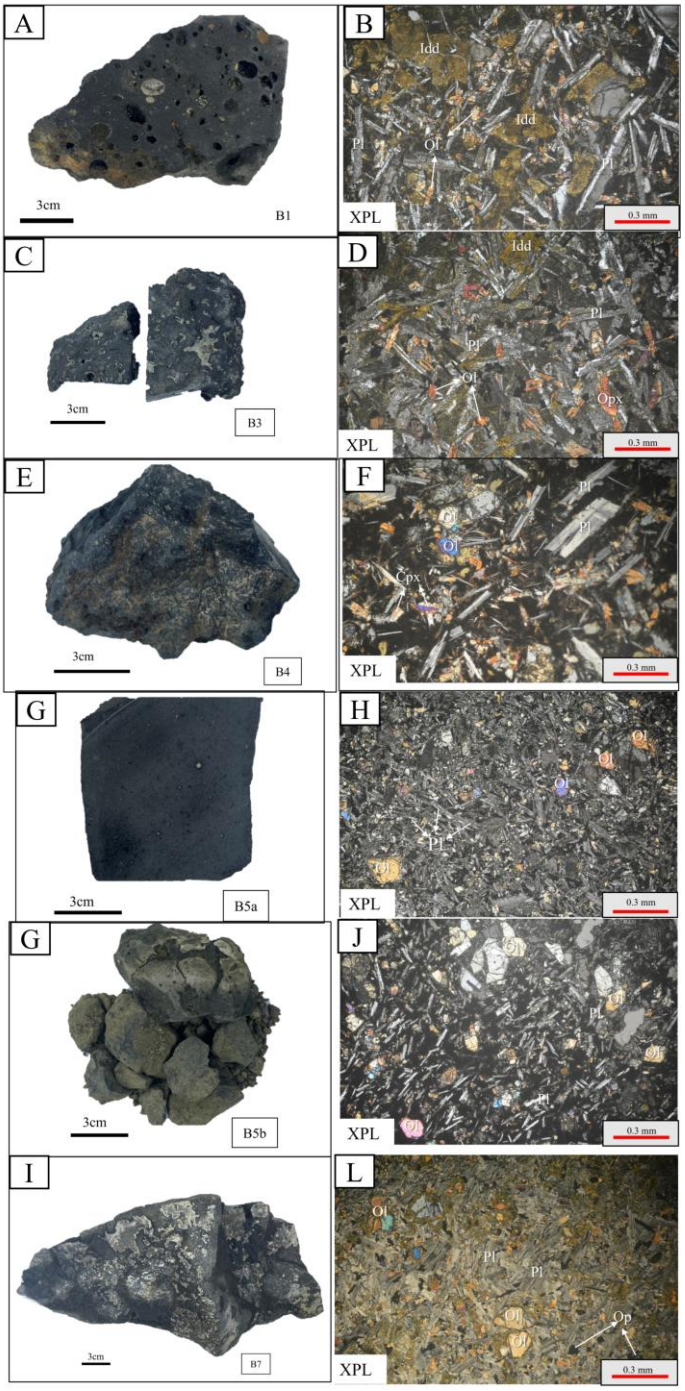

Fig. 3. (A), (C), (E),(G),(I), (K) Hand specimen of basalt samples and (B),(D),(F),(H),(J),(L) Under cross-polarized light (XPL). Abbreviation: Ol: olivine, Pl: plagioclase, Idd:iddingsite, Cpx:clinopyroxene, Opx: orthopyroxene .

Ten samples were analyzed using X-ray Diffraction (XRD) to identify the mineral composition of the basalts and soil in Ratanakiri province. The results of XRD analysis and petrographic thin section are shown in (Table 1).

According to XRD analysis, the basalts (B1, B5a, B5b, and B7) contain plagioclase, pyrophyllite, diopside, nepheline, forsterite, augite, fassaite serpentine group minerals, dickite, cristobalite, ilmenite, and hematite. The lateritic soil samples consist of augite, serpentine group and ilmenite (Fig. 4).

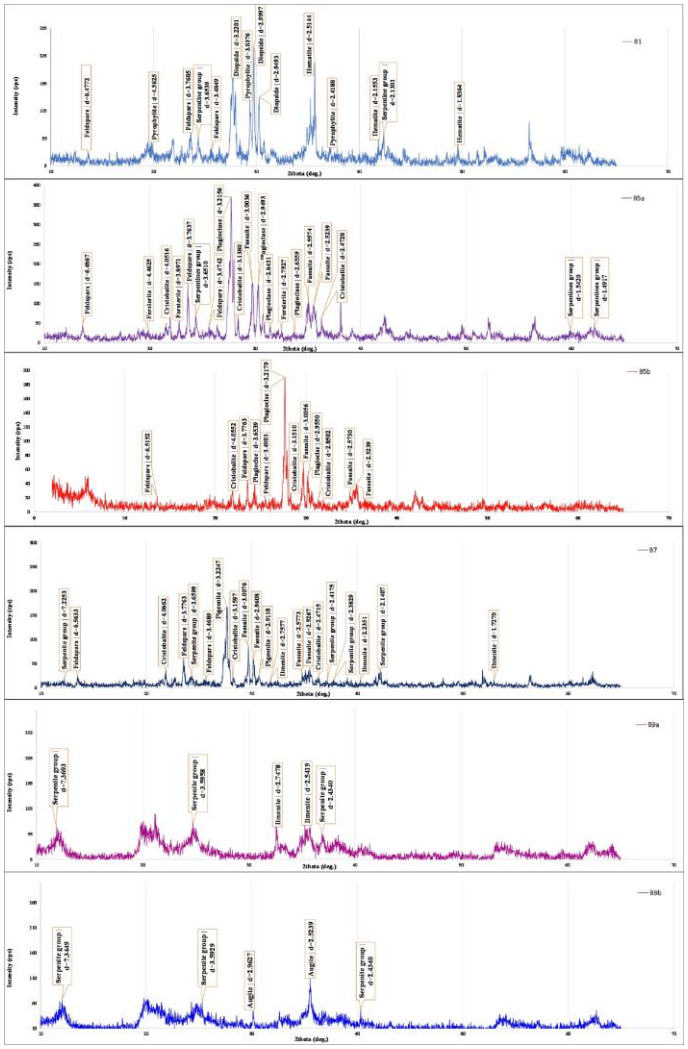

Fig. 4. Mineralogy data of basalts by X-ray diffraction analysis (XRD).

The outcrop displays a clear wethering profile from surface to depth. The upper zone consists of reddish-brown lateritic soil (Zone B and Zone C). Bellow these zones, massive basalt and wethering basalt (Zone D and one E) are represents (Fig. 5).The weathering profile observed in the study area reveals a well defind vertical sequence of soil and rock layers developd over basaltic bedrock. At the surface, the topmost later consists of a thin (50cm) topsoil enrichd with organic mater, support vegetaion and making the active zone of biological activity, underlain by a 1.50m thick reddish-brown lateritic soil containing ilmenite and serpentine group minerals.

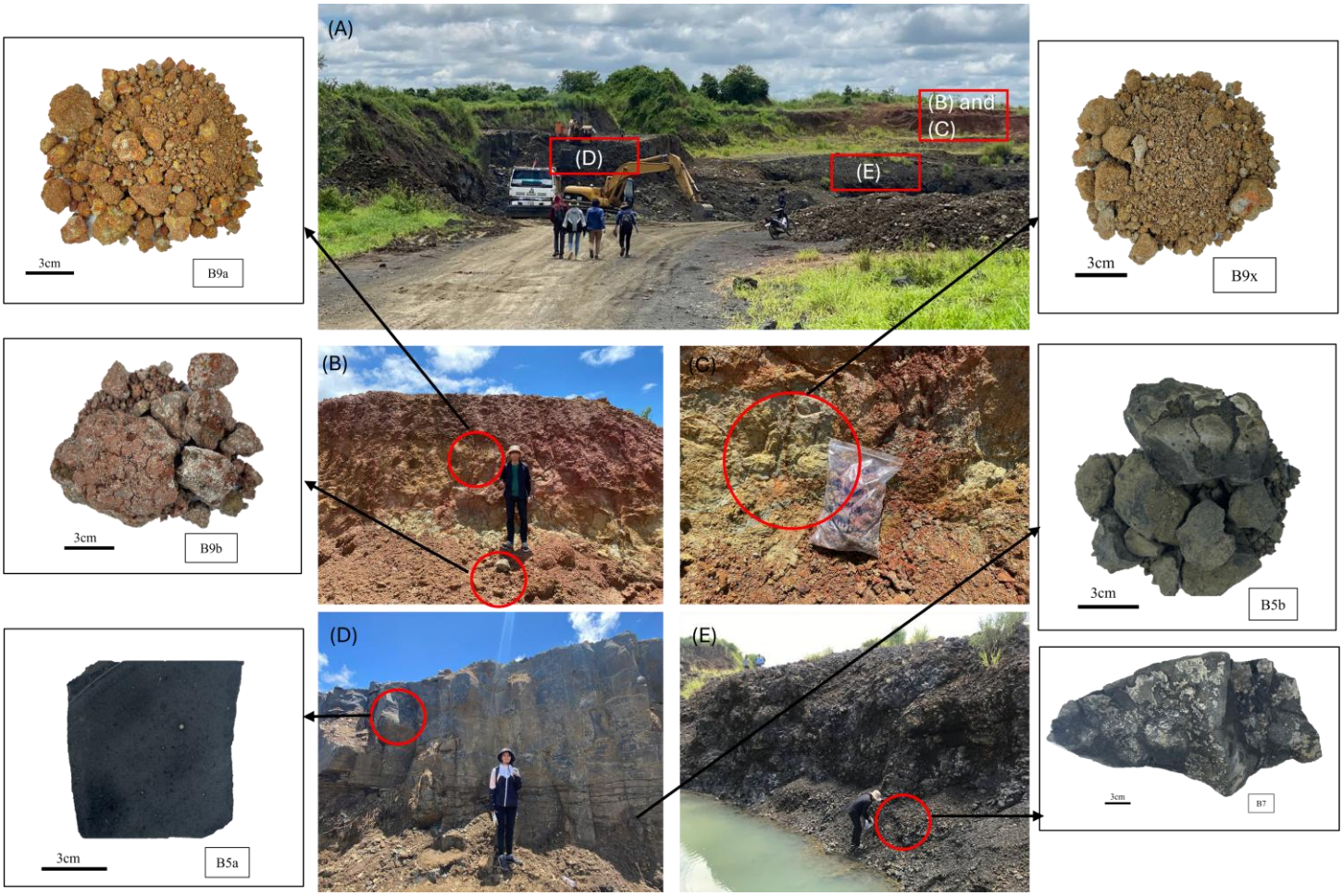

Fig. 5. (A) General view of regolith, saprolite, and sap rock levels in the basalt profile. (B) Laterite profile. (C) Laterite with clay. (D) and (E) Basalt.

This followed by a 50 cm pale yellow lateritic layer with augite soil enriched with cristobalite, forsterite, plagioclage,fassaite, and serpentine group minerals. Beneath the soils, a 1.80m massive, silthly altered basalt zone contains plagioclase, cristobalite, and fassaite. This transitions into a 0.80m moderately altered basalt with increased serpentine and fassaite. The deepest layer is a 2.30m altered basalt rich in serpentine, plagioclase, cristobalite, forsterite, ilmenite, and pigeonite (Fig. 6).

Table 1. Mineralogy of samples by XRD and petrography.

Sample ID	Mineralogy by XRD	Mineralogy by Thin section
B1	Feldspars, Pyrophylite, Serpentine group , Diopside , Hematite,	Plagioclase, Olivine ,Iddingsite.
B2	Serpentine group, K-feldspars, Nepheline	Plagioclase, Olivine
B3	Dickite, Serpentine group, Plagioclase, Ilmenite, Augite	Plagioclase, Orthopyroxene, Olivine
B4	Serpentines group, Plagioclase, Augite,	Plagioclase, Olivine
B5a	Cristobalite, Feldspars, Forsterite, Plagioclase, Serpentine group, Fassaite	Plagioclase, Olivine
B5b	Feldspars, Cristobalite,Plagioclse, Fassaite,	Plagioclase, Olivine
B7	Serpentines group, Fassaite, Feldspars, Cristobalite, Forsterite, Pigeonite, Ilmenite.	Plagioclase, Olivine, opaque mineral
B9a	Serpentines group and Ilmenite.	No Data
B9b	Serpentines group, Augite	No Data

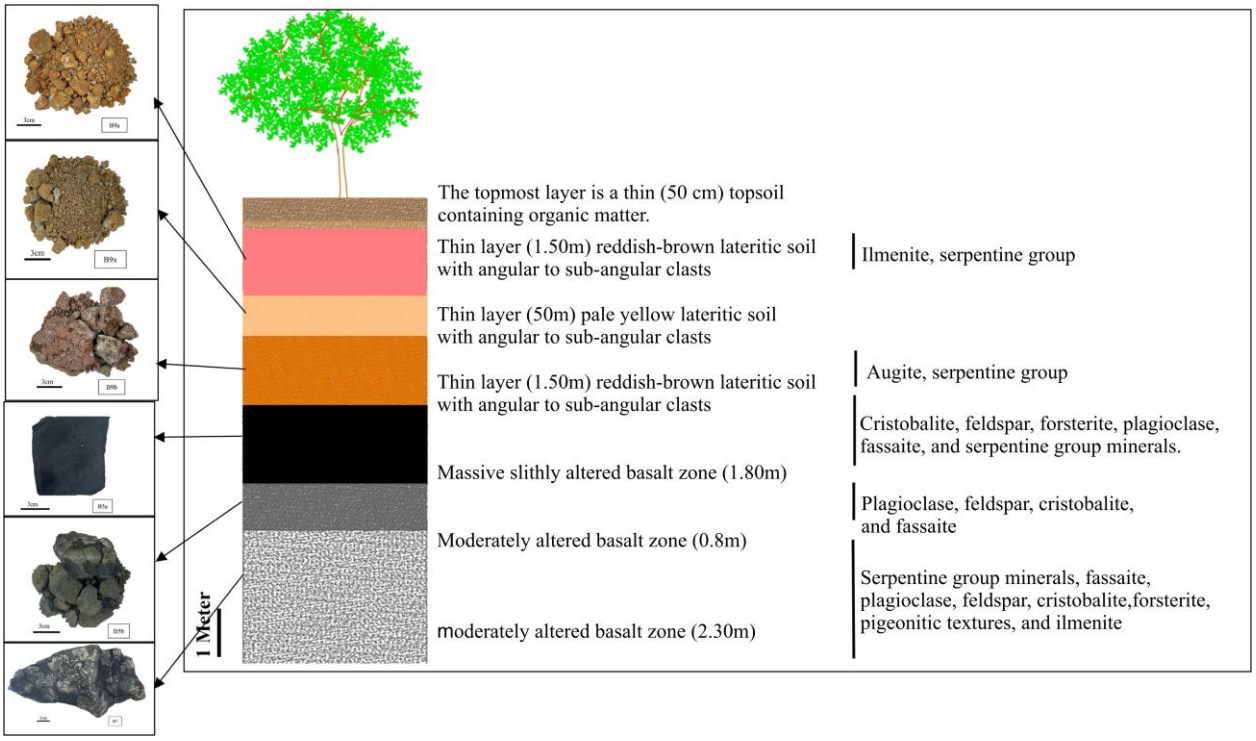

Fig. 6. The model of basaltic and soil profile in Ratanakiri province.

3.2 Geochemistry

Table 2. Summary of major oxide (wt.%) of XRF results.

Major Oxides (wt. %)	B1	B2	B3	B4	B5a	B5b	B6	B7	B8	B9a	B9b	B9x
SiO_2	47.15	47.59	47.92	48.28	4.97	46.88	44.12	45.88	49.37	44.37	39.67	28.18
TiO_2	2.02	1.95	1.74	1.64	1.82	2.15	2.16	1.79	1.99	1.71	3.04	3.14
Al_2O_3	12.59	13.99	13.13	11.65	14.02	13.58	13.82	15.56	11.28	10.21	22.68	19.57
Fe_2O_3	12.97	12.19	11.62	13.84	12.31	14.62	13.42	12.08	12.63	12.65	25.90	33.82
MnO	0.21	0.16	0.16	0.16	0.17	0.15	0.16	0.17	0.15	0.23	0.26	0.30
MgO	9.78	10.81	11.94	10.40	10.82	9.48	8.17	8.79	12.42	11.08	2.26	1.91
CaO	9.73	8.34	7.48	6.17	7.79	7.79	7.14	8.11	6.46	9.05	0.19	0.09
Na_2O	1.45	1.39	1.48	0.47	3.02	1.11	0.77	2.88	0.32	1.04	0.00	0.00
K_2O	0.74	1.62	1.54	1.10	1.12	0.93	1.85	1.66	0.97	0.67	0.10	0.03
P_2O_5	0.76	0.77	0.39	0.47	0.44	0.33	0.43	0.57	0.32	0.67	0.12	0.84
LOI	1.90	2.15	3.01	6.79	2.34	2.69	7.64	2.19	4.76	8.47	6.40	11.81
Total	99.29	100.98	100.41	100.98	103.83	99.71	99.68	99.68	100.66	100.15	100.62	99.68
Zr(ppm)	234	209	137	157	140	151	205	164	155	177	218	266
Y(ppm)	25	24	22	19	22	44	19	17	22	22	59	37
Nb(ppm)	-	-	34	35	24	16	56	42	-	42	42	56

Major oxides of basalts are represented as weight percentages of whole rocks (Table 2). The samples exhibit losses on ignition (LOI) ranging from 1.90% to 6.79%. The SiO_2 concentrations range from 47.149 wt% to 49.97 wt%, while total alkali concentrations range from 1.61 wt% to 3.02 wt%.

The TAS diagram for volcanic rock from [9] is used to categorize volcanic rock types. As a result, all samples have been classified as basalt.

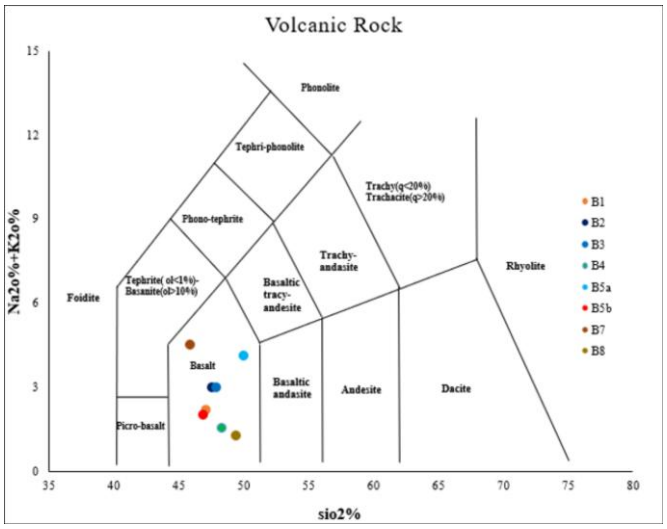

Fig. 7 TAS diagram for Volcanic rock [9].

Based on trace elements, basaltic rocks demonstrate a significant difference, especially Zr, Ti, Nb, and Y. The ratio of Zr/TiO_2 and Nb/Y follows the diagram [10] and samples are classified as alkali basalt. That generated from the same alkaline magma series.

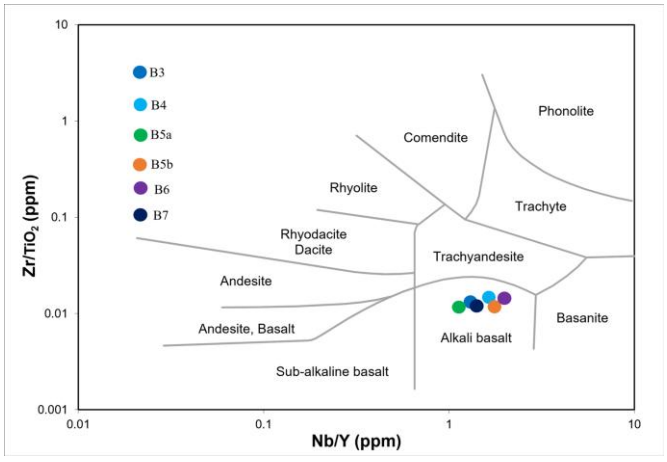

Fig. 8. Plot of Zr/TiO_2 against Nb/Y for the basaltic rocks [10].

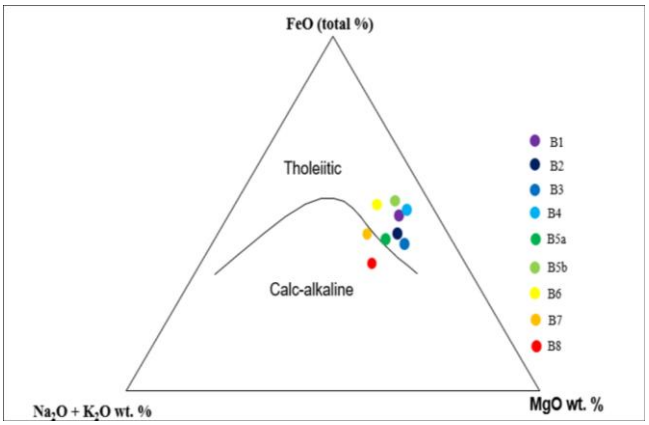

Fig. 9. The AFM diagram shows the boundary between the calc-alkaline field and the tholeiitic field [11].

An AFM diagram (Na_2O + K_2O + MgO + FeO total) [11] (Fig. 10) is used to discriminate between tholeiitic and calc-alkaline series. Sample B8 is plotted within the Calc-alkaline series, and B5a and B7 were plotted within the transition between the Tholeiitic and Calc-alkaline series, for B1, B2, B3, B4, R5b, and B6 are plotted within the Tholeiitic. Basaltic rocks in Ratanakiri region of northestern Cambodia are predominantly the tholeiitic, with a minor presence of calc-alkaline basalts. Theses basalts are dated to the Quaternary period [8]. Similarly, basalts in southern Vietnam are mostly tholeiitic, with small proportion of alkaline variaties, and are dated to the Late Cenozoic period [12,13,14]. In the central Thailand, basalts exhibit transitional gechemcal characteristics between tholeiitic and calc-alkaline compositions and are broadly assigned to the Cenozoic period [15].

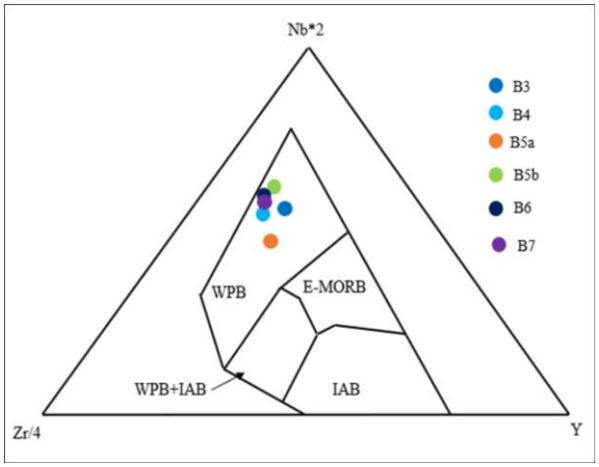

Fig. 10. Nb×2-Zr/4-Y triangular diagram [16].

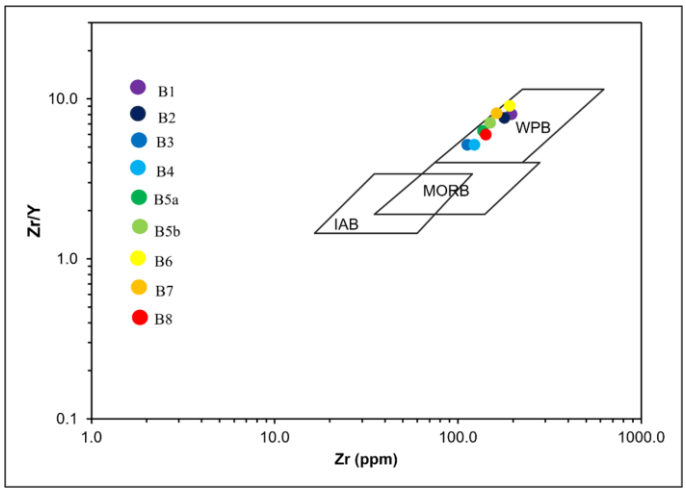

Fig. 11. Zr–Zr/Y diagram [17].

Nb×2-Zr/4-Y triangular diagram (Fig. 10, [16]), basalts plot within The within-plate basalt (WPB). Furthermore, these samples fall in the within plate basalt fields in the Zr/Y versus Zr diagram (Fig. 11, [17]).

4. CONCLUSIONS

The basalts observed in the study area composed of primarily of plagioclase, olivine, orthopyroxene, clinopyroxene and iddisite. Through petrographic analysis, samples from Ratanakiri were categorized into plagioclase-olivine basalt, plagioclase-orthopyroxene-olivine basalt, and plagioclase-clinopyroxene-olivine basalt.

Geochemicaly, basaltic in Ratanakiri is classified as alkali basalt and plot within the within-plate basalt (WPB), as indicated by the Nb*2-Zr/4-Y triangle diagram and Zr/Y with Zr diagrams.

Basalts in Ratanakiri are mainly tholeiitic to with minor calc-alkaline types formed during Quaternary. In central Thailand, they show transitional tholeiitic to calc-alkaline features (Cenozoic), while in southern Vietnam, they are mostly tholeiitic from Late Cenozoic.

ACKNOWLEDGMENTS

We sincerely express our gratitude for the generous support provided by the Laboratory-Based Education (LBE) initiative under the Project for Strengthening Engineering Education and Research for Industrial Development in Cambodia. We would also like to extend our appreciation to the Institute of Technology of Cambodia (ITC), Faculty of Geo-Resources and Geotechnical Engineering, Department of Geology, the Ministry of Mines and Energy, Cambodia, and the Department of Mines and Energy of Ratanakiri Province for their valuable collaboration and assistance.

REFERENCES

[1] Fedorov, P. I., & Koloskov, A. V. (2005). Cenozoic volcanism of southeast Asia. PETROLOGY C/C OF PETROLOGIIA, 13(4), 352.

[2] Zeug, M., Nasdala, L., Wanthanachaisaeng, B., Balmer, W. A., Corfu, F., & Wildner, M. (2018). Blue zircon from Ratanakiri, Cambodia. Journal of Gemmology, 36, 112-132.

[3] Singtuen, V., & Phajan, S. (2021). Petrographic and geochemical data of high alkaline basalts, Sisaket Terrain, NE Thailand. Data in Brief, 39, 107540.

[4] Metcalfe, I. (2011). Palaeozoic–Mesozoic history of SE Asia. Geological Society, London, Special Publications 355, pp. 7–35.

[5] Metcalfe, I. (2011). Palaeozoic–Mesozoic history of SE Asia. Geological Society, London, Special Publications 355, pp. 7–35.

[6] ESCAP, (1993). Atlas of Mineral Resources of the ESCAP Region. Cambodia. Explanatory Brochure. Economic and Social Commission for the Asia and the Pacific, United Nations, New York, v. 10, p. 87.

[7] Tien PC, An LD, Bach LD, Bac DD, Vongdara B, Phengthavongsa B, Danh T, Dy ND, Dung HT, Hai TQ, Khuc V, Kun SC, Long PD, Ly MN, My NQ, Ngan PK, Ngoc N, Ratanavong N, Quoc NK, Quyen NV, Aphaymani S D, Thanh TD, Tri TV, Truyen MT and Xay TS. (1990). Geology of Cambodia, Laos, and Vietnam. Explanatory Note to the Geological Map of Cambodia, Laos, and Vietnam at 1:1 000 000 Scale. The Geological Survey of Vietnam.

[8] GDMR-JICA (2010) Geological Map of Cambodia, 1:200,000. General Department of Mine Resources-JICA, Phnom Penh.

[9] Le Bas, et al. (1991). The IUGS systematics of igneous rocks Journal of the Geological Society, pp. 825—833.

[10] Winchester, J. A., & Floyd, P. A. (1977). Geochemical discrimination of different magma series and their differentiation products using immobile elements. Chemical geology, 20, 325-343.

[11] Irvine, T. N., & Baragar, W. R. A. (1971). A Guide to the Chemical Classification of the Common Volcanic Rocks. Canadian Journal of Earth Sciences, 8(5), 523-548.

[12] Hoang, N., & Flower, M. (1998). Petrogenesis of Cenozoic basalts from Vietnam: implication for origins of a 'diffuse igneous province'. Journal of Petrology, 39(3), 369-395.

[13] Hoang, N., Flower, M.F.J., Carlson, R.W. (1996). Major, trace element, and isotopic compositions of Vietnamese basalts: Interaction of hydrous EM1-rich asthenosphere with thinned Eurasian lithosphere. Geochimica et Cosmochimica Acta 60, 4329-4351.

[14] Hoang, N., Flower, M.F.J., Chi, C.T., Xuan, P.T., Quy, H.V., Son, T.T. (2013). Collision induced basalt

eruptions at Pleiku and Buon Me Thuot, south-central Viet Nam.Journal of Geodynamics 69, 65-83.

[15] Sriwichai, M., Rachanark, B., Assavapanuvat, P., Wattanachareekul, P., Makakum, C., Watcharamai,T., Ardkham, P., Chaikam, A., Phujareanchaiwon, C., &Srisunthon, P. (2018). Preliminary Study on Petrography and Geochemistry of Basaltic Rock in Central Phetchabun, Thailand. Bulletin of Earth Sciences of Thailand, 10(1), 44–54.

[16] Meschede, M. (1986). A method of discriminating between different types of mid-ocean ridge basalts and continental tholeiites with the Nb–Zr–Y diagram. Chem. Geol. 56 (3), 207218.Fedorov, P. I., & Koloskov, A. V. (2005). Cenozoic volcanism of southeast Asia. PETROLOGY C/C OF PETROLOGIIA, 13(4), 352.

[17] Pearce, J.A., Cann, J.R. (1973). Tectonic setting of basic volcanic rocks determined using trace element analyses. Earth Planet. Sci. Lett. 19, 290–300.

Techno-Science Research Journal V13 (Special Issue) (2025) P 126-133

I.T.C

Content list available at ITC

Techno-Science Research Journal

Journal Homepage: www.ric.itc.edu.kh

Techno-Science Research Journal

Influence of light intensity, temperature, pH, and CO2 concentration on microalgae growth and lipid content

Chin Kav[1*], Chhit Mary[3], Chet Heang[3], Or Chanmoly[1,2], Heng Ratha[1,2], Yoeun Sereyvath[3]

[1] *Faculty of Geo-resources and Geotechnical Engineering, Institute of Technology of Cambodia, Russian Federation Blvd., P.O. Box 86, Phnom Penh, Cambodia*

[2] *Research and Innovation Center, Institute of Technology of Cambodia, Russian Federation Blvd., P.O. Box 86, Phnom Penh, Cambodia*

[3] *Faculty of Chemical and Food Engineering, Institute of Technology of Cambodia, Russian Federation Blvd., P.O. Box 86, Phnom Penh, Cambodia*

Received: 1 November 2024; Revised: 1 January 2025; Accepted: 20 June 2025; Available online: October 2025

Abstract: *The global demand for biodiesel is on the rise and microalgae can absorb carbon dioxide emissions to produce biofuel. This study aims to investigate the influence of light intensity, CO_2 concentration, temperature, and pH on the growth of Acutodesmus dimorphus species and their lipid content. The light intensity will be varied across levels of 3000, 4000, 5000, and 6000 lux, while CO_2 concentrations will be set at 0% (ambient air), 5%, 10%, and 15%. Temperature will be tested within the ranges of 25 °C, 30 °C, 35 °C, and 40 °C, alongside pH levels of 6.0, 6.6, 7.2, and 7.8, with the AF-6 medium was selected as the growth medium to be used. The cultivation period is 20 days before harvesting, and microalgae growth and lipid content were assessed through UV-Vis spectroscopy, cell-dried biomass analysis, and Soxhlet extraction respectively. After a cultivation period of 20 days, the results showed that the highest growth rate and lipid content of microalgae were achieved at a light intensity of 6000 lux and 15 % CO_2 concentration. At 25 °C temperature with optimal biomass and lipid content, whereas 7.2 pH highest growth rate of biomass with 6.6 pH of lipid content. As the light intensity and CO_2 concentration rise, microalgae and lipid content growth also increase. Conversely, higher temperatures and pH levels do not lead to increased microalgae or lipid content growth. According to the result, Acutodesmus dimorphus species can capture high concentrations of CO_2 which contributes to reducing CO_2 emission and produces biofuel.*

Keywords: Acutodesmus dimorphus, Light intensity, CO_2 concentration, pH, Temperature

1. INTRODUCTION

The increasing global population is driving up the demand for fuel energy at an unprecedented rate. The extensive reliance on fossil fuels around the globe results in their depletion and pushes them nearer to exhaustion because of their unsustainable and nonrenewable characteristics. Consequently, biofuels are emerging as an increasingly viable option worldwide in place of fossil fuels [1]. Microalgae are single-celled photosynthetic organisms that use light and carbon dioxide with temperature and pH as also crucial parameters to grow and produce biomass. On the other hand, microalgae are well known as a low-cost third-generation feedstock for biodiesel, capable of producing more oil per unit area in a relatively short time compared to other types of plants [2]. Their capacity to store significant quantities of biological products within their cells and their high photosynthetic efficiency make them promising candidates for industrial raw materials. Moreover, growing microalgae does not require fertile soil, large amounts of freshwater, herbicides, or pesticides, unlike conventional crops, which means they do not compete for vital resources. Cultivating microalgae can also help mitigate atmospheric carbon dioxide levels through photosynthesis, thereby aiding in addressing the greenhouse effect and global warming. Various factors such as light, temperature, CO_2 supply, nutrient composition of the culture medium, pH, and bioreactor properties affect the production of microalgal biomass and its biochemical content [3].

In this study, the observation influences light intensities CO_2 concentration, temperature, and pH supply on the cultivation and oil characteristics of microalgae for Biodiesel

* Corresponding author: Chin Kav
E-mail: *kavchin3@gmail.com;* Tel: *+855 11 553 410*

Production. *Uv-vis spectroscopy* and cell-dried biomass must observe the growth of microalgae. The result of this study after 20 days of cultivation, the optimum light intensities, CO_2 concentration, temperature, pH, biomass, and lipid content are also discussed.

2. METHODOLOGY

2.1 Cultivation system

Acutodesmus dimorphus was obtained from the Algae and biomass research laboratory at the Malaysia-Japan International Institute of Technology and was used as the model algal species. *Acutodesmus dimorphus* was studied using a simple closed photobioreactor made of glass, size 11cm (diameter), and size 20cm (height) with a total volume of 3L. The cultivation was started with a volume of 2L of microalgae suspension consisting of AF6 medium with pH 6.6 and concentrated microalgal stock. Pre-cultures were diluted to an Absorbance (OD750nm) of 0.25 for each experiment, which was determined by a UV/VIS spectrophotometer (Agilent Cary 60). The cultivation under four conditions is illustrated in **Fig. 1**.

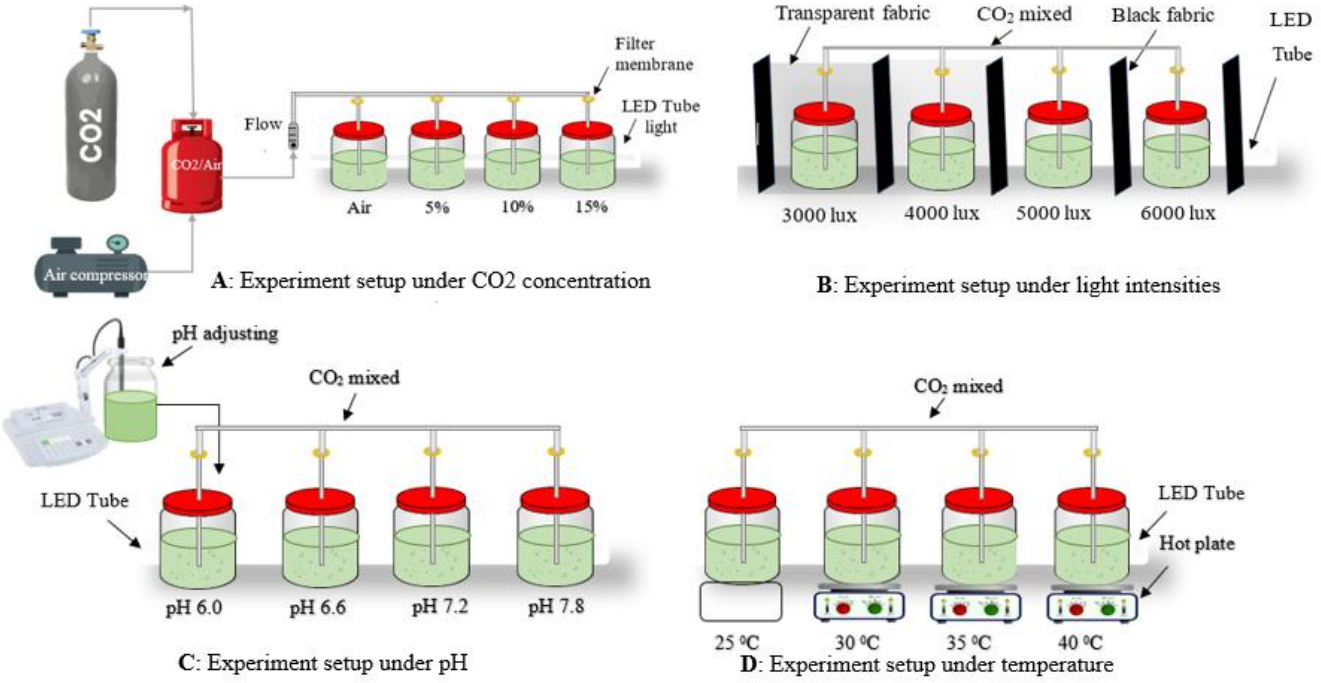

Fig. 1. Cultivation conditions under light intensity, CO_2, pH, and temperature.

2.2. Light experiment setup

The cultures were kept at varied distances from the light source, an LED tube lamp, to investigate the effects of different light intensities on microalgae growth. Each set of four experimental flasks was exposed to different light intensities (3000, 4000, 5000, and 6000 Lux). 10% CO_2 is the fixed concentration for this experiment. The flask's core was used to measure the light intensity using a digital lux meter (HS1010).

2.3. CO_2 experiment

The cultures were maintained in a continuous CO_2 environment at four distinct concentrations: ambient air, 5, 10, and 15%, respectively. For this experiment, the light intensity is set to 6000 Lux. An air compressor was used to supply ambient air to the culture media via a membrane filter (0.45µm).

CO_2 (from a CO_2 cylinder) was combined with air (from an air compressor) and then went through a CO_2/Air mixer tank to determine the precise concentration for CO_2 concentrations of 5, 10, and 15%. Following passage through a membrane filter (0.45 µm), the gas was added to the growth medium from the gas mixer tank containing the precise CO_2 concentration.

2.4. pH experiment setup

Cultivating microalgae at different pH levels requires precise optimization to promote their growth. During the cultivation process, the pH was held at designated values of 6.0, 6.6, 7.2, and 7.8. The initial setup involved incubating a microalgae stock in an AF-6 culture medium at a 1:10 ratio

within 2000 mL volumes. The pH was modified using hydrogen chloride or sodium chloride, based on the required pH level, and was accurately monitored using a pH meter (pH 6, 6.6, 7.2, and 7.8). While cultivating under various pH conditions, other parameters were regulated to facilitate growth, including a CO_2 concentration with a flow rate of 10%, maintained by a gas flow meter at a consistent rate of 100 ml per minute. The temperature was controlled at 32 ± 1°C (ambient temperature), and the cultures received light at an intensity of 6000 lux from LED fluorescent lamps.

2.5. Temperature experiment setup

Optimizing temperature conditions for microalgae cultivation is essential to enhance growth. Throughout the cultivation process, the cultures were consistently maintained at varying temperatures of 25°C, 30°C, 35°C, and 40°C. To begin, a stock of the microalgae species *Acutodesmus dimorphus* was prepared and incubated in an AF-6 culture medium at a dilution of 1:10 in 2000mL. For the cultivation at 25°C, an air conditioner was employed to lower the temperature from ambient levels, while the cultivation at 30°C occurred at room temperature. The temperatures of 35°C and 40°C were maintained using hot plates, with a thermometer for monitoring. To facilitate growth under these different temperature settings, a CO_2 level of 10% was sustained using a gas flow meter set at a constant flow rate of 100 ml per minute. The pH was also kept steady at 6.6, which is the natural pH of the medium, and the cultures were exposed to a light intensity of 6000 lux from LED fluorescent lights. Additionally, the cultivation was replicated under various temperature conditions.

2.6. Monitoring microalgae growth

To evaluate growth, a 2mL sample was collected from each photobioreactor daily to measure optical density using a UV-Vis spectrophotometer (Agilent Cary 60) at a wavelength of 750 nm. If the absorbance readings exceeded 1.0, the algal suspensions were diluted appropriately, and the actual OD750 was calculated by multiplying the OD750 value by the dilution factor. It is important to note that the culture medium was gently stirred before sampling to ensure homogeneity.

2.7. Harvesting and determining of algal biomass

Microalgae were cultivated for 20 days, followed by their collection through a membrane filtration method. The algal culture was filtered using 0.45µm filters with a 50mm diameter, utilizing gravity, pressure, or vacuum, which resulted in the algae being retained as a concentrated paste. For drying, aluminum foil was shaped into containers to hold the pellets. Initially, the empty aluminum foil containers were formed into crucibles and weighed on a high-precision balance. The wet biomass was then placed into the weighed aluminum foil crucibles and dried in an oven at 60°C for 24 hours. After the drying procedure, the samples were allowed to cool in a desiccator for 15 minutes before being weighed again using the high-precision balance.

2.8. Extraction of total lipid

The lipid was extracted from dried microalgal biomass using a Soxhlet apparatus (SER 148/6 series). Around 1 g of dried biomass was initially placed in a cellulose thimble. The lipid extraction took place in three stages: immersion for 60 minutes, washing for 60 minutes, and recovery for 15 minutes, using 70 mL of n-hexane at a temperature of 130°C in the Soxhlet apparatus. Once the extraction was complete, the resulting lipids were distilled in an oven for 30 minutes at 105°C to separate the lipids from the n-hexane solvent.

3. RESULTS AND DISCUSSION

3.1. Condition setup effect on microalgae growth

A.dimorphus was studied under light intensities, pH, CO_2 concentration, and temperature conditions. The growth of microalgae was observed every day by using a UV-Vis spectrophotometer to observe the growth rate of microalgae with dried biomass. A result of growth rate and biomass was illustrated in **Table 1**.

Table 1 shows the absorbance values and biomass on the final day of cultivation.

Condition setup	At 20 days of cultivation	
	Absorbance (OD_{750nm})	Biomass (g/L)
3000 lux	1.442 ± 0.056	0.589 ± 0.031
4000 lux	1.549 ± 0.042	0.607 ± 0.032
5000 lux	1.645 ± 0.017	0.730 ± 0.032
6000 lux	1.703 ± 0.014	0.761 ± 0.028
pH 6.0	1.579 ± 0.096	0.695 ± 0.044
pH 6.6	1.831 ± 0.039	0.813 ± 0.016
pH 7.2	1.909 ± 0.005	0.849 ± 0.002
pH 7.8	1.645 ± 0.083	0.726 ± 0.038
Ambient Air	0.628 ± 0.003	0.303 ± 0.003
CO_2 5%	0.918 ± 0.004	0.379 ± 0.001
CO_2 10%	1.424 ± 0.053	0.681 ±0.037
CO_2 15%	1.803 ± 0.026	0.819 ± 0.036
CO_2 25 °C	2.051 ± 0.069	0.915 ± 0.032
30 °C	1.658 ± 0.049	0.732 ± 0.023
35 °C	1.588 ± 0.011	0.699 ± 0.005
40 °C	1.302 ± 0.065	0.567 ± 0.030

The growth of *A. dimorphus* over 20-day periods exposed to varying light intensities is illustrated in Fig. 2. As light intensity increased, the growth patterns of the microalgae changed. The absorbance and biomass values on the final day of cultivation are shown in Table 1. The results of the experiment indicate that light intensity had a considerable impact ($p<0.05$) on absorbance and biomass at the end of the cultivation period. However, there were no significant differences ($p>0.05$) in biomass among the light intensities of 3000 lux, 4000 lux, 5000 lux, and 6000 lux. At the light intensity of 3000 lux, the lowest absorbance and biomass were recorded, demonstrating a slower growth rate compared to the other conditions. On day 20 of cultivation, the highest absorbance and biomass were observed across all light intensity conditions, with the 6000 lux setting achieving the peak absorbance of 1.703 ± 0.014 and biomass of 0.761 ± 0.028 g/L. The variation in growth rates among the four light intensity cultures suggests that 6000 lux was more conducive to the growth of A. dimorphus than the other light levels. Similar results were found by [4], who conducted a study on the growth of the microalgae Chlorella vulgaris under different light intensities (50, 80, and 110 µmol/m²/sec), identifying warm white light at 80 µmol/m²/sec (approximately 6000 lux) as the optimal intensity for microalgae growth. Conversely, saturation light intensity refers to the level of light intensity that achieves the highest growth rates; raising the light intensity beyond this level will not substantially boost growth rates [5]. Nonetheless, in the course of this study, the cultures did not attain a saturation of light intensity given the tested growth conditions.

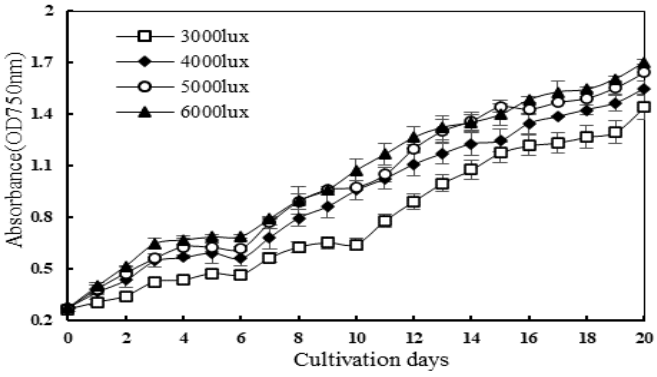

Fig. 2. The growth rate of *A. dimorphus* under light intensities.

The growth of microalgae reflects the use of CO_2 for sustaining photosynthetic activity, with its extent affected by the mass transfer of CO_2 into the cells [6]. The investigation into growth under different CO_2 concentrations demonstrated a notable impact on the patterns of cell growth curves, as illustrated in Fig. 3. The curve indicates that the absorbance of microalgae increased daily. It was noted that the growth rate of A. dimorphus significantly relied on CO_2 concentration. Table 1 depicts the absorbance and biomass of microalgae after 20 days of cultivation. Statistical analysis showed a significant impact of CO_2 on the absorbance and biomass of microalgae ($p<0.05$). However, a non-significant difference ($p>0.05$) was observed between the biomass achieved under air supply and 5% CO_2. The study's findings indicated that *A. dimorphus* exhibited a slower growth rate under air supply due to the absence of a carbon source, recording an absorbance of 0.628 ± 0.003 and a biomass of 0.303 ± 0.003 g/L after 20 days. The highest absorbance of 1.803 ± 0.026 and biomass of 0.819 ± 0.036 g/L were observed on day 20 with 15% CO_2 supply. This study illustrates that cultivating *A. dimorphus* at various CO_2 concentrations reveals that 15% CO_2 leads to enhanced growth and greater biomass than other conditions. A similar observation by [7] found that 15% CO_2 concentration was optimal for growing the microalgae *Scenedesmus sp*. Generally, increasing carbon dioxide concentration accelerates the photosynthesis process in various microalgae strains due to the higher availability of CO_2 promoting its diffusion from bulk concentration to the active usage site. Nevertheless, it is important to note that CO_2 concentration should not exceed the optimal level the strains can tolerate [8].

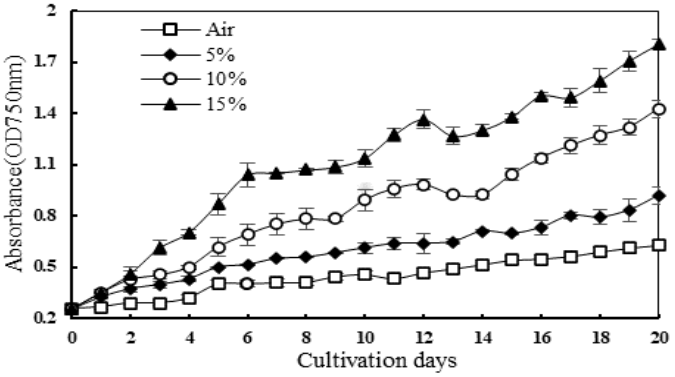

Fig. 3. Effect of CO_2 concentration on *A. dimorphus* growth.

Over 20 days, the effect of temperature on microalgae biomass was examined, as depicted in Fig. 4. The growth rate values of optical density were recorded as 2.051± 0.069, 1.658 ±0.049, 1.588 ± 0.011, and 1.302 ± 0.065 at temperatures of 25, 30, 35, and 40°C, respectively. Additionally, the growth after 20 days of cultivation got a value of biomass 0.915 ± 0.032 g/L, 0.732 ± 0.023 g/L, 0.699 ± 0.005 g/L, and 0.567 ± 0.030 g/L at temperature 25°C, 30°C, 35°C, and 40°C, respectively. The maximum biomass was noted at 25°C with 0.915 ± 0.032 g/L of biomass. There were no statistically significant differences in biomass concentrations between 25°C and 30°C, and also between 30°C and 35°C ($p > 0.05$). Conversely, at 40°C, the biomass level (0.45 ± 0.12 g/L) showed a significant decrease ($p < 0.05$) when compared to 25°C. Previous [9], [10] reported higher biomass concentrations for marine microalgae, including C. vulgaris, M. aeruginosa, P. subcapitata, and S. salina, between the temperatures of 25°C and 30°C. The outcomes of this study were similar to those of Kalinina et al. [11] but yielded lower results compared to El-Sheekh et al.,2017 [12]. This difference may stem from variations in the strains of

microalgae and the experimental conditions, including factors such as light intensity, nutrient levels, CO_2, and pH. Additionally, biomass production can lead to increased cell death and potential culture loss, as it tends to be suppressed at temperatures that are less than optimal and significantly decreased at temperatures that exceed the optimal range [13]. The investigation determined that the optimal temperature for maximizing microalgae biomass concentration is 25°C. Managing temperature is essential in microalgae cultivation for biofuel production, since temperatures higher than this can result in a notable decline in productivity and an increase in cell mortality.

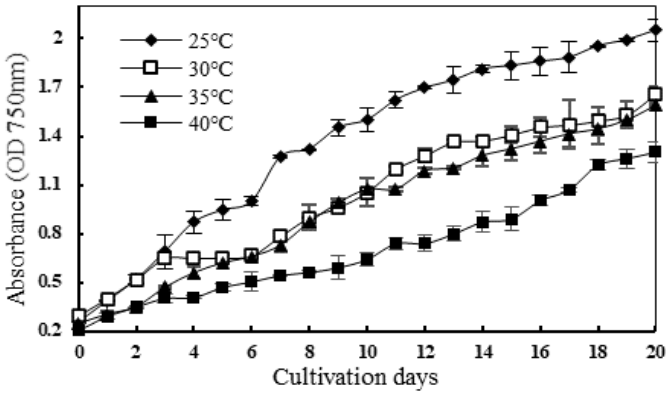

Fig. 4. The growth rate of *A. dimorphus* under temperature.

During a 20-day growth period, the impact of pH levels on the growth rate and biomass concentrations of microalgae was investigated, as illustrated in **Fig. 5**. At pH values of 6.0, 6.6, 7.2, and 7.8, the absorbance UV-Vis spectroscopy obtained were 1.579 ± 0.096, 1.831 ± 0.039, 1.909 ± 0.005, and 1.645 ± 0.0.083 with biomass 0.695 ± 0.044, 0.813 ± 0.016, 0.849 ± 0.002, 0.726 ± 0.038 g/L respectively. The pH 6.0 shows the lowest concentration of biomass at 0.695 ± 0.044 g/L. The differences in biomass concentrations did not reach statistical significance ($p > 0.05$) for pH levels 6.0, 6.6, and 7.8. The pH level of 7.2 produced the highest biomass concentration of 0.849 ± 0.002 g/L, significantly greater ($p < 0.05$) than the other pH levels. This indicates that a pH of 7.2 is important for optimizing the growth of microalgae. According to [14], both low and high pH levels can decrease the rate of photosynthesis. Elevated pH can hinder the absorption of nutrients and trace metals, whereas acidic conditions may disrupt photosystem processes and reduce the function of enzymes related to photosynthesis. The optimal pH range for the production of microalgae biomass is generally identified as being between 6.5 and 8.5, as reported by [15]. This range represents the favorable conditions for many species of microalgae. Although they investigated different strains such as C. vulgaris, the outcomes of this research align with those from [16] [17], who also observed that peak biomass occurred close to neutral pH. Based on the results of this study, a pH of 7.2 is optimal for enhancing microalgal biomass concentration and fostering increased photosynthetic and metabolic activity.

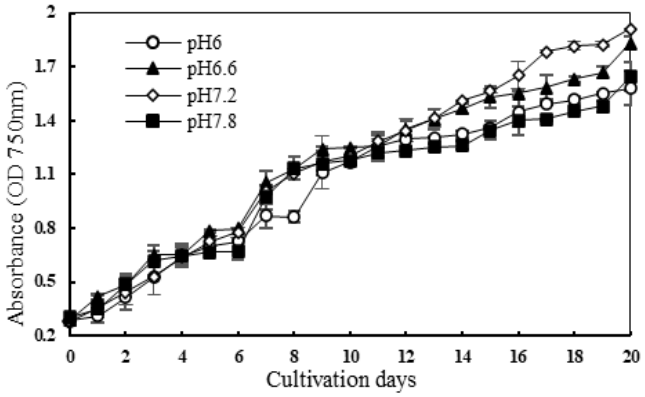

Fig. 5. Effect of pH condition on *A. dimorphus* under period 20 days**.**

3.3. Condition setup effect on lipid content

Based on the results regarding lipid content **Fig. 6**, increasing light intensity resulted in higher lipid content for *A. dimorphus*. The data indicated that light intensity significantly influenced ($p<0.05$) the lipid content of *A. dimorphus.* The lipid content measurements were 6.98 ± 0.38%, 8.92 ± 0.18%, 11.02 ± 0.13%, and 14.86 ± 0.29% at light intensities of 3000 lux, 4000 lux, 5000 lux, and 6000 lux, respectively [18]. TAG is the primary component of neutral lipids, and its synthesis requires a considerable amount of ATP and NADPH produced through photosynthesis. Thus, when exposed to high light energy levels, the excess energy may be utilized for lipid accumulation per biomass unit through photosynthesis.

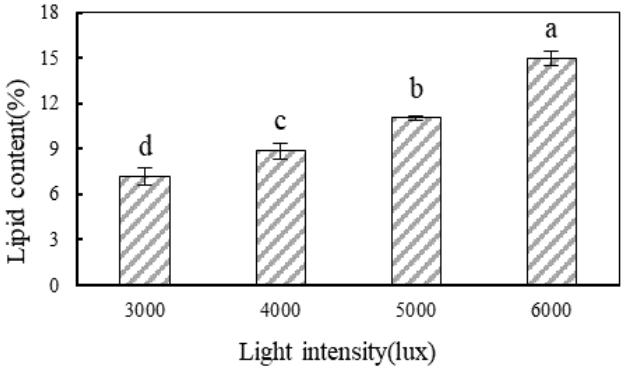

Fig. 6. Total lipid content of Microalgae under various light intensities.

Based on statistical analysis, different concentrations of CO_2 significantly influenced the lipid content of *A. dimorphus* ($p<0.05$). However, the lipid content observed in both air supply and 5% CO_2 conditions was found to be statistically insignificant ($p>0.05$). The total lipid content under air supply, as well as with 5%, 10%, and 15% CO_2 aeration, were measured at 7.58 ± 0.26%, 7.88 ± 0.12%, 12.07 ± 0.20%, and

17.47 ± 0.13%, respectively **Fig. 7**. The highest total lipid content was recorded when the culture was supplied with 15% CO_2. Thus, it is possible to enhance the lipid content in these species by utilizing higher concentrations of CO_2. CO_2 plays a crucial role in photosynthesis, impacting both biomass and lipid production. Additionally, sufficient levels of CO_2 are necessary for triacylglycerol (TAG) synthesis to take place within the microalgae [19].

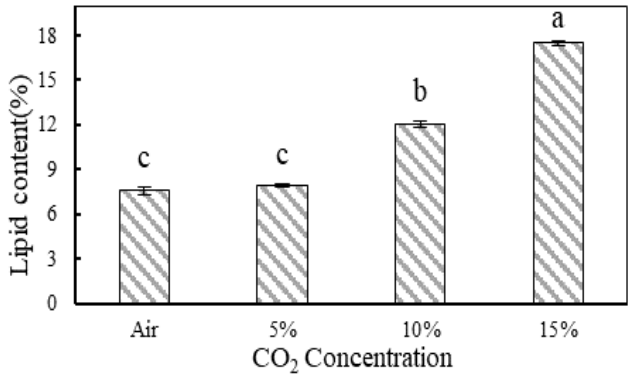

Fig. 7. Total lipid content of Microalgae under various CO2 Concentrations.

Using Soxhlet extraction at varying temperatures, the research examined lipid maximization, as illustrated in **Fig. 8**. The lipid content values recorded were 10.39 ± 0.33% at 40°C, 13.53 ± 0.28% at 35°C, 12.09 ± 0.17% at 30°C, and 16.88 ± 0.14% at 25°C. The highest total lipid content was observed at 25°C, measuring 16.88 ± 0.14%, while the lowest was at 40°C, at 10.39 ± 0.33%. A statistically significant difference in total lipid content was identified between 25°C and 40°C ($p < 0.05$). Based on the enhanced lipid yield at 25°C, this temperature is deemed optimal for Soxhlet extraction, as it promotes an effective extraction duration and aligns well with solvent polarity, making it well-suited for the diffusion-based mechanism that facilitates the Soxhlet process. According to Bakuei et al. and Assunção et al. [20] [21] lipid breakdown can lead to reduced yields at elevated temperatures, particularly those above 30°C. When the total lipid content from this study was compared to previous research, the results were similar to those reported by Yun et al. [22], who used Soxhlet extraction on the same species, *Acutodesmus dimorphus*. However, in contrast to the findings of [23] [24], the lipid content was lower, likely due to the different growth conditions and the lipid extraction methods used for *Acutodesmus dimorphus*. The research indicated that Soxhlet extraction with hexane is optimal for maximizing lipid recovery in *Acutodesmus dimorphus* at a temperature of 25°C. Managing temperature is vital for enhancing lipid extraction processes, as temperatures beyond this threshold can lead to lipid degradation and diminished yields.

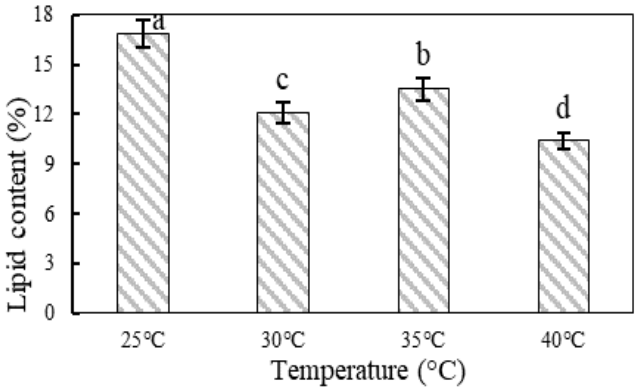

Fig. 8. Effect of temperature on the lipid content of *A. dimorphus*

Using Soxhlet extraction, the impact of pH on the total lipid content of microalgae was assessed. As shown in **Fig. 9**, the lipid content measured 7.53 ± 0.21%, 14.72 ± 0.43%, 11.00 ± 0.19%, and 10.89 ± 0.08% for pH levels of 6.0, 6.6, 7.2, and 7.8, respectively. The highest lipid content 14.72 ± 0.43% occurred at pH 6.6, whereas the lowest lipid yield 7.53 ± 0.21% was noted at pH 6.0. There was no significant difference ($p > 0.05$) in lipid content between pH 7.2 and 7.8. Significant differences ($p < 0.05$) were observed between these pH levels and both pH 6.0 and 6.6. The optimal lipid yield at pH 6.6 can be attributed to favorable conditions for lipid extraction, including an ideal pH range, suitable solvent polarity, adequate extraction time, and effective cell disruption. Lower pH levels, such as 6.0, were linked to reduced lipid yields, while higher pH levels likely led to lipid oxidation and degradation [25] [26]. When comparing the total lipid content from this study to previous research, the results align with those from [27], who also utilized Soxhlet extraction on the same *Acutodesmus dimorphus* species. However, the lipid content was lower than that reported by [28]. These discrepancies may be attributed to differences in cultivation conditions, extraction techniques (such as the Bligh and Dyer method), or the use of different microalgae species, like *Botryococcus braunii* studied by [28]. Furthermore, the results from this study indicate that lipid content reaches its peak at pH 6.6, while biomass concentration peaks at pH 7.2, where microalgae thrive through efficient nutrient absorption that enhances biomass. Conversely, mild stress at pH 6.6 prompts microalgae to accumulate more lipids as a survival mechanism. Under stress conditions such as nutrient limitation or elevated CO_2 concentration, microalgae adapt their metabolism to boost lipid production and storage, even if total biomass might decline [29] [30]. Microalgae can also alter the pH of their environment through their metabolic activities. For instance, during photosynthesis, they consume CO_2, which can increase the pH of the medium.

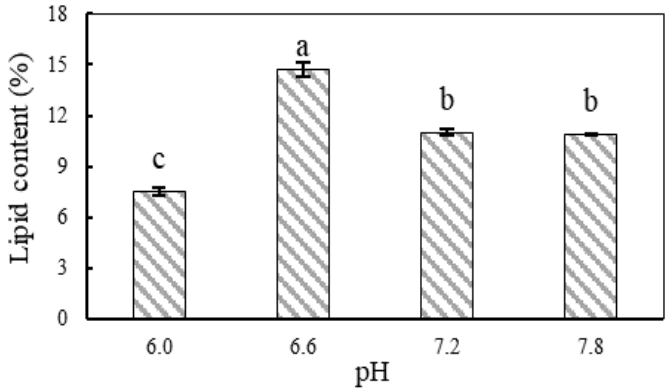

Fig. 9. Effect of pH on the lipid content of microalgae after 20 days.

4. CONCLUSIONS

A. dimorphus was grown under four conditions different with varying light intensities, CO_2 levels, temperature, and pH to assess its growth, biomass, and lipid accumulation. The findings reveal considerable enhancements in the growth, biomass, and lipid levels of A. dimorphus when suitable light intensities and CO_2 conditions are applied. Additionally, There were two parameters temperature and pH were applied to microalgae cultivation. Among the light intensity variations studied, the optimal growth rate and lipid content yield of *A. dimorphus* were observed at a light intensity of 6000 lux, resulting in a biomass of 0.761±0.028 g/L and a lipid content of 14.86 ± 0.29%. Furthermore, A. dimorphus exhibited accelerated growth rates, biomass accumulation, and lipid content when supplied with 15% CO_2, yielding a biomass of 0.819±0.036 g/L and a lipid content of 17.47 ± 0.13%. The difference under temperature supplied on A. dimorphus 25 ^{0}C of temperature obtained a high amount of 0.915 ± 0.032 g/lL of biomass with 16.88 ± 0.14% of lipid content. Moreover, the high growth rate of biomass under 7.2 pH with biomass of 0.849 ± 0.002 g/L, whereas the optimal growth rate for lipid content under 6.8 pH with 14.72 ± 0.43% of lipid content. Based on the results and discussions presented, microalgae represent a sustainable energy source due to their lipid content and play a role in decreasing CO_2 emissions through photosynthesis.

ACKNOWLEDGMENTS

The project was funded by the Laboratory-Based Education (LBE). Thanks to the Laboratory for Nanostructure and Chemical Analysis, Institute of Technology of Cambodia for UV-vis analysis.

REFERENCES

[1] M. I. Khan, J. H. Shin, and J. D. Kim, "The promising future of microalgae: current status, challenges, and optimization of a sustainable and renewable industry for biofuels, feed, and other products," Microb. Cell Factories, vol. 17, no. 1, p. 36, Mar. 2018, doi: 10.1186/s12934-018-0879-x.

[2] F. Ideris et al., "Progress on Conventional and Advanced Techniques of In Situ Transesterification of Microalgae Lipids for Biodiesel Production," Energies, vol. 15, no. 19, Art. no. 19, Jan. 2022, doi: 10.3390/en15197190.

[3] V. Bialevich, V. Zachleder, and K. Bišová, "The Effect of Variable Light Source and Light Intensity on the Growth of Three Algal Species," Cells, vol. 11, no. 8, p. 1293, Apr. 2022, doi: 10.3390/cells11081293.

[4] A. Khalili, G. D. Najafpour, G. Amini, and F. Samkhaniyani, "Influence of nutrients and LED light intensities on biomass production of microalgae Chlorella vulgaris," Biotechnol. Bioprocess Eng., vol. 20, no. 2, pp. 284–290, Apr. 2015, doi: 10.1007/s12257-013-0845-8.

[5] V. Bialevich, V. Zachleder, and K. Bišová, "The Effect of Variable Light Source and Light Intensity on the Growth of Three Algal Species," Cells, vol. 11, no. 8, Art. no. 8, Jan. 2022, doi: 10.3390/cells11081293.

[6] R. A. S. Lestari, E. P. Nurlaili, and P. Kusumo, "The effect of carbon dioxide concentration and the dimension of photobioreactor on the growth of microalgae Nannochloropsis sp.," presented at the 4th international conference on industrial, mechanical, electrical, and chemical engineering, Surakarta, Indonesia, 2019, p. 030109. doi: 10.1063/1.5098284.

[7] L. Patil and B. Kaliwal, "Effect of CO_2 Concentration on Growth and Biochemical Composition of Newly Isolated Indigenous Microalga Scenedesmus bajacalifornicus BBKLP-07," Appl. Biochem. Biotechnol., vol. 182, no. 1, pp. 335–348, May 2017, doi: 10.1007/s12010-016-2330-2.

[8] K. Mohammed, I. Abubakar, G. Tanimu, and S. Abdurrazzak, "The Effect of Carbon dioxide Concentration on the Rate of Microalgae Growth, CO_2 Uptake and Nutrient Removal from Wastewater," vol. 17, pp. 79–91, Jan. 2017.

[9] A. L. Gonçalves, J. C. M. Pires, and M. Simões, "The effects of light and temperature on microalgal growth and nutrient removal: an experimental and mathematical approach," RSC Adv., vol. 6, no. 27, pp. 22896–22907, 2016, doi: 10.1039/C5RA26117A.

[10] K. Ranglová, G. E. Lakatos, J. A. C. Manoel, T. Grivalský, and J. Masojídek, "Rapid screening test to estimate temperature optima for microalgae growth using photosynthesis activity measurements," Folia Microbiol. (Praha), vol. 64, no. 5, pp. 615–625, Sep. 2019, doi: 10.1007/s12223-019-00738-8.

[11] A. Kalinina et al., "Study of the Influence of the Temperature and Time of Microalgae Cultivation on the

Reproduction Rate of Chlorella and Scenedesmus Microalgae When Cultured in a Tubular Photobioreactor," Microbiol. Res., vol. 14, no. 4, Art. no. 4, Dec. 2023, doi: 10.3390/microbiolres14040142.

[12] M. El-Sheekh, A. El-Fatah Abomohra, M. Abd El-Azim, and R. Abou-Shanab, "Effect of temperature on growth and fatty acids profile of the biodiesel producing microalga Scenedesmus acutus," Base, Jan. 2017, doi: 10.25518/1780-4507.15291.

[13] M. Hawrot-Paw and M. Sąsiadek, "Optimization of Microalgal Biomass Production in Vertical Tubular Photobioreactors," Energies, vol. 16, no. 5, Art. no. 5, Jan. 2023, doi: 10.3390/en16052429.

[14] M. L. Bartley, W. J. Boeing, B. N. Dungan, F. O. Holguin, and T. Schaub, "pH effects on growth and lipid accumulation of the biofuel microalgae Nannochloropsis salina and invading organisms," J. Appl. Phycol., vol. 26, no. 3, pp. 1431–1437, Jun. 2014, doi: 10.1007/s10811-013-0177-2.

[15] J. Assunção, H. M. Amaro, T. Tavares, F. X. Malcata, and A. C. Guedes, "Effects of Temperature, pH, and NaCl Concentration on Biomass and Bioactive Compound Production by Synechocystis salina," Life, vol. 13, no. 1, Art. no. 1, Jan. 2023, doi: 10.3390/life13010187.

[16] A. Cortés Téllez, S. Sánchez-Fortún, M. García-Pérez, and M. C. Bartolomé Camacho, "Effects of pH on the growth rate exhibited of the wild-type and Cd-resistant Dictyosphaerium chlorelloides strains," Limnetica, vol. 37, Jul. 2018, doi: 10.23818/limn.37.19.

[17] T. T. A. Le and T. Nguyen, "Potential of hospital wastewater treatment using locally isolated Chlorella sp. LH2 from cocoon wastewater," Bioresource. Bioprocess., vol. 11, no. 1, p. 35, Apr. 2024, doi: 10.1186/s40643-024-00748-6.

[18] A. Difusa, J. Talukdar, M. C. Kalita, K. Mohanty, and V. V. Goud, "Effect of light intensity and pH condition on the growth, biomass and lipid content of microalgae Scenedesmus species," Biofuels, vol. 6, no. 1–2, pp. 37–44, Mar. 2015, doi: 10.1080/17597269.2015.1045274.

[19] S. Pandey, I. Narayanan, R. Selvaraj, T. Varadavenkatesan, and R. Vinayagam, "Biodiesel production from microalgae: A comprehensive review on influential factors, transesterification processes, and challenges," Fuel, vol. 367, p. 131547, Jul. 2024, doi: 10.1016/j.fuel.2024.131547.

[20] N. Bakuei, G. Amini, G. Najafpour, M. Jahanshahi, and M. Mohammadi, "Optimal cultivation of Scenedesmus sp. microalgae in a bubble column photobioreactor," Indian J. Chem. Technol., vol. 22, pp. 20–25, Jan. 2015.

[21] J. Assunção, H. M. Amaro, T. Tavares, F. X. Malcata, and A. C. Guedes, "Effects of Temperature, pH, and NaCl Concentration on Biomass and Bioactive Compound Production by Synechocystis salina," Life, vol. 13, no. 1, Art. no. 1, Jan. 2023, doi: 10.3390/life13010187.

[22] H.-S. Yun, M.-K. Ji, Y.-T. Park, E.-S. Salama, and J. Choi, "Microalga, Acutodesmus obliquus KGE 30 as a potential candidate for CO_2 mitigation and biodiesel production," Environ. Sci. Pollut. Res., vol. 23, no. 17, pp. 17831–17839, Sep. 2016, doi: 10.1007/s11356-016-6971-z.

[23] B. Z. Darki, J. Seyfabadi, and S. Fayazi, "Effect of nutrients on total lipid content and fatty acids profile of Scenedesmus obliquus," Braz. Arch. Biol. Technol., vol. 60, p. e17160304, May 2017, doi: 10.1590/1678-4324-2017160304.

[24] D. Jha, V. Jain, B. Sharma, A. Kant, and V. K. Garlapati, "Microalgae-based Pharmaceuticals and Nutraceuticals: An Emerging Field with Immense Market Potential," ChemBioEng Rev., vol. 4, no. 4, pp. 257–272, Aug. 2017, doi: 10.1002/cben.201600023.

[25] P. Imbimbo, L. D'Elia, D. Liberti, G. Olivieri, and D. M. Monti, "Towards green extraction methods from microalgae learning from the classics," Appl. Microbiol. Biotechnol., vol. 104, no. 21, pp. 9067–9077, Nov. 2020, doi: 10.1007/s00253-020-10839-x.

[26] I. M. R. Fattah et al., "Lipid Extraction Maximization and Enzymatic Synthesis of Biodiesel from Microalgae," Appl. Sci., vol. 10, no. 17, p. 6103, Sep. 2020, doi: 10.3390/app10176103.

[27] J. Grobler, K. G. Harding, M. Smit, S. Ramchuran, P. Durand, and M. Low, "Biodiesel production potential of an indigenous South African microalga, Acutodesmus bajacalifornicus," Sci. Afr., vol. 13, p. e00952, Sep. 2021, doi: 10.1016/j.sciaf.2021.e00952.

[28] J. Boni, S. Aida, and K. Leila, "Lipid Extraction Method From Microalgae Botryococcus Braunii As Raw Material To Make Biodiesel With Soxhlet Extraction," J. Phys. Conf. Ser., vol. 1095, p. 012004, Sep. 2018, doi: 10.1088/1742-6596/1095/1/012004.

[29] Y. A. Alkhamis, R. T. Mathew, G. Nagarajan, S. M. Rahman, and M. M. Rahman, "pH induced stress enhances lipid accumulation in microalgae grown under mixotrophic and autotrophic condition," Front. Energy Res., vol. 10, Oct. 2022, doi: 10.3389/fenrg.2022.1033068.

[30] A. Udayan et al., "Production of microalgae with high lipid content and their potential as sources of nutraceuticals," Phytochem. Rev., vol. 22, no. 4, pp. 833–860, Aug. 2023, doi: 10.1007/s11101-021-09784-y.

Techno-Science Research Journal V13 (Special Issue) (2025) P 134-141

Content list available at ITC

Techno-Science Research Journal

Journal Homepage: www.ric.itc.edu.kh

Techno-Science Research Journal

Estimation of Groundwater Recharge Using Monitoring Well Data in the Yogyakarta-Sleman Groundwater Basin, Indonesia

Heru Hendrayana[1,3*], Indra Agus Riyanto[2], Doni Prakasa Eka Putra[1,3], Wahyu Wilopo[1,3], Agung Harijoko[1]

[1] *Department of Geological Engineering, Faculty of Engineering, Universitas Gadjah Mada, Yogyakarta 55281, Indonesia*
[2] *Department of Geography Information Science, Faculty of Science, Technology, Engineering, and Mathematics, Universitas Maha Karya Asia, Yogyakarta, Indonesia*
[3] *Groundwater Working Group (GWWG), Universitas Gadjah Mada, Yogyakarta 55281, Indonesia*

Received: 1 November 2024; Revised: 1 January 2025; Accepted: 20 June 2025; Available online: October 2025

Abstract: *Yogyakarta is one of the largest provinces in Indonesia, and it heavily utilizes groundwater. However, the rise of urban development, population growth, and tourism annually pose significant threats to these resources. To mitigate excessive water extraction, 38 monitoring wells have been installed across the recharge, transition, and discharge areas of the Yogyakarta-Sleman Basin. This study aims to calculate groundwater recharge using Healy and Cook's water-table fluctuation method equation. Groundwater level data from 2023-2024 collected from these wells indicate groundwater level fluctuations ranging from 0.75 to 5 meters. The calculated groundwater recharge rates exhibit three distinct distribution value patterns: 1,200 to 1,700 mm/year in the recharge area of Sleman District, 500 to 1,200 mm/year in the transition zone of Yogyakarta City, and less than 500 mm/year in the discharge area of Bantul District.*

Keywords: Groundwater Level, Monitoring Well, Groundwater Recharge, Yogyakarta-Sleman Groundwater Basin

1. INTRODUCTION

Groundwater monitoring wells are one of the key parameters in global groundwater management [1]. These wells are essential for monitoring & protecting groundwater usage and assessing its environmental impacts [2,3]. They're also used in planning groundwater use, taxation, and implementing usage restrictions [4,5]. Data from monitoring wells also provide valuable insights into aquifer characteristics concerning seasonal variations, land-use changes, climate change, and lithological differences [6]-[9] (Arnaud et al., 2022; Wolf et al., 2022; Elmahdy & Mohammed, 2023; Huang et al., 2024). They also provide data to calculate groundwater recharge over long and short periods [10,11].

Groundwater recharge calculations have been conducted using various methods, including water budget analysis, groundwater modeling, unsaturated and saturated physical methods, chemical tracers, and conceptual models [12]. One of the most commonly used methods worldwide is the water table fluctuation method [13]-[16]. This method provides accurate calculations by utilizing long-term data and reflecting aquifer dynamics [17], using groundwater level time data series and specific yield parameters from the aquifer. The water table fluctuation method is recognized for its easiness, simplicity, and practicality in groundwater recharge calculations [18]. It also can serve as a solid foundation for developing quick and dynamic groundwater management policies.

The Yogyakarta-Sleman groundwater basin is one of Indonesia's regions with many monitoring wells. In practice, these monitoring wells in the Yogyakarta-Sleman groundwater basin are mainly used only to monitor groundwater level fluctuation. Groundwater usage in this basin is relatively high due to domestic, hotel, and industrial activities [18]. This is driven by the rapid increase in industrial wells & massive land use changes [19]. This study aims to calculate groundwater recharge in the Yogyakarta-Sleman groundwater basin for 2023-2024, updating previous assessments from 2020-2022, which utilized data from 8 monitoring wells [20]. Expanding the dataset to 38 monitoring wells, this study's findings are expected to support developing and formulating temporal groundwater management policies.

* Corresponding author: Heru Hendrayana
E-mail: *heruha@ugm.ac.id*

2. METHODOLOGY

This study utilizes monitoring well data from January 2023 to April 2024, provided by DINAS PU ESDM DI Yogyakarta Office. The monitoring well data series captures seasonal changes and variations, covering the rainy-dry-rainy cycle. Thirty-eight monitoring wells were used, distributed across groundwater recharge, transition, and groundwater discharge areas (Fig. 1). The data collected includes groundwater level depths, while specific yield data was obtained from secondary shapefile data provided by DINAS PU ESDM DI Yogyakarta. Rainfall data from January 2023 to April 2024 was sourced from the Balai Besar Wilayah Sungai (BBWS) Serayu-Opak.

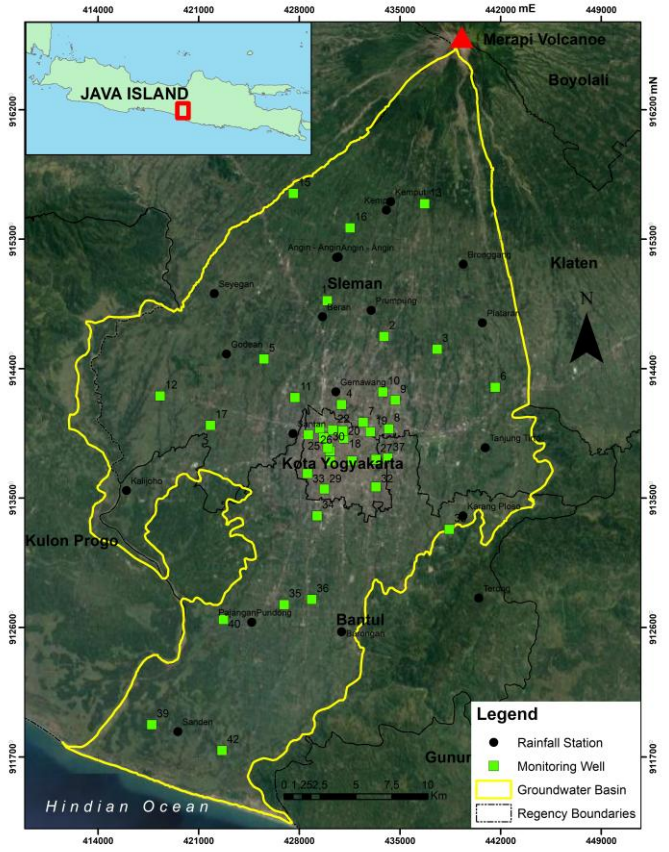

Fig. 1. Study Area (Basemap Source : BIG, 2004)

Groundwater recharge calculation using the water table fluctuation method followed Equation 1 as Healy and Cook [21] outlined. The value of Δh (change in water-table height over time) was obtained from processing monitoring well data using Microsoft Excel to get a graph of water table fluctuations. It is determined by subtracting the highest peak value of the water table rise and the lowest point of the recession curve extrapolation (Fig. 2). Specific yield data, sourced from secondary data, was processed by inputting the location attributes of each monitoring well into a particular yield shapefile using ArcGIS, producing a varying specific yield for each well. After obtaining each component, each well's groundwater recharge values were calculated in Excel using Equation 1. The results of groundwater recharge values are then interpolated using the Inverse Distance Weighting (IDW) method in GIS to generate a spatial distribution map displaying the spatial distribution of groundwater recharge values. The Inverse Distance Weighting (IDW) method has a lower Root Mean Square Error (RMSE) value when compared to the Kriging and Spline methods.

The analysis conducted in this study includes mapping the spatial distribution of groundwater recharge values in the Yogyakarta-Sleman groundwater basin based on their values, comparing the value of groundwater recharge obtained with previous studies [20], and examining the correlation pattern between monitoring well data and rainfall patterns. The outcomes of this study are in the form of a groundwater recharge map for the Yogyakarta-Sleman basin, a groundwater recharge calculations table of each well, and graphs showing the correlation between rainfall patterns and groundwater level fluctuations.

$$\Delta Sgw = R = Sy \,.\, \Delta H/\Delta t \qquad \text{(Eq. 1)}$$

where:

$\Delta S^{gw}/R$ = Groundwater recharge
S_y = Specific yield
ΔH = The difference between the peak of the rise & low point of the extrapolated antecedent recession curve at the time of the peak
Δt = Time difference of ΔH

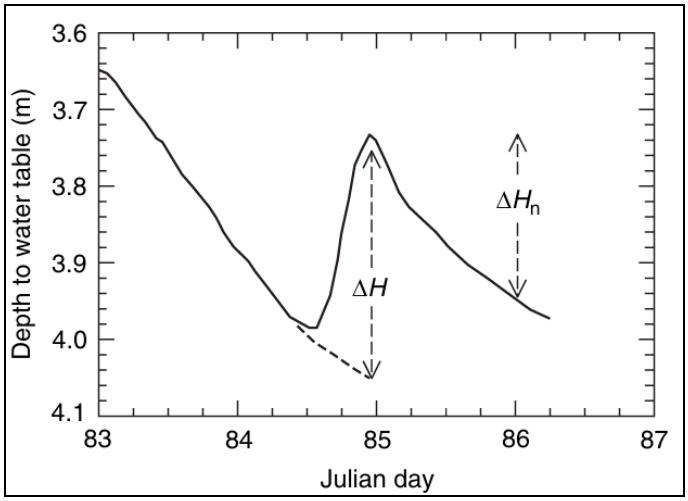

Fig. 2. The concept of groundwater recharge measurement using the water table fluctuation method [12]

3. RESULTS AND DISCUSSION

The calculation results from 38 monitoring wells show that ΔH values vary from 0.75 to 5 meters (Fig. 3). The highest ΔH

value of 5 meters was observed at well number 1 in the recharge area (north), while the lowest ΔH value was recorded at well number 35 in the discharge area (south). The highest ΔH range value pattern was found in the recharge and transition areas where groundwater is heavily utilized by industries, in contrast to the discharge area in wells (well numbers 31, 32, 34, 35, 36, 38, 39, 40, and 42), which exhibited low ΔH range value pattern due to low industrial activities (Table 1). Land use, particularly settlements in Yogyakarta City and Sleman Regency, also contributes to groundwater level fluctuations [18,22]. The increasing number of industries extracting groundwater annually in the Yogyakarta-Sleman basin further impacts ΔH values [19]. Similar patterns were also observed in ΔH values in the previous study from 2018-2022 at Yogyakarta-Sleman based, which ranged from 0.9 – 4.4 meters [20].

The graphs of specific yield values from secondary data display a diverse pattern in the Yogyakarta-Sleman groundwater basin (Fig. 3), with most monitoring wells having a specific yield of 0.24. The Map of Specific Yields of the Yogyakarta-Sleman Groundwater Basin can be observed in Fig. 4. The lowest specific yield value is found along the coastal area, with a value of 0.09 due to the high abundance of clay. In contrast, the highest values of 0.31-0.34 are found in the recharge area dominated by sand material. It is observed that the specific yield values in this study differ from those in Razi et al. [20], which used pumping test equations to calculate the specific yield values. In this study, the specific yield was computed using the Freeze and Cherry (1979) method [23], while Razi et al. [20] applied the Beretta and Stevenazzi (2018) equation. Razi et al. [20] reported lower specific yield values with a range of 0.13-0.2, which is relatively lower than this study's 0.09-0.31 range. These differences in specific yield values will affect the calculations of groundwater recharge.

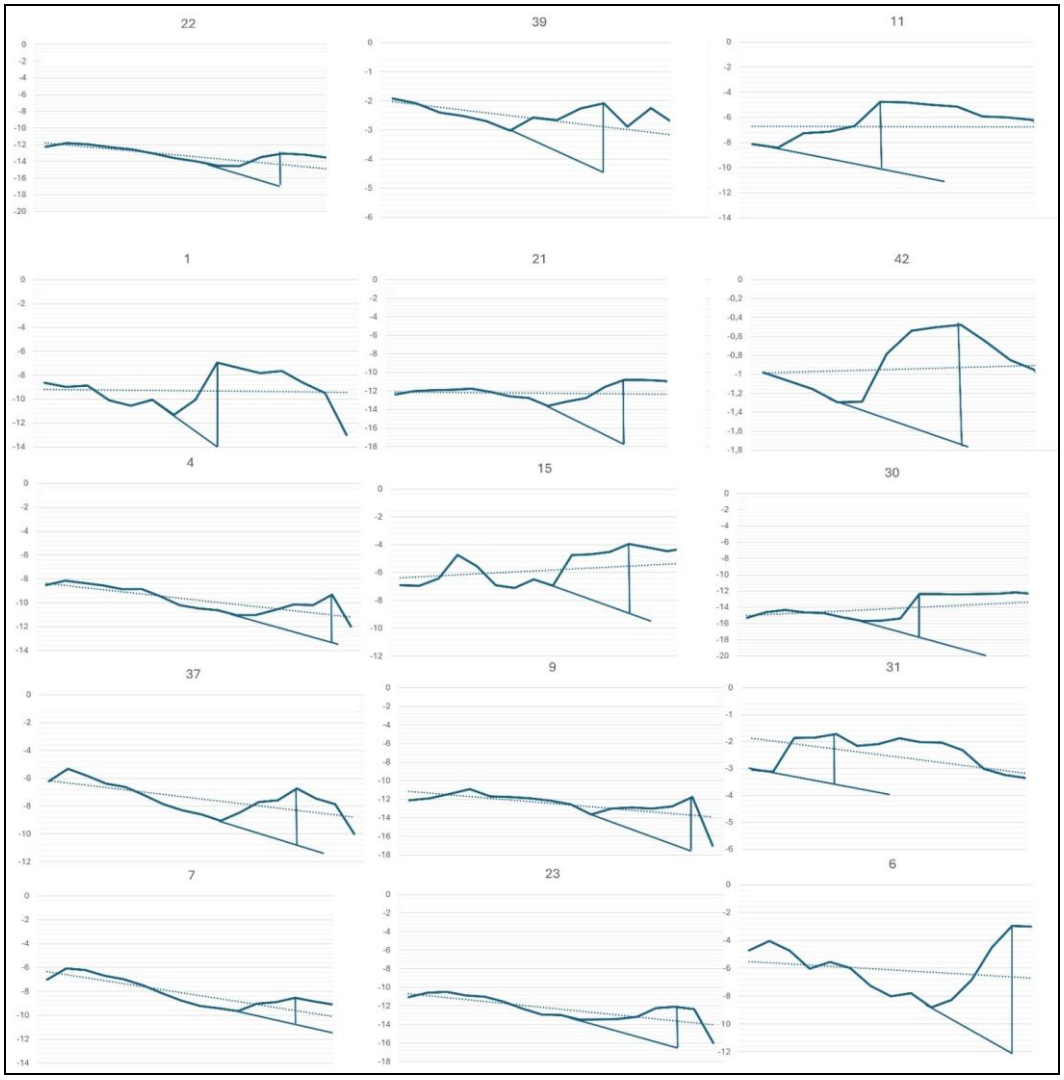

Fig. 3. Captions Graph of ΔH Calculations in the Yogyakarta-Sleman Groundwater Basin

The geology of the study area includes both Old Volcanic Deposits from Merapi and Young Volcanic Deposits from Merapi (see Fig. 5). The Old Volcanic Deposits consist of breccia, agglomerate, and lava flows, while the Young Volcanic Deposits include tuff, ash, breccia, agglomerate, and lava flows [24]. The aquifers in the study area consist of the Yogyakarta Aquifer (Upper), which is made up of materials such as sand, gravel, silt, and clay, and the Sleman Formation (Lower), composed primarily of sand and gravel [25].

Table 1. Calculating Groundwater Recharge Using 2023-2024 Monitoring Well Data

Monitoring Well	Delta H (m)	SY	Recharge (m/years)	Recharge (mm/years)
1	5	0,34	1,7	1.700
2	3,5	0,34	1,19	1.190
3	5	0,24	1,2	1.200
4	4	0,24	0,96	960
5	3,2	0,34	1,088	1.088
6	5	0,24	1,2	1.200
7	2,1	0,24	0,504	504
8	3	0,24	0,72	720
9	5	0,24	1,2	1.200
10	2,2	0,24	0,528	528
11	3	0,34	1,02	1.020
12	1,4	0,249	0,3486	349
13	4	0,31	1,24	1.240
14	2,4	0,24	0,576	576
15	4	0,34	1,36	1.360
16	1,9	0,34	0,646	646
17	2	0,249	0,498	498
18	3,5	0,24	0,84	840
20	5	0,24	1,2	1.200
21	5	0,24	1,2	1.200
22	3,8	0,24	0,912	912
23	4	0,24	0,96	960
24	3,7	0,24	0,888	888
25	4,1	0,24	0,984	984
26	4	0,24	0,96	960
27	3,8	0,24	0,912	912
28	2,2	0,24	0,528	528
29	3	0,24	0,72	720
30	5	0,24	1,2	1.200
31	1,9	0,24	0,456	456
32	2,1	0,24	0,504	504
34	1,2	0,24	0,288	288
35	0,75	0,17	0,1275	128
36	2	0,14	0,28	280
38	2,8	0,14	0,392	392
39	2,5	0,09	0,225	225
40	2	0,172	0,344	344
42	1,3	0,09	0,117	117

The groundwater recharge calculations in the Yogyakarta-Sleman basin, based on ΔH values and specific yield from 38 monitoring wells, show a range between 117 to 1,700 mm/year (Table 1). Overall, the recharge distribution decreases from upstream to downstream, with values exceeding 1,200 mm/year in the recharge area (Sleman Regency), 500-1,200 mm/year in the transition area (Yogyakarta City), and less than 500 mm/year in the discharge area (Bantul Regency) (**Fig. 6**). This pattern is influenced by the declining topography and equipotential lines from upstream to downstream, along with lithology variations, resulting in lower recharge values downstream [26].

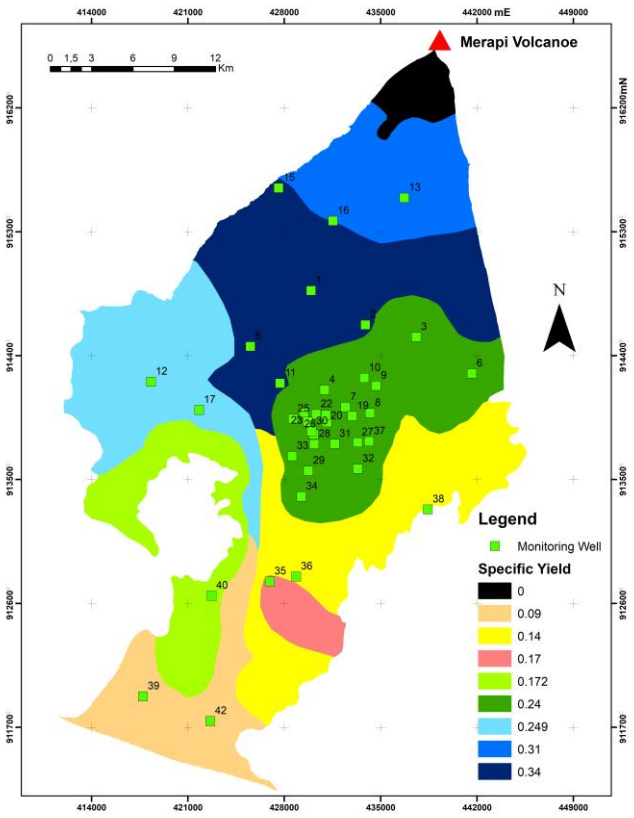

Fig. 4. Specific Yield Map Distribution in the Yogyakarta-Sleman Groundwater Basin

The findings of this study indicate a broader range of values compared to the analysis conducted from 2018 to 2022. Razi et al. [20] reported recharge values between 140 and 1,500 mm per year for that period, which are slightly lower than the range of 117 to 1,700 mm per year observed in 2023-2024. As previously mentioned, the primary difference between these results is due to variations in specific yield. The ΔH values between the two periods are relatively similar, with the discrepancies mainly attributed to differences in rainfall.

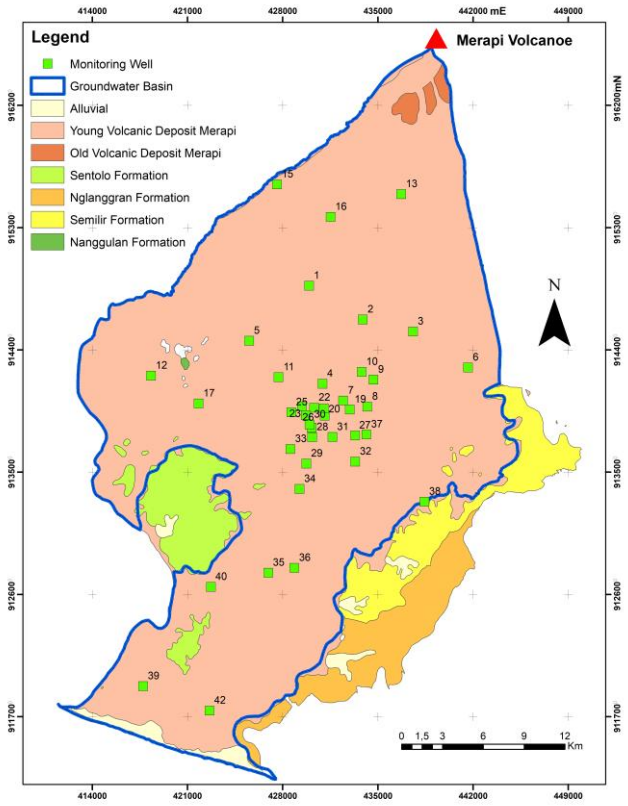

Fig. 5. Geology of the Yogyakarta-Sleman Groundwater Basin

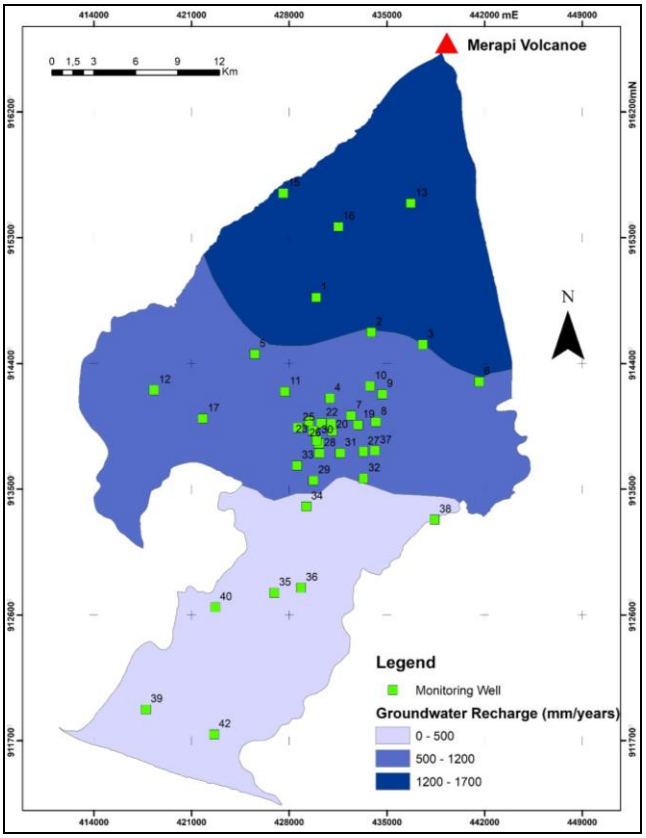

Fig. 6. Annual Groundwater Recharge in the Yogyakarta-Sleman Groundwater Basin

The recharge estimates derived from this study's water level fluctuation method are consistent with findings from other research. Specifically, studies using the chloride budget method in the upstream area of the Yogyakarta-Sleman basin reported groundwater recharge values ranging from 1,400 to 1,700 mm/year [27]. Additionally, the water budget method indicated values between 1,100 and 1,500 mm/year [28].

Wilopo et al. [27] noted that the dynamics of groundwater levels and rainfall exhibit a strong positive correlation. This is also evident in the study location, as shown in Fig. 7, which illustrates the monthly rainfall pattern and water level fluctuations from the 2023-2024 monitoring wells, indicating a positive relationship. The results from nine rainfall observation stations and 38 monitoring wells reveal a consistent pattern: groundwater levels decrease during the dry season and rise during the rainy season. Similar patterns were observed in the long-term rainfall data from 2018-2022, indicating a strong correlation between rainfall data and groundwater dynamics [21]. The results of the correlation analysis (R^2) between rainfall at the station and water level indicate a strong correlation, with values ranging from 0.5 to 0.79 (see Table 1). This suggests that fluctuations in rainfall are closely related to changes in water level dynamics.. This relationship is attributed to rainfall replenishing groundwater, influencing changes in groundwater levels.

Additionally, other factors, such as land use, also influence water levels. This observation aligns with the predominant land use in the Groundwater Basin, particularly due to the presence of settlements (see Fig. 8). Previous temporal studies support these findings, showing a significant increase in the number of settlements in the study area from 1996 to 2021 [19]. Furthermore, the distribution of monitoring wells in the area is entirely located within residential, industrial, and hotel zones. This situation is likely to reduce groundwater recharge, as the land is mostly developed, leaving minimal areas available for water absorption.

Table 2. Rainfall Correlation

Rainfall Station	Well Monitoring	R2
Sanden	39,42	0,52
Pundong	40,35,36	0,79
Karang Ploso	38	0,56
Godean	12,17,5	0,63

Fig. 7. Rainfall and Groundwater Fluctuation Patterns (January 2023 - June 2024)

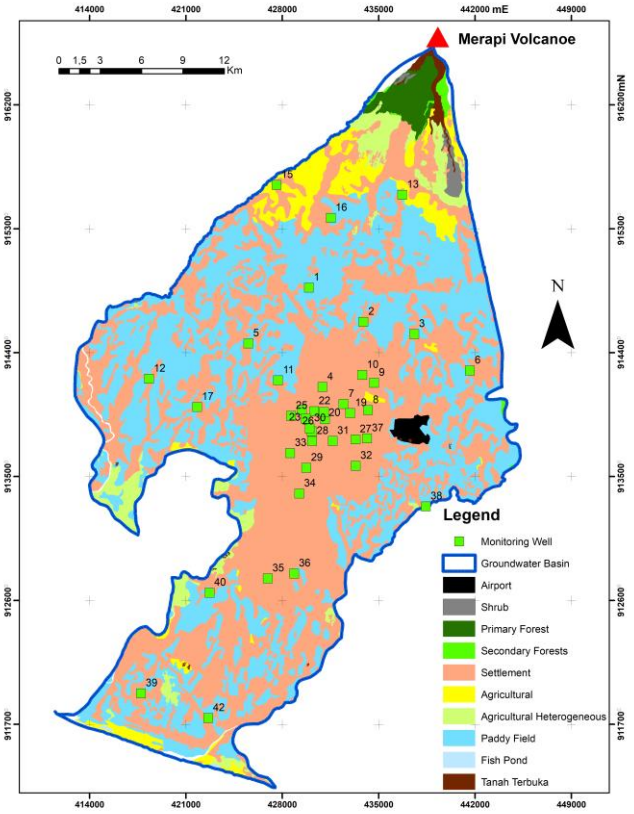

Fig. 8. Landuse in Study Area (Basemap Source : KLHK, 2019)

4. CONCLUSIONS

The analysis of groundwater recharge calculations using the water level fluctuation method in the Yogyakarta-Sleman groundwater basin reveals a recharge range of 100 to 1,700 mm/year. Spatial interpolating recharge values from monitoring wells demonstrated a general trend of decreasing recharge from upstream to downstream. The highest recharge values (1,200–1,700 mm/year) are found in the recharge area; the transition zone in Yogyakarta City shows medium values (500–1,200 mm/year). In contrast, the discharge area in Bantul City has the lowest values (< 500 mm/year). Overall, the recharge values obtained from the water level fluctuation method are relatively consistent with those derived from other methods, such as the water and chloride budgets. Comparisons of recharge calculations of this analysis of the 2023-2024 period with the same techniques and areas from 2018-2022 reveal minor differences, suggesting that a short data period can effectively represent groundwater recharge conditions. This study also displays how rainfall significantly influences water level fluctuations and recharge values in the Yogyakarta-Sleman Groundwater Basin.

ACKNOWLEDGMENTS

The authors express gratitude to DINAS PU ESDM DI Yogyakarta for providing essential data supporting this research. They also acknowledge the Department of Geological Engineering at Universitas Gadjah Mada for their valuable support throughout the study.

REFERENCES

[1] S. Jasechko, H. Seybold, D. Perrone, Y. Fan, M. Shamsudduha, R.G. Taylor, O. Fallatah & J.W. Kirchner,"Rapid groundwater decline and some cases of recovery in aquifers globally," Nature, vol. 625, no. 7996, pp. 715–721, 2024. https://doi.org/10.1038/s41586-023-06879-8.

[2] M. Palma, S. Maggio, C. Cappello, A. Congedi & S. de Iaco,"Spatio-temporal modeling of groundwater quality deterioration and resource depletion," Hydrogeology Journal, vol. 31, no. 6, pp. 1443–1461, 2023, https://doi.org/10.1007/s10040-023-02692-9

[3] J. Chilton & S. Foster,"Long datasets for improved understanding, management and protection of groundwater," Hydrogeology Journal, vol. 32, no. 2, pp. 347–352, 2024. https://doi.org/10.1007/s10040-023-02759-7

[4] R.M. Gailey, J.R. Lund & J.R. Philipp,"Domestic-well failure mitigation and costs in groundwater management planning: observations from recent groundwater sustainability plans in California, USA," Hydrogeology Journal, vol. 30, no. 2, pp. 417–428, 2022. https://doi.org/10.1007/s10040-021-02431-y

[5] N. Mejia, T.J. Scheytt & M. Murillo,"Hydrogeological characterization and utilization of the Siguatepeque aquifer, Honduras," Hydrogeology Journal, vol. 32, no. 2, pp. 557–575, 2024. https://doi.org/10.1007/s10040-023-02718-2

[6] L. Arnaud, A. Gutierrez, I. Zegoulli & N. Gonomy. Modelling groundwater flow in the Plaine du Nord–Massacre shallow aquifer, Haiti. ," Hydrogeology Journal, vol. 30, pp. 1399–1415, 2022.https://doi.org/10.1007/s10040-022-02469-6/Published

[7] C. Wolf, J.J. Gurdak, Z. Lauffenburger, L. Nanus & E. Maurer,"Controls on recharge in thick vadose zones under climate variability and change," Hydrogeology Journal, vol. 30, no. 5, pp. 1637–1655, 2022. https://doi.org/10.1007/s10040-022-02504-6

[8] S.I. Elmahdy & M.M. Mohamed,"The impact of land use land cover on groundwater level and quality in the Emirate of Abu Dhabi, UAE: an integration approach using remote sensing and hydrological data," Geocarto International, vol. 38, no. 1, pp. 2023. https://doi.org/10.1080/10106049.2023.2272664

[9] J. Huang, J. Wang, Y. Zhou, T. Fang, B. Ning, G. Song T. Huang, L. Li, Z. Yang, Q. lv, F. Pu, Z. Li, & W. Wang,"A dynamic harmonic regression approach to estimating groundwater evapotranspiration based on diurnal groundwater-level fluctuations," Hydrogeology Journal, vol. 32, no. 1, pp. 253–266, 2024. https://doi.org/10.1007/s10040-023-02719-1

[10] J. C. Maréchal, P. Perrochet & Y. Caballero," Computing natural recharge using the water-table fluctuation method: where to site an observation well," Hydrogeology Journal, vol. 31, no. 7, pp. 1991–1995, 2023. https://doi.org/10.1007/s10040-023-02707-5

[11] J. Sun, B. Li, W. Wang, X. Yan, Q. Li & Z. Li," Variations and controls on groundwater recharge estimated by combining the water-table fluctuation method and Darcy's law in a loess tableland in China," Hydrogeology Journal, vol. 32, no. 2, pp. 379–394, 2024. https://doi.org/10.1007/s10040-023-02722-6

[12] C.W. Healy, *Estimating groundwater recharge*. New York: Cambridge University Press, 2010.

[13] M. Blarasin, F. Bécher Quinodóz, A. Cabrera, E. Matteoda, N. Alincastro & J.G. Albo,"Weekly and Monthly Groundwater Recharge Estimation in A Rural Piedmont Environment using the Water Table Fluctuation Method," International Journal of Environmental & Agriculture Research (IJOEAR), vol. 2, no. 5, pp. 104-113, 2016.

[14] M.B. Addisie,"Groundwater recharge estimation using water table fluctuation and empirical methods," H2Open Journal, vol. 5, no. 3, pp. 457–468, 2022. https://doi.org/10.2166/h2oj.2022.026

[15] H.H. Ware, T.D. Mengistu, B.A. Yifru, S.W. Chang & I.M. Chung,"Assessment of Spatiotemporal Groundwater Recharge Distribution Using SWAT-MODFLOW Model and Transient Water Table Fluctuation Method," Water (Switzerland), vol. 15, no. 11, 2023. https://doi.org/10.3390/w15112112

[16] K. Alghafli, X. Shi, W. Sloan, M. Shamsudduha, Q. Tang, A. Sefelnasr & A.A. Ebraheem,"Groundwater recharge estimation using in-situ and GRACE observations in the eastern region of the United Arab Emirates," Science of the Total Environment, vo. 867, 2023. https://doi.org/10.1016/j.scitotenv.2023.161489

[17] D. Walker, G. Parkin, P. Schmitter, J. Gowing, S.A. Tilahun, A.T. Haile & A.Y. Yimam,"Insights From a Multi-Method Recharge Estimation Comparison Study," Groundwater, vol. 57, no. 2, pp. 245–258, 2019. https://doi.org/10.1111/gwat.12801

[18] A. Y. Yimam, F. K. Sishu, T. T. Assefa, T. S. Steenhuis, M. R. Reyes, R. Srinivasan & S. A. Tilahun," Modifying the water table fluctuation method for calculating recharge in sloping aquifers," Journal of Hydrology: Regional Studies, vol. 46, 2023. https://doi.org/10.1016/j.ejrh.2023.101325

[19] H. Hendrayana, A. Harijoko, I.A. Riyanto, A. Nuha & Ruslisan,"Groundwater Chemistry Characterization in The

South and Southeast Merapi Volcano, Indonesia," Indonesian Journal of Geography, vol. 55, no. 1, pp. 10–29, 2023. https://doi.org/10.22146/ijg.76433

[20] M.H. Razi, W. Wilopo & D.P.E. Putra,"Spatiotemporal analysis of groundwater level trends and recharge rate estimation in the unconfined aquifer of Yogyakarta-Sleman Groundwater Basin, Indonesia." Journal of Degraded and Mining Lands Management, vol. 11, no. 1, pp. 4887–4897, 2023. https://doi.org/10.15243/jdmlm.2023.111.4887

[21] R. W. Healy & P. G. Cook,"Using groundwater levels to estimate recharge," Hydrogeology Journal, vol. 10, no. 1, pp. 91–109, 2002. https://doi.org/10.1007/s10040-001-0178-0

[22] H. Hendrayana, A. Nuha, I.A. Riyanto & B. Aprimanto,"Kajian Perubahan Muka Airtanah di Cekungan Airtanah Yogyakarta-Sleman," Majalah Geografi Indonesia, vol. 35, no. 1, pp. 30–40, 2021. https://DOI:10.22146/mgi.62396

[23] Engineering Faculty Team UGM, *Pemetaan Zonasi Konservasi Air Tanah di Cekungan Air Tanah Yogyakarta-Sleman*. Yogyakarta: ESDM, 2011.

[24] W. Rahardjo, R. Sukandarrumidi, H.M.D. Rosidi, *Geology map of Yogyakarta*. Jakarta: Geologycal Survey of Indonesia, 1997.

[25] M.H. Razi, W. Wilopo, D.P.E P, "Specifying groundwater recharge zones through hydrogeochemical and isotopic analyses in a multilayer volcanic aquifer: a case study in the Yogyakarta-Sleman Groundwater Basin, Indonesia," Hydrogeology, vol 32, pp. 2167-2183. https://doi.org/10.1007/s10040-024-02849-0

[26] C.W. Fetter, *Applied Hydrogeology 4th Edition*. New York: Macmillan College Publishing Company,2001.

[27] R. D. C. Adi, W. Wilopo & H. Setiawan," Groundwater recharge estimation using chloride mass balance method on the southern slope of Merapi Volcano, Indonesia," International Journal of Advances in Applied Sciences, vol. 12, no. 3, pp. 265–273, 2023. https://doi.org/10.11591/ijaas.v12.i3.pp265-273

[28] S. P. W. Gunawan, T. Machimura, T. Matsui & H. Hendrayana,"water budget assessment under rapid urbanization in yogyakarta, indonesia using a distributed water balance model," international journal of geomate, vol. 25, no. 111, pp. 24–32, 2023. https://doi.org/10.21660/2023.111.3853

[29] S. P. W. Gunawan, T. Machimura, T. Matsui & H. Hendrayana,"water budget assessment under rapid urbanization in yogyakarta, indonesia using a distributed water balance model," international journal of geomate, vol. 25, no. 111, pp. 24–32, 2023. https://doi.org/10.21660/2023.111.3853

Techno-Science Research Journal V13 (Special Issue) (2025) P 142-149

Content list available at ITC

Techno-Science Research Journal

Journal Homepage: www.ric.itc.edu.kh

Techno-Science Research Journal

Pullout Resistance of Tyfo® FibrAnchors Inserted into Relatively High Strength Concrete Specimen

Henghout CHEA[1*], Narith PROK[2], Sovann Sathya RATH[2], Sovanvichet LIM[2], Wee Keong ONG[3]

[1] *Material and Structural Engineering, Institute of Technology of Cambodia, Russian Federation Blvd., P.O. Box 86, Phnom Penh, Cambodia*

[2] *Research and Innovation Center, Institute of Technology of Cambodia, Russian Federation Blvd., P.O. Box 86, Phnom Penh, Cambodia*

[3] *Assistant General Manager, Fyfe Asia Pte Ltd, 6 Clementi Loop #02-20, Singapore 129814*

Received: 1 November 2024; Revised: 1 January 2025; Accepted: 20 June 2025; Available online: September 2025

Abstract: *Strengthening with Fiber Reinforced Polymer (FRP) involves using composite material to enhance the structural performance of existing structures or components. External bonding of FRP plates or sheets has emerged as a popular method for strengthening reinforced concrete. The issue FRP application is debonding, which happens when externally bonded FRP detaches from the reinforced concrete member due to the concrete's poor tensile strength. To address this issue, anchor systems can prevent or delay debonding failure. This study aims to perform both experimental and numerical simulation. This involves determining the most effective depths and diameters for embedding fiber anchors into high-strength (40MPa) concrete specimens confined by Glass Fiber-Reinforced Polymer (GFRP) and formulating an equation to represent the relationship derived from the test outcomes. A total of 72 specimens were tested under monotonic uniaxial tension force. Test parameters included the anchor diameter (10mm, 12mm, 15mm, 20mm, and 25mm) and embedment depth of the anchor (50mm, 100mm, 150mm, and 200mm).*

The experimental results indicated that the failure mode and pullout resistance of Tyfo® Fibr anchors are significantly influenced by diameter and embedment depth. The pullout resistance increases as the diameter and embedment depth of the anchor increase. Furthermore, the analytical study established equations for predicting the pullout resistance of the Tyfo® Fibr Anchor and the corresponding mode of failure. The proposed equation for concrete strength of 40 MPa will be combined with equations suitable for concrete strengths of 20 MPa and 30 MPa. Consequently, this study is able to predict the optimal fiber anchor diameter and embedment depth for various concrete compressive strengths..

Keywords: Fiber Reinforced Polymers, Experimental Simulation, Analytical Modeling, Pullout Resistance, Numerical Simulation

1. INTRODUCTION

Strengthening with Fiber Reinforced Polymer (FRP) uses composite materials to improve the structural performance of existing structures. This method is widely used in civil engineering due to the high strength-to-weight ratio, corrosion resistance, and durability of FRP materials, which are made of a polymer matrix reinforced with glass, carbon, or aramid fibers. A common issue with FRP applications is debonding, where the FRP detaches from reinforced concrete due to its weak tensile strength. ACI 440.2R-08 [1] suggests that anchor systems can delay or prevent different types of debonding by effectively distributed load.

There is still insufficient research data on anchorage to fully integrate FRP anchorage systems. Some studies on FRP anchors have been carried out, including those by Kim and Smith [2, 3], as well as Eligehausen et al [4].

Current research has developed equations to predict the pullout resistance of fibers, but these are limited to concrete strengths of 20MPa [5] and 30MPa [6]. Insufficient equations exist for concrete strengths over 30 MPa, highlighting the need for further study. This research aims to expand on existing data by exploring the performance of fiber anchors for concrete strength 40MPa, which presents a valuable research opportunity.

* Corresponding author: CHEA Henghout
E-mail: *cheahenghout@gmail.com;* Tel: *+855 69 703 636*

The objectives of this study are to:

- Analyze the pullout resistance and failure modes of fiber anchors for concrete strength 40Mpa confined with Glass Fiber Reinforced Polymer (GFRP).
- Develop equations to predict pullout resistance based on experimental results.
- Validate the equations through numerical simulations.
- Integrate the equations for concrete strength 40 MPa with those for 20 MPa and 30 MPa.

2. METHODOLOGY

A total of 72 Tyfo® Fibr Anchors were embedded in uncracked concrete cylinders using Tyfo® S epoxy and confined with Tyfo® SEH-25A composite. The investigation used concrete specimens with a compressive strength of 40 MPa to analyze the failure mechanism and ultimate failure load, focusing on the effects of embedment depth and anchor diameter on the pullout test. Table 1 summarizes the number of specimens tested for each case.

Table 1. Summary of Test Specimens

Embedment Depth (mm)	Anchor Diameter (mm)				
	10	12	15	20	25
50	4	4	4	4	4
100	4	4	4	4	4
150	4	4	4	4	4
200	-	-	4	4	4

2.1 Specimen

The specimen details are presented in Figure 1. In this experiment, concrete cylinders with a diameter of 150 mm and a height of 300 mm were utilized. These cylinders were confined with GFRP laminate that had a 150 mm overlap length. Each anchor had varying diameters and embedment depths but maintained a consistent free length of 200 mm, which was post-installed in the concrete cylinders.

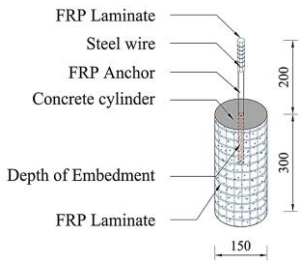

Fig. 1. Depicts A Representation of The Specimen.

2.2 Material

2.2.1 Concrete

The specimens were mixed at the laboratory following ASTM Standards (ASTM C192), with the mix composition outlined in Table 2.

Table 2. Concrete Mixes Design for 1 m^3

Compressive Strength-cylinder (MPa)	Water (kg)	Hydrolique Cement (kg)	Gravel (kg)	Sand (kg)
40	216.1	424.90	1043.9	707.9

2.2.2 Tyfo® S Epoxy

The experiment utilized Tyfo® S Epoxy, provided by Fyfe Asia Pte Ltd [7]. According to the manufacturer's specifications in Table 3, Tyfo® S Epoxy is a low-viscosity, high-strength and two-component epoxy matrix commonly used as a chemical adhesive for bonding applications.

Table 3. Properties of Tyfo® S Epoxy

Property	Test Value
Tensile strength (MPa)	72.4
Tensile Modulus (GPa)	3.18
Elongation Percent (%)	5.00
Compressive Strength (MPa)	86.2
Compressive Modulus (GPa)	3.2
Flexural Strength (MPa)	123.4
Flexural Modulus (GPa)	3.12

2.2.2 Tyfo® Fibr Anchors

Tyfo® Fibr anchors supplied by Fyfe Asia Pte Ltd, known as Tyfo® SEH Composite Anchors [8]. These anchors are composed of uni-directional reinforcing glass fiber bundles mixed with Tyfo® S Epoxy. Figure 2 shows an image of Tyfo® SEH Anchors. Their typical mechanical properties are outlined in Table 4

Fig. 2. Tyfo® SEH Anchors.

Table 4. Properties of Tyfo® SEH Anchors

	Tensile Strength (MPa)	Tensile Modulus (GPa)	Ultimate Elongation (%)
Dry fiber	3240	72.4	4.5
Composite Anchor			
Test value	575	26.1	2.2
Design value	460	20.9	1.76

2.2.3 GFRP Laminate

GFRP laminate known as Tyfo® SEH-25A Composite, which consists of Tyfo® S Epoxy and Tyfo® SEH-25A reinforcing fabric [9]. Several characteristics of the laminate are detailed in Table 5.

Fig. 3. Tyfo® SHE-25A

Table 5. Properties of Composite Laminate Glass fiber

Property composite laminate	Test Value	Design Value
Tensile strength in primary fiber direction (MPa)	521	417
Tensile Modulus (GPa)	26.1	20.9
Elongation at break (%)	2.00	1.76
Tensile Strength in 90° to primary direction (MPa)	25.8	20.7
Laminate Thickness (mm)	0.50	0.50

2.3 Preparation Experimental Specicmen

After 28 days of curing the concrete cylinder specimen, a hole was drilled vertically through the center to match the FRP anchor's diameter. Following the drilling, the anchor holes were cleaned with a brush and air compressor. A brush was also used to clean the surrounding surface of the specimen before wrapping. The FRP laminate was then attached to the concrete using epoxy, with each laminate initially saturated with epoxy before being wrapped around the concrete cylinder.

Fig. 4. The drilling and laminate wrapping process

Afterward, dust was removed from the holes using an air compressor to ensure they were clean, and the holes were filled with epoxy. The anchor was then inserted and secured with elastic bands for alignment. After one day of drying to harden the anchor, the FRP laminate was wrapped around the anchor head with steel wire. Each specimen was prepared for testing after curing for five days.

Fig. 5. Inserting Anchor Process

2.4 Test Set-Up and Procedure

Seventy-two Tyfo® SEH Anchor specimens were prepared for testing after curing. Figure 6 shows the concrete cylinders placed in the steel plate frame of the testing apparatus, which has a hole diameter of 120 mm.

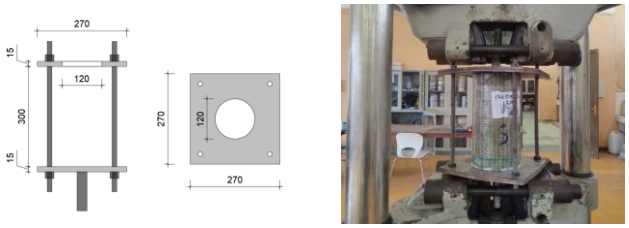

Fig. 6. The Process of Pullout Test

After the specimen tests, it was observed that the pullout load of each Tyfo® SEH Anchor, recorded by the testing machine, represented the maximum load reached before failure.

Two failure modes were noted under the applied pullout force: combined cone bond failure (CB) and anchor rupture failure (RF).

Fig. 7. Failure Mode from The Experimental Testing

3. RESULTS AND DISCUSSION

Based on the experimental results, the average pullout value and the standard deviation are displayed in Figure 8.

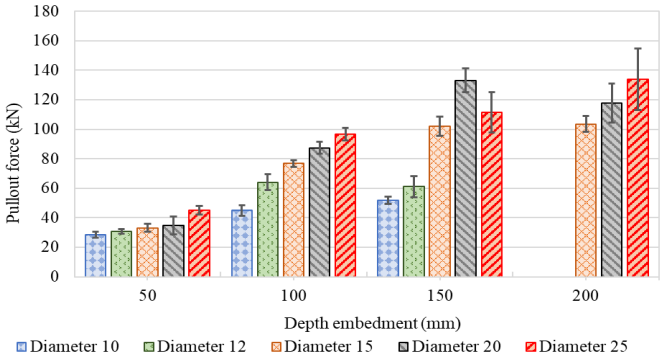

Fig. 8. Averge Pullout Force of Anchor

Following a thorough review of the experimental results, it was determined to exclude data points involving an anchor diameter of 25 mm with an embedment depth greater than 100 mm from the analysis. During the application of the pullout force, the GFRP sheet confinement ruptured, causing the concrete to fracture. As a result, the pullout force did not reach its maximum value under these confinement conditions.

3.1 Ratio of Anchor Embedment Depth to Anchor Diameter

The relationship between the pullout load and the ratio of anchor embedment depth to diameter is categorized by different failure modes, as illustrated in Figure 9. The transition point between CB failure and RF failure happens when the (h_{emd} /d) ratio is approximately 10. According to the scatter plot, RF failure only one appears with ratio values below 10, whereas when the (h_{emd}/d) ratio exceeds 10, RF failure occurs frequently.

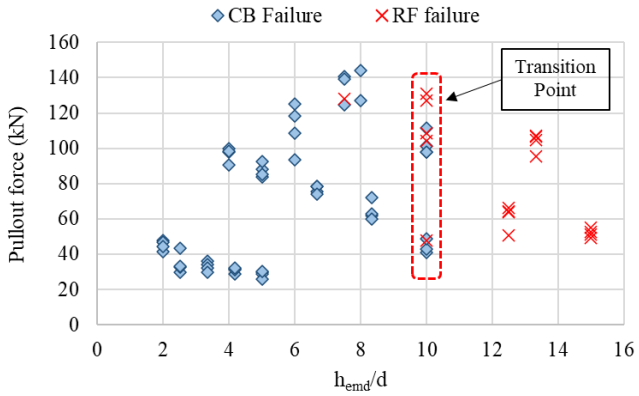

Fig. 9. Pullout Load versus Ratio of Anchor Embedment Depth to Anchor Diameter

3.2 Combined Cone-Bond Failure (CB)

Assuming that the bond stress is uniformly distributed along the embedment depth of the anchor (Cook et al., 1998) [10], the uniform bond stress can be calculated using

$$\tau = F_u / \pi\, d\, h_{emd} \qquad \text{(Eq. 1)}$$

where:

τ = uniform bond stress
F_u = pullout force
d = diameter of anchor
h_{emd} = embedment depth of anchor

3.3 Anchor Rupture Failure (RF)

The tensile capacity of fiber anchors, after applying epoxy to the glass fibers, can be determined by multiplying the tensile strength of the composite anchor.

$$F_{frp} = f_{frp} A_{frp} \qquad \text{(Eq. 2)}$$

where:

f_{frp} = Tensile Strength for composite anchor 575 MPa
A_{frp} = Cross sectional of anchor

3.4 Pullout Resistance of a Single FRP Anchor Focusing on Predicting Failure Mode for Best-Fit Model

Based on the experimental results, when focusing on predicting failure mode, the model describing the pullout resistance of a single FRP anchor is given as:

$$N_{u\_pre} = \min(N_{cb}, N_{rf}) \qquad \text{(Eq. 3)}$$

where:

$N_{cb} = 35.028 d^{-0.319}\, d\pi h_{emd}$ (combined cone-bond)
$N_{rf} = 6.123 d^{-0.72}\, A_{frp} f_{frp}$ (anchor rupture)

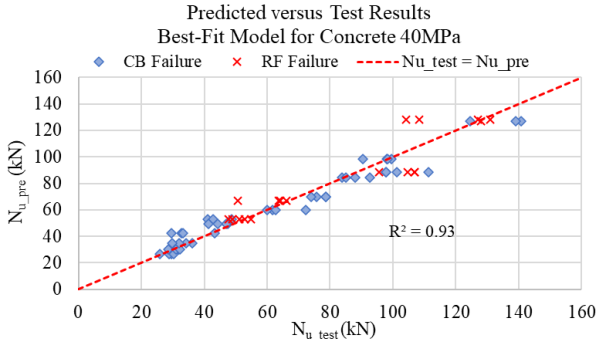

Fig. 10. Best-Fit Model Predicted versus Test results for Concrete 40MPa

3.5 Pullout Resistance of a Single FRP Anchor: Predicting Failure Mode for a Design Model with a 95th Percentile Lower Bound

A tolerance of 5% is permitted in testing practices to accommodate variability in testing conditions and variations in material properties. Additionally, Kim and Smith (2010) [3] stated that the design model for anchor pullout is based on a 5% exceedance or the 95th percentile lower bound.

$$N_{r\text{-}pre\_0.95} = \min(N_{r\text{-}cb\_0.95}, N_{r\text{-}rf\_0.95}) \quad \text{(Eq. 4)}$$

where:

$N_{r\text{-}cb\_0.95} = \gamma_{cb\_0.95} N_{cb}$

$N_{cb} = 35.028 d^{-0.319} d\pi h_{emd}$ (combined cone-bond)

$N_{r\text{-}rf\_0.95} = \gamma_{rf\_0.95} N_{rf}$

$N_{rf} = 6.123 d^{-0.72} A_{frp} f_{frp}$ (anchor rupture)

calibration factor

$\gamma_{cb\_0.95} = 0.75$ (calibration factor for CB)

$\gamma_{rf\_0.95} = 0.80$ (calibration factor for RF)

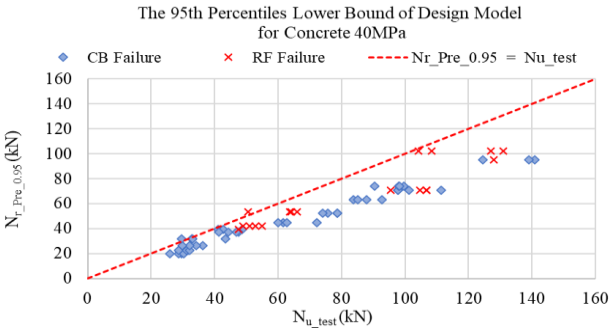

Fig. 11. The 95th Percentiles Lower Bound of Design Model for Concrete 40MPa

Figure 12 presented a three-dimensional representation of equation (4). The relationship between the anchor's diameter and embedment depth reveals key observations about the failure mode, indicating that the anchor pullout strength is ultimately constrained by the anchor rupture strength.

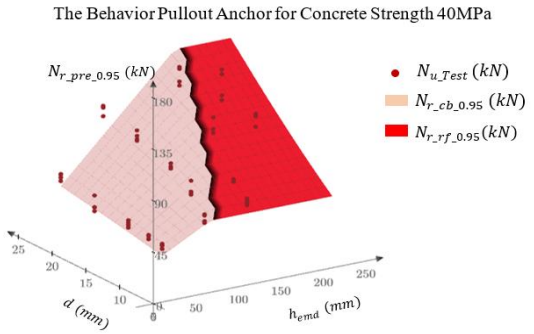

Fig. 12. The Behavior of Pullout Anchors: 95th Percentile Lower Bound Design Model for Concrete Strength 40MPa

4. INTERGRATE CONCRETE STRENGTH STUDY

According to currently research [11], improvements were made using data with strengths of 30MPa and 20MPa for the integrated concrete strength study.

4.1 Integrate Study for Concrete Strength Between 30MPa and 40MPa

For the study of integrated concrete strengths 30MPa and 40 MPa, in the case of CB failure, there were 46 specimens for concrete strength 40MPa and 54 specimens for concrete strength 30MPa. Additionally, 64 specimens exhibited RF failure. The focusing on predicting failure mode, the model describing the pullout resistance N_{u_pre} of a single FRP anchor for the concrete strength between 30MPa and 40MPa is given as:

$$N_{u\_pre} = \min(N_{cb}, N_{rf}) \quad \text{(Eq. 5)}$$

where:

$N_{cb} = 3.695 d^{-0.424} f_c'^{0.688} d\pi h_{emd}$ (combined cone-bond)

f_c' = concrete cylinder compressive strength

$N_{rf} = 12.735 d^{-1.015} A_{frp} f_{frp}$ (anchor rupture)

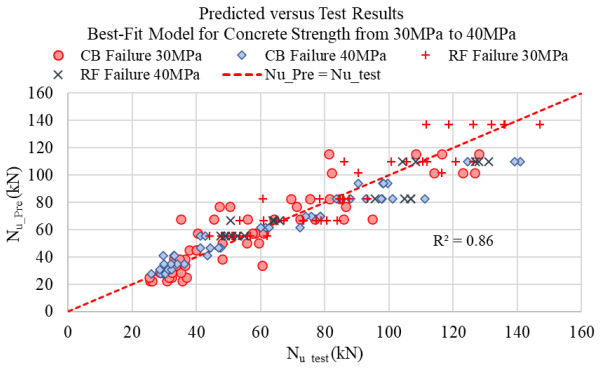

Fig. 13. Best-Fit Model for Concrete Strength from 30MPa to 40MPa

The 95th percentile lower bound for the design model equation is following:

$$N_{r\text{-}pre\_0.95} = \min(N_{r\text{-}cb\_0.95}, N_{r\text{-}rf\_0.95}) \quad \text{(Eq. 6)}$$

where:

$$N_{r\text{-}cb\_0.95} = \gamma_{cb\_0.95}\, N_{cb}$$
$$N_{cb} = 3.695 d^{-0.424} f_c'^{0.688} d\pi h_{emd} \text{ (combined cone-bond)}$$

$$N_{r\text{-}rf\_0.95} = \gamma_{rf\_0.95}\, N_{rf}$$
$$N_{rf} = 12.735 d^{-1.015} A_{frp}\, f_{frp} \quad \text{(anchor rupture)}$$

Calibration factor for concrete strength form 30MPa to 40MPa:

$$\gamma_{cb\_0.95} = 0.12\, f_c'^{0.497} \quad \text{(calibration factor for CB)}$$
$$\gamma_{rf\_0.95} = 0.75 \quad \text{(calibration factor for RF)}$$

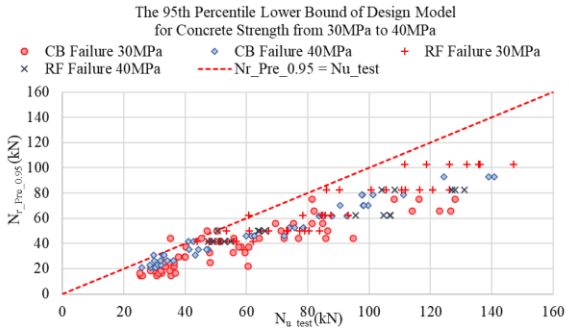

Fig. 14. The 95th Percentile Lower Bound of Design Model for Concrete Strength from 30MPa to 40MPa

4.2 Integrate study for concrete strength from 20MPa to 40MPa

For the study integrated concrete strengths of 20 MPa, 30 MPa, and 40 MPa. For the 20 MPa concrete strength, 62 specimens exhibited CB failure, while 98 specimens experienced RF failure. The pullout resistance of a single FRP anchor across concrete strengths ranging from 20 MPa to 40 MPa is detailed as follows:

$$N_{u\_pre} = \min(N_{cb}, N_{rf}) \quad \text{(Eq. 7)}$$

where:

$$N_{cb} = 15.225\, d^{-0.628} f_c'^{0.448} d\pi h_{emd} \text{ (combined cone-bond)}$$
$$N_{rf} = 12.236\, d^{-1.005} A_{frp}\, f_{frp} \quad \text{(anchor rupture)}$$

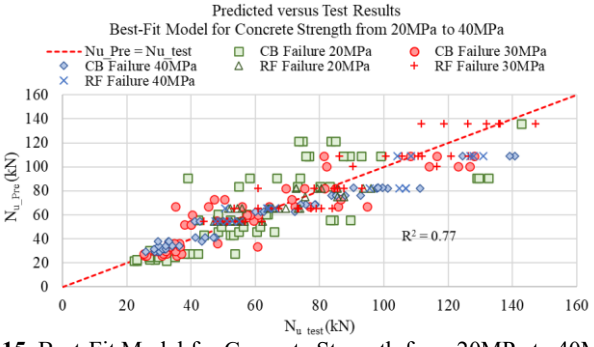

Fig. 15. Best-Fit Model for Concrete Strength from 20MPa to 40MPa

Allowing for a 5% margin of error, the 95th percentile lower bound for the design model equation is as follows:

$$N_{r\text{-}pre\_0.95} = \min(N_{r\text{-}cb\_0.95}, N_{r\text{-}rf\_0.95}) \quad \text{(Eq. 8)}$$

where:

$$N_{r\text{-}cb\_0.95} = \gamma_{cb\_0.95}\, N_{cb}$$
$$N_{cb} = 15.225\, d^{-0.628} f_c'^{0.448} d\pi h_{emd} \text{ (combined cone-bond)}$$

$$N_{r\text{-}rf\_0.95} = \gamma_{rf\_0.95}\, N_{rf}$$
$$N_{rf} = 12.236\, d^{-1.005} A_{frp}\, f_{frp} \quad \text{(anchor rupture)}$$

Calibration factor for concrete strength form 20MPa to 40MPa:

$$\gamma_{cb\_0.95} = 0.235 f_c'^{0.31} \quad \text{(calibration factor for CB)}$$
$$\gamma_{rf\_0.95} = 0.80 \quad \text{(calibration factor for RF)}$$

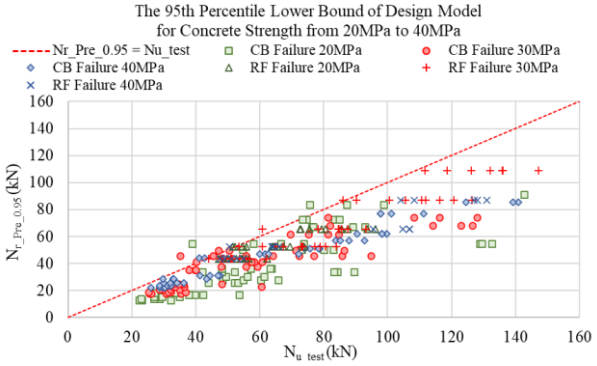

Fig. 16. The 95th Percentile Lower Bound of Design Model for Concrete Strength from 20MPa to 40MPa

5. NUMERICAL SIMULATION

5.1 Modeling Procedure

The following steps were taken to model the samples in Abaqus: A quarter model of a 3D deformable solid was created for a concrete cylinder with a diameter of 75 mm, and the top surface was shaped according to the anchor's diameter, incorporating a 0.2 mm epoxy layer. The model was then partitioned along the sketched surface. Additionally, a quarter model of a 3D deformable wire was created for the FRP laminate, also with a radius of 75 mm. Material properties were assigned to all components, including the concrete, FRP anchor, epoxy, and FRP laminate.

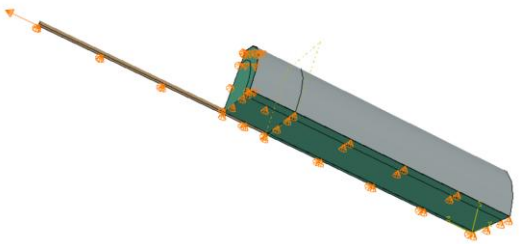

Fig. 17. Model of Numerical Simulation

The Abaqus model revealed the stress distribution during fiber anchor pullout, showing how stress is transferred and concentrated along the anchor. The initiation and progression of concrete damage under the applied pullout force show that the steel frame has no significant effect on the overall behavior of the system, as shown in figure 18.

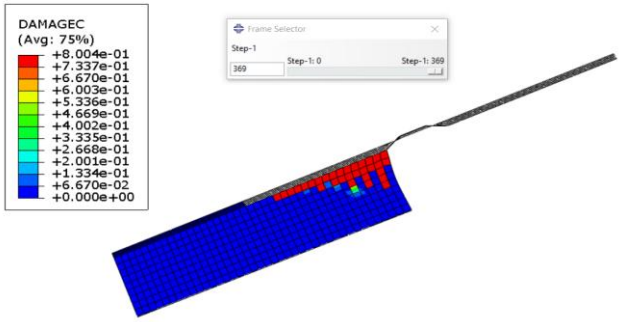

Fig. 18. The Pullout Behavior of an Anchor Embedded in Concrete Cylinder

The analysis model results were derived from 16 series of specimens, each defined by varying combinations of anchor diameter and embedment depth. These ranges, as described in Figure 19 to 23.

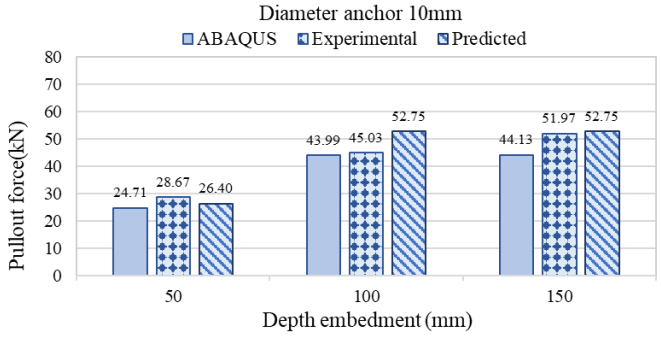

Fig. 19. Abaqus Force compared to Pullout Force and The Predicted Equation for a 10mm Anchor Diameter

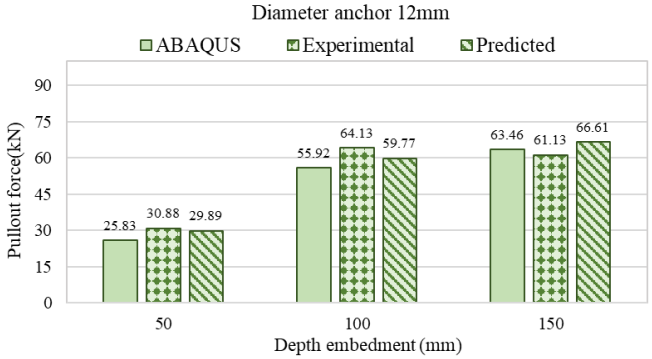

Fig. 20. Abaqus Force compared to Pullout Force and The Predicted Equation for a 12mm Anchor Diameter

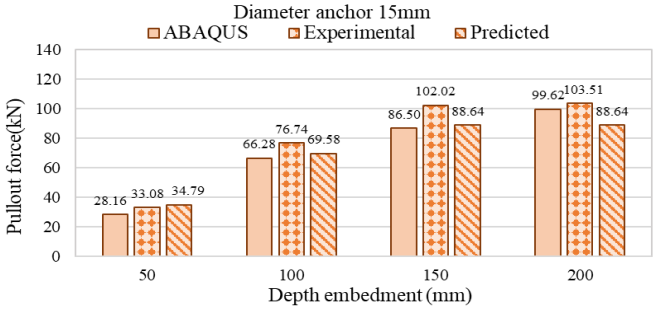

Fig. 21. Abaqus Force compared to Pullout Force and The Predicted Equation for a 15mm Anchor Diameter

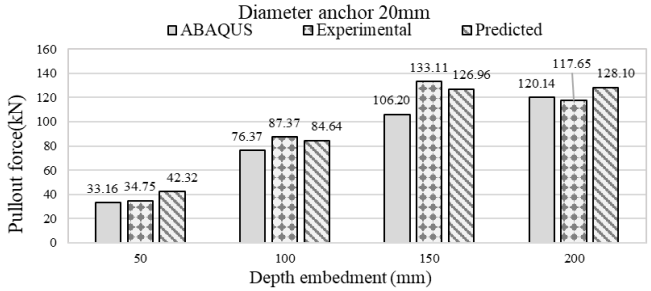

Fig. 22. Abaqus Force compared to Pullout Force and The Predicted Equation for a 20mm Anchor Diameter

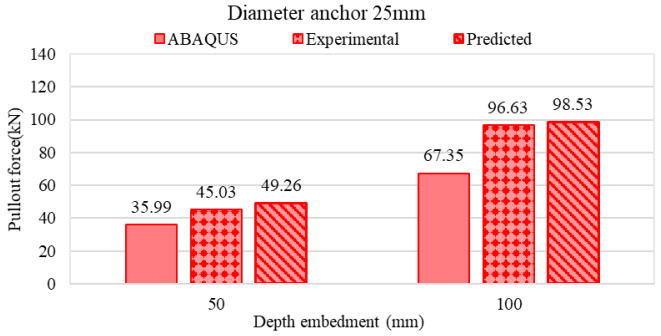

Fig. 23. Abaqus Force compared to Pullout Force and The Predicted Equation for a 25mm Anchor Diameter

Furthermore, the failure modes observed from both the pullout tests and the numerical simulation are also presented in Table 6.

Table 6. The Comparison Failure Mode (Experimental /Numerical simulation)

Embedment Depth (mm)	Diameter of anchor (mm)				
	10	12	15	20	25
10	CB/CB	CB/CB	CB/CB	CB/CB	CB/CB
100	CB/CB	CB/CB	CB/CB	CB/CB	CB/CB
150	CB/CB	CB/CB	CB/CB	CB/CB	-
200	-	-	RF/CB	RF/CB	-

The predicted equation in best-fit model is comparable with the experimental data and numerical, showing only a minor discrepancy.

6. CONCLUSIONS

Based on the findings from the experimental, analytical, and numerical studies, the following conclusions can be drawn:

- The pullout capacity of fiber anchors is greatly influenced by anchor diameter and embedment depth.
- The transition point between CB failure and RF failure occurs when the (h_{emd}/d) ratio is approximately 10. whereas when the (h_{emd}/d) ratio exceeds 10, RF failure occurs frequently.
- The optimal embedment depth is 150mm for 10mm and 12mm diameter anchors, and 200mm for 15mm and 20mm diameters.
- The proposed equation in a best-fit model for concrete strength 40MPa indicates a very strong fit between the predicted and observed data.
- The proposed equation effectively predicts the pullout resistance of Tyfo® fibr anchors and accurately represents the failure mode, aligning well with both experimental and numerical results.
- In the integrated concrete strength study, the best-fit model achieves R^2 values of 0.86 for 30 MPa and 40 MPa concrete strengths, and 0.77 for 20 MPa, 30 MPa, and 40 MPa.
- A 5% error margin is incorporated into the design model to accommodate uncertainties such as material variability, construction discrepancies, and measurement inaccuracies, enhancing safety and reliability.

For recommendations, a prediction equation focusing on concrete strengths between 30MPa and 40MPa is more effective than one covering 20MPa to 40MPa, as 20MPa concrete often exhibits significant data fluctuations, affecting prediction accuracy. Additionally, for practical applications, the quality of workmanship is crucial to the performance of the anchor.

ACKNOWLEDGMENTS

The author extends gratitude to the Faculty of Civil Engineering at the Institute of Technology of Cambodia for their laboratory and technical support. The author also appreciates the funding and composite materials provided by Fyfe Asia Pte Ltd.

REFERENCES

[1] ACI 440.2 R-08. Guide for the design and construction of externally bonded FRP systems for strengthening concrete structures.
[2] S. J. Kim and S. T. Smith, "Behaviour of handmade FRP anchors under tensile load in uncracked concrete," Advances in Structural Engineering, vol. 12, no. 6, pp. 845-865, 2009.
[3] S. J. Kim and S. T. Smith, "Pullout strength models for FRP anchors in uncracked concrete," Journal of composites for construction, vol. 14, no. 4, pp. 406-414, 2010.
[4] R. Eligehausen and G. Sawade, "A fracture mechanics based description of the pull-out behavior of headed studs embedded in concrete," 1989.
[5] A. Mengla, P. Narith, R. Sovann Sathya, L. Sovanvichet, and O. Wee Keong, "Experimental and Numerical Study of Tyfo® Fibranchors Embedded in Low Compressive Strength Concrete Cylinder," Techno Science Research Journal, vol. 12, 2024.
[6] T. Lymeng, P. Narith, R. Sovann Sathya, L. Sovanvichet, and O. Wee Keong, "Experimental And Numerical Study Of Tyfo® Fibranchors Inserting To Concrete Cylinder Confined By Glass Fiber Reinforcing Polymer," Techno-Science Research Journal vol. 12, 2024.
[7] Tyfo® S Saturant Epoxy, 2015. [Online]. Available: http://www.fyfeco.com.
[8] Tyfo SEH Composite Anchors. [Online]. Available: http://www.fyfeasia.com.
[9] Tyfo® SHE-25A Composite. [Online]. Available: http://www.fyfeco.com.
[10] R. A. Cook, J. Kunz, W. Fuchs, and R. C. Konz, "Behavior and design of single adhesive anchors under tensile load in uncracked concrete," Structural Journal, vol. 95, no. 1, pp. 9-26, 1998.
[11] Y. Vanny, "Validation on Proposed Equation for Pullout Resistance of Tyfo® FibrAnchors Inserted into Concrete Cylinder," Master's Thesis, Institute Of Technology Of Cambodia, 2024.

Techno-Science Research Journal V13 (Special Issue) (2025) P 150-157

Content list available at ITC

Techno-Science Research Journal

Journal Homepage: www.ric.itc.edu.kh

Techno-Science Research Journal

Numerical Evaluation of Cyclic Behavior of Short BRBs from Steel and Shape Memory Alloy (SMA)

Kimtong Theng[1], Piseth Doung[1,2*]

[1] *Department of Civil Engineering, Institute of Technology of Cambodia, Russian Federation Blvd., P.O. Box 86, Phnom Penh, Cambodia*

[2] *Research and Innovation Center, Institute of Technology of Cambodia, Russian Federation Blvd., P.O. Box 86, Phnom Penh, Cambodia*

Received: 1 November 2024; Revised: 1 January 2025; Accepted: 20 June 2025; Available online: October 2025

Abstract: *Buckling-Restrained Braces (BRBs) are a type of bracing component that is highly effective in seismic resistance in the building frames and other structures. BRBs are designed to prevent buckling under compression. Unlike BRBs, short BRBs require less space and are easier to repair as compared to conventional braces in frame systems. BRBs made from normal steel can experience significant issues, such as structures often require repairs due to damage and resilience drift after earthquakes. A novel material in civil engineering, Shape Memory Alloys (SMAs), can recover their original shape after significant deformation due to their unique properties. In this study focuses on applying a numerical model for short BRBs with a steel core, and investigating the mechanical behavior of short BRBs from SMAs and small-scale SMA BRBs under cyclic loading based on previous experimental studies. The results showed as force-drift hysteresis loops, and provided good agreements and inaccuracy results between numerical and experimental studies. For steel short BRBs, necking failure occurred at the core, consistent with experimental observations. However, the constitutive material model of SMA, interaction, and constraints must be further investigated to ensure the accuracy to real-world experimental. The more extensive experimental studies, particularly the full scale SMA BRBs with steel frame, should be further studied. Moreover, the simulation of SMA in BRBs will likely focus on refining simulation models, exploring the use of SMA-BRBs in various structural applications, and optimizing their design for enhanced seismic performance.*

Keywords: Buckling-Restrained Braces, Cyclic Loading Shape, Numerical Simulation, Shape Memory Alloy

1. INTRODUCTION

In seismic design, the ability of a structure to resist seismic load is critical for ensuring structural safety and stability. Bracing systems are often used to improve the lateral strength and stiffness of the structures. However, conventional braces are prone to buckling under large compressive forces during seismic events. Buckling-Restrained Braces (BRBs) were developed to solve the buckling problems that occur in conventional braces [1],[2]. BRBs are designed to prevent buckling under compression while maintain their full design strength capacities in tension. The basic components of the BRBs typically consist of a steel core, mortar, and an outer steel tube. The steel core usually undergoes significant inelastic deformation, while the mortar with an outer steel tube functions as an encasement for the core to provide lateral support against buckling. To fulfill architectural and mechanical demand, including reparability, 1short BRBs, typically buckling-restrained knee braces (BRKBs) were further developed for seismic applications [3],[4],[5],[6]. BRKBs in braced frame improve post-earthquake reparability and reduce obstruction compared to conventional systems. Despite the advancements of BRBs, interest has grown in integrating Shape Memory Alloys (SMAs) into seismic-resistant systems. SMA is a unique type of alloy that has the ability to recover its original shape after undergoing large deformation through unloading (superelasticity) and heat (shape memory effect) [7],[8]. In the structural engineering field, SMAs

* Corresponding author: Piseth Doung
Email: *piseth@itc.edu.kh*

have the potential to reduce post-earthquake damage, repair costs, and downtime.

Furthermore, SMA-based BRBs possess several challenges. Their high cost, compared to carbon steel, limits large-scale applications. Additionally, the complex cyclic behavior of SMAs requires advanced material models for accurate simulation. Recent studies have focused on SMA applications in small-scale devices or local members, with limited exploration in full structural bracing systems like BRBs [9],[10],[11].

This study aims to fulfil the gap in the literature with conduct a numerical assessment of the cyclic behavior of short BRBs from steel and SMAs, namely steel short BRBs (SS-BRBs), SMA short BRBs (SMA S-BRBs) and small-scale short BRBs (SS SMA-BRBs). The purpose to validate numerical models against experimental results and gain further insights into the mechanical behavior of these hybrid structure systems. Numerical simulations were performed using Abaqus/CAE and validated against experimental data.

The main objectives of this research are:

1. To develop and validate numerical models for steel short BRBs (SS-BRBs), SMA short BRBs (SMA S-BRBs), and small-scale short BRBs (SS SMA-BRBs) with existing experimental data.
2. To discuss areas where material models need refinement for better numerical accuracy and provide recommendations for future research on SMA-based structural systems.

2. NUMERICAL MODELING

The process of numerical assessment began with modeling the structural components in Abaqus/CAE, followed by analysis and comparison with the existing experimental results. The process flow is illustrated in Fig. 1. Quasi-static implicit analysis, a feature in Abaqus/CAE, was performed.

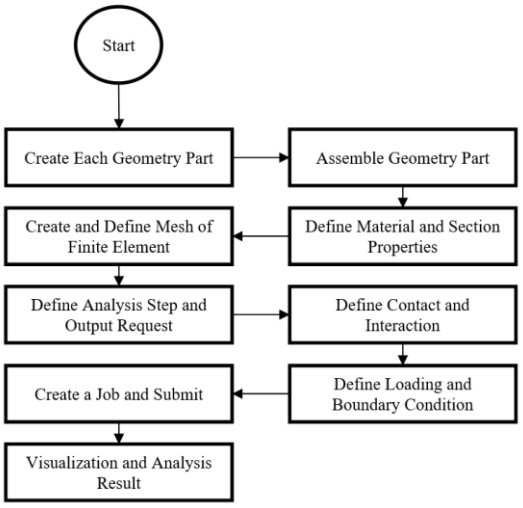

Fig.1 Flowchart of the numerical simulation process in Abaqus/CAE

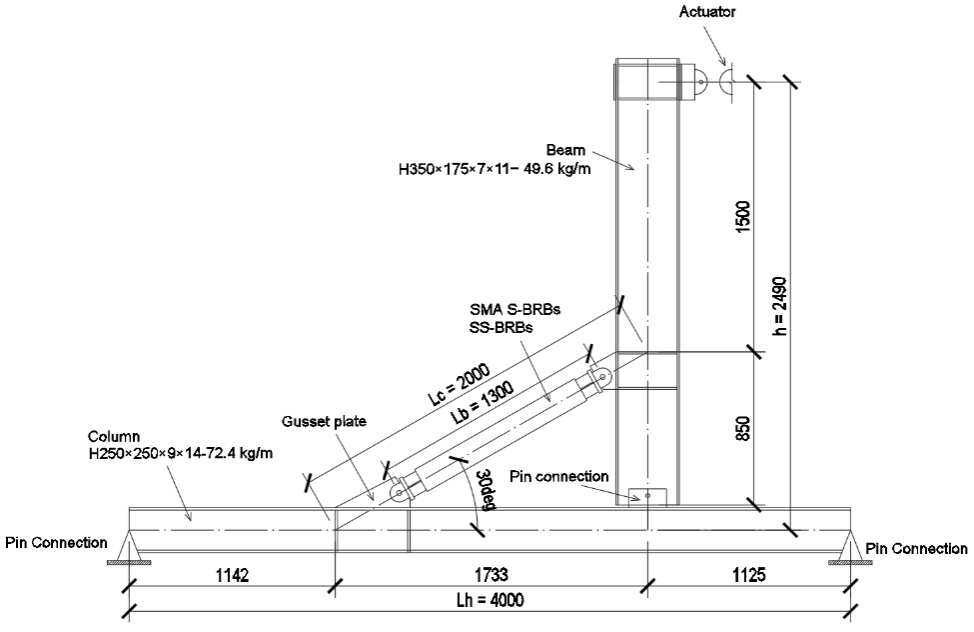

Fig. 2 Overview of geometry of SS-BRB and SMA S-BRB specimen

2.1 Geometry Modeling

In this study, three short BRB specimens with different geometries were modeled, based on the actual sizes from the existing tests. The SS-BRB and SMA S-BRB were conducted base on full-scale sub-assemblies set up given by Junda et al., 2018 [12] and Srisupornwichai et al., 2022 [13], - representing half of a horizontal column, half of a vertical beam and gusset plates as shown in Fig. 2. The cross-section and cutting view of the SS-BRB are shown in Fig. 3, while the details of the SMA S-BRB are provided in Fig. 4. The SS SMA-BRB specimen was modeled based on the small-scale experimental setup by Qui et al., 2023 [14], as shown in Fig. 5.

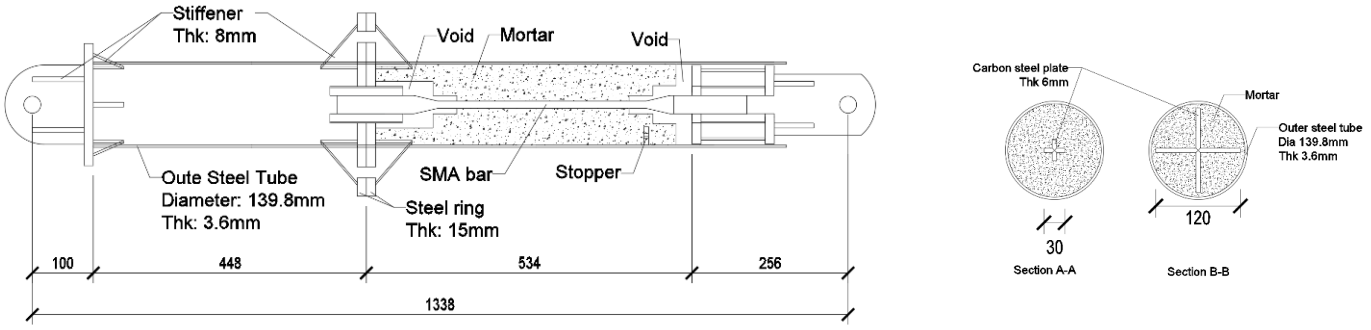

(a) Cutting view of SS-BRB

(b) Cutting section of SS-BRB

Fig. 3 Section detailing of SS-BRB

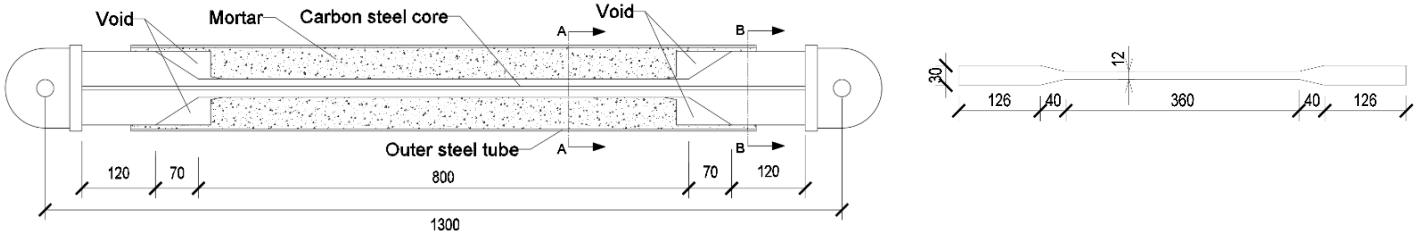

(a). Cutting view of SMA S-BRB

(b). SMA bar in SMA S-BRB

Fig. 4 Section detailing of SMA S-BRB

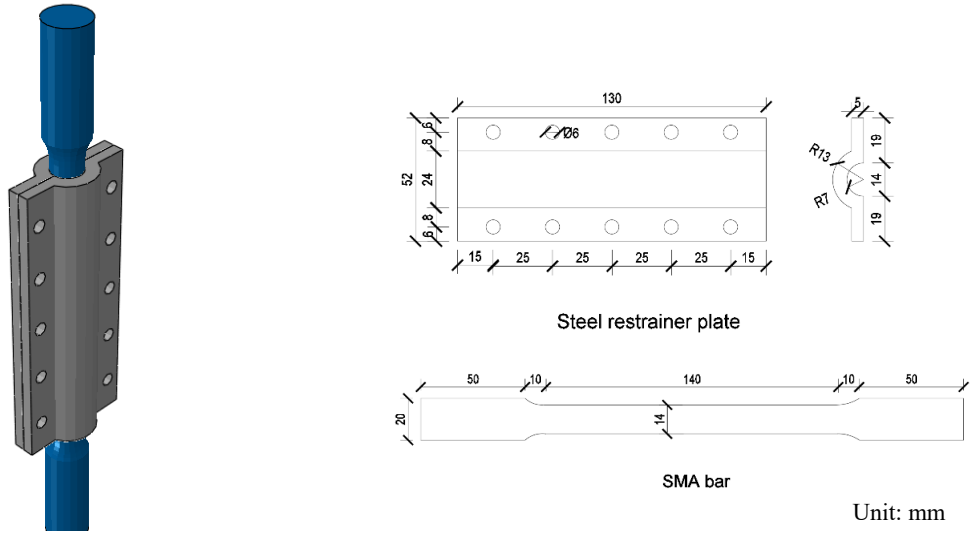

(a) Overview of SS SMA-BRB

(b) Section detailing of SS SMA-BRB

Fig. 5 Detail specimen of SS SMA-BRB

2.2 Material Properties

In the numerical modeling, choosing a comprehensive representation of the material characteristics is the most critical-part to ensure reliability. The SMA used in this model is a NiTi (Nickel-Titanium) alloy, modeled using the built-in superelasticity model available in Abaqus/CAE v2019, as shown in Fig.6. The input parameters were collected from an experiment test by Qui et al., 2023 [9], and are shown in Table 1. The carbon steel material used in the short BRBs was defined following ATSM A36 and ASTM A572 grade 50. The steel core of the SS-BRB specimen, modeled based on ASTM A36 properties from Narendra et al., 2019 [15], is detailed in Table 2. This material was modeled as a combined isotropic and kinematic hardening in Abaqus/CAE to accurately capture the hardening of material behavior under high cyclic stress like steel core. Moreover, ASTM A572 grade 50 material properties sourced from Sajid and Kiran, 2018 [16], was defined for non-critical members such as beam, column, steel restrainer plates, outer steel tube, and gusset plates. The detailed material properties parameters are shown in Table 3. The mortar was modeled as concrete damaged plasticity, following a study by Sovann, (2023) [17], and property inputs listed in Table 4.

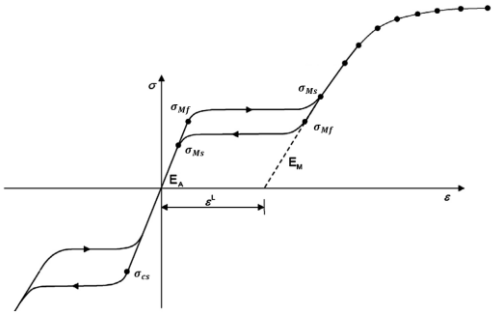

Fig. 6 Uniaxial superelastic response on NiTi alloy [18]

Table 1 Super Elasticity Input Parameters [9]

Specimen	E_A (GPa)	ν_A	E_M (GPa)	ν_M (MPa)	ϵ_L	σ_{Ms} (MPa)	σ_{Mf} (MPa)	σ_{As} (MPa)	σ_{Af} (MPa)	σ_{cs} (MPa)
SMA S-BRB (core bar) SS SMA-BRB (core bar)	20	0.33	19.4	0.33	0.026	350	436	310	200	350

Table 2 Combined Hardening Steel Model Input Parameters of ASTM A36 [15]

Specimen	E (GPa)	ν	σ_0 (MPa)	C_1 (MPa)	γ_1	Q_∞ (MPa)	b
SS-BRB (core part) SMA S-BRB (outer tube) SS SMA-BRB (restraint plate)	200	0.2	351.6	3447	50	137.89	10

Table 3 Steel Plasticity Input Parameters of ASTM A572 grade 50 [16]

Specimen	E (GPa)	ν	F_y (MPa)	F_u (MPa)	ϵ_u
SS-BRB (beam & column) SMA S-BRB (beam & column)	200	0.2	345	450	0.21%

Table 4 Concrete Damage Plasticity Input Parameters of Mortar [17]

Specimen	E (MPa)	ν	D_c	k	f_b/f_{c0}	k_c	μ
SS-BRB (core part) SMA S-BRB (outer tube)	26976	0.2	35º	0.1	50	2/3	0

Note: D_c is denoted as the dilation angle, k is denoted as eccentricity, k_c is ratio of the second stress. μ is denoted as viscosity

2.4 Mesh and Element Type of Finite Eelement

In finite element analysis, meshing and the selection element type and size are essential factors to avoid convergence issues, ensure model accuracy, and also reduce computational time. Two element types were used in this short BRBs model. Eight-node linear hexahedral solid elements with reduced integration (C3D8R) were applied to model braces with finer meshes concentrated in areas of high stress expected, such as the steel core part and critical section of the SMA bar. The steel-core was meshed with an element size equal to its thickness. Mesh size for critical section of the SMA bar of SMA S-BRBs and SS SMA-BRBs specimen were used approximately 6mm

and 1.5mm, respectively. Mortar and outer steel tube were meshed with element size of 12mm. On the other hand, Frame members (column and beam), considered lower-interest regions, were modeled using linear quadrilateral shell elements with reduced integration (S4R) to reduce computational time while maintaining accuracy. The beam divide as six mesh elements across both flanges and web, while the column divide as four mesh elements across the flanges and eight across the web.

2.5 Surface Contact

The interactions in the model were used as surface-to-surface contact. The tangential friction coefficients were 0.2 for the steel core to mortar interface and 0.3 for the outer steel tube to mortar interface [19]. On the other hand, The friction coefficient between the SMA bar and the steel restrainer plate was 0.3 [20]. For each specimen interaction surface, the normal behavior was defined as hard contact and allowed separation.

2.6 Boundary Condition

Fig. 7 illustrates the boundary conditions of the SS-BRB and SMA S-BRB specimens, modeled to match the conditions from the physical experiment. Both specimens were integrated into the same beam-column frame, with horizontal cyclic loading applied at the top of the vertical frame member (beam member). A reference point was established to control this cyclic displacement, enabling capture the hysteretic behavior of the braces.

For simplification, high-strength bolts at braces to frame and column-to-beam connections were not modeled explicitly but were modeled as a perfect contact with coupling constraints connect to hinge connector (Ux=Uy=Uz=UR2=UR3=0). Boundary conditions of column (horizontal frame member) were modeled as pinned (Ux=Uy=Uz=0) at both end, and an additional restraint (Uz = 0) was applied to the beam to prevent out-of-plane deformation during loading.

Fig. 8 shows the detailed boundary condition of the SS-SMA-BRB specimen, which was subjected to displacement-controlled axial cyclic loading. Bolted connections of the steel restrainer plates, as used in experiments, were simplified using MPC constraints for simplified modeling purposes.

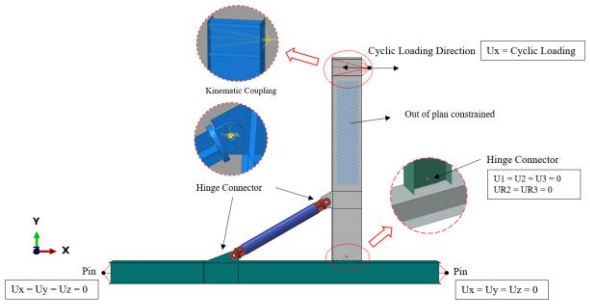

Fig. 7. Boundary condition for SS-BRBs and SMA S-BRBs specimen

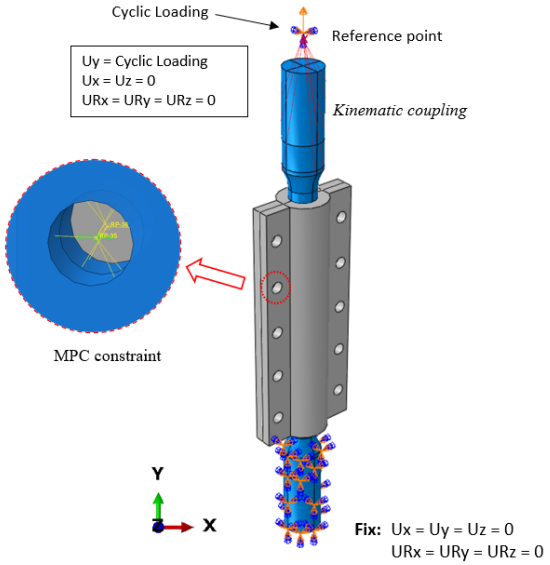

Fig. 8. Boundary condition for SS-BRBs and SS SMA-BRBs specimen

2.7 Loading Protocol

Two cyclic loading protocols were applied in the model. The first was used for SS-BRB and SMA S-BRB specimens, while the second was applied to SS SMA-BRBs. The first loading protocol (Fig. 9) was displacement-controlled, based on beam rotation drift ratio (Δ_b) of 0.25%, 0.5%, 0.75%, 1%, 1.5%, 2%, 3%, 4%, 5%, and 6%, with each amplitude repeated twice. The second protocol (Fig. 10) was strain-controlled, targeting SMA bar strain amplitude of 1%, 2%, 3%, 4%, and 5%, also applied in two cycles per amplitude.

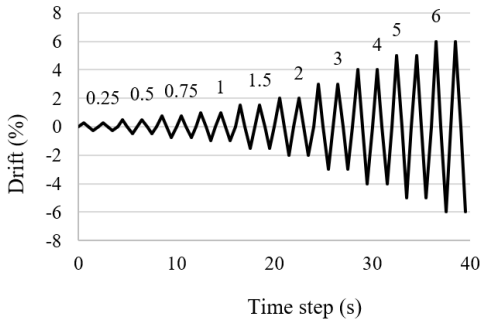

Fig. 9. Cyclic loading amplitude for SS-BRBs & SMA S-BRBs specimen [12]

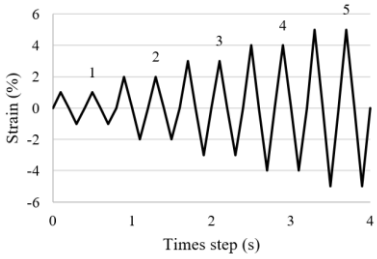

Fig. 10. Cyclic loading amplitude of SS SMA-BRBs specimen [14]

2.8 Model Validation

The three numerical models described above are validated by comparing experimental results in the literature [11],[12], [13].

Junda et al.[12] conducted an experimental study of large-scale sub-assemblage of short BRBs that were tested within a frame under cyclic loading. Three specimens were tested. The first specimen, selected for finite element analysis (FEA) study, featured pinned connections. The second and third specimens employed single-plate shear connections, with two different bolt sizes used between them. Short BRBs have an overall length of 1.3m and a core length of 0.8m with a core area of 324 mm^2. The short BRBs core had yield and ultimate stresses of 263 MPa and 379 MPa, respectively. High-strength grout was used to provide lateral support and prevent buckling of the steel core. As a result, there were slight pinching was observed in the hysteresis loops due to gaps at the pin connections. All of the specimen, yielding began at a drift of about 0.75%. For first specimen can carry a load capacity up to 6% drift but the second specimen had to stop at 5% drift due to bolt fracture, while the third specimen failed in the second cycle of 6% drift due to core fracture.

Srisupornwichai et al.[13] conducted an experiment focused on investigating the mechanical characteristics of two short BRB specimens by using carbon steel SS400 and NiTi SMA bar as a core part. In the finite element analysis (FEA) study was chosen short BRB specimen with NiTi SMA bar. Similar to the above experiment, the test configuration also was conducted within a frame under cyclic loading. The short BRBs were divided into two sections: one consisting of just the outer steel tube, and the other featuring an outer steel tube filled with mortar. In the mortar-filled section, there is a core with 690mm length. The result report showed that short BRBs using SS400 bar as core retain residual strain after serving cyclic loading while short BRBs using SMAs bar as the core could keep their original form.

Qui et al. [14] presented an experimental investigation of the mechanical behavior of small-scale short BRBs resist to cyclic loading. The brace was combined NiTi SMA bar with a steel buckling-restrained plate, which was selected FEA study. The SMA bar has a length of 260mm length and a diameter of 14mm. There are two 5mm thickness steel restrainer plates to encase the SMA bar. As a result, the specimen had higher strength and stiffness under compression than under tension. Tensile yielding occurred at approximately 43 kN with a deformation of 3.0 mm, while compressive yielding occurred at around 66 kN with 2.7 mm deformation. At the maximum deformation, the compressive strength reached 120 kN, and the tensile strength reached 56 kN.

3. RESULTS AND DISCUSSION

3.1 Hysteretic Response

The availability of experimental results from SS-BRB, SMA S-BRB, and SS SMA-BRB specimens facilitates comparison with numerical simulations. Fig. 11 presents a comparison of the force-drift hysteresis response between the experimental and numerical of the SS-BRB specimen. The numerical results provided fairly matched hysteresis loop compared with the experimental results. In numerical results, the hardening material behavior in each cycle both loading and unloading was well captured. However, the experimental curve exhibited a pitching behavior, likely due to a gap in the bolt-pin connection, whereas the numerical model utilized rigid hinge connectors. Unlike the SS-BRB, the numerical simulation of the SMA S-BRB exhibited notable discrepancies, as shown in Fig. 12. The hysteretic response curve from experimental results show narrow loops with minimal residual drift, demonstrating the superelastic recentering behavior of NiTi SMA. In contrast, the numerical model overestimates in residual deformation and lack to capture the superelastic behavior of SMA bar. These discrepancies are attributed to limitations in the constitutive SMA model and simplified assumptions regarding boundary conditions and interface interactions. Fig. 13 presents the SS SMA-BRB results, where numerical and experimental hysteresis loops showed good agreement. The hysteretic curve of the loading and unloading cycle exhibited the recentering ability of superelastic SMA.

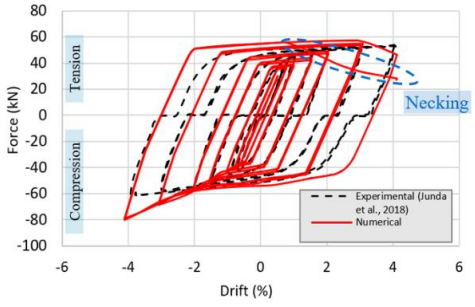

Fig. 11 Comparison between hysteretic response experimental and numerical results for SS-BRB

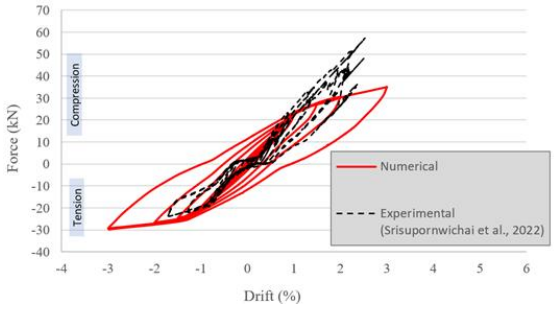

Fig. 12 Comparison between hysteretic response experimental and numerical results for SMA S-BRB

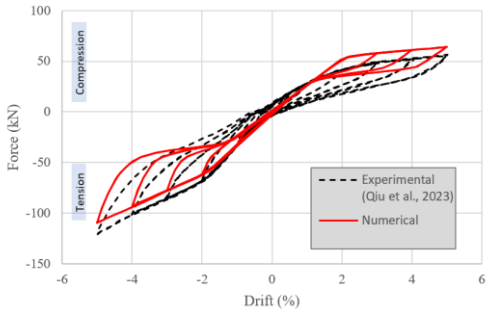

Fig. 13. Comparison between hysteretic response experimental and numerical results for SS SMA-BRB

3.2 Failure Modes

Following the simulation of cyclic loading, the failure modes were detected in the SS-BRB specimen, while both SMA S-BRBs and SS SMA-BRB specimens do not seem any notable failure. Fig. 14 shows critical stress concentration at the core of the SMA S-BRB specimen that was obtained at the 4% drift cycle. Similarly, the SS SMA-BRB specimen (Fig.15) did not show notable deformations at 4% drift. As shown in Fig. 16, necking occurred in the middle of the yield core segment similarly in the actual experimental. Additionally, high compressive stress was identified at both ends of the mortar void zone, likely due to the core stretching against the confinement material and pushing through the void between the restrainers, as shown in Fig. 17.

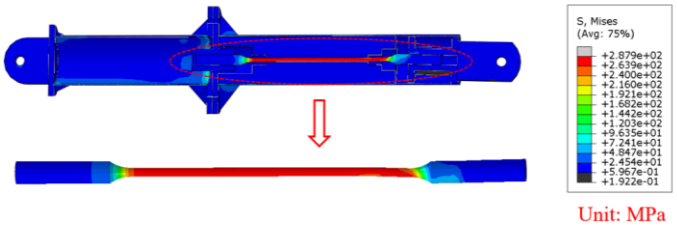

Fig. 14. Numerical result of Von Mises equivalent stress distribution of SMA S-BRB specimen at 4% drift ratio.

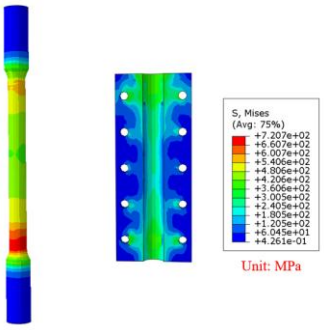

Fig. 15. Numerical result of Von Mises equivalent stress distribution of SS SMA-BRB specimen at 4% strain ratio.

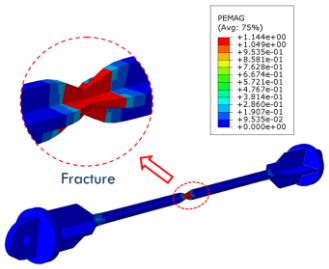

Fig. 16. Illustration of tensile failure of steel core SS-BRB specimen from numerical (Plastic Strain Magnitude) at 4% drift ratio

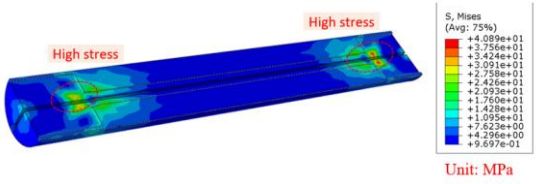

Fig. 17. Numerical result of Von Mises equivalent stress distribution in the mortar of SS-BRB specimen at 4% drift ratio.

4. CONCLUSIONS

In this study, the finite element analysis was carried out to investigate the performance ability for BRBs from steel and SMA by comparing the results with existing experiments. After investigating, the main findings are summarized as follows.

(1) The numerical results of SS-BRB specimen showed a fairly matched force-drift hysteresis response compared with the experimental result, which means the modeling and analysis procedure for the steel BRB is acceptable for numerical study. More than that, it was observed that the SS-BRB specimen exhibited tensile fracture failure at the steel core, indicating that the numerical simulation study provided a correct prediction as experimental observation.

(2) The SMA S-BRB specimen showed slightly difference in the load-displacement drift hysteresis loop between numerical and experimental results. This issue caused major reconsideration in both experimental setup and numerical modeling when it comes to sub-assemblage testing.

(3) The SS SMA-BRB specimen provided a good agreement of force-drift hysteresis response between numerical simulation and experiment. The hysteretic curve of the loading and unloading cycle exhibits the recentering ability of superelastic SMA and the modeling techniques are considered to be acceptable for performance numerical analysis of small or local scale BRBs.

Furthermore, as the numerical results for SMA S-BRB specimen showed inaccuracy, it is suggested to reconsideration in expanding the investigation to sub-assemblage testing and modeling techniques that focus on constitutive model material, interaction, and constraint.

ACKNOWLEDGMENTS

The authors would like to thank colleagues from the Department of Civil Engineering at King Mongut's University of Technology Thonburi in Thailand for providing technical support, including experimental data.

REFERENCES

[1] A. F. Ghowsi and D. R. Sahoo, "Near-field earthquake performance of SC-BRBs with optimal design parameters of SMA," *J. Constr. Steel Res.*, vol. 175, p. 106321, 2020.

[2] A. Watanabe, M. Fujimoto, A. Wada, E. Saeki, and T. Takeuchi, "Development of unbonded brace," *Dev. unbonded brace. Nippon Steel Corp. Build - ing Constr. Urban Dev. ment Div. Tokyo ment Div. Tokyo*, vol. 115, no. 1, pp. 91–96, 1990.

[3] J. Kim and Y. Seo, "Seismic design of steel structures with buckling-restrained knee braces," *J. Constr. Steel Res.*, vol. 59, no. 12, pp. 1477–1497, 2003.

[4] S. Leelataviwat, B. Suksan, J. Srechai, and P. Warnitchai, "Seismic Design and Behavior of Ductile Knee-Braced Moment Frames," *J. Struct. Eng.*, vol. 137, no. 5, pp. 579–588, 2011.

[5] T. Munkhunur, H. Tagawa, and X. Chen, "Steel rigid beam-to-column connections strengthened by buckling-restrained knee braces using round steel core bar dampers," *Eng. Struct.*, vol. 250, 2022.

[6] P. Doung and S. Leelataviwat, "Direct seismic design methods for buckling-retrained knee-braced frames with single plate shear connections," *Techno-Science Res. J.*, vol. 10, no. 1, pp. 25–32, 2022.

[7] L. G. Machado and D. C. Lagoudas, "Introduction to Shape Memory Alloys," in *Shape Memory Alloys*, 2008.

[8] C. Naresh, P. S. C. Bose, and C. S. P. Rao, "Shape memory alloys: A state of art review," *IOP Conf. Ser. Mater. Sci. Eng.*, vol. 149, no. 1, 2016.

[9] C. Qiu, Y. Yang, J. Liu, and T. Jiang, "Test of a novel self-centering brace using SMA slip friction damper," *J. Constr. Steel Res.*, 2023.

[10] C. Qiu, C. Fang, D. Liang, X. Du, and M. C. H. Yam, "Behavior and application of self-centering dampers equipped with buckling-restrained SMA bars," *Smart Mater. Struct.*, vol. 29, no. 3, 2020.

[11] C. Qiu and X. Du, "Seismic performance of multistory CBFs with novel recentering energy dissipative braces," *J. Constr. Steel Res.*, 2020.

[12] E. Junda, S. Leelataviwat, and P. Doung, "Cyclic testing and performance evaluation of buckling-restrained knee-braced frames," *J. Constr. Steel Res.*, vol. 148, pp. 154–164, Sep. 2018.

[13] W. Srisupornwichai, T. Thirabanchasak, and S. Srisamai, "Application of shape memory alloy in civil engineering," 2022.

[14] C. X. Qiu, T. Y. Jiang, J. W. Liu, and X. L. Du, "Self-centering knee-braced steel frames with buckling-restrained NiTi SMA bars: component test and structural behavior," *Gongcheng Lixue/Engineering Mech.*, vol. 40, no. 10, pp. 33–46, Oct. 2023.

[15] P. V. R. Narendra, K. Prasad, E. H. Krishna, V. Kumar, and K. D. Singh, "Low-Cycle-Fatigue (LCF) behavior and cyclic plasticity modeling of E250A mild steel," *Structures*, vol. 20, pp. 594–606, Aug. 2019.

[16] H. U. Sajid and R. Kiran, "Influence of high stress triaxiality on mechanical strength of ASTM A36, ASTM A572 and ASTM A992 steels," *Constr. Build. Mater.*, vol. 176, pp. 129–134, 2018.

[17] D. Sovann, "Assessment of the behavior of postinstalled bundled reinforcement in concrete under combined loadings using finite element method," Master's dissertation, Dep. Civil Eng., Institute of Technology of Cambodia, 2023.

[18] ABAQUS, *ABAQUS Analysis User's Manual Version 2020*. 2020.

[19] B. Sitler and T. Takeuchi, "Higher-mode buckling and friction in long and large-scale buckling-restrained braces," *Struct. Des. Tall Spec. Build.*, vol. 30, no. 1, Jan. 2021.

[20] N. M. Mirzai and J. W. Hu, "Pilot study for investigating the inelastic response of a new axial smart damper combined with friction devices," *Steel Compos. Struct.*, vol. 32, no. 3, pp. 373–388, 2019.

Techno-Science Research Journal V13 (Special Issue) (2025) P 158-162

Content list available at ITC

Techno-Science Research Journal

Journal Homepage: www.ric.itc.edu.kh

Techno-Science Research Journal

Modified Diatomite with Alkaline Activation and $KMnO_4$ Impregnation for Ethylene Scavenging

Theara Yann[1], Charinee Winotapun[2], Phanny Yos[3], Lee Hwei Voon[4], Orathai Boondamnoen[1*]

[1]*Department of Materials Science, Faculty of Science, Chulalongkorn University, Bangkok 10330 Thailand*
[2]*PTT MCC BIOCHEM Co., Ltd., 555/2 Energy Complex Tower, Building B 14th Floor, Vibhavadi Rangsit Road, Chatuchak, Bangkok 10900, Thailand*
[3]*Research Innovation Center, Institute of Technology of Cambodia, Materials Science and Structure, Institute of Technology of Cambodia, Russian Federation Blvd., P.O. Box 86, Phnom Penh 12156, Cambodia*
[4] *Nanotechnology and Catalysis Research Centre, Universiti Malaya, 50603 Kuala Lumpur, Malaysia*

Received: 1 November 2024; Revised: 1 January 2025; Accepted: 20 June 2025; Available online: October 2025

Abstract: *Fruits and vegetable usually accelerate ripening and degrading due to production of ethylene gas, the hormone gas which is released from fresh fruits and vegetable after harvest. Therefore, ethylene scavengers in powder form are commonly used in packaging to preserve the postharvest quality of fresh products. The naturally-based adsorbent is the preferred choice for safe packaging applications. In this study, the raw diatomite (R-DA) was activated with alkaline at 85 °C for 1 h. Subsequently, alkaline-activated diatomite (Alk-DA) was impregnated with 1.5 N of potassium permanganate ($KMnO_4$) to improve its ethylene scavenging. The characteristics of raw and modified diatomite were analyzed using Attenuated Total Reflectance-Fourier Transform Infrared (ATR-FTIR) spectroscopy, X-Ray Fluorescence (XRF) spectrometry, X-Ray Diffraction (XRD), and Gas Chromatography (GC). The results revealed there was reduced the amount of SiO_2 and formation the more silanol group on the surface diatomite after activated with NaOH. Moreover, the tetrahedral Mn-O stretching vibration appeared on the Potassium permanganate impregnated Alk-DA (Alk-DA-P) without any shift in chemical structure of diatomite. Furter, there was a significant increase in ethylene removal capacity, approximately 41% for Alk-DA and 77% for Alk-DA-P compared to R-DA.*

Keywords: Alkaline activated, diatomite, ethylene scavenger, $KMnO_4$ impregnated, surface area

1. INTRODUCTION

Ethylene is typically produced by fresh fruits and vegetables after they are harvested. This gas accelerates the ripening process of fruits and vegetable. Additionally, high concentration of ethylene lead to detrimental effects on quality and the shelf-life of fruits and vegetables [1]. Even at low concentrations, typically within the range of 10-100 nL/L, ethylene can exert significant effects on the chemical stability and physical characteristics of fruits and vegetables [2]. Reducing and elimination the level of ethylene in the packaging possible is to prolong the shelf-life of fresh fruit and reduce the postharvest losses. Generally, ethylene scavengers are utilized to control and remove the concentration of ethylene in form of sachet [3].

Potassium permanganate ($KMnO_4$) is one of the highest effective ethylene eliminate compared to other ethylene scavenger. It oxidized with ethylene gas onvert to CO_2 water irreversible [4]. In humidity content, $KMnO_4$ attacks the double bond in the C_2H_4 molecule and oxidizes it. When ethylene is oxidized by $KMnO_4$, it produces acetaldehyde, which is then oxidized to acetic acid, then carbon dioxide, and water. As displayed in reaction equation (3-4) below [3, 5].

$$3CH_2CH_2 + 2KMnO_4 + H_2O \rightarrow 2MnO_2 + 3CH_3CHO + 2KOH \quad \text{(Eq. 1)}$$

$$CH_3CHO + 2KMnO_4 + H_2O \rightarrow 3CH_3COOH + 2MnO_2 + 2KOH \quad \text{(Eq. 2)}$$

$$3CH_3COOH + 8\ KMnO_4 \rightarrow 6CO_2 + 8MnO_2 + 8KOH + H_2O \quad \text{(Eq. 3)}$$

* Corresponding author: *Orathai Boondamnoen*
E-mail: *orathai.b@chula.ac.th*

Overall oxidation reaction is

$$3CH_3COOH + 12KMnO_4 \rightarrow 6CO_2 + 12MnO_2 + 12KOH \quad \text{(Eq. 4)}$$

Base on the reaction procedure, the color of potassium permanganate powder will change from purple to dark brown, due to the permanganate anion (MnO_4^-) being converted to MnO_2. However, $KMnO_4$ cannot directly use with product due to its toxicity. To ensure safety and practicality, $KMnO_4$ is placed on trays or dishes or sachet, and introduced into or onto carriers including silica gel, activated carbon, activated alumina metal oxides, clay, zeolite, and layer silicates [4, 5]. Due to surface adsorption, ethylene can physically adsorb to porous surfaces. To increase its surface area and exposure to air, which can improve the efficacy of its oxidation. Additionally, the cooperation of $KMnO_4$ with porous substances can be attained by creating an adsorption-oxidation system that combines physical adsorption from porous substances with chemical oxidation via $KMnO_4$ [6].

Diatomite is a lightweight, fine-porous sedimentary rock composed of the opaline skeletons of diatomic algae, primarily made of silica. It typically comprises silicon dioxide (SiO_2) about 87-91%, along with aluminum oxide (Al_2O_3) and ferric oxide (Fe_2O_3) [7]. Due to its high porosity (80-90% voids), low thermal conductivity, chemical inertness, and large specific surface area, diatomite has been extensively studied for various industrial applications, including filtration, pharmaceuticals, and agriculture. It is also utilized as an adsorbent in the petroleum, food, and chemical industries. The presence of silanol (Si-OH) groups on its surface enhances its attraction to organic compounds, but natural diatomite often lacks sufficient Si-OH groups [8, 9]. As a result, chemical and physical activation techniques, including acid and alkaline treatments, are employed to enhance its affinity properties to organic compounds. [10].

The study aimed to evaluate the feasibility of using low-cost local diatomite as an effective removal for ethylene gas. Various forms of diatomite; Raw (R-DA), alkaline activated (Alk-DA), and $KMnO_4$ impregnated (DA-P) were prepared and analyzed for their efficiency in ethylene removal, along with their chemical functional groups and structural properties.

2. METHODOLOGY

2.1 Materials

Diatomite (Diatomacius earth) medical grade was supplied by TTK Science Co., Ltd. Sodium Hydroxide NaOH (Micropearls), AR1325 was purchased from RCI Labscan Limited, Thailand. Potassium Permanganate (Grade AR, KemAus™) KA414 was purchased from S.M.Chemical Supplies Co.,Ltd.

2.2 Preparation of alkaline-activated diatomite (Alk-DA)

Raw diatomite (R-DA) was purified using distilled water and activated with NaOH. Specifically, a 10% w/v solution of the purified particles was prepared with 5.0 mol/L of NaOH, stirred at 500 rpm for 1 h at 85 °C. Afterward, centrifugation is performed at 4000 rpm for 30 minutes to separate the components and washed with distilled water until pH netralize. Finally, the sample was dried in an oven at 80 °C for 24 h.

2.3 Preparation of potassium permanganate impregnated diatomite (Alk-DA-P)

The 5 g of alkaline-activated diatomite (Alk-DA) was immersed in 100 mL of 1.5 N $KMnO_4$ and sake for 2 min. After that it was kept at a low temperature (15-20 ºC) for 2h. Then, centrifuge at 4000 rpm for 45 min to separate the supernatant from the pellet. Finally, the pellet is dried in the oven at 50 ºC for 2 days.

2.4 Structural and chemical element analysis

Attenuated Total Reflectance-Fourier Transform Infrared (ATR-FTIR) spectroscopy was employed to assess the transmittance across a wave number range of 4000 to 400 cm^{-1}. The study examined the interaction between NaOH, $KMnO_4$ and the particles during the modifying process. The elemental composition and crystallographic structure of samples were determined using X-Ray Fluorescence (XRF) spectrometer (Rigaku MiniFlex 600C) and X-Ray Diffraction (XRD) (Rigaku MiniFlex 600C X-Ray Diffractometer) with x-ray target Cu-Ka radiation, 600w, scanning range of 2θ 10-90 degree.

2.5 Ethylene removal capacity testing

The ethylene removal capacity of R-DA, Alk-DA, and Alk-DA-P were evaluated using a Gas Chromatograph (Agilent 6890N) with a flame ionization detector. Approximately 0.4-0.5 g of samples were placed in sealed glass jars, into which 3 ppm of ethylene gas was injected. The jars were incubated at 25 °C for 0, 3, 12, and 24 h. After incubation, the headspace gas was collected and analyzed by gas chromatography. The amount of ethylene in the headspace was calculated and expressed in percentage of ethylene removal, based on comparisons with a standard curve and retention times.

3. RESULTS AND DISCUSSION

3.1 Attenuated Total Reflectance-Fourier Transform Infrared (ATR-FTIR) analysis

The Attenuated Total Reflectance-Fourier Transform Infrared (ATR-FTIR) spectra of the chemical functional groups in raw diatomite (R-DA), alkaline activated diatomite (Alk-DA), pure $KMnO_4$, and $KMnO_4$-impregnated Alk-DA (Alk-DA-P) were showed in Fig. 1. The ATR-FTIR spectra revealed sharp

bands at 1093 cm^{-1} and 473 cm^{-1}, indicating Si-O-Si stretching and bending vibrations. A smaller band at 617 cm^{-1} was attributed to Si-O-Al stretching due to alumina [11]. Bands at 795 cm^{-1} and 1617 cm^{-1} were associated with OH vibrations from absorbed water. Alk-DA samples displayed a band at 3422 cm^{-1}, attributed to H-bonded OH vibrations of silanol groups formed from NaOH activation [12]. The FTIR spectra of pure $KMnO_4$ showed bands at 902 cm^{-1} and 925 cm^{-1} for Mn-O stretching, which were also present in Alk-DA-P without any positional shift, indicating no chemical interaction between diatomite and $KMnO_4$ [13, 14].

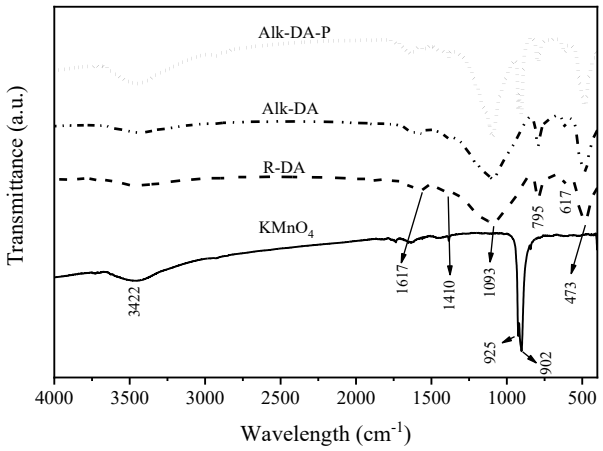

Fig. 1. ATR-FTIR spectra of R-DA, $KMnO_4$, Alk-DA and Alk-DA-P.

3.2 X-Ray Fluorescence (XRF) analysis

The chemical composition of R-DA, Alk-DA, and Alk-DA-P was analyzed using X-Ray Fluorescence (XRF) as showed in Table 1. The results showed that SiO_2 is the primary component of R-DA at 91.15%, along with trace amounts of Al_2O_3, MnO, P_2O_5, K_2O, and Fe_2O_3. After impregnated with $KMnO_4$, the MnO amount increased significantly, while the SiO_2 content decreased following activation with NaOH, indicating silicon leaching during the alkaline activation process [15].

Table 1. The chemical composition of R-DA, Alk-DA, and Alk-DA-P (%wt).

Samples	SiO_2	Al_2O_3	MnO	P_2O_5	K_2O	Fe_2O_3
R-DA	91.15	1.86	0.05	1.17	0.79	3.17
DA-P	89.91	2.23	0.06	1.11	0.39	3.62
Alk-DA-P	66.09	1.45	18.72	0.81	0.46	0.57

3.3 X-Ray Diffraction (XRD) analysis

The structure of R-DA, Alk-DA, and Alk-DA-P were analyzed by using X-Ray Diffraction (XRD). The results, shown in Fig. 2. illustrated diffraction peaks at 2θ of 21.77°, 28.23°, 31.18°, and 35.94°, indicating the presence of crystalline silica (SiO_2), specifically cristobalite, in all samples. However, the intensity of the peak at 21.77° decreased in the Alk-DA, and Alk-DA-P compared to R-DA, suggesting that the diatomite structure was partially destroyed after activation with NaOH and impregnation with $KMnO_4$ [15]. In addidion, the diffraction peaks located at 2θ: 19.55, 23.93, 24.95, 25.88, 26.62, 27.57, 30.29, 34.90, 40.96° which were assigned to the present of $KMnO_4$ in the Alk-DA-P [16, 17].

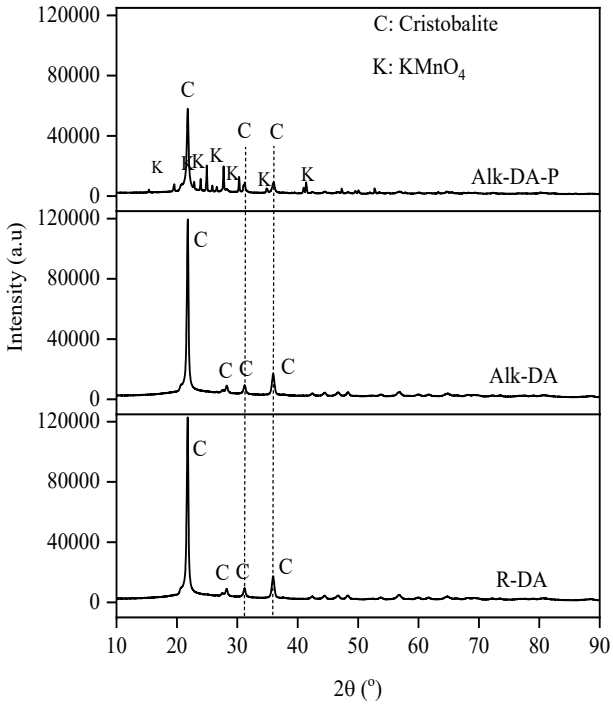

Fig. 2. XRD patterns of R-DA, Alk-DA and Alk-DA-P.

3.4 Ethylene removal capacity testing

The ethylene removal capability of R-DA, Alk-DA, $KMnO_4$, and Alk-DA-P at 3, 12, and 24 h incubation was shown in the Fig. 3. The results demonstrated that Alk-DA had higher ethylene removal capability compared to R-DA, and $KMnO_4$. The ethylene removal increased rapidly within the first at 3 h for all samples. From 3 to 12 and 24 h, R-DA, and $KMnO_4$ exhibited a gradual increase in capability. In contrast, the ethylene removal of Alk-DA exhibited a significant increase even after 3 h. The ethylene removal capability increased maybe due the specific surface area of diatomite was increase after activated with NaOH [18]. Moreover, the ethylene removal of Alk-DA-P was superior compared to $KMnO_4$, R-DA, and Alk-DA. The total of ethylene removal of R-DA, Alk-DA, $KMnO_4$, and Alk-DA-P were obtained approximately 21.26, 36.21,

28.55, and 93.48% at 24 h, respectively. The ethylene removal capability of pure $KMnO_4$ was significantly lower than that of impregnated particles probably because pure $KMnO_4$ would undergo oxidation upon when attached to ethylene. In contrast, the $KMnO_4$ impregnated on Alk-DA could perform both oxidation and adsorption. The impregnation of $KMnO_4$ into the Alk-DA particles enhances their performance by facilitating better interaction and oxidation of ethylene molecules, thereby leading to more efficient removal [3].

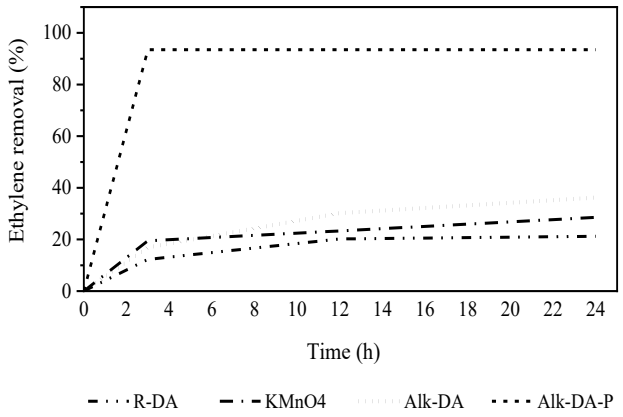

Fig. 3. Ethylene removal capacity of R-DA, $KMnO_4$, Alk-DA, and Alk-DA-P.

4. CONCLUSIONS

This research highlights the effectiveness of diatomite modified through alkaline activation and impregnated with $KMnO_4$ for ethylene scavenging. Characterization confirmed the reduction the amount of SiO_2 and formation of Si-OH groups with Alk-DA and showed tetrahedral Mn-O stretching vibrations from $KMnO_4$ impregnation without shift the chemical structure of diatomite. The ethylene removal capacity of diatomite improved with these modifications, with the Alk-DA-P achieving the highest removal rate of 93.48%. The study concludes that the enhanced ethylene adsorption capacity of Alk-DA-P is linked to its ability to promote better interaction and oxidation of ethylene molecules.

Future research should investigate the impregnation of potassium permanganate using various concentrations of $KMnO_4$ and different amounts of diatomite. Additionally, the effectiveness of the modified diatomite should be assessed in terms of its ability to extend the shelf life of fresh fruits under various storage conditions.

ACKNOWLEDGMENTS

The author expresses gratitude to the Department of Materials Science at Chulalongkorn University, Thailand and the Higher Education Institution Project, Institute of Technology of Cambodia, Cambodia for their financial support. The author also thanks the International Research Partnership Fund (IRP2024) for facilitating international research collaboration and acknowledges the support from the National Metal and Materials Technology Center in Thailand and the Nanotechnology and Catalysis Research Centre at Universiti Malaya for their facilities assistance.

REFERENCES

[1] A. Ebrahimi, M. Zabihzadeh Khajavi, A. M. Mortazavian, H. Asilian-Mahabadi, S. Rafiee, M. Farhoodi, and S. Ahmadi, "Preparation of novel nano–based films impregnated by potassium permanganate as ethylene scavengers: An optimization study," *Polymer Testing,* vol. 93, 2021.

[2] K. Sadeghi, Y. Lee, and J. Seo, "Ethylene Scavenging Systems in Packaging of Fresh Produce: A Review," *Food Reviews International,* vol. 37, no. 2, pp. 155-176, 2019.

[3] G. Awalgaonkar, R. Beaudry, and E. Almenar, "Ethylene-removing packaging: Basis for development and latest advances," Compr Rev Food Sci Food Saf, vol. 19, no. 6, pp. 3980-4007, Nov 2020.

[4] M. A. Mariah, J. M. Vonnie, K. H. Erna, N. M. Nur'Aqilah, N. Huda, R. Abdul Wahab, and K. Rovina, "The Emergence and Impact of Ethylene Scavengers Techniques in Delaying the Ripening of Fruits and Vegetables," *Membranes,* vol. 12, no. 2, p. 117, 2022.

[5] M. H. Hernández, G. B. Martínez Hernández, F. Avalos-Belmontes, M. A. Castillo-Campohermoso, J. C. Contreras-Esquivel, and F. Artés-Hernández, "Potassium Permanganate-Based Ethylene Scavengers for Fresh Horticultural Produce as an Active Packaging," *Food Engineering Reviews,* vol. 11, no. 3, pp. 159-183, 2019.

[6] C. Wang and A. Ajji, "Development of a novel ethylene scavenger made up of pumice and potassium permanganate and its effect on preservation quality of avocados," *Journal of Food Engineering,* vol. 330, p. 111101, 2022.

[7] S. I. Suzan and Q. S. Ali, "Evaluation of Egyptian diatomite for filter aid applications,"

Physicochemical Problems of Mineral Processing vol. 47, pp. 113-122, 2011.

[8] S. É. Ivanov and A. V. Belyakov, "Diatomite and its applications," *Glass and Ceramics,* vol. 65, no. 1-2, pp. 48-51, 2008.

[9] S. Kollalu, B. P. Nagabovanalli, and D. M. Jean, "Diatomaceous earth as source of silicon on the growth and yield of rice in contrasted soils of Southern India," *Journal of Soil Science and Plant Nutrition,* vol. 18, no. 2, pp. 344-360, 2018.

[10] S. Sinpichai, R. Yuangsawad, and D. Na-Ranong, "Effects of Acid and Alkaline Treatments on Efficiency of Diatomaceous Earth in Removal of Tetracycline in Aqueous Solution," *ASEAN Engineering Journal,* vol. 13, no. 3, pp. 173-179, 2023.

[11] J. Madejova´, M. Janek, P. Komadel, H. H.-J., and H. C. Moog, "FTIR analyses of water in MX-80 bentonite compacted from high salinary salt solution systems," *Applied Clay Science,* vol. 20, pp. 255-271, 2002.

[12] B. Xue, T. Yi, D. Li, F. Li, and F. Luo, "The effect of alkali treatment and organic modification of diatomite on the properties of diatomite composite separators," *New Journal of Chemistry,* vol. 46, no. 48, pp. 23268-23275, 2022.

[13] V. D. S C, L. G. Prasad, E. Kumar, D. Muthuraj, and V. Jothy, "Structural, Optical, and AC Conductivity Properties of Polyaniline/Manganese dioxide nanocomposites via In Situ Polymerization," 05/01 2018.

[14] S. A. Moon, B. K. Salunke, B. Alkotaini, E. Sathiyamoorthi, and B. S. Kim, "Biological synthesis of manganese dioxide nanoparticles by Kalopanax pictus plant extract," *IET Nanobiotechnol,* vol. 9, no. 4, pp. 220-5, Aug 2015.

[16] N. Chanka, W. Donphai, M. Chareonpanich, K. Faungnawakij, G. Rupprechter, and A. Seubsai, "Potassium Permanganate-Impregnated Amorphous Silica-Alumina Derived from Sugar Cane Bagasse Ash as an Ethylene Scavenger for Extending Shelf Life of Mango Fruits," *ACS Omega,* vol. 9, no. 6, pp. 6749-6760, Feb 13 2024.

[17] M. E. Becerra, N. P. Arias, O. H. Giraldo, F. E. López Suárez, M. J. Illán Gómez, and A. Bueno López, "Soot combustion manganese catalysts prepared by thermal decomposition of KMnO4," *Applied Catalysis B: Environmental,* vol. 102, no. 1-2, pp. 260-266, 2011.

[18] B. Erdoğan and M. Akbelen, "Ethylene Adsorption on Acid-Treated Clay Minerals," *Adsorption Science & Technology,* vol. 30, pp. 265-274, 03/01 2012.

Techno-Science Research Journal V13 (Special Issue) (2025) P 163-170

Content list available at ITC

Techno-Science Research Journal

Journal Homepage: www.ric.itc.edu.kh

Techno-Science Research Journal

Validation on Proposed Equation for Pullout Resistance of Tyfo® Fibranchors Inserted into Concrete Cylinder

Vanny Yam[1*], Narith Prok[2], Sovann Sathya Rath[2], Sovanvichet Lim[2], Wee Keong Ong[3]

[1]*Materials Science and Structure, Institute of Technology of Cambodia, Russian Federation Blvd., P.O. Box 86, Phnom Penh, Cambodia*

[2]*Research and Innovation Center, Institute of Technology of Cambodia, Russian Federation Blvd., P.O. Box 86, Phnom Penh, Cambodia*

[3]*Assistant General Manager, Fyfe Asia Pte Ltd, 6 Clementi Loop #02-20, Singapore 129814*

Received: 1 November 2024; Revised: 1 January 2025; Accepted: 20 June 2025; Available online: October 2025

Abstract: *Fiber-Reinforced Polymers (FRP) are widely used in various industries, including construction, to enhance the strength and durability of structures. Glass Fiber-Reinforced Polymer (GFRP) anchors are crucial in preventing the debonding of FRP from concrete substrates and facilitating load transfer within structural elements. This study needs to improve previous experimental results to refine the proposed equation due to inconsistencies observed. The scope of the study involves 60 specimens of Tyfo® FibrAnchors with varying diameters (10 mm, 12 mm, 15 mm, 20 mm, and 25 mm) and embedding depths (50 mm, 100 mm, 150 mm, 200 mm, and 250 mm) inserted into concrete cylinders confined by GFRP laminate. Due to inconsistencies in the experimental data from the previous study, 48 specimens were chosen to replace certain cases, and 12 more specimens used for validate the proposed equations. This research lies in its improved experimental methodologies to improve and refine current equations using updated data. The proposed equations for predicting the pullout resistance and failure modes of fiber anchors inserted into concrete cylinders with concrete compressive strengths from 20 MPa to 30 MPa have been developed. Additionally, the numerical simulations were conducted using Abaqus software to verify the proposed equations. The results of this research Best-Fit Model and design model for pullout resistance of a single FRP anchor based on failure mode have been proposed for using with the concrete strength from 20 MPa to 30 MPa.*

Keywords: FRP Anchors, Pullout Resistance, Concrete Cylinder, Experimental, Numerical Simulation

1. INTRODUCTION

Fiber-reinforced polymers (FRP) are composite materials consisting of a polymer matrix reinforced with fibers [1]. These materials are extensively utilized in various industries, including construction, for enhancing the strength and durability of structures. FRP anchor systems are essential for delaying or preventing the debonding of externally bonded FRP from the concrete substrate, addressing the issue of low tensile strength.

Additionally, anchor systems serve to facilitate load transfer at critical points within structural elements and can offer a ductile failure mode, contrasting with the abrupt and brittle failure modes associated with FRP debonding and rupture.

Current research has made significant steps in improving the test setup for fiber anchors inserted into concrete cylinders confined by GFRP. These improvements have led to enhanced results in the ultimate failure load, particularly in concrete specimens with compressive strengths of 20 MPa and 30 MPa. Despite these existing data, the experimental results from previous research need to be verified and improved, as some of the results observed were inconsistent, which can affect the proposed equations [2], [3].

The research aims to conduct experimental and numerical simulations to achieve several primary objectives:

- To improve the existing equations
- To integrate the equations of concrete compressive strengths from 20 MPa to 30 MPa
- To verify the proposed equations with numerical simulations.

2. METHODOLOGY

The experimental study utilized a total of 48 Tyfo® Fiber anchor specimens inserted into the concrete cylinders,

* Corresponding author: Yam Vanny
E-mail: *vannyyam.vanny@gmail.com;* Tel: *+855 10 434 804*

measuring 150 mm in diameter and 300 mm in height. All concrete cylinders were enveloped with a single layer of GFRP laminate, ensuring a 150 mm overlap length. The investigation focused on analyzing the effects of two key variables: anchor diameters and embedment depths. The upper portion of the anchor head was enveloped with an 80×300 mm GFRP laminate and reinforced with steel wire, as illustrated in Fig. 1, to mitigate the risk of the anchor tearing when conducting the pullout test.

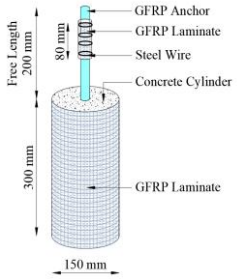

Fig. 1. Representation of the specimen

Due to inconsistencies in the experimental data from the previous study, specific specimens were selected to replace some cases for further investigation to enhance the accuracy and reliability of the experiment results and improve the proposed equation.This study conducted two concrete strengths of 20 MPa and 30 MPa. The specimens that were selected for each case are presented in Table 1.

Table 1. Summary of test specimens for both concrete strengths

Embedment depth (mm)	Anchors diameter (mm)									
	10		12		15		20		25	
	Concrete Strengths (MPa)									
	20	30	20	30	20	30	20	30	20	30
50	-	-	4	-	-	4	-	-	4	-
100	4	-	4	-	-	-	4	4	-	-
150	-	-	-	-	-	2	-	2	4	4
200	-	-	-	4	-	-	-	-	-	-
250	-	-	-	-	-	-	-	-	4	-
Total	48									

2.1 Material and property

2.1.1 Concrete Specimen

The concrete cylinders were formulated in accordance with ASTM Standards [4] and possesses compressive strengths of 20 MPa and 30 MPa at the age of 28 days. The composition of the concrete mixture, is detailed in Table 2.

Table 2. The composition of concrete mix per 1 m^3

Compressive strength (MPa)	Water (kg)	Cement (kg)	Gravel (kg)	Sand (kg)
20	209.25	280.38	1055.06	839.06
30	209.25	345.87	1036.12	801.33

2.1.2 Epoxy

The experimental setup utilized Tyfo® S Epoxy, known for its low viscosity and high strength properties. This two-component epoxy matrix, commonly used as a chemical adhesive for bonding purposes, aligns closely with the manufacturer's specified typical epoxy qualities outlined in Table 3.

Table 3. Properties of Tyfo® S Epoxy [5]

Property	Typical test value
Tensile Strength	72.4 MPa
Tensile Modulus	3.18 GPa
Elongation Percent	5.00%
Compressive Strength	86.2 MPa
Compressive Modulus	3.2 GPa
Flexural Strength	123.4 MPa
Flexural Modulus	3.12 GPa

2.1.3 GFRP Anchor

The experiment employs Tyfo® SEH Composite Anchors, featuring uni-directional reinforcing glass fiber bundles infused with Tyfo® S Epoxy. Fig. 2 displayed Tyfo® SEH Anchors. Furthermore, Table 4 outlines the standard mechanical properties related to Tyfo® SEH Anchors.

Fig. 2. Tyfo® SEH Anchors

Table 4. Properties of Tyfo® SEH Anchors [6]

	Tensile Strength (MPa)	Tensile Modulus (GPa)	Ultimate Elongation (%)
	Dry fiber		
	3240	72.4	4.5
	Composite anchor		
Test value	575	26.1	2.2
Design value	460	20.9	1.76

2.1.4 GFRP Laminate

The Tyfo® SEH-25A composite, illustrated in Fig. 3, is a specialized uni-directional glass fabric utilized within the FRP System. The composite gains enhanced strength and flexibility. Table 5 outlines some properties of this laminate.

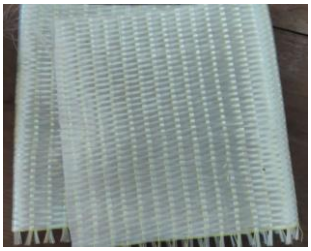

Fig. 3. Tyfo® SEH-25A reinforcing fibric

Table 5. Properties of Tyfo® SEH-25A Composite [7]

Properties	Test Value	Design Value
Tensile Strength in primary fiber direction (MPa)	521	417
Tensile Modulus (GPa)	26.1	20.9
Elongation at break (%)	2.0	1.76
Tensile Strength in 90° to primary direction (MPa)	25.8	20.7
Laminate Thickness (mm)	0.5	0.5

2.2 Specimen preparation for experimental

When the concrete cylinder reached 28 days, a hole was drilled according to the diameter and embedment depth of GFRP anchor at the central point of the concrete cylinder situated on the circular surface and cleaned by using the air compressor.

Fig. 4. Process of hole drilling of concrete cylinder

The surfaces around the concrete cylinder and holes were then thoroughly cleaned with water and left to dry for a day before wrapping the GFRP laminate. The GFRP laminate was saturated with epoxy before being wrapped around the concrete cylinder, as shown in Fig. 5.

Fig. 5. Wrapping process of GFRP laminate

The dust and debris were removed using the air compressor before filling the holes with epoxy. The GFRP anchors were saturated in epoxy and then inserted into the pre-drilled holes, as shown in Fig. 6.

Fig. 6. Process of GFRP anchor installation

A day after anchor installation, the upper end of the GFRP anchor was wrapped with the GFRP laminate and tightened using steel wire, as shown in Fig. 7.

Fig. 7. Process of wrapping GFRP laminate at the top end of the GFRP anchor

2.3 Pullout test

After wrapping the upper end of the GFRP anchor, the pullout test of the GFRP anchor was conducted after 3 days of curing. Prior to the test, the specimen was placed in a steel plate frame to facilitate installation into the testing machine displayed in Fig. 8. The steel plate frame consists of two steel plates, one with a 120 mm diameter hole and 150 mm of thickness where the free end of the GFRP anchor was inserted into the top wedge grips of the machine, and another plate welded to a large steel bolt for connection with the bottom wedge grips of the machine, as depicted in Fig. 9.

Fig. 8. Placing the specimen in the steel plate frame

Fig. 9. Process of pullout test

The pullout test was conducted on the specimen with a loading rate of 10 N/s. The pullout loads were continuously monitored and recorded by the load cell of the testing machine. Following the testing process, two failure modes were observed: combined cone-bond failure (CB) as depicted in Fig. 10, and anchor rupture failure (RF) as illustrated in Fig. 11.

Fig. 10. Combined cone-bone failure (CB)

Fig. 11. Anchor rupture failure (RF)

3. RESULTS AND DISCUSSION

3.1 Combined Cone-Bond Failure (CB)

When the anchor diameters were 10 mm, 12 mm, and 15 mm, the CB failures occurred between 50 and 100 mm of embedment depth, while anchor diameters of 20 mm and 25 mm failed in CB for all embedment depths of this study for a concrete strength of 20 MPa. Additionally, for a concrete strength of 30 MPa, the CB failures occurred when the anchor diameters were 10 mm and 12 mm with the embedment depth between 50 mm and 100 mm, while anchor diameters of 15 mm, 20 mm, and 25 mm failed in CB for all embedment depth

Assuming a uniform distribution of bond stress along the anchor's embedment depth (Cook, 1998) [8], the average bond stress can be calculated as follows:

$$\tau = \frac{F_u}{\pi d h_{emd}} \qquad \text{(Eq. 1)}$$

Where: F_u is pullout load, d is diameter of anchor, and h_{emd} is embedment depth of anchor

3.2 Anchor Rupture Failure (RF)

Anchor rupture failure (RF) occurs when the tensile strength of the anchor is lower than the bond strength between the anchor and concrete. This indicates that the embedment depth of the anchor is sufficient to prevent different concrete failures, and the anchor consequently reaches its tensile capacity. Anchor ruptures were observed on specimens of small anchor diameters of 10 mm, 12 mm, and 15 mm at embedment depths ranging from 150 mm to 250 mm for a concrete strength of 20 MPa. Additionally, for a concrete strength of 30 MPa, the RF failures occurred when the anchor diameters of 10 mm, and 12 mm at embedment depths ranging from 150 mm to 250 mm, while the anchor diameters of 15 mm, 20 mm, and 25 mm failed in RF at embedment depths of 200 mm and 250 mm. The theoretical capacity of the anchor was calculated using:

$$F_{FRP} = A_f f_{FRP} \qquad \text{(Eq. 2)}$$

Where:

f_{FRP} = 575 MPa : Tensile strength of FRP anchor

$A_f = \frac{\pi}{4} d^2$: Sectional area of anchor

3.3 Best-Fit Model for Pullout Resistance of a Single FRP Anchor Based on Failure Mode

An individual FRP anchor's pullout resistance (N_u) is given by $N_u = \min(N_{cb}, N_{rf})$.

3.3.1 Concrete Strength 20 MPa

Best-fit model for pullout resistance of a single FRP anchor for a concrete strength of 20 MPa is therefore given as:

$$N_u = \min(N_{cb}, N_{rf}) \qquad \text{(Eq. 3)}$$

$$N_{cb} = (198.14 d^{-1.065}) \pi d h_{emd}$$
$$N_{rf} = (11.181 d^{-0.981})\, A_{FRP}\, f_{FRP} \qquad \text{(Eq. 4)}$$

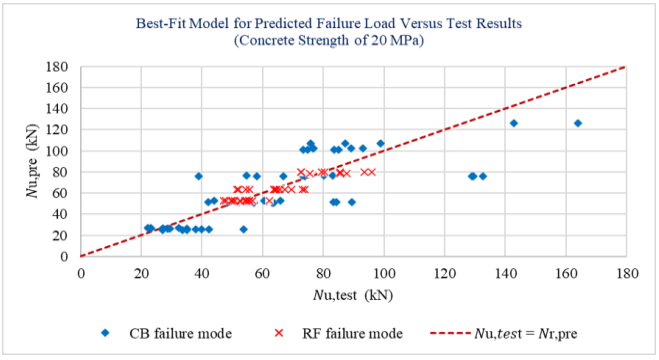

Fig. 12. Predicted failure loads versus test results for concrete strength of 20 MPa

3.3.2 Concrete Strength 30 MPa

Best-fit model for pullout resistance of a single FRP anchor for a concrete strength of 30 MPa is therefore given as:

$$N_u = \min(N_{cb}, N_{rf}) \qquad \text{(Eq. 5)}$$

$$N_{cb} = (50.735 d^{-0.527}) \pi d h_{emd} \qquad \text{(Eq. 6)}$$

$$N_{rf} = (6.122 d^{-0.712})\, A_{FRP}\, f_{FRP} \qquad \text{(Eq. 7)}$$

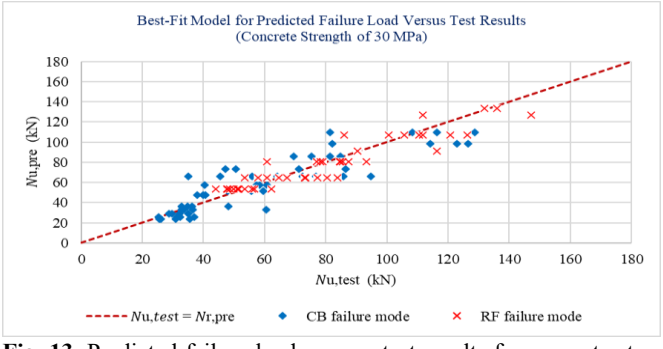

Fig. 13. Predicted failure loads versus test results for concrete strength 30 MPa

3.3.3 Concrete Strengths from 20 MPa to 30 MPa

Best-fit model for pullout resistance of a single FRP anchor for integrating between concrete strengths of 20 and 30 MPa is therefore given as:

$$N_u = \min(N_{cb}, N_{rf}) \quad \text{(Eq. 8)}$$

$$N_{cb} = [38.334(d)^{-0.796}(f'_c)^{0.296}]\pi d h_{emd} \quad \text{(Eq. 9)}$$

$$N_{rf} = (12.121 d^{-1.008})\, A_{FRP}\, f_{FRP} \quad \text{(Eq. 10)}$$

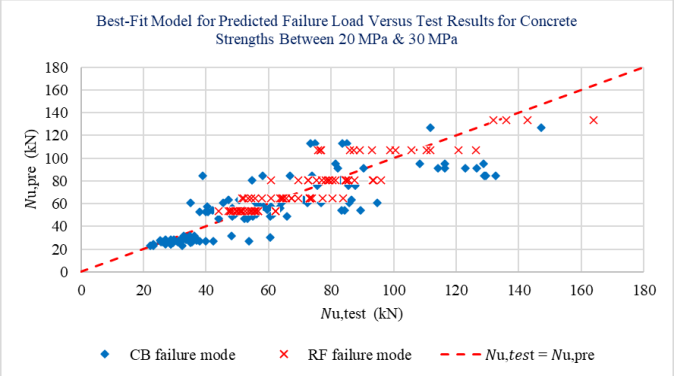

Fig. 14. Predicted failure loads versus test results for concrete strengths of 20 MPa and 30 MPa

3.4 Design Model for Pullout Resistance of a Single FRP Anchor Based on Failure Mode

The key elements for the design model, the pullout resistance of the FRP anchor for design, are denoted by (Nr,pre) and given by Nr,pre = min(τ'cb·Ncb, α'rf·Nrf), where τ'cb is the calibration factor for the design model for CB failure mode and α'rf is RF failure mode. The percentage of the test results exceeding the proposed equation results is denoted by PE. Additionally, according to Kim and Smith (2010) [9], PE for design model is 5%.

The calibration factors for the design model to obtain the percentage of the test results exceeding the proposed equation results, PE 5%, are presented in Table 6.

Table 6. The calibration factors for design model

The calibration factor	CB failure mode (τ'_{cb})	RF failure mode (α'_{rf})
Concrete strength 20 MPa	0.71	0.82
Concrete strength 30 MPa	0.70	0.81
Concrete strengths from 20 MPa to 30 MPa	0.68	0.81

3.4.1 Concrete Strength 20 MPa

Design model for pullout resistance of a single FRP anchor for a concrete strength 20 MPa is therefore given as:

$$N_{r,pre} = \min(0.71 \cdot N_{cb}, 0.82 \cdot N_{rf}) \quad \text{(Eq. 11)}$$

$$N_{cb} = (198.14 d^{-1.065})\pi d h_{emd} \quad \text{(Eq. 12)}$$

$$N_{rf} = (11.181 d^{-0.981})\, A_{FRP}\, f_{FRP} \quad \text{(Eq. 13)}$$

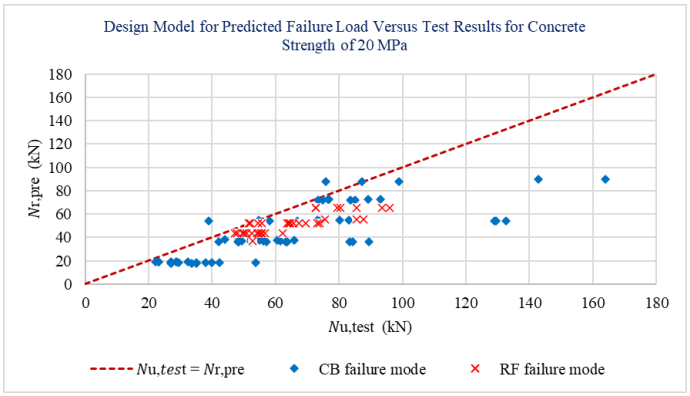

Fig. 15. The design model for predicted versus test results for a concrete strength of 20 MPa

3.4.2 Concrete Strength 30 MPa

Design model for pullout resistance of a single FRP anchor for a concrete strength 30 MPa is therefore given as:

$$N_{r,pre} = \min(0.7 \cdot N_{cb}, 0.81 \cdot N_{rf}) \quad \text{(Eq. 14)}$$

$$N_{cb} = [38.334(d)^{-0.796}(f'_c)^{0.296}]\pi d h_{emd} \quad \text{(Eq. 15)}$$

$$N_{rf} = (12.121 d^{-1.008})\, A_{FRP}\, f_{FRP} \quad \text{(Eq. 16)}$$

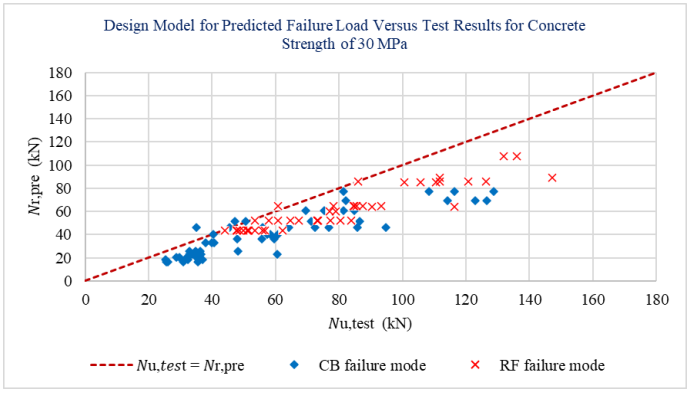

Fig. 16. The design model for predicted versus test results for a concrete strength 30 MPa

3.4.3 Concrete Strengths from 20 MPa to 30 MPa

Design model for pullout resistance of a single FRP anchor for integrating between concrete strengths of 20 MPa and 30 MPa is therefore given as:

$$N_{r,pre} = \min(0.68 \cdot N_{cb}, 0.81 \cdot N_{rf}) \quad \text{(Eq. 17)}$$

$$N_{cb} = [38.334(d)^{-0.796}(f'_c)^{0.296}]\pi d h_{emd} \quad \text{(Eq. 18)}$$

$$N_{rf} = (12.121 d^{-1.008})\, A_{FRP}\, f_{FRP} \quad \text{(Eq. 19)}$$

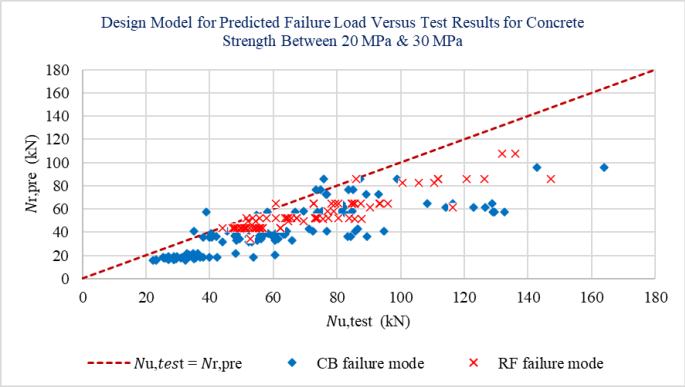

Fig. 17. The design model for predicted versus test results for integrating between concrete strengths of 20 MPa and 30 MPa

4. NUMERICAL SIMULATION

4.1 Modeling procedure

The model was defined as quarter of 3D cylinder (deformable solid) with radius 75 mm and 300 mm in height as shown in Fig. 12. The method of creating the model was outlined as follows:

- Define a quarter of 3D deformable solid for a concrete cylinder of diameter 75mm.
- Sketch the top surface of the concrete according to the diameter of the anchor, assuming an epoxy thickness of 0.2 mm.
- Then partition the cell according to the sketched surface. Define a quarter of 3D deformable wire for FRP laminate of radius 75 mm.
- Assign the material to each component (concrete, GFRP anchor, epoxy, and GFRP laminate).
- Generate meshes for each specimen component.
- Apply appropriate boundary conditions to the model for accurate results.
- Establish the analysis steps by defining the loading conditions, such as displacement or load increments.
- Run the analysis and monitor the specimen response.

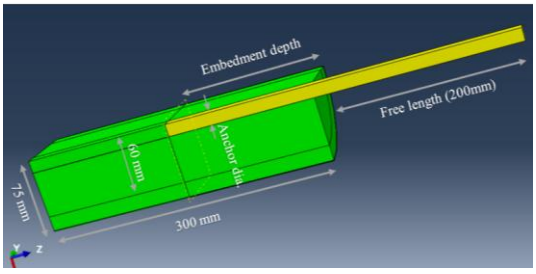

Fig. 18. Details of the model

The static general procedure was used in this simulation. The load was applied 8.0 mm of displacement at the top of the anchor. The boundary condition was used:

- On both sides of the concrete and anchor surfaces in the X and Y axis directions, the displacement was applied u_1=0 and u_2=0.
- On the top surface of the concrete, 15 mm from the side was applied u_3=0 in the Z axis.

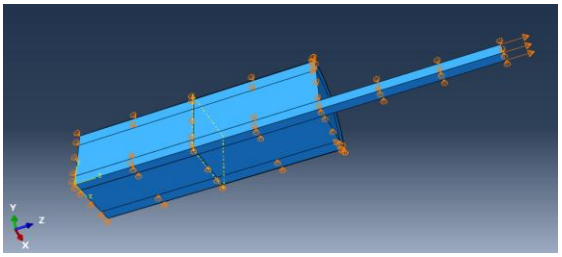

Fig. 19. Loading and boundary condition of the model

In this modeling, structured meshing was used. Fig. 20 displays the mesh for each component. Concrete, GFRP laminate, GFRP anchor and epoxy were assigned the element type of standard stress with default setting for element deletion.

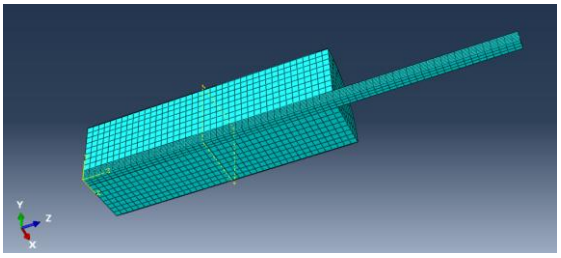

Fig. 20. Meshing for each component

4.2 Results of analysis

For every concrete strength, a total of 25 specimens with different anchor diameters (10 mm, 12 mm, 15 mm, 20 mm, and 25 mm) and embedment depths (50 mm, 100 mm, 150 mm, 200 mm, and 250 mm) have been created. The force at failure of anchor was measured at the moment of anchor rupture or when the concrete damage was reached, which is indicated by the breakdown of the concrete elements. The stress for the GFRP anchor and the concrete when the anchor failed in the RF mode is depicted in Fig. 19.

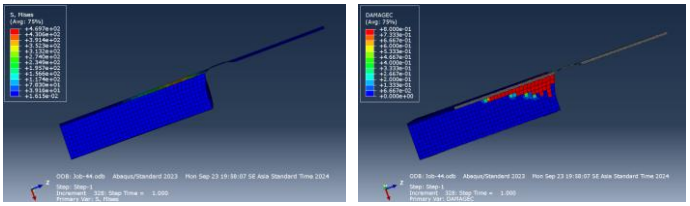

Fig. 21. Stress on the GFRP anchor and concrete for RF failure mode

The results of the analysis obtained from Abaqus compared to the results from the experimental test and the proposed equation for a concrete strength of 20 MPa and 30 MPa for all series of specimens are presented in Figs. 22 to 31.

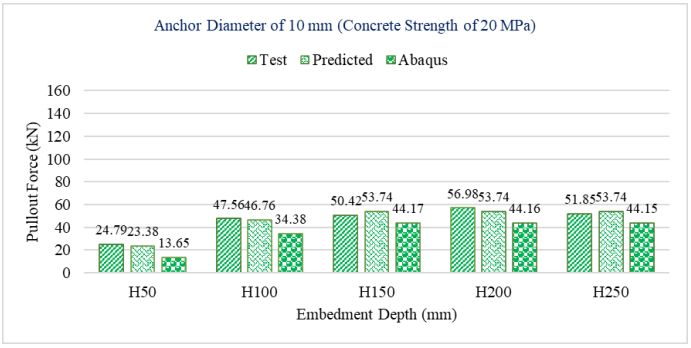

Fig. 22. Pullout force from test, predicted equation and Abaqus for anchor diameter of 10 mm

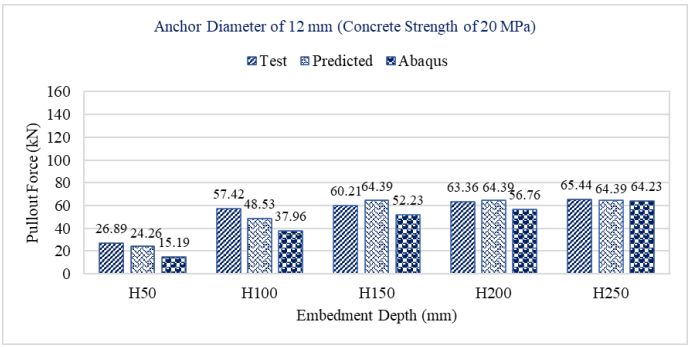

Fig. 23. Pullout force from test, predicted equation and Abaqus for anchor diameter of 12 mm

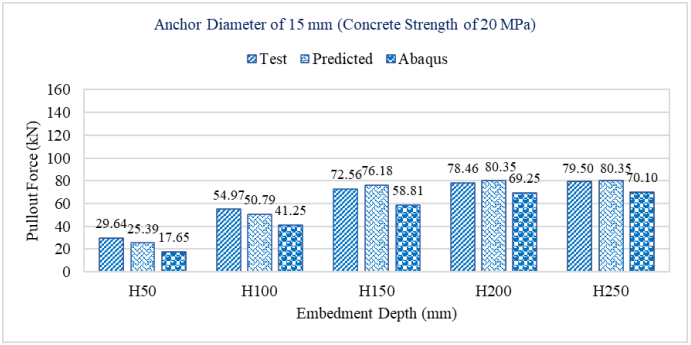

Fig. 24. Pullout force from test, predicted equation and Abaqus for anchor diameter of 15 mm

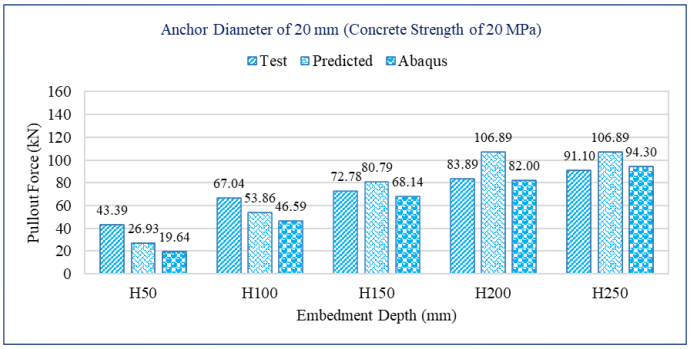

Fig. 25. Pullout force from test, predicted equation and Abaqus for anchor diameter of 20 mm

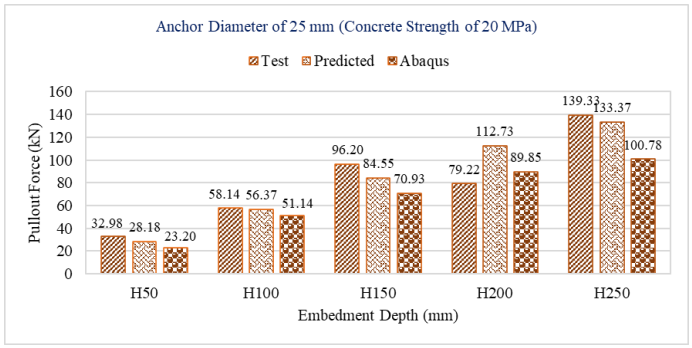

Fig. 26. Pullout force from test, predicted equation and Abaqus for anchor diameter of 25 mm

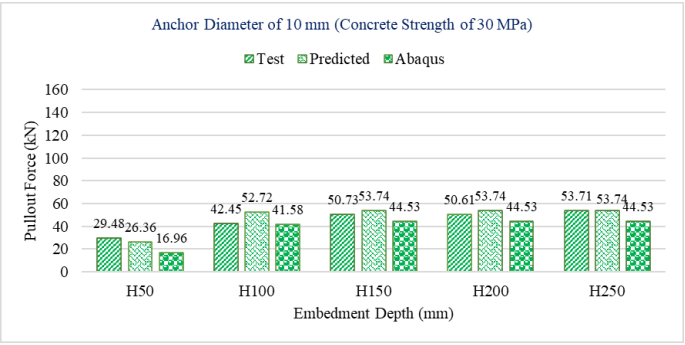

Fig. 27. Pullout force from test, predicted equation and Abaqus for anchor diameter of 10 mm

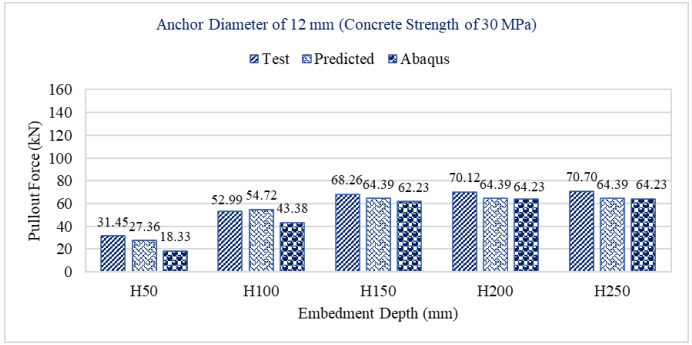

Fig. 28. Pullout force from test, predicted equation and Abaqus for anchor diameter of 12 mm

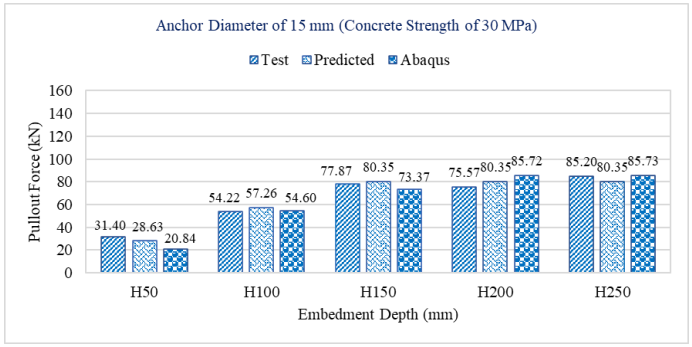

Fig. 29. Pullout force from test, predicted equation and Abaqus for anchor diameter of 15 mm

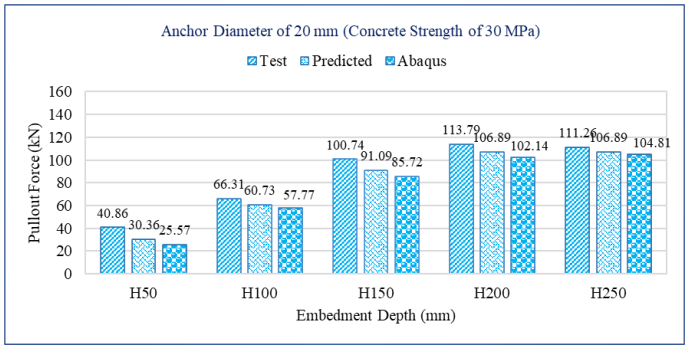

Fig. 30. Pullout force from test, predicted equation and Abaqus for anchor diameter of 20 mm

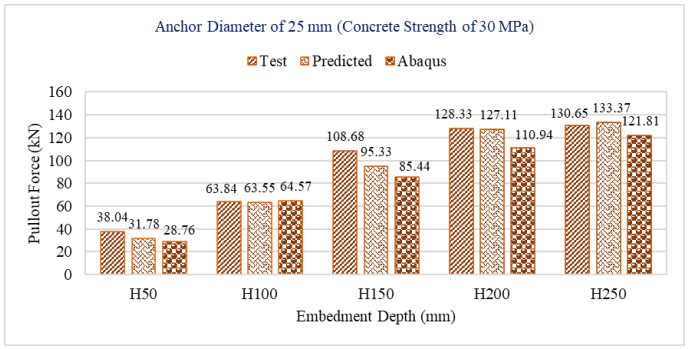

Fig. 31. Pullout force from test, predicted equation and Abaqus for anchor diameter of 25 mm

Table 6. Failure mode from Abaqus for both concrete strengths

Anchors diameter (mm)		10	12	15	20	25
Concrete strength (MPa)		20/30	20/30	20/30	20/30	20/30
Embedment depth (mm)	50	CB	CB	CB	CB	CB
	100	CB	CB	CB	CB	CB
	150	RF	CB	CB	CB	CB
	200	RF	CB/RF	CB	CB	CB
	250	RF	RF	CB	CB	CB

Most of the Abaqus results indicate close accordance with the experimental and proposed equation results. And all of the results produced from Abaqus are slightly lower than the results obtained from the proposed equation and experiment.

5. CONCLUSIONS

According to the results from the experimental, analytical, and numerical investigations presented in this paper, the following conclusion may be drawn:

- The existing equation for the predicted failure load for concrete strengths of 20 MPa and 30 MPa has been improved using the updated data.
- The best-fit model integrated of concrete strengths between 20 MPa and 30 MPa for the predicted failure load has been proposed.
- The design models for the predicted failure load with concrete strengths of 20 and 30 MPa and the design model for the predicted failure load integrated concrete strengths between 20 and 30 MPa have been proposed.
- The results from the proposed equation for the predicted failure load for both concrete strengths demonstrate good accuracy compared to the results from test and Abaqus.

ACKNOWLEDGMENTS

The author would like to express gratitude to the Faculty of Civil Engineering at the Institute of Technology of Cambodia for invaluable laboratory and technical support and extend the warmest thanks to Fyfe Asia Pte Ltd, which provided funding and materials.

REFERENCES

[1] S. C. Das and M. Nizam, "Applications of fiber reinforced polymer composites (FRP) in civil engineering," *International journal of advanced structures and geotechnical engineering*, vol. 3, no. 3, pp. 299-309, 2014.

[2] A. Mengla, P. Narith, R. Sovann Sathya, L. Sovanvichet, and O. Wee Keong "Experimental and Numerical of Tyfo® Fibr Anchors Embedded in Low Compressive Strength Concrete Cylinder," *Techno Sience Research Journal,* Vol. 12, 2024.

[3] T. Lymeng, P. Narith, R. Sovann Sathya, L. Sovanvichet, and O. Wee Keong "Experimental and Numerical Study of Tyfo® Fibr Anchors Inserting to Concrete Cylinder Confined by Glass Fiber Reinforcing Polymer," *Techno Sience Research Journal,* Vol. 12, 2024.

[4] A. Standard, "Standard practice for making and curing concrete test specimens in the laboratory," *ASTM International,* 2016.

[5] AEGION, 2015. Tyfo® S Saturant Epoxy.

[6] AEGION, 2018. Tyfo® SEH Composite Anchors.

[7] AEGION, 2005. Tyfo® SEH-25A Composite using Tyfo® S Epoxy.

[8] R. A. Cook, J. Kunz, W. Fuchs, and R. C. Konz, "Behavior and design of single adhesive anchors under tensile load in uncracked concrete," *Structural Journal,* vol. 95, no. 1, pp. 9-26, 1998.

[9] S. J. Kim and S. T. Smith, "Pullout strength models for FRP anchors in uncracked concrete," *Journal of composites for construction,* vol. 14, no. 4, pp. 406-414, 2010